CHARLES UNIVERSITY IN PRAGUE
Faculty of Mathematics and Physics
and
UNIVERSITY PARIS XI IN ORSAY

DOCTORAL THESIS

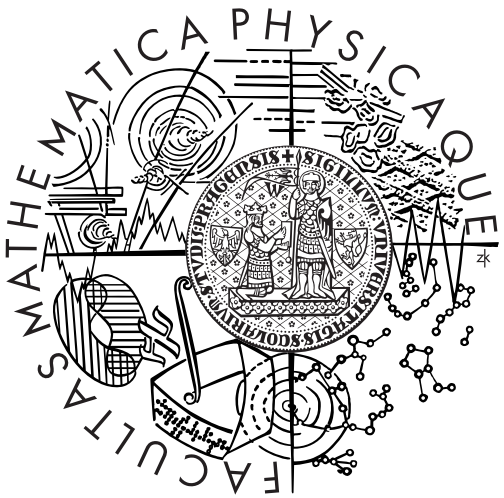

Oldřich KEPKA

QCD and Diffraction in the ATLAS Experiment at the LHC

November 2009

Institute of Physics of the Academy of Sciences, Prague
and
Particle Physics Division, CEA, Saclay

Supervisors: Mgr. Alexander Kupčo, Ph.D.
Dr. Christophe Royon

Field of Study: Physics, Nuclear and Particle Physics

THÈSE
DE DOCTORAT DE L'UNIVERSITÉ PARIS XI
et
DE L'UNIVERSITÉ CHARLES, PRAGUE

Spécialité
Champs, Particules, Matière

présentée par

Oldřich KEPKA

pour obtenir les grades de

DOCTEUR DE L'UNIVERSITÉ PARIS XI
et
DE L'UNIVERSITÉ CHARLES, PRAGUE

QCD et diffraction dans l'expérience ATLAS au LHC

Thèse soutenue le 6 Novembre 2009 devant le jury composé de :

Etienne AUGÉ	Président
Laurent FAVART	Rapporteur
Alexander KUPČO	Membre invité (co-encadrant)
Ken PEACH	
Albert de ROECK	
Christophe ROYON	Directeur de thèse
W. James STIRLING	Rapporteur
Josef ŽÁČEK	

Thèse préparée au Service de Physique des Particules du CEA de Saclay
et
à l'Institut de Physique, Académie des Sciences de Prague

Acknowledgment

First of all, I would like to express many thanks to my supervisor Christophe Royon from CEA Saclay who closely followed my work during the three-year Ph.D. studies. His deep understanding of experimental issues and methods in modern particle physics helped me to absorb quickly through discussions the rather complicated subjects: Diffraction and Quantum Chromodynamics. I appreciate that I could organize my work in the way which suited me the best.

Also important was the help of my second advisor Alexander Kupčo from the Institute of Physics, Academy of Science in Prague. The interesting discussions which we held during lunches shaped my understanding of particle physics. I am grateful to him for providing me with the code for the proton tracking inside LHC ring. Both my advisors were extremely helpful especially when I was writing the thesis, giving comments and corrections regardless of their actual geographic locations.

In addition, I am indebted to Maarten Boonekamp from CEA Saclay. Although we had only couple of discussions, they always turned to be very useful and stimulated my work significantly. I enjoyed them very much. It was him who answered many my questions concerning the implementation of forward processes inside the Monte Carlo generator and motivated further studies on the rapidity gap definition in the ATLAS calorimeter.

Listing the closest collaborators, I should not omit to mention Emilien Chapon, the talented bright young undergraduate with whom it was a pleasure to work on the anomalous quartic coupling studies. I would also like to thank Robi Pechanski and Cyrille Marquet from the theory division in Saclay for proposing me to work with them on two papers concerning the BFKL predictions, Jean-Francois Laporte for discussions on the muon reconstruction, and Laurent Schoeffel for explanations of the H1 diffractive measurements. I am also grateful to Vojtěch Juránek who never hesitated to help solving problems concerning the ATLAS software. Special thanks to my good friend Jiří Kvita for the long nights playing guitars and for proof-reading parts of my manuscript. Also, I very much appreciate Susan Juza's comments on my English.

The acknowledgment must also be given to SPP/IRFU CEA Saclay and Institute of Physics, Academy of Science in Prague headed respectievely by Bruno Mansoulié (followed later by Ursula Bassler), and by Jiří Chýla, and of course the personnel in these institutes who solved many of my non-physics related problems stemming often simply from my double affiliation. I was happy to get to known the young chemist Kevin O'Cleirigh who helped me to improve my French and made the life in Massy-Palaiseau more enjoyable. Merci.

On the other hand, it is an honor to thank Etienne Augé for accepting to be a president of my jury, and Ken Peach, Albert de Roeck, and Josef Žáček to be members of the committee. Moreover, I express especially many thanks to Laurent Favart and W. James Stirling for reading the manuscript and writing the thesis reports.

Last but not least, I would like to thank my parents Zdeňka Kepková and Oldřich Kepka for encouraging me in almost anything what I have done, and to Zuzana Bilická for staying close to me even if far away.

I declare that I completed this thesis myself with the use of cited literature only. I agree with using this thesis.

Saclay, November 2, 2009 Oldřich Kepka

Dedicated to my parents.

QCD and Diffraction in the ATLAS Experiment at the LHC

Author:	Oldřich Kepka
Department:	Institute of Physics of the Academy of Sciences, Prague
Supervisors:	Mgr. Alexander Kupčo, Ph.D.
	Dr. Christophe Royon
e-mail address:	kupco@fzu.cz
	royon@hep.saclay.cea.fr

key words:	particle diffraction, two-photon exchange, exclusive production, anomalous coupling, forward physics

Abstract:

This thesis is devoted to study the hard diffractive and exclusive events at the experiment ATLAS. Right after the start-up of a new proton accelerator LHC in CERN they will be identified using the rapidity gap method. We therefore developed an alternative definition of the observed energy in the ATLAS calorimeter to identify diffractive and exclusive events. During the high luminosity operation of the accelerator, forward detectors (AFP) recently proposed to be installed far from the interaction point approaching the beam at few millimeters will allow to tag the intact scattered protons in these events unambiguously.

The simplest exclusive production is due to the exchange of two photons. We implemented two-photon exchanges in FPMC generator and analyzed the two-photon production of W and Z-pairs decaying leptonically to calculate sensitivities on triple and quartic anomalous gauge couplings of electroweak boson to photons. The obtained results are remarkable mainly for the quartic couplings. Their current limits can be improved by almost two orders of magnitude with early data and by four orders of magnitude using large luminosity and AFP detectors. In addition, we used two-photon dimuon events to determine the time needed to align one of the AFP stations with respect to beam to a desired precision.

Another type of exclusive events is the central exclusive production (CEP) initiated by the exchange of two gluons. We compared in detail the prediction of the available models to the Tevatron exclusive dijet data. This is crucial to predict the cross section at the LHC where the CEP of Higgs boson is an important part of the AFP physics program.

QCD et diffraction dans l'expérience ATLAS au LHC

Auteur :	Oldřich Kepka
Departement :	l'Institut de Physique, Académie des Sciences de Prague
Directeurs de thèse :	Mgr. Alexander Kupčo, Ph.D.
	Dr. Christophe Royon
Adresse électronique :	kupco@fzu.cz
	royon@hep.saclay.cea.fr

Mots clés :	diffraction, échange de deux photons, production exclusive, couplage anormal, physique à l'avant

Résumé:

Dans cette thèse, nous étudions la diffraction dure et d'événements exclusifs dans l'expérience ATLAS au LHC. Dès le démarrage du LHC, il sera possible d'identifier de tels événements en utilisant la méthode des domaines en rapidité vides d'énergie. Une méthode alternative pour mesurer l'énergie dans le calorimèter et identifier de tels événements est developpée. Nous décrirons également l'installation de détecteurs de protons à l'avant (AFP) approchant la ligne de faisceau à quelques millimètres qui sont nécessaires à haute luminosité.

La production diffractive exclusive la plus simple est due à l'échange de deux photons, processus qui a été implémenté dans le générateur FPMC. On utilise dans cette thèse la production de paires de bosons Z et W pour calculer les sensibilités dans les couplages de jauge anormaux trilinéaires et quartiques entre les bosons électrofaibles et le photon. Les résultats sont particulièrement importants pour les couplages quartiques où la sensibilité actuelle peut être ameliorée par presque deux ordres de grandeur avec les premières données, et quatre ordres de grandeur à haute luminosité en utilisant les détecteurs à l'avant. D'autre part, les événements dimuons produits par échange de photons sont également importants pour aligner les détecteurs à l'avant.

Un autre type d'événements diffractifs exclusifs concerne la production centrale initiée par l'échange de deux gluons. On a comparé en detail la prédiction des modèles exclusifs de production de jets avec les mesures realisées au Tevatron. Ceci est crucial pour prédire les sections efficaces de production de boson de Higgs au LHC qui est une part importante du programme de physique d'AFP.

QCD a difrakce v experimentu ATLAS na urychlovači LHC

Autor:	Oldřich Kepka
Katedra:	Fyzikální ústav akademie věd v Praze
Vedoucí práce:	Mgr. Alexander Kupčo, Ph.D.
	Dr. Christophe Royon
e-mail vedoucích:	kupco@fzu.cz
	royon@hep.saclay.cea.fr

klíčová slova:	částicová difrakce, dvoufotonová produkce, exkluzivní produkce, anomální vazba, dopředná fyzika

Abstrakt:

Tato doktorská práce je věnována studiu procesů tvrdé difrakce a exkluzivních případů v experimentu ATLAS. Ty budou v zápětí po spuštění nového protonového urychlovače LHC v CERNu identifikovány pomocí takzvaných mezer v rapiditách (rapidity gaps). Pro tento účel byla vyvinuta nová definice viditelné energie v kalorimetru detektoru ATLAS a aplikována na výběr difrakčních a exkluzivních případů. V práci je taktéž popsána instalace dopředných detektorů (AFP) umístěných do vzdálenosti několika milimetrů od svazku, které umožní detekování těchto událostí při vysokých luminozitách přímo registrováním odražených protonů.

Nejjednodušší typ exkluzivní produkce je založen na výměně dvou fotonů. Ta byla implementována do FPMC generátoru a využita ke studiu dvoufotonové produkce bozonových párů W a Z, rozpadajících se leptonově, a k výpočtům citlivostí na vazebné konstanty stojící v tří a čtyřbozonových diagramech obsahujících alespoň jeden foton. Obdržené výsledky jsou zajímavé zejména pro čtyřbozonové vazebné konstanty, jejichž znalost může být zlepšena téměř faktorem sto s prvními daty na LHC a faktorem deset tisíc s použitím vysoké luminozity a dopředných detektorů. Navíc dvoufotonová produkce párů mionů byla využita k odhadnutí doby potřebné k poziční kalibraci těchto dopředných detektorů s požadovanou přesností.

Dalším typem exkluzivních případů je centrální exkluzivní produkce (CEP) založená na výměně dvou gluonů. V práci byly detailně srovnány dostupné modely s daty exkluzivních dijetových případů měřenými na urychlovači Tevatron. To je důležité zejména pro predikce účinných průřezů CEP Higgsova bozonu na LHC, tedy procesu, jenž hraje významnou roli ve fyzikálním programu AFP.

Personal contributions

This document summarizes results published in some of the following articles or conference proceedings:

- Next-leading BFKL effects in forward-jet production at HERA,
  O. Kepka, C. Royon, C. Marquet and R. B. Peschanski,
  Phys. Lett. B **655** (2007) 236, hep-ph/0609299.

- Next-to-leading BFKL phenomenology of forward-jet cross sections at HERA,
  O. Kepka, C. Royon, C. Marquet and R. B. Peschanski,
  Eur. Phys. J. C **55** (2008) 259, hep-ph/0612261.

- Search for exclusive events using the dijet mass fraction at the Tevatron,
  O. Kepka and C. Royon,
  Phys. Rev. D **76** (2007) 034012, [arXiv:0704.1956 [hep-ph]].

- Probing anomalous triple gauge boson $WW\gamma$ coupling at the LHC
  D. d'Enterria, M. Klasen and K. Piotrzkowski,
  Photon-LHC-2008 : Proceedings of the International Workshop on High-Energy Photon Collisions at the LHC, 2008.

- Anomalous $WW\gamma$ coupling in photon-induced processes using forward detectors at the LHC,
  O. Kepka and C. Royon, Phys. Rev. D **78** (2008) 073005, [arXiv:0808.0322 [hep-ph]].

- Forward Physics Monte Carlo,
  M. Boonekamp, V. Juranek, O. Kepka, C. Royon,
  Proceedings of the workshop: HERA and the LHC workshop series on the implications of HERA for LHC physics, arXiv:0903.3861 [hep-ph], 2007.

- Gaps between jets at hadron colliders in the next-to-leading BFKL framework,
  F. Chevallier, O. Kepka, C. Marquet and C. Royon,
  Phys. Rev. D **79** (2009) 094019, [arXiv:0903.4598 [hep-ph]].

- Probing $WW\gamma\gamma$ and $ZZ\gamma\gamma$ quartic anomalous couplings with 10 pb^{-1} at the LHC,
  E. Chapon, O. Kepka, C. Royon,
  arXiv:0908.1061 [hep-ph], 2009.

Contents

Introduction 1

The strong interaction is one of the four fundamental forces present in the Universe. Quantum Chromodynamics (QCD) is the mathematical formulation of strong interaction, the theory that describes interactions of quarks through the exchange of eight color mediators called gluons. The strength of the interaction is governed by the strong coupling constant α_s which is a free parameter and has a very interesting characteristic. It evolves as a function of the momentum involved in the interaction. At high momentum, the partons (quarks and gluons) inside hadrons behave almost as free independent particles since the strong interaction is small. At small momentum or equivalently at large characteristic distances, the coupling constant is large and the strong interaction bounds partons tightly. Colored partons are thus never observed alone, but are confined in colorless hadrons. The partonic structure of hadrons is described in terms of so called parton density functions which are measured.

The structure of hadrons is probed in collision experiments. When a probe strucks a parton inside the proton for instance, the parton is scattered off at large transverse momentum in such an inelastic event and makes the rest of the hadron system color uneven. The system has to reorganize its color field since only colorless states can be observed due to confinement. Consequently, a large number of particles with small transverse momenta called proton remnants leave the interaction, and populate the central detector. The proton is broken.

In early pp experiments and later in ep collisions at HERA, a non-negligible fraction of events with large transverse momentum exhibited an interesting feature. Rapidity gaps, the regions of the detector completely devoid of particles between the central object and the outgoing proton remnants were observed. Such events are denoted as hard diffractive events. Quite unexpectedly about 10%, a large fraction of the non-diffractive events showed rapidity gaps at HERA.

The events with rapidity gaps result from a complicated gluon exchange (at least two) appearing as a colorless exchange between the proton and the central system. However, since a hard scale is involved in these processes, the proton structure can be still described in terms of the diffractive parton density functions whose evolution is predicted by perturbative QCD in the same way as in the inelastic case. The color which is carried out by the interacting parton from the proton is balanced by the emission of soft partons. These transform into remnant particles in the final state. However, since they are well collimated along the interacting parton, the rapidity gap in a forward region is observed.

At hadron-hadron colliders, the fraction of diffractive events is smaller due to additional interactions, which may occur between the outgoing intact protons before and after the hard collision. The color flow triggered by these soft interactions gives rise to particles which spoil the rapidity gap signature of the

diffractive event. At the Tevatron, we observe about 1% of diffractive events, whereas we expect about 0.3% at the LHC due to the higher center-of-mass energy of the collisions.

In this thesis, we study not only the mentioned hard diffractive processes, but also exclusive processes, another kind of unique events with extremely large rapidity gaps. The novel interactions of events were observed at the Tevatron. In the so called Central Exclusive Production (CEP), only the central system is created in addition to two outgoing intact protons, and nothing else. These events are governed by the exchange of two perturbative gluons in a colorless state and exhibit large rapidity gaps since no remnants are present. Such clean event topologies imply a novel new experimental technique. By detecting the two outgoing protons, one can reconstruct the mass of the created object in the central detector very precisely. In addition, due to the fact that the production has to fulfill certain selection rules, the produced system has to be a $J^{CP} = 0^{++}$ state to a good approximation. Hence, if a single particle is produced in CEP, its quantum numbers are uniquely determined irrespective of the decay channels by observing only a handful of events.

Having sufficiently energetic proton beams, the exclusive interaction can also be initiated by the exchange of two photons. The invariant mass of the photons spans up to 1 TeV scales at the LHC. This makes the two-photon physics particularly interesting since we can study for instance the interaction of electroweak bosons in detail with an over-constrained kinematic information and test the SM at high energies where new production mechanisms could appear.

Diffractive and exclusive events are possible to be detected with the rapidity gap requirement only. However, the main features of these processes can be well explored when the central detector is instrumented with additional forward detectors measuring scattered proton momenta from the tracks left in detectors installed close to the beam and far away from the interaction point of the central detector. Determining the fractional momentum loss of the scattered protons ξ_1, ξ_2, the centrally produced mass is reconstructed as $W = \sqrt{s\xi_1\xi_2}$, where $\sqrt{s}$ is the center-of-mass energy of the beams. The CDF Collaboration at the Tevatron $p\bar{p}$ collider is equipped with a forward proton detector which tags, however, the scattered antiprotons only. At the LHC, central detectors ATLAS/CMS will be equipped with forward detectors on both sides around the experiment interaction points for the first time[1] and it will be a great opportunity to test the QCD predictions in hard diffraction, but more importantly study the new exclusive productions of Standard Model (SM) and perhaps also Beyond Standard Model signals.

In this thesis, we aim to study the mentioned diffractive and exclusive productions at the Tevatron and the LHC. Both signatures of the diffractive and exclusive events, rapidity gaps or proton tagging, are used for various studies. The document starts with a review of the Standard Model in Chapter 2 with the emphasis on diffraction phenomenology at HERA and the Tevatron. The central exclusive and two-photon productions are discussed with respect to the expected forward physics program at the LHC. In Chapter 3, the LHC machine and the ATLAS central detector are described. A short discussion of the rate of multiple interactions at the LHC which is relevant for the diffractive analyses can be found there.

Diffractive and exclusive processes are used throughout the thesis. They were therefore implemented in the FPMC Monte Carlo with the aim to accomodate all of them in one simulation framework. In Chapter 4 we detail the work covering the implementation of new HERA diffractive parton densities and the implementation of the two-photon physics processes in the generator.

[1] AFP detectors have currently been recognized by the ATLAS management as a possible upgrade of the ATLAS detector (November 2009).

The physics analysis starts in Chapter 5 in which the extraction of an exclusive signal at the Tevatron is performed and compared to available models of central exclusive production. In Chapter 6 we describe the Atlas Forward Physics project to install the proton tagging detector around the ATLAS interaction point. We discuss the detector sub-systems and also the particle tracking inside the LHC optics which is required to transport scattered protons from the interaction point of ATLAS to the forward detector stations. Two-photon dimuon events are studied as a method to align the forward detectors. In Chapter 7, sensitivities to anomalous triple and quartic couplings of the photon to electroweak W/Z gauge bosons are investigated and a new measurement is proposed to constrain the anomalous quartic couplings not only with forward detectors at high luminosity, but also using early data. The thesis concludes with the presentation of a method to identify diffractive and exclusive events with the rapidity gap method using the ATLAS calorimeter system in Chapter 8, which is a part of the preparative work for the early data at the LHC.

Standard Model of Particle Physics

2

This chapter begins with an overview of the Standard Model before introducing diffraction from a historical perspective and discussing the necessary formalism of Regge theory which is present in modern models of diffraction. Next, some aspects of diffraction at HERA and their implication on hard diffraction at hadron colliders are discussed. We finish by an overview of exclusive processes which are expected to be studied at the LHC.

2.1 Standard model of particle physics

The Standard Model of particle physics is a quantum field theory based on a non-abelian broken symmetry $\mathrm{SU}(3)_C \otimes \mathrm{SU}(2)_L \otimes \mathrm{U}(1)_Y$ describing the strong and electroweak interaction, where C is the color charge, L denotes the left handed coupling of the weak isospin doublets, and Y is the weak hypercharge. Fermion matter fields interact via vector bosons which are the mediators of the interactions arising from the requirement of a local gauge symmetry such that the Lagrangian is invariant under different transformation parameters in every space-time point.

The matter fields come in three generations. The left-handed components of the particles transform as doublets:

	Generations			Charge
	I.	II.	III.	
leptons	$\begin{pmatrix} \nu_e \\ e^- \end{pmatrix}_L$	$\begin{pmatrix} \nu_\mu \\ \mu^- \end{pmatrix}_L$	$\begin{pmatrix} \nu_\tau \\ \tau^- \end{pmatrix}_L$	$\begin{matrix} 0 \\ -1 \end{matrix}$
quarks	$\begin{pmatrix} u \\ d \end{pmatrix}_L$	$\begin{pmatrix} c \\ s \end{pmatrix}_L$	$\begin{pmatrix} t \\ b \end{pmatrix}_L$	$\begin{matrix} +\frac{2}{3} \\ -\frac{1}{3} \end{matrix}$

while the right handed components transform as singlets under the $\mathrm{SU}(2)_L$ symmetry. Each generation consists of two leptons carrying a lepton quantum number. Electron e, muon μ and tau τ carry the same charge corresponding to the charge $-|e|$ of an electron. Each charged lepton is accompanied by a neutrino ν, its neutral lepton partner which has a very small mass.

Quark matter fields are constituents of hadrons, carrying color as a quantum number. As for leptons, there are two quarks per generation differing in the electromagnetic charge by one unit. However, the charge is a fraction of 3. The six flavors of quarks are the following: the up, charm, and top quarks u, c, t carry a charge 2/3 whereas the down, strange, and bottom quarks d, s, b carry a charge -1/3. All the matter fields have also their antiparticle partners which have same mass but all quantum numbers opposite. With the discovery of the last matter fields, the top quark and the tau neutrino ν_τ, about ten years ago at the Tevatron, the symmetry between quark and lepton generations was experimentally confirmed.

A global symmetry of a Lagrangian is directly linked to a conservation of some quantum number (Noethers' theorem). For example, the Lagrangian of the Standard Model possesses a global symmetry which yields a conservation of the electric charge. If the global symmetry is elevated to be a local one, such that the Lagrangian preserves the symmetry in every space-time point, the free matter fields start to interact. Fermion fields interact between each other through exchanges of gauge bosons which arise from the local gauge symmetry of the theory. Gauge bosons couple to the matter fields by the corresponding charge of the interaction. Four fundamental interactions are found in Nature: the electromagnetic, weak, strong interactions and gravity.

The electromagnetic interaction is mediated by a massless photon and couples to the electrically charged objects. It is mediated to infinite distances. The weak interaction is transmitted by the weak gauge bosons $W^\pm$ and Z which interact with a field through the weak hypercharge Y. Since the weak bosons have a substantial mass, the weak interaction is short-distance. The weak interaction causes instability of some nuclei that decay through the beta decay. The color charge of quark fields allows them to interact through strong interaction. The strong interaction is mediated via massless fields called gluons. There are three colors and eight gluons. The strong interaction is short-distance growing with an increasing distance. Thus, the quarks are confined to form stable hadronic colorless systems like a proton.

Matter and gauge fields are said to be fundamental which means that their sub-structure was not revealed at distances down to 10^{-18} m up to now [1]. The description of gravity, the last fundamental force of Nature, which is believed to be mediated by a graviton particle, is not yet incorporated in the Standard Model.

The spontaneous symmetry breaking of the Standard Model is a mechanism which gives mass terms to the fermion and boson fields. The symmetry is broken to $\mathrm{SU}(3)_C \otimes \mathrm{SU}(2)_L \otimes \mathrm{U}(1)_Q$ maintaining the $\mathrm{SU}(2)_L$ invariance and renormalizibility of the theory whilst the $\mathrm{U}(1)_Q$ symmetry responsible for electromagnetic interaction emerges. The appearance of a new heavy scalar particle, the Higgs boson, is an essential feature of such mechanism and its observation in future colliders would grant a deep understanding of the origin of mass.

A more detailed discussion of the Standard Model follows in the next sections. The main principles of Quantum Electrodynamics are mentioned followed by the discussion of the electroweak unification and electroweak symmetry breaking. Some aspects of the strong interactions and proton structure are summarized before focusing on diffraction which is the main topic of this thesis.

2.2 Quantum electrodynamics

Quantum Electrodynamics (QED) is a theory based on the abelian gauge group $U(1)_Q$ which describes the interaction of charged spin-1/2 fermion fields with the massless neutral spin-1 photon. Fermion fields ψ of mass m are described by the relativistic Dirac Lagrangian density

$$\mathscr{L}_D = \bar{\psi}(x)(i\partial_\mu \gamma^\mu - m)\psi(x) \tag{2.1}$$

where γ^μ are the Dirac matrices.

The fermion interaction with a photon is obtained by generalizing the global $U(1)_Q$ symmetry to a local one. We easily see that the local transformation $\psi'(x) = e^{i\omega(x)}\psi(x)$ leaves the mass term of the density (2.1) unchanged whereas the kinetic term gives rise to the gradient of the field phase coupled to the vector current

$$\mathscr{L}'_D = -\bar{\psi}\gamma^\mu \psi \partial_\mu \omega(x) + \mathscr{L}_D \tag{2.2}$$

The new term can be canceled by introducing a new interaction in the Lagrangian. It is convenient to do so by replacing the derivative ∂_μ by the covariant derivative

$$D_\mu = \partial_\mu + iA_\mu(x) \tag{2.3}$$

which has the correct transformation property $D'_\mu = e^{i\omega} D_\mu e^{-i\omega}$ as long as the new field A_μ (called Yang-Mills field) transforms as

$$A_\mu(x)' = A_\mu(x) + \frac{1}{e}\partial_\mu \omega(x) \tag{2.4}$$

So promoting the global phase invariance of the free matter-field Lagrangian to the local gauge one, we had to introduce a new vector gauge field which added a dynamics to the non-interacting theory.

We still have to supply the Lagrangian with a kinetic term $-\frac{1}{4}F_{\mu\nu}F^{\mu\nu}$ for the field A_μ, in order to interpret it as a physical field satisfying the equation of motion. $F_{\mu\nu} = \partial_\mu A_\nu - \partial_\nu A_\mu$ is the electromagnetic field tensor which is already gauge invariant under the local gauge transformation. On the other hand, the corresponding mass term for the vector field is forbidden by the requirement of the local symmetry. The new vector field is therefore massless. The new interacting term which makes a photon to couple to a fermion and an anti-fermion, makes the model of Quantum Electrodynamics complete.

2.3 The weak interaction

The weak interaction is a flavor-changing, parity-violating force mediated by spin-1 vector boson particles. Two of the mediators, $W^\pm$, have the electric charge $\pm|e|$ of the electron and mediate charged-current interactions, whereas Z, the electrically neutral boson mediates neutral-current interactions. The weak bosons $W^\pm$ and Z couple to leptons and quarks, photons and to themselves. The parity violation of the weak interaction is maximal which comes from the fact that the gauge bosons couple only to the left handed components of fermions and not to the combination of left and right fields.

The oldest and best known process caused by the weak interaction is the nuclear beta decay. The term “weak” comes from the fact that the transition rates caused by this force are orders of magnitude smaller than those of any other fundamental force. This suggested that the new force has to have a weak coupling. The weak interaction was originally described by the contact four-fermion interaction with an effective parity-conserving coupling of a unit operator. To explain strange meson (K^+) decays into

pions, Lee and Yang suggested to abandon the assumption of parity symmetry [2]. The parity violation was first shown by Wu et al. [3] who studied the beta decays of the polarized nucleus Co^{60}. Later experiments confirmed the parity violation in weak interaction [4], which led to a vector-axial current structure and was quite successful in describing a wide range of processes such as the pion decay rate $\pi^- \to \mu^+ \bar{\nu}_\mu$ for instance.

Embedding intermediate bosons into the framework describing the weak interaction made the theory of weak interactions better-defined at high energies. It closely linked the strength of the weak force with the considerably large mass of the vector boson and led eventually to the unification of the electromagnetic and weak interaction into one electroweak theory in the 1960's.

2.4 Electroweak unification

Weinberg and Salam [5] realized that the electromagnetic and weak interaction can be unified within non-abelian gauge theory. The simplest group which accommodates the parity-violating weak interaction and the parity-conserving electromagnetic interaction is $\mathrm{SU}(2)_L \times U(1)_Y$. Besides describing at that time known charged-current interactions mediated via the gauge $W^\pm$ bosons, the new concept also predicted the existence of neutral currents which were observed in neutrino experiments thirteen years later [6].

The direct observation of the two weak bosons in UA1 and UA2 experiments in 1983 [7] made the electroweak theory well established.

2.5 Electroweak symmetry breaking

The unified theory provided a relation between the $W^\pm$ and Z masses, but the mechanism through which the bosons acquire their mass remained to be solved. Fermion masses could not be introduced directly into the Lagrangian because they would break the gauge invariance. A new concept of mass generation was therefore developed based on the spontaneous symmetry breaking of the gauge group $\mathrm{SU}(2)_L \times U(1)_Y$ into $\mathrm{U}(1)_Q$, preserving the symmetry of the electromagnetic interaction while giving masses to the weak gauge bosons.

The so-called Higgs mechanism [4] starts by the consideration of a gauge invariant and covariant Lagrangian for a complex $\mathrm{SU}(2)$ doublet Φ

$$\mathscr{L} = (D_\mu \Phi)^\dagger (D^\mu \Phi) + \mu^2 \Phi^\dagger \Phi - \lambda (\Phi^\dagger \Phi)^2 - \frac{1}{4} \vec{F}_{\mu\nu} \cdot \vec{F}^{\mu\nu} - \frac{1}{4} \vec{B}_{\mu\nu} \cdot \vec{B}^{\mu\nu} \tag{2.5}$$

The covariant derivative is given by

$$D_\mu = \partial_\mu - ig\vec{A}_\mu \cdot \vec{\tau}/2 - ig' B_\mu \tag{2.6}$$

where A^a_μ and B_μ are the Yang-Mills fields corresponding to the $\mathrm{SU}(2)_L$ and $\mathrm{U}(1)_Y$ gauge groups (τ^a are the Pauli matrices)[1]. The kinetic terms of the fields are constructed from the field tensors $\vec{F}_{\mu\nu} = \partial_\mu \vec{A}_\nu - \partial_\nu \vec{A}_\mu + g\vec{A}_\mu \times \vec{A}_\nu$ and $B_{\mu\nu} = \partial_\mu B_\nu - \partial_\nu B_\mu$.

This Lagrangian represents a dynamics of a system in a Mexican hat-like potential which has a degenerate global minimum $v = \mu/\sqrt{\lambda}$. The symmetry of the Lagrangian is broken using the local

[1] A specific value of the scalar field hypercharge $Y_\Psi = 1/2$ was set without losing generality.

gauge freedom, choosing one such specific minimum with a particular choice of the Φ field (U-gauge)

$$\Phi_U = \begin{pmatrix} 0 \\ \frac{1}{\sqrt{2}}(v+H(x)) \end{pmatrix} \tag{2.7}$$

The new scalar field $H(x)$ originates from the perturbation about a new ground state. Rewriting the Lagrangian for Φ in U-gauge and keeping the kinetic and mass terms, we get

$$\begin{aligned} \mathscr{L} &= \frac{1}{2}\partial_\mu H \partial^\mu H - \mu^2 H^2 \\ &- \frac{1}{4}F^1_{\mu\nu}F^{1\mu\nu} + \frac{1}{8}v^2 g^2 (A^1_\mu)^2 \\ &- \frac{1}{4}F^2_{\mu\nu}F^{2\mu\nu} + \frac{1}{8}v^2 g^2 (A^2_\mu)^2 \\ &- \frac{1}{4}F^3_{\mu\nu}F^{3\mu\nu} - \frac{1}{4}B_{\mu\nu}B^{\mu\nu} + \frac{1}{8}v^2 (gA^3_\mu - g'B_\mu)^2 \end{aligned} \tag{2.8}$$

First we see that due to the breaking of the ground state symmetry, the scalar field $H(x)$ obtains a mass $\mu/\sqrt{2}$ and becames a degree of freedom that we identify as the Higgs particle. Second, the Yang-Mills fields A^1_μ, A^2_μ acquire a mass. Since these fields are related to the charged-current mediators $W^\pm$ through a relation $W^\pm = 1/\sqrt{2}\,(A^1_\mu \pm iA^2_\mu)$, the W bosons become massive $m_W \equiv m_{A^1} = m_{A^2} = 1/2vg$. On the other hand, the interpretation of the fields A^3_μ and B_μ is unclear since they mix as $gA^3_\mu - g'B_\mu$. To disentangle them in the Lagrangian, we perform a rotation in the spectrum and define

$$\begin{aligned} Z_\mu &= A^3_\mu \cos\theta_W - B_\mu \sin\theta_W \\ A_\mu &= A^3_\mu \sin\theta_W + B_\mu \cos\theta_W \end{aligned} \tag{2.9}$$

as the physical degrees of freedom where

$$\cos\theta_W = \frac{g}{\sqrt{g^2+g'^2}} \qquad \sin\theta_W = \frac{g'}{\sqrt{g^2+g'^2}} \tag{2.10}$$

The A_μ field does not have a corresponding mass term in the Lagrangian and is interpreted as the massless photon of the electromagnetic interaction. The Z_μ field becomes the mediator of neutral-currents and has a mass given by $m_Z = \frac{1}{2}v(g^2+g'^2)^{1/2} = M_W/\cos\theta_W$. Its mass is tightly linked with the W mass via the weak mixing angle θ_W (current world average $m_W = 80.398 \pm 0.025\,\text{GeV}$, $m_Z = 91.1876 \pm 0.0021\,\text{GeV}$, $\sin^2\theta_W = 0.231 \mp 0.00023$ [1]).

Another important aspect of the Higgs mechanism is that it does not only generate masses for the intermediate vector bosons but also for fermions. The direct introduction of fermion masses is not allowed by the gauge invariance but they can be introduced via the Yukawa coupling of the Higgs field Φ to either the left quark doublets and up- or down-quark singlets, or to lepton left doublets and neutrino or electron singlets. In the original version of the SM, neutrinos were considered massless since no experiment was able to measure their mass. However, neutrino mass terms can be generated with the Higgs mechanism as well. The non-zero neutrino mass was first indicated by R. Davis [8] in neutrino disappearing experiment and than discovered by series of neutrino oscillation experiments. After the spontaneous symmetry breaking is carried out, all fermions have a mass term of the form $-m_i(\bar{\psi}_{iL}\psi_{iR} + h.c.)$ where i is any quark or lepton. By construction, this mechanism also defines the

type of Higgs boson interactions with fermions which has the form $m_i/m_W \bar{\psi}_i \psi_i H$ whose strength is directly proportional to the fermion mass.

It is important to notice that the mass quark eigenstates are not identical to the eigenstates of the weak interaction. The charged-currents change the flavor of the mass quark eigenstates q. They are related to the weak eigenstates which couple to the W bosons by the Cabbibo-Kobayashi-Maskawa (CKM) unitary matrix

$$\begin{pmatrix} d' \\ s' \\ b' \end{pmatrix} = \begin{pmatrix} V_{ud} & V_{us} & V_{ub} \\ V_{cd} & V_{cs} & V_{cb} \\ V_{td} & V_{ts} & V_{tb} \end{pmatrix} \begin{pmatrix} d \\ s \\ b \end{pmatrix} \tag{2.11}$$

which expresses the quark flavor participating in flavor-changing currents i in terms of mass eigenstate quark flavors j by V_{ij}. This in general complex matrix allows to embody the CP violation effects in the quark sector which were observed experimentally for example in the kaon or B (mesons containing strange and bottom quarks, respectively) decays.

2.6 Quantum chromodynamics

Quantum Chromodynamics (QCD) [9] is a theory based on the $\mathrm{SU}(3)_C$ color group. The requirement of the local gauge symmetry of the Lagrangian involving colored quark fields gives rise to massless gluon vector bosons which can interact with themselves. The particular structure of the $\mathrm{SU}(3)_C$ group implies such interaction between gluons that leads to an asymptotic freedom of the theory and a confinement which ensures the propagation of the color neutral states to macroscopic distances.

The QCD Lagrangian reads

$$\mathscr{L} = -\frac{1}{4}(F^a_{\mu\nu})^2 + \sum_{k=\{flavors\}}^{n_f} \bar{\psi}^j_k (i\not{D} - m)_{ij} \psi^i_k + \mathscr{L}_{\text{gauge}} + \mathscr{L}_{\text{ghost}} \tag{2.12}$$

where

$$(D_\mu)_{ij} = \delta_{ij}\partial_\mu - igA^a_\mu \frac{\lambda^a_{ij}}{2} \tag{2.13}$$

$$F^a_{\mu\nu} = \partial_\mu A^a_\nu - \partial_\nu A^a_\mu + g f^{abc} A^b_\mu A^c_\nu \tag{2.14}$$

There are eight $a = 1 \ldots 8$ spin-1 massless gluon fields A^a_μ which mediate the strong interaction and quark fields ψ^i_k for each color i and flavor k. The gauge invariance of the QCD Lagrangian is associated with the coupling of the strong interaction g. The kinetic term $-\frac{1}{4}F^a_{\mu\nu}F^{a\mu\nu}$ generates the gluon self-interaction. The structure coefficients f_{abc} are related to the generators of the $\mathrm{SU}(3)_C$ color group Gell-Mann matrices λ^a_{ij} by $[\lambda^a, \lambda^b] \equiv \mathrm{i}\lambda^c$, defining the corresponding Lie algebra.

The gauge fixing term $\mathscr{L}_{\text{gauge}}$ must be introduced in order to perform perturbative calculations. Otherwise, the propagators for the gluon fields are not defined. The gauge fixing terms must be supplemented with a corresponding ghost Lagrangian $\mathscr{L}_{\text{ghost}}$ to cancel unphysical degrees of freedom of the gluon field which would appear in the physical measurable quantities otherwise.

2.6.1 Asymptotic freedom and confinement

An application of Feynman rules to compute scattering amplitudes for a given process at the leading order is mostly straightforward. However, when advancing to higher orders of perturbation theory in

the coupling of the strong interaction $\alpha_s \equiv g^2/4\pi$, one must inevitably deal with Feynman diagrams which contain fermion or boson loops. An evaluation of such diagrams leads to an integration over arbitrary large momentum since in the relativistic theory there is no intrinsic cut-off on the momentum. The theory would predict infinite cross sections and would be incapable to describe real processes. Such divergences are denoted as UV divergences as they originate in the integration over an ultra-high momentum. Renormalization is a prescription to isolate the divergences and remove them consistently from the physically measurable quantities [9]. This introduces an additional mass scale μ – the point where the subtractions which remove the divergent terms are performed. The renormalization leads to the redefinition of the bare quantities which are part of the QCD Lagrangian such as the coupling constant α_s, fermion masses, the fermion ψ_k^j and boson A_μ^a fields. Their renormalized counterparts are introduced which are physically relevant, whereas the bare ones are not.

The procedure of subtracting these divergences requires that the renormalized coupling depends on a characteristic scale of a process Q^2. The dependence can be written as

$$\alpha_s(Q^2) = \frac{1}{b\ln(Q^2/\Lambda^2)} = \frac{4\pi}{11 - \frac{2}{3}n_f \ln(Q^2/\Lambda_{\mathrm{QCD}})} \tag{2.15}$$

where n_f is the number of active flavors and $\Lambda_{\mathrm{QCD}} \sim 200\,\mathrm{MeV}$ is a scale where the coupling diverges[2]. The perturbative calculation cannot be done for small scales below $Q \sim 1\,\mathrm{GeV}$ which is the typical mass of the light hadrons. The parameter $b = (33 - 2n_f)/12\pi$ (value at leading order) follows from the structure of the $\mathrm{SU}(3)$ under consideration and it has the following consequences for the coupling α_s: the coupling constant is running, meaning that it is large at low momentum and small at large momentum. At large Q^2 where the coupling is small, there exists an asymptotic freedom, and the perturbative calculations can be used. At small Q^2 or equivalently at large distances the coupling is large so the true degrees of freedom, quarks and gluons, are confined within hadrons and not observed individually.

2.6.2 Proton structure and evolution equation

Long time before a collision, a particle is said to be bare which means that it is composed of its valence quarks only. It evolves until the time of an interaction when it is said to be dressed which means that is accompanied by a coherent field of virtual quarks and gluons, the partons. A probe particle scatters off the dressed hadron whose structure is described by the parton density function $f_i(x, Q^2)$. The function gives a probability to find a parton i carrying a longitudinal momentum fraction x of the mother particle and having a virtuality Q^2.

The proton structure cannot be calculated perturbatively from the first principles of QCD because it involves small distance effects where the strong coupling is large. However, it is possible to predict its Q^2 scale dependence perturbatively using the Dokshitzer-Gribov-Lipatov-Altarelli-Parisi (DGLAP) evolution equations, which effectively resum the leading powers of $[\alpha_s(Q^2)\ln(Q^2)]^n$ [9]. They describe how the proton structure changes when the proton is looked at different space resolutions or equivalently, how the picture changes as a function of the virtuality Q^2 of the probe. The differential evolution

[2] The formula (2.15) is obtained in the leading order.

equation in $t \equiv Q^2$ can be written as

$$t\frac{\partial}{\partial t}\begin{pmatrix} q_i(x,t) \\ g(x,t) \end{pmatrix} = \frac{\alpha_s(t)}{2\pi}\sum_{q_j,\bar{q}_j}\int_x^1 \frac{\mathrm{d}\xi}{\xi} \times \begin{pmatrix} P_{q_iq_j}\left(\frac{x}{\xi},\alpha_s(t)\right) & P_{q_ig}\left(\frac{x}{\xi},\alpha_s(t)\right) \\ P_{gq_j}\left(\frac{x}{\xi},\alpha_s(t)\right) & P_{gg}\left(\frac{x}{\xi},\alpha_s(t)\right) \end{pmatrix}\begin{pmatrix} q_j(x,t) \\ g(x,t) \end{pmatrix} \tag{2.16}$$

Here the functions $P_{q_iq_j}, P_{q_ig}, P_{gq_j}, P_{gg}$ are the splitting functions or evolution kernels, calculable perturbatively as a power series in α_s. The differential equations have to be provided with initial conditions. Because they cannot be calculated from the perturbative approach, they are fitted from data at some not too low scale $Q_0^2 \sim \text{few}\,\text{GeV}^2$.

One of the most important features of QCD is that in many cases, the production cross sections can be factorized, i.e. it can be expressed as a convolution of the parton distribution functions and the cross section of the corresponding sub-process. For instance, for a parton pair production in hadron-hadron collisions, we have (omitting the explicit Q^2 dependence)

$$\sigma_{k,l} = \sum_{i,j}\int \mathrm{d}x_1\mathrm{d}x_2\hat{\sigma}_{i,j\to k,l}(x_1,x_2,\alpha_s)\otimes f_i(x_1)\otimes f_j(x_2) \tag{2.17}$$

where $\hat{\sigma}_{i,j\to k,l}$ is the sub-process cross section of two partons i,j denoting the partons k,l. $f_i(x)$ are the parton density functions of initial hadrons depending on the momentum fraction x, and α_s is the strong coupling constant.

There exist another type of evolution equations in the x variable. They are relevant when cross sections are not dominated by the large $\ln(Q^2)$ terms but by $\ln(1/x)$ instead, when x is small. In this case, the alternative to DGLAP evolution is called Balitsky-Fadin-Kuraev-Lipatov (BFKL) equations which resum terms $\alpha_s\ln(1/x)$ into all orders [9].

A particle scattering can be decomposed into two processes of different typical time scales. When the hard interaction occurs, hard partons of typically large transverse momentum emerge from the interaction. The production cross section in a hadron collision is generally determined as in (2.17) as a convolution of the sub-process cross section and the parton densities which depends on the momentum transfer scale. Long time after the interaction, colored partons from the hard process and the ones from the remnants of the broken protons start to restore their color fields. The restoration is governed by long distance QCD effects characterized by small typical momentum transfer and the topology of the event is not much altered. The hadronization occurs which means that the colored partons interact to produce colorless hadrons in the final state. Since the soft processes do not change the topology of the event, showers of particles are observed in the direction of the hard partons originating from the hard interaction. These showers are called particle jets. Complicated multi-jet events are now studied at hadron-hadron colliders but most importantly, the first observed three-jet configuration originating in $q \to qg$ splitting in e^+e^- collisions at PETRA confirmed the existence of the gluon field in 1979.

2.7 Diffraction

In high energy physics, the term diffraction originally denoted the elastic scattering of hadrons at small angles. Later the definition expanded to cover a range of processes which are governed by a similar

mechanism, the exchange of quantum numbers of the vacuum, as it will be discussed. In case of the elastic scattering, there is no color flow between collided hadrons, the event is free of the proton remnants and shows large regions devoid of particles called rapidity gaps. On the contrary, if one of the colliding protons is broken yielding proton remnants, but a rapidity gap is present on the other side, the process is called single diffractive dissociation. In fact, the term covers two situations: first the proton on the side of the rapidity gap can stay intact or second, it may dissociate into a system of one or more particles having the same overall quantum numbers and very similar mass as the proton. The important point is, however, that we observe the rapidity gap in both cases.

Diffractive dissociation processes are generically soft, i.e. governed by exchanges with typically small momentum transfers p_T. Their description in terms of QCD is therefore intricate because the running coupling becomes large at small momentum transfers and calculation based on perturbative expansion becomes unjustified. Since these processes represent a significant fraction of the scattering hadronic cross section, many models have been proposed to grasp the main features of the production mechanism even though their link to QCD is less evident.

Among others, the Regge theory turned out to be extremely successful. It emerged from the efforts to build up a fundamental theory of strong interactions based primarily on the analytical properties and unitarity of scattering amplitudes in the 1960s. Back then, the interest in quantum field theory declined as it was incapable to explain the fundamental question why colored partons, appearing to be the true degrees of freedom that correctly describe the baryon and meson spectra, and giving a correct description of the hadron magnetic moments, elude to be observed. Later, when the asymptotic freedom and confinement were discovered, QCD became an established theory well confirmed experimentally. The Regge theory survived until today as an effective theory of diffraction.

Regge theory models the hadronic interaction in terms of exchanges of reggeons and pomerons which are effective interactions parameterizing in a rather economic way the complicated soft gluon exchange which lies beneath. A simple parameterization which is rooted in the general properties of the scattering matrix allowed Donnachie and Landshoff [11] to perform fits of a large set of scattering data with small momentum transfer. Event though very successful, the true nature of the reggeons and pomerons in terms of QCD remained hidden.

The later UA8 and HERA experiments showed that diffractive scattering is not only a soft process, but a hard diffractive component exists also. For example, jets with large momentum transfer were observed in addition to the scattered proton. This stimulated later developments in which the structure of the diffractive events was described in terms of parton density functions in a very similar way as in non-diffractive production.

In the following sections we review some predictions of Regge theory which will reappear throughout the thesis. We also mention the extraction of the pomeron structure functions at HERA relevant for the following discussion of diffraction at the Tevatron and the LHC.

2.8 Regge theory

In order to present the main results of the Regge theory, it is useful to recall some basic definitions related to particle scattering. In relativistic quantum theory, the scattering operator (or S-matrix) $|f\rangle = S|i\rangle$ describes the transition between an initial state $|i\rangle$ and a final state $|f\rangle$. The in and out free particle states $|i\rangle, |f\rangle$ are defined at times $-\infty$ and ∞, respectively, and form complete sets of states. The transition

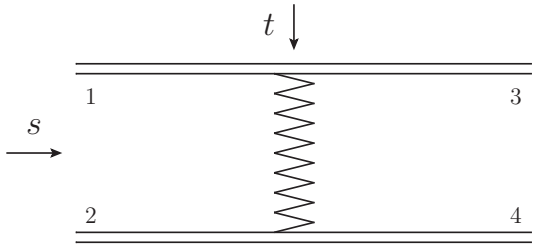

Figure 2.1: Scheme of the reggeon exchange in the reaction $12 \to 34$ with Mandelstam variables $s = (p_1 + p_2)^2$ and $t = (p_1 - p_3)^2$.

operator T defined as $S = 1 + \mathrm{i}T$ expresses the dynamics of the evolution when the initial states did not remain unchanged and underwent some interaction. The S-matrix elements can be decomposed as

$$S_{fi} \equiv \langle f|S|i\rangle = \delta_{fi} + \mathrm{i}T_{fi} = \delta_{fi} + \mathrm{i}(2\pi)^4\delta^4(p_f - p_i)\mathscr{A}(i \to f) \tag{2.18}$$

where in the last expression the four-momentum conservation is explicitly written out by the corresponding delta distribution. $\mathscr{A}(i \to f)$ is the probability amplitude that the state i will evolve to the state f. In the case of the two body process $12 \to 34$, the scattering amplitude is a function of two of the standard Mandelstam variables s,t,u; $\mathscr{A}(s,t)$ for instance, s, expressing the energy of the collision and t reflecting the momentum transfer connected with the scattering polar angle θ of the first particle.

Following from the analyticity and crossing symmetries of the amplitude [12], [13], the Regge theory states that the scattering amplitude $\mathscr{A}_{12\to34}(s,t)$ shown in Figure 2.1 can be related to the crossed one $\mathscr{A}_{\bar{1}\bar{3}\to\bar{2}\bar{4}}(s',t')$ where $s' = t$, $t' = s$ and $\bar{2},\bar{3}$ are the antiparticles of $2,3$, respectively. In other words, it relates the high energy behavior of the s-channel amplitude to the t-channel one provided that one substitutes antiparticles of 2, 3 and their four-momenta $-p$. The partial wave expansion for this crossed amplitude is given by

$$\mathscr{A}_{\bar{1}\bar{3}\to\bar{2}\bar{4}}(s',t') = \sum_{l=0}^{\infty} a_l(s')P_l(\cos\theta) \tag{2.19}$$

where θ is the center-of-mass scattering angle linked to s', t' and particle masses, and P_l corresponds to the Legendre polynomials. $a_l(s')$ are the partial wave amplitudes associated with the exchange of orbital momentum l. Two complex functions are constructed $a_\eta(l,t)$ with $\eta = +1$ and $\eta = -1$ as the analytical continuation to the complex l of the two following sequences $\{a_l(t), l = 0,2,4,\dots\}$ and $\{a_l(t), l = 1,3,5,\dots\}$, respectively. The functions $a_\eta(l,t)$ interpolate between the points $a_l(t)$ of the partial wave amplitudes. In the simplest case to which we restrict ourselves in order to show the main idea, there is only one singularity of $a_\eta(l,t)$ with a t-dependent simple pole (Regge pole) at $l = \alpha(t)$. These Regge poles correspond to resonances or bound states of increasing angular momentum (i.e. spin) exchanged in the t-channel for different t. The Regge trajectory interpolates such resonances or bound states in the $l \times |t|$ plane.

It can then be shown that in the high energy limit, the s-channel amplitude is

$$\mathscr{A}_{12\to34}(s,t) = \beta_{13}\beta_{24}\zeta_\eta(\alpha(t))\left(\frac{s}{s_0}\right)^{\alpha(t)} \tag{2.20}$$

where s_0 is an arbitrary scale factor, $\beta_{13}(t)$ and $\beta_{24}(t)$ are unknown functions of t associated with the vertices in Figure 2.1 and

$$\zeta_\eta(\alpha(t)) = \frac{1+\eta e^{-i\pi\alpha(t)}}{\sin\pi\alpha(l)} \tag{2.21}$$

is the signature factor, depending on the signature η of the Regge trajectory $\alpha(t)$ [13].

The important feature of (2.20) is that the s-channel asymptotic behavior is determined by the properties of the partial-wave amplitude in the crossed channel where a family of resonances or bound states are exchanged. This gives the power law dependence driven by the Regge trajectory $\alpha(t)$. Second, a factorization of the amplitude to two unknown functions β_{13}, β_{24} associated with the appropriate vertices in Figure 2.1 is important if the same Regge trajectory appears in different processes. It can be measured in one process and used for predictions elsewhere.

Equation (2.20) has an immediate impact on total and elastic cross sections. Since the total cross section is directly related by the optical theorem to the scattering amplitude, using (2.20) we obtain

$$\sigma_{\text{tot}} \simeq \frac{1}{s}\text{Im}\,\mathscr{A}(s,t=0) \sim s^{\alpha(0)-1} \qquad s\to\infty \tag{2.22}$$

For the elastic cross section we get in the high energy limit

$$\frac{d\sigma_{\text{el}}}{dt} = \frac{1}{16\pi s^2}|\mathscr{A}(s,t)|^2 \sim s^{2\alpha(t)-2} \qquad s\to\infty \tag{2.23}$$

Hence, in the high energy limit, the total and elastic cross sections are determined only by a Regge trajectory $\alpha(t)$ which can be obtained from the amplitude analyses of the process in the crossed channel by studying its t dependence. Note that in the high energy limit, the total cross section is fully determined by the value of the Regge trajectory at $t=0$ only.

Conventionally, only the properties of the Regge trajectory up to the linear term are considered, such as

$$\alpha(t) = \alpha(0) + \alpha' t \tag{2.24}$$

where $\alpha(0)$ and α' are denoted as the trajectory intercept and the slope, respectively.

The leading mesonic trajectories, i.e. those with the largest $\alpha(0)$, were fitted in data giving a reggeon intercept $\alpha(0)\approx 0.5$, as shown in Figure 2.2. Note that the reggeon trajectory interpolates mesonic trajectories of different quantum numbers. For instance, f_2 carries parities $P=+1, C=+1$ whereas ρ carries $P=-1, C=-1$, and similarly for the other trajectories. According to (2.22), a reggeon intercept smaller than one means that the total hadronic cross section should be a monotonically decreasing function of s.

2.9 Concept of the pomeron

With the increase of beam energies of early hadron colliders, the total cross section could be measured at higher center-of-mass energies. A rise of the total cross section as a function of the center-of-mass energy was observed, which was in contradiction with the mechanism based on a reggeon exchange that predicted a slow decrease of the total cross section. It concerned the pp, $p\bar{p}$ cross sections where the turning points of the increase are found to be around $\sqrt{s}=10,\ 20\,\text{GeV}$, respectively, but it also concerned other hadronic scatterings like $\pi^{\pm}p$, $K^{\pm}p$, etc.

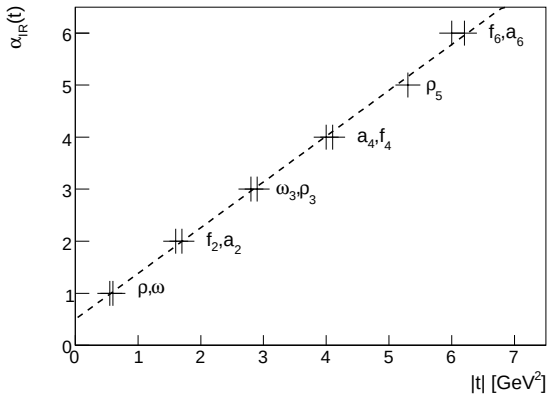

Figure 2.2: Leading mesonic trajectories ρ, f_2, a_2, ω, etc., all superimposed and interleaved by a reggeon trajectory $\alpha_{\mathbb{R}}(t) = 0.5 + 0.9\,|t|$ (reproduction of figure 5.6 from [15]).

Donnachie and Landshoff showed that a large set of scattering data is well fitted with a combination of two different Regge trajectories which are traditionally called the Reggeon ($\mathbb{R}$) and the Pomeron ($\mathbb{P}$) trajectories. In marked contrast with the reggeon, the pomeron intercept is $\alpha_{\mathbb{P}}(0) > 1$ and can account for the growth of the total cross section (see (2.22)). It should be noted that the pomeron trajectory is not associated with any real particle exchange in the t-channel as for the reggeon, but really only parameterizes the partonic activity which takes place in hadron scattering. The fits to the total cross section led to [11]

$$\sigma_{\text{tot}} = Xs^{0.0808} + Ys^{-0.4525} \tag{2.25}$$

Apart from the coefficients X, Y which are process specific, the high energy behavior is governed by the pomeron and reggeon intercepts $\alpha_{\mathbb{P}}(0) = 1.0808$ and $\alpha_{\mathbb{R}}(0) = 0.5475$.

The pomeron couples to quarks in a very similar way as the photon, i.e. with a constant coupling, but with a Regge signature such that it has even C- and P-parities. The elastic or diffractive dissociation processes with small momentum transfers governed by the pomeron originate in soft interaction of partons, but with the overall exchange of the vacuum quantum numbers.

In spite of the great success of the Regge theory based on the reggeon and pomeron exchanges, there is not a real understanding what the soft pomeron actually is in terms of QCD up to now. With respect to the quantum numbers of the pomeron, the exchange can be viewed in the lowest order of QCD as a two-gluon exchange. The pomeron does not correspond to any real resonance, but its recurrences $J^{PC} = 0^{++}, 2^{++}, \ldots$ result in complicated soft gluon exchange. They are called glueballs. One such glueball candidate 2^{++} was presented in [14]; however, 0^{++} has never been observed. These gluonic exchanges are not short-distance interactions, hence the applicability of perturbative methods to understand the real nature of the pomeron is limited.

Regge theory can give a prediction for more complicated hadronic reactions. Consider a process which is a single-inclusive reaction $1 + 2 \to 3 + X$ where X is an unresolved hadronic system of mass M^2. If particle 3 has the same quantum number as particle 1 we have the single diffractive dissociation. The calculation of the cross section can be done in the so-called triple-Regge limit [15] with a triple-pomeron vertex (neglecting $\mathbb{PPR}$ coupling, true in asymptotic s). In the limit $s \gg M^2 \gg t$ when the mass of the created object X is relatively small with respect to the process energy but larger than the

momentum transfer t, the differential cross section is given by

$$s\frac{\mathrm{d}^3\sigma^{\mathrm{SD}}}{\mathrm{d}M^2\mathrm{d}t} = \frac{1}{16\pi^2}|g_{\mathbb{P}}(t)|^2\left(\frac{s}{M^2}\right)^{2\alpha_{\mathbb{P}}(t)-1}\sigma_{\mathbb{P}}(M^2) \tag{2.26}$$

where $g_{\mathbb{P}}(t)$ is a function which includes terms associated with a triple-pomeron vertex and $\sigma_{\mathbb{P}}(M^2)$ is the cross section of the interaction between the pomeron and particle 2, characterized by the energy M^2 in their center-of-mass frame. The power dependence $2\alpha_{\mathbb{P}}(t)-1$ will reappear in the description of diffraction at HERA and hadron colliders. Comparing formulae (2.26) and (2.22), it is interesting to notice that the Regge theory expectation for the ratio of single diffractive to the total cross section at high energy is

$$\frac{\sigma^{\mathrm{SD}}}{\sigma_{\mathrm{tot}}} \sim s^{\alpha_{\mathbb{P}}(0)-1} \tag{2.27}$$

and since $\alpha_{\mathbb{P}}(0) > 1$, the ratio increases as a function of s.

2.10 From soft to hard pomeron

The observation of the jet production with high transverse momentum in diffractive $p\bar{p}$ scattering in the UA8 experiment [16] opened up the possibility to understand diffractive processes in terms of partons. Jet distributions were similar to those in inelastic parton-parton scattering suggesting the parton scattering underneath, but the scattered protons were detected in forward spectrometers, and the process had no relationship with inelastic events in which the proton is broken up.

Ingelman and Schlein proposed in 1985 to assign parton density functions to the pomeron and to describe the process with hard jets as the scattering of the proton partonic components off the partons in the pomeron [19]. The probability to emit a pomeron in these hard diffractive events is governed by the same Regge type formulae as in soft diffraction but the trajectory $\alpha(t)$ can be different. The proposal marked the turning point from which the pomeron started to be viewed differently in soft and hard events. In the first case, the pomeron is described by its trajectory only, whereas in the latter, it is a compound object with a partonic content.

A deeper understanding of hard diffraction came with H1 [17] and ZEUS [18] HERA experiments. The diffractive events at HERA make a significant subset of inclusive neutral and charged current Deep Inelastic Scattering (DIS) data stemming from the processes $e^{\pm}p \to e^{\pm}X'$ and $e^{\pm}p \to \bar{\nu}_e(\nu_e)X'$. The electron/positron of four-momentum k couples to the electroweak bosons ($\gamma, W^{\pm}, Z$) of four-momentum $q \equiv k - k'$ which itself interacts with the proton arriving from the opposite direction with a momentum P. The observation of a large fraction, about 10%, of diffractive events, came as a surprise. In these events a large rapidity gap in the direction of the outgoing proton was observed in addition to hard jets in the central detectors corresponding to the exchange of a colorless object.

The main achievement of the HERA diffractive program is that diffractive events with either large rapidity gap or with a proton detected in forward proton taggers can be described in terms of universal partons densities that could be used elsewhere. To summarize the procedure how diffractive density functions are obtained, it is necessary to introduce the kinematic variables which are used to describe the DIS processes. We start with the standard DIS variables: the weak boson virtuality Q^2, the longitudinal momentum fraction of the proton carried by the struck interacting parton x, and the inelasticity of the

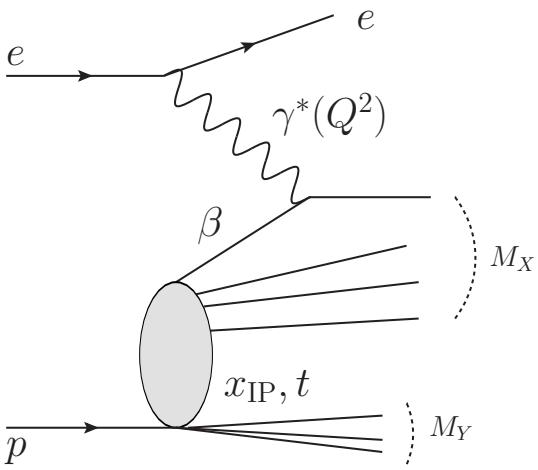

Figure 2.3: Scheme of a neutral current diffractive DIS process $ep \to eXp$ via a virtual photon exchange. The mass of the centrally created system X is M_X while the mass of the proton dissociated system Y is M_Y. The momentum fraction of the proton carried by the colorless object $x_{\mathbb{P}}$ and the momentum fraction of the colorless object carried by the interacting parton β are shown.

process y, which are defined as

$$\begin{aligned} Q^2 &\equiv -q^2 \\ x &\equiv \frac{Q^2}{2P\cdot q} \\ y &\equiv \frac{P\cdot q}{P\cdot k} = \frac{Q^2}{sx} \end{aligned} \tag{2.28}$$

The masses of the electron(positron)-proton and gauge boson-proton system are $s = (k+P)^2$ and $W^2 = (q+P)^2$, respectively.

The hadronic final state in diffractive DIS (DDIS) is composed of two systems: X which comprises the produced system X in the center of the detector and the system Y of the proton or its dissociated products (which have the same overall quantum numbers as the initial proton except the spin since the angular momentum can be exchanged in the interaction). The diffractive DIS in which the proton dissociated is depicted in Figure 2.3. If the masses M_X, M_Y are small compared to the γ-proton mass W, there is a large rapidity gap devoid of hadronic activity observed between the two systems. The diffractive process can then be defined as an exchange of a colorless object of well defined four-momentum. The longitudinal momentum fraction $x_{\mathbb{P}}$ of the proton carried out by the colorless object, and β the momentum fraction of the struck quark with respect to the colorless object can then be defined as

$$\begin{aligned} x_{\mathbb{P}} &= \frac{q\cdot(P-p_Y)}{q\cdot P} \\ \beta &= \frac{Q^2}{2q\cdot(P-p_y)} = \frac{Q^2}{Q^2+M_X} \end{aligned} \tag{2.29}$$

if one assumes that the colorless object is made of partons. p_Y is the four-momentum of system Y. The β variable can be related to the Bjorken scaling variable x through $x = x_{\mathbb{P}}\beta$ and β can be interpreted as

the momentum fraction taken by the quark from the colorless object if it has a partonic structure. The squared four-momentum transfer of the proton is $t = (P - p_Y)^2$ and is usually very small $|t| < 1\,\mathrm{GeV}^2$ in diffractive processes.

The successful description of the diffractive data relies on two types of factorization which allowed to describe those processes in the same way as the non-diffractive ones. First, it was proved that the collinear factorization holds not only in inelastic DIS but also in the diffractive DIS [23]. The cross section is then given by a convolution of the partonic sub-process, which is the same as in inelastic DIS $\sigma^{ei}_{\mathrm{sub}}(x,Q^2)$, and of the diffractive parton distribution functions (DPDF) of the proton $f_i^D(x,Q^2,x_{\mathbb{P}},t)$ (cf. also (2.17))

$$\mathrm{d}\sigma^{ep\to eXY} = f_i^D(x,Q^2,x_{\mathbb{P}},t) \otimes \mathrm{d}\sigma^{ei}_{\mathrm{sub}}(x,Q^2) \tag{2.30}$$

The DPDF $f_i^D(x,Q^2,x_{\mathbb{P}},t)$ are interpreted as a probability to find a parton i carrying the proton longitudinal momentum x, having a virtuality Q^2, under the condition that the proton which lost a momentum fraction $x_{\mathbb{P}}$ stayed intact or dissociated to a system with the same quantum numbers as the proton (the two cases turn to be similar up to a normalization factor of the parton densities). Since the struck partons carry a color from the proton, the proton system has to reorganize its structure. The chance that it will reorganize to exactly a color neutral proton state is limited, thus diffractive hard processes have smaller cross sections than the non-diffractive ones.

The second type of factorization is based on the observation of diffractive HERA data. The so-called proton-vertex factorization suggests that the DPDF can be further decomposed into a flux depending on $x_{\mathbb{P}}$ and t only and a term depending on β and Q^2

$$f_i^D(x,Q^2,x_{\mathbb{P}},t) = f_{\mathbb{P}/p}(x_{\mathbb{P}},t) \cdot f_i(\beta = x/x_{\mathbb{P}},Q^2) \tag{2.31}$$

In terms of this parameterization, the diffractive process is viewed as an exchange of a colorless pomeron whose parton structure is described by the parton distributions $f_i(\beta,Q^2)$, where β is the fraction of the pomeron momentum taken out by the interacting parton and Q^2 the quark virtuality. The form of the pomeron flux is motivated by the Regge theory for SD (cf. (2.26) with a substitution $M^2/s = \xi$) and reads

$$f_{\mathbb{P}/p}(x_{\mathbb{P}},t) = A_{\mathbb{P}} \cdot \frac{e^{B_{\mathbb{P}} t}}{x_{\mathbb{P}}^{2\alpha_{\mathbb{P}}(t)-1}} \tag{2.32}$$

where the $\alpha_{\mathbb{P}}(t) = \alpha_{\mathbb{P}}(0) + \alpha'_{\mathbb{P}} t$ is the pomeron trajectory.

The HERA data show that the proton-vertex factorization holds well in a large range of $x_{\mathbb{P}}$ and β. Note however, that a sub-leading exchange is needed to get a correct description of the HERA data at low β and high $x_{\mathbb{P}}$. The sub-leading exchange corresponds to an additional reggeon trajectory. With the assumption that the reggeon obeys the same proton-vertex factorization as the pomeron (2.31), the DPDFs are factorized as

$$f_i^D(x,Q^2,x_{\mathbb{P}},t) = f_{\mathbb{P}/p}(x_{\mathbb{P}},t) \cdot f_i^{\mathbb{P}}(\beta = x/x_{\mathbb{P}},Q^2) + n_{\mathbb{R}}\, f_{\mathbb{R}/p}(x_{\mathbb{R}},t) \cdot f_i^{\mathbb{R}}(\beta = x/x_{\mathbb{R}},Q^2) \tag{2.33}$$

2.10.1 Diffractive parton densities

The measurement of the DPDFs performed by the H1 and ZEUS Collaboration is slightly different. H1 uses a forward spectrometer to measure the momentum loss $x_{\mathbb{P}}$ and momentum transfer t of the proton. In this way, the proton dissociation is removed because the proton is unambiguously tagged. We

note that the ZEUS Collaboration uses a different method to select diffractive events. In the so called M_x-subtraction method, the diffractive sample is defined as the excess contribution in the $\ln M^2$ spectra above the exponential fall-off of the non-diffractive peak which can be precisely fitted. In general, the obtained parton densities in the pomeron agree after corrections (due to proton dissociation which is a normalization factor, and due to detector acceptance), though there are also differences which are still to be fully understood.

In the following, the DPDFs are extracted (we will describe the procedure performed by the H1 Collaboration) in terms of a light flavor singlet distribution $\Sigma(z)$ consisting of u, d and s quarks and anti-quarks assuming $u = d = s = \bar{u} = \bar{d} = \bar{s}$, and gluon distribution $g(z)$. The variable z is the longitudinal momentum fraction of the proton taken by the parton participating in the sub-process (i.e. it is $z = \beta$ at leading order and $\beta < z$ at higher orders of the perturbation series). The general form of the singlet and gluon distributions of the pomeron used in the fits [20] is

$$z f_i^{\mathbb{P}}(z, Q^2) = A_i z^{B_i} (1-z)^{C_i} \tag{2.34}$$

where A_i, B_i, C_i are unknown parameters fitted to data. On the other hand, the structure of the sub-leading reggeon exchange in (2.33) is assumed to be the same as the structure of the pion [25] which quite surprisingly fits the data well. The reggeon intercept and slope, and the pomeron slope are fixed as they were obtained from different measurement using the forward spectrometer [24] (however originally, the reggeon and pomeron structure were fitted together using the H1 central detector only identifying diffractive events with the rapidity gap method). The extracted pomeron and reggeon trajectories are $\alpha_{\mathbb{P}}(0) = 1.118$, $\alpha'_{\mathbb{P}} = 0.06$, $\alpha_{\mathbb{R}}(0) = 0.5$, $\alpha'_{\mathbb{R}} = 0.3$. The hard pomeron has a higher intercept than the soft one ($\alpha_{\mathbb{P}}(0) = 1.0808$).

The DPDFs fits determine the quark and gluon partonic structure of the pomeron (2.34) with the pomeron intercept governing the pomeron energy dependence (2.32). The parton densities are fitted at the initial scale $Q_0^2 = 2 - 3\,\mathrm{GeV}^2$, and are evolved to the Q^2 of the process using the next-to-leading DGLAP evolution equations (2.16). The H1 results are given in Figure 2.4 for the quark singlet distribution (left) and the gluon distribution (right). The data constrain very well the quark distribution for the whole range of β accessible by the measurement $0.0043 < \beta < 0.8$ and for a range of Q^2 up to $\sim 1000\,\mathrm{GeV}^2$. The gluon density at small Q^2 is however well constrained only up to $\beta \sim 0.3$. At high β close to one, the uncertainty on the gluon is large. This is illustrated by two different fits, Fit A and Fit B, which give an overall good description of data, but their gluon component at high z is much different. Both fits have different assumptions on the parameterization of the gluon density at the initial scale which yields non-compatible predictions on the gluon density at high β while leading to the correct description of data. We note that adding also the dijet data in the QCD fits allows to reduce the uncertainty on the large β gluon density.

As shown in Figure 2.4, the pomeron is predominantly composed of gluons. The fraction of gluons in the pomeron increases with Q^2 as a result of the DGLAP evolution. This is also demonstrated in Figure 2.5 where the $\ln Q^2$ derivative of the reduced diffractive cross section is shown. The reduced cross section $\sigma_r^{D(3)}$ is free of kinetic factors coming from the electron-photon part of the process, and is related to total cross section (2.30) by[3]

$$\frac{\mathrm{d}^3\sigma^{ep\to eXY}}{\mathrm{d}x_{\mathbb{P}}\,\mathrm{d}x\,\mathrm{d}Q^2} = \frac{2\pi\alpha^2}{xQ^4} \cdot Y_+ \cdot \sigma_r^{D(3)}(x_{\mathbb{P}}, x, Q^2) \tag{2.35}$$

[3]For y not so close to unity, the contribution corresponding to the exchange of longitudinal virtual photons can be neglected and the total cross section takes the form (2.35).

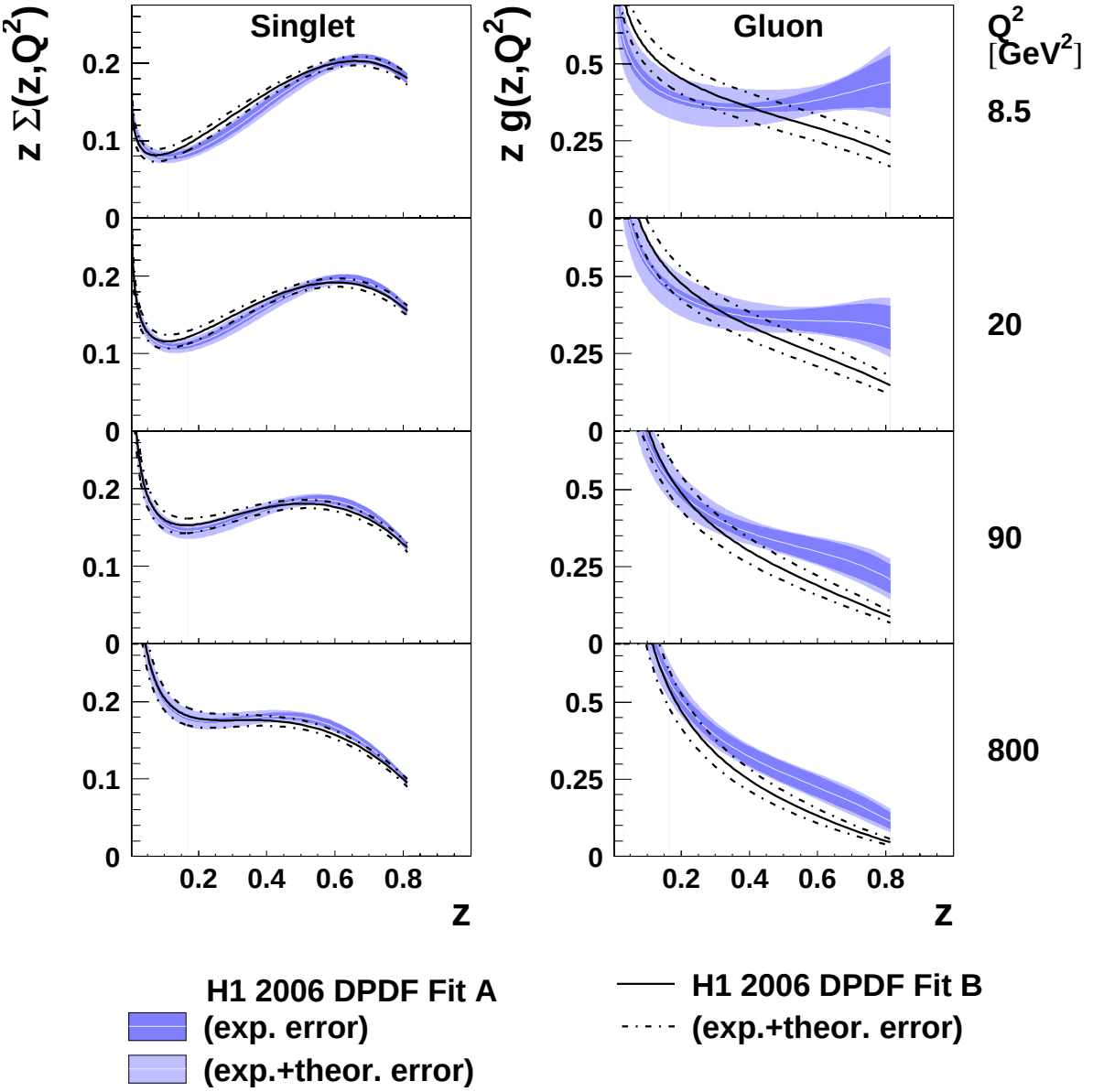

Figure 2.4: Comparison of the total quark singlet and gluon distribution function obtained for two fits "H1 2006 DPDF FitA" and "H1 2006 DPDF FitB" with their total uncertainties shown. The fits give the same results for the quark distributions but differ in the case of the gluon at high $z = \beta$. The current H1 fits indicate that the DPDF are compatible with "FitB" when diffractive dijet measurement is included in the fit.

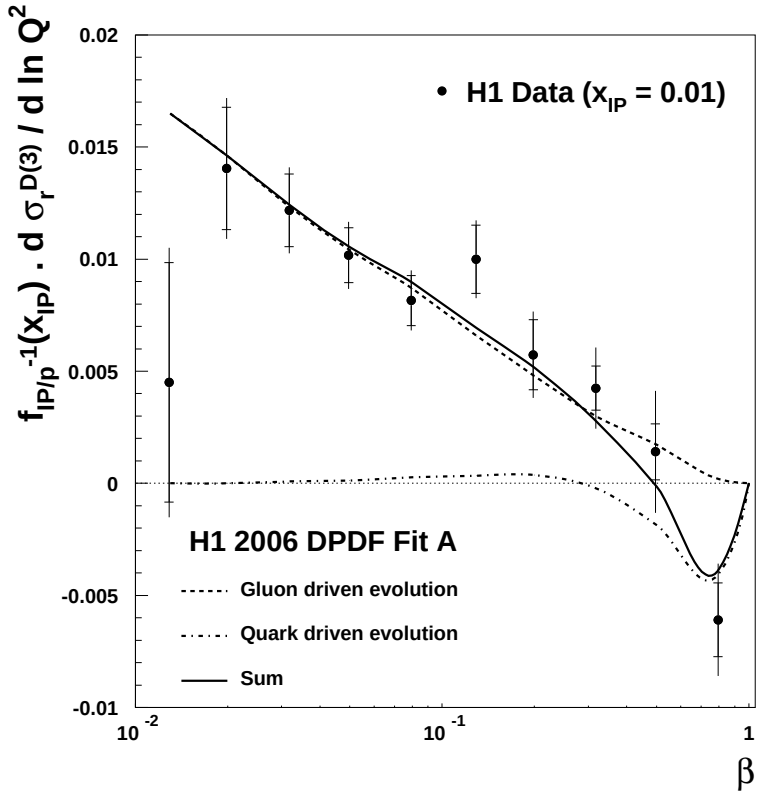

Figure 2.5: Logarithmic Q^2 derivative of the diffractive reduced cross section (2.35) in DIS which is predicted by the DGLAP evolution and is in good agreement with data. Contribution of every event was normalized by the pomeron flux to show the DGLAP dynamics over a large data sample of various $x_{\mathbb{P}}$. The Q^2 evolution is driven mainly by the gluons in the pomeron.

where the integration over t has been performed and Y_+ is given by the inelasticity y as $Y_+ = 1+(1-y)^2$. The logarithmic dependence of the cross section is predicted by the DGLAP evolution and therefore is a direct test of the evolution mechanism of DPDFs. We see that the evolution is driven mainly by gluons over a large range of β. At $\beta \sim 1$ the quark and gluon evolutions are similar. In this region the uncertainties of the gluon DPDF are large.

The parton densities at H1 were extracted in neutral-current interactions tagging the outgoing intact proton and reconstructing the DDIS kinematics from the scattered electron regardless what object has been produced in the central detector. Important point is that they proved to be universal within DDIS data, successfully describing also neutral current data as well as other diffractive measurements with specific final states like dijets, charm production, etc.

We have seen that the understanding of the proton structure in diffractive and diffractive dissociation processes has developed from the Regge picture of soft reggeon and pomerons, to the perturbative partonic structure of the pomeron in semi-inclusive processes measured at HERA. As will be shown in the following, the diffractive parton density functions measured in DIS are used to compare with Tevatron diffractive data and also to make predictions at the LHC where new diffractive phenomena are studied.

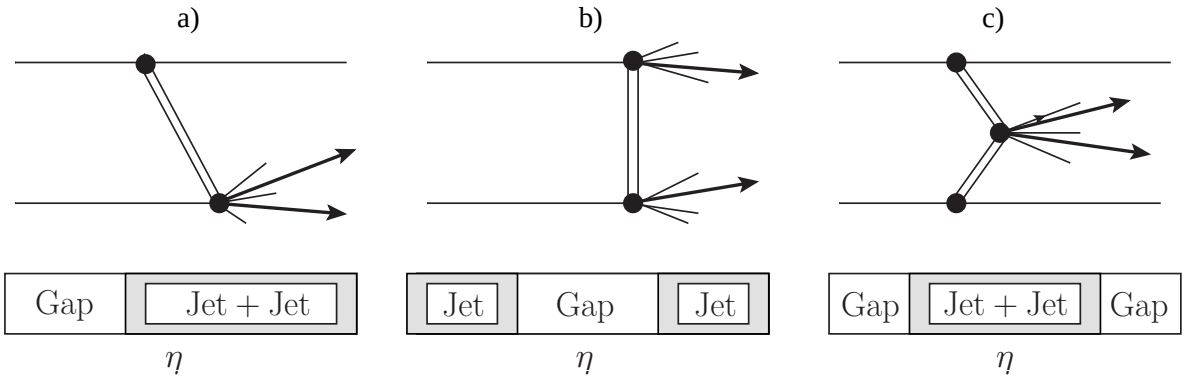

Figure 2.6: Three main colorless exchanges at hadron-hadron collider: a) single diffractive dissociation (or single diffraction), b) double diffractive dissociation c) double pomeron exchange. See text for further description.

2.11 Hard diffraction at the Tevatron

At hadron-hadron colliders such as the Tevatron or the LHC, new hard diffractive processes are studied. The diffractive structure of both protons can be investigated. The description of hard diffractive processes faces however a difficulty contrary to the case in deep-inelastic scattering. It was proved that the factorization of the cross section into the parton density functions and the hard subprocess cross section does not hold [26]. The additional soft interactions, either in the initial or final states, can spoil the signature of the diffractive event with rapidity gaps. It is important to understand the way how the factorization is broken and how it effects hard diffraction in hadron-hadron scattering.

The observation made at the Tevatron suggests that the factorization breaking results in an overall suppression factor, little depending on the kinematics of the hard interaction or the type of the hard interaction. Apart from this factor, the diffractive structure function of the proton can still be decomposed into the pomeron flux and the pomeron parton densities as in ep interactions. The hard diffractive processes are viewed as being due to the exchange of the hard pomeron. We should emphasize however that with more precise measurements, the survival probability might reveal its dependence on the process kinematics and that the general assumption of the constant supression factor does not have to be true.

Three basic colorless exchanges at the hadron collider with a characteristic hard scale depicted in Figure 2.6 are the following:

a) Single diffractive dissociation (SD) - the colorless object coupling to the upper proton is described by Regge theory, the proton stays intact (or dissociates to a system of similar mass as of the proton). In the lower vertex, the proton-pomeron interaction probes the partonic structures of the proton and pomeron. The creation of the high mass object X is described by perturbative QCD. The lower proton is destroyed and proton remnants are present on the side of the broken proton whereas a rapidity gap between the intact proton and the object X is observed. Typical objects X studied in single diffraction are a dijet system and the production of electroweak bosons W/Z.

b) Double diffractive dissociation - the colorless object interacts with both protons as in non-diffractive processes. The partonic structure of a pomeron inside both protons is probed. There are two X and Y hadronic systems of substantial mass on either side due to two hard pomeron-proton interactions. The central rapidity region is empty due to the exchange of a colorless object. The systems

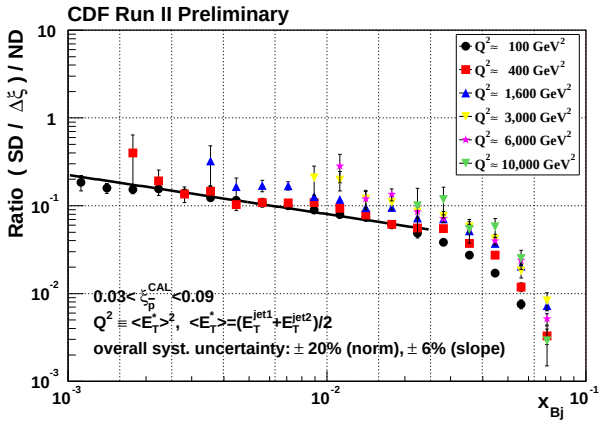

Figure 2.7: Ratio of diffractive to non-diffractive dijet event rates as a function of Bjorken-x (momentum fraction of parton in the antiproton) for different values of $E_T^2 = Q^2$.

X, Y are typically jets. Such events have jets in very forward region of the detector separated by a large gap across the whole detector.

c) Double pomeron exchange (DPE) - two colorless objects are emitted from both protons. Their partonic components are resolved and create a heavy mass object X in the central detector in the pomeron-pomeron interaction. The event is characterized by two rapidity gaps between the central object and the protons. Through the exchange of two pomerons a dijet system, WW and ZZ pair, or Drell-Yan pair can be created for instance.

A better understanding of hard diffraction and of the pomeron structure was achieved by the Tevatron DØ and mainly CDF experiments. Diffractive events were selected with the rapidity gap method requesting no reconstructed objects in the forward region of the detector like forward calorimeter or the beam shower counters which registered the forward particle flow of the collision. Later in Run I and Run II, the CDF Collaboration used in addition the forward Roman Pot Spectrometer installed about 60 meters from the interaction point to tag the outgoing intact antiprotons $\bar{p}$ which in diffractive events lose a longitudinal momentum fraction $\xi \equiv |\vec{p}_{\mathrm{b}}| - |\vec{p}'|/|\vec{p}_{\mathrm{b}}|$ ($\xi = x_{\mathbb{P}}$ at HERA) and are deflected out of the circulating beam. $\vec{p}_{\mathrm{b}}$ is the beam momentum and $\vec{p}'$ denotes the outgoing proton momentum. This allows to measure the properties of the diffractive structure function precisely, test the predictions of the Ingelman-Schlein factorized model, and understand the way how factorization is broken.

Significant measurements of single diffractive production of dijets and electroweak boson, double pomeron exchange of dijets, and their implication for understanding the factorization breakdown and the exclusive production are going to be discussed in some detail in the following sections.

2.12 Pomeron structure at Tevatron

The first measurements at the Tevatron concerning hard diffraction studied the SD dijet production $p\bar{p} \to jjX \oplus p(\bar{p})$ where X denotes the pomeron remnants and $\oplus$ a rapidity gap between the dijet jj system and the intact proton [27, 28, 29, 30]. Assuming that the pomeron is composed of partons, the scheme of the single diffractive dijet process is essentially the same as in DIS Figure 2.3, except that a

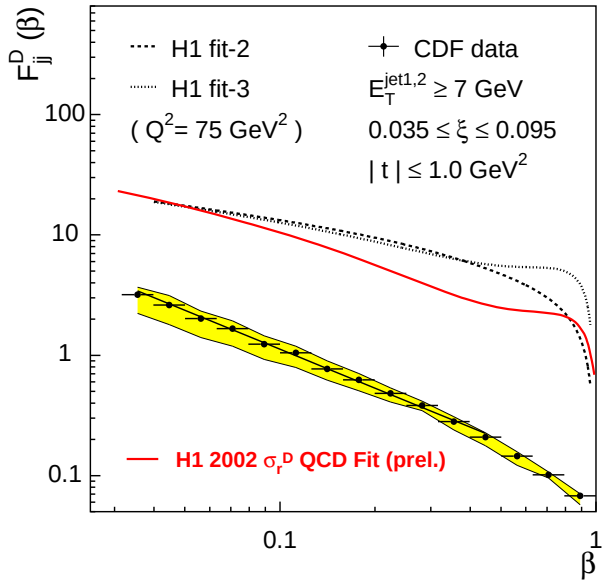

Figure 2.8: Dijet diffractive structure function F_{JJ}^D as a function of β, measured by CDF [30]. The dotted and dashed lines are the expectations based on the diffractive parton densities measured in diffractive DIS by H1 [32].

partonic structure of a proton is probed instead of an electron emitting a photon. As in DDIS, the proton momentum fraction loss ξ and the momentum of the pomeron taken away by the interacting parton β are related to the Bjorken scaling variable x as $x = \xi\beta$. The proton momentum fraction taken away by the interacting parton is determined in each event from the transverse energy E_T and pseudorapidity η of the jets i using

$$x = \frac{1}{\sqrt{s}} \sum_{i=1}^{n} E_T^i e^{-\eta^i} \tag{2.36}$$

The gluon and quark content of the exchanged pomeron can be investigated comparing the single diffractive (SD) and non-diffractive (ND) dijet events. It was observed that SD dijet events constitute about 1% of the ND dijet cross section. The shape of the jet transverse momentum distribution in SD dijets is the same as in ND sample suggesting that the parton evolution in SD and ND is driven by the same DGLAP mechanism. This fact is confirmed by measuring the ratio of diffractive to non-diffractive events as a function of Bjorken-x shown in Figure 2.7. The ratio does not change over a large range of $Q^2 \equiv < E_T^* >^2$, $< E_T^* > = (E_T^{\text{jet1}} + E_T^{\text{jet2}})/2$ indicating that the pomeron parton structure evolves as the one of the proton.

The t dependence of SD events was measured for events up to high Q^2 and no dependence of the shape of the t distribution on Q^2 was found. This signals the proton vertex $t - Q^2$ factorization.

2.13 Factorization breaking

In order to investigate the factorization breaking at hadron colliders, the SD structure function is measured and compared to the one obtained at HERA. In leading order QCD, the ratio $R(x,\xi)$ of the SD to non-diffractive (ND) rates is equal to the ratio of the antiproton SD to ND structure functions. Therefore, the diffractive structure function is obtained by multiplying the known ND structure function by

$R(x,\xi)$. The corresponding inclusive structure function can be written as

$$F_{jj} = x\left(g(x) + \frac{4}{9}\sum_f [q_f(x) + \bar{q}_f(x)]\right) \tag{2.37}$$

where $g(x)$ is the gluon and $\bar{q}_f(x)$, $q_f(x)$ are the (anti)quark densities which are multiplied by a factor of 4/9 to account for color factors. The diffractive structure function F_{jj}^D is obtained as $F_{jj}^D(\beta)$=$R(x,\xi)F_{jj}(x)$ and changing variable x to β where $\beta \equiv x/\xi$ (note that the ratio $R(x,\xi)$ was integrated over t and jet transverse momentum E_T).

The CDF Collaboration also noticed that the β and ξ dependences of the structure function can be factorized. For fixed β, the dependence $\xi^{-0.9\pm0.1}$ indicates that the dijet production is dominated by the pomeron exchange [30]. Indeed, the Regge theory predicts $\xi^{-\alpha(0)} \sim \xi^{-1.1}$ for the pomeron, whereas the dependence is $\sim \xi$ for the reggeon exchange as can be seen from (2.32). Should the factorization of the single diffractive cross section hold, the production cross section could be written as a convolution of the sub-matrix cross section, the pomeron flux factor and the parton densities of the pomeron as

$$\mathrm{d}\sigma^{pp\to p\oplus jjX} = f_{\mathbb{P}/p}(\xi,t)\cdot f_{i/\mathbb{P}}(\beta = x/\xi,\mu)\cdot f_{j/p}(x_2,\mu)\otimes \mathrm{d}\sigma^{ij}_{\mathrm{sub}}(\beta,x_2,\mu) \tag{2.38}$$

where $f_{\mathbb{P}/p}(\xi,t)$ is the pomeron flux as in (2.32) parameterized by the pomeron trajectory $\alpha(t) = \alpha(0) + \alpha' t$, $f_{i/\mathbb{P}}(\beta,\mu)$ is the density function of a parton i carrying the pomeron momentum fraction β, $f_{j/p}(x_2,\mu)$ is the density function of a parton j carrying the proton momentum fraction x_2 and μ is the factorization and renormalization scale set equal. The sub-process cross section $\mathrm{d}\sigma^{ij}_{\mathrm{sub}}$ is the same as in inelastic hadron-hadron scattering. The factorization of the cross section (both collinear and proton-vertex factorization) was proved to hold between the Tevatron data themselves within uncertainties. However, the existence of the universal factorization in diffraction could not be demonstrated as anticipated.

The diffractive parton density functions as measured at HERA can be plugged into the above formula for $f_{i/\mathbb{P}}(\beta,\mu)$ with the fitted value of the pomeron trajectory $\alpha(t)$. Using also the proton PDF $f_{i/p}$ measured in inelastic scattering and extracted for example by CTEQ or MSTW groups [33], the direct comparison of the HERA prediction with the structure function extracted at the Tevatron can be made. It is shown in Figure 2.8. The measurement of the diffractive structure function F_{jj}^D disagrees mainly in normalization. It is suppressed approximately by a factor of 10 at the Tevatron with respect to HERA. The suppression is attributed to additional soft partonic interactions which spoil the gap formed by the pomeron exchange and also break the outgoing proton. The probability that the event with rapidity gaps survives the soft exchanges is called the soft survival probability factor $\langle |S|^2 \rangle$. As mentioned, it was found to be to a great extent independent of the details of the process (i.e. does not depend on ξ, t, β, Q^2) . The HERA prediction and the Tevatron measurement also disagree in shape for $\beta > 0.4$. Since the dijet production at the Tevatron is gluon dominated, this is usually attributed to the uncertainty on the gluon density at high β when extracted at HERA, but it could also signal the β dependence of the survival probability factor.

The factorization breaking was also observed in SD W, b-quark, J/ψ productions and double diffractive production of events with a gap between jets (Jet+Gap+Jet). The corresponding SD to ND ratios are summarized in the Table 2.13 [32]. All processes yield similar SD to ND ratios $\sim$ 1% and lead to the same factorization breaking. An interesting result is that the fraction of SD events decreases as a function of the center-of-mass energy as seen for Jet+Gap+Jet data. This indicates that the survival probability factor decreases as the center-of-mass energy of the collision increases.

Hard process	$\sqrt{s}$[GeV]	R=SD/ND	Kinematic region
$W(\to e\nu)$+Gap	1800	1.15 ± 0.55	E_T^e, $\not{E}_T > 20$ GeV
Jet+Jet+Gap	1800	0.75 ± 0.1	$E_T^{\text{jet}} > 20$ GeV, $\eta^{\text{jet}} > 1.8$
$b(\to e+X)$+Gap	1800	0.62 ± 0.25	$\lvert\eta^e\rvert < 1.1$, $p_T^e > 9.5$ GeV
$J/\psi(\to \mu\mu)$+Gap	1800	1.45 ± 0.25	$\lvert\eta^\mu\rvert < 0.6$, $p_T^\mu > 2$ GeV
Jet+Gap+Jet	1800	1.13 ± 0.16	$E_T^{\text{jet}} > 20$ GeV, $\eta_{\text{jet}} > 1.8$
Jet+Gap+Jet	630	2.7 ± 0.9	$E_T^{\text{jet}} >$ GeV, $\eta^{\text{jet}} > 1.8$

Table 2.1: SD to ND event ratio for forward and central gap processes at CDF [32]. Similar results were found by the DØ Collaboration.

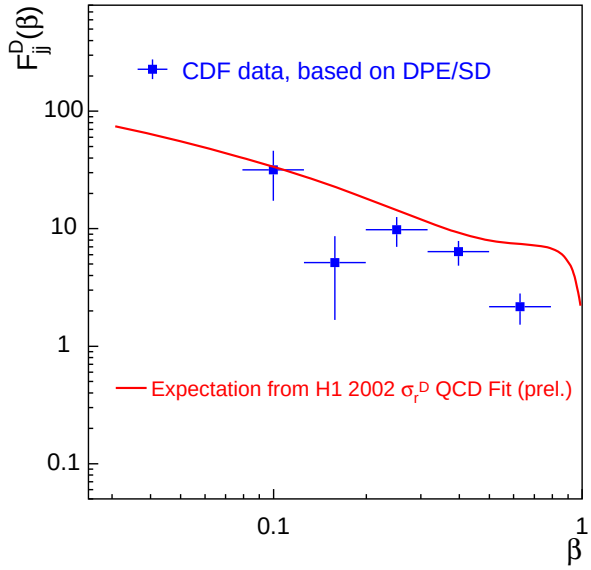

Figure 2.9: The dijet SD diffractive structure function F_{JJ}^D measured on the proton side in DPE events with a leading antiproton at CDF [30] compared to the expectations from the H1 parton densities measured in DDIS at HERA [32].

2.13.1 Restoring factorization

The rapidity gap formation was also studied in the DPE events where two rapidity gaps are present on each side of the central dijet system. The double-ratio D of dijet production in SD over ND events, R_{ND}^{SD}, to that of DPE over SD, R_{SD}^{DPE} was measured. If factorization holds, the D ratio would be unity. However, if an additional soft exchange between the protons occurs, it spreads over the whole rapidity region. Either both rapidity gaps in DPE events survive, or are spoiled at the same time. Therefore, the ratio is expected to be proportional to the survival probability factor (not squared) and factorization is expected to break in the D ratio. It was measured to be 0.19 ± 0.07 and confirmed that the formation of the second gap is not suppressed. Moreover, when the structure function was measured in DPE events where already one gap was present and compared to the HERA expectation, no factorization breaking was found as is seen Figure 2.9.

2.14 Rapidity gap survival probability

Processes involving rapidity gaps have to be corrected for initial and final-state interactions and the additional interaction between spectator partons. Since the hard interaction occurs at short distance and does not change the quantum numbers of the protons, it does not influence the rescattering. On the other hand, the soft interaction can change the proton momenta and the hard scattering would have to be convoluted with the soft exchanges. This difficulty disappears if one works in the impact parameter space. The probability of the process is then a product of the hard scattering cross section multiplied by the probability that the two protons go through each other.

The soft rescattering amplitude governs also the elastic and total cross sections and can be extracted from data. The survival probability is related to the scattering amplitude $a(s,\mathbf{b})$ in the impact parameter space as

$$S(s,\mathbf{b}) = 1 + ia(s,\mathbf{b}) \tag{2.39}$$

where $\mathbf{b}$ is the impact parameter. In general, the gap survival probability will be close to 1 at large $\mathbf{b}$ where the overlap between the projectile hadrons is small. On the other hand, it is generally believed that the elastic amplitude at the Tevatron approaches the black-disk limit $a(s,\mathbf{b}) = i$ for small $\mathbf{b}$ where the survival probability vanishes.

Any fit of the differential elastic cross section can be used to estimate the gap survival probability. The simple approach assumes that the hard interaction occurs really at short distance where the elastic amplitude is purely imaginary. Taking the fits of the elastic cross section at the Tevatron $\mathrm{d}\sigma_{el}/\mathrm{d}t \sim \exp(2B_{el}t)$, one can arrive at a survival probability factor less then 1% [37] which is rather pessimistic. When the problem is treated more correctly (for example taking into account the elastic t-dependence which is not exactly an exponential, a non-zero contribution of the real part of the elastic scattering amplitude, etc.) the theoretical predictions agree with data which exhibit the survival probability factor $\mathcal{O}(0.1)$ at the Tevatron.

The theoretical predictions [39, 40, 41] for CEP at the LHC are about a factor of 3 smaller and they vary approximately by a factor of 3. In [38], the survival $\left\langle |S|^2 \right\rangle$ was predicted to be 0.03 at the LHC. The survival probability factor for single diffractive processes is higher, about 6% [42]. In two-photon scattering (to be mentioned later), the impact parameter of the scattering protons $\mathbf{b}$ is larger than in diffractive scattering. Consequently, the survival probability factor is bigger. The theoretical predictions of the survival probability factor in two-photon processes are 0.75 for the Tevatron and 0.9 for the LHC [38]. These values of the survival probability factors are adopted throughout the thesis as a default.

2.15 Central exclusive QCD production

Central Exclusive Production (CEP) is a special type of event with two intact proton. The whole energy of the colorless exchange is used to produce the central system of interest without producing pomeron remnants. Rapidity gaps between the object like a dijet system for example produced at central rapidities and the intact protons are therefore large. Another interesting consequence of the process exclusivity is that the mass of the central system can be precisely matched to the momentum fraction loss of the two intact protons. This allows a very precise mass reconstruction of the created final state central system if both forward protons are detected.

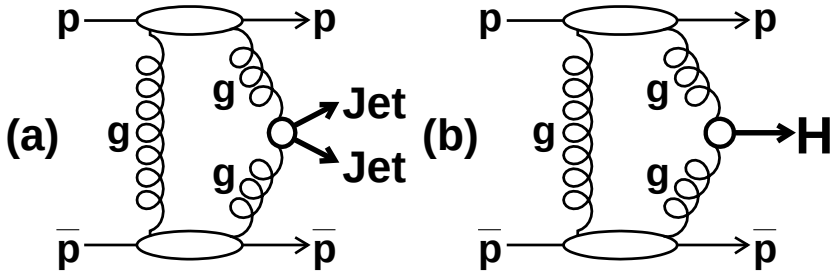

Figure 2.10: Leading order diagrams for (a) exclusive dijet and (b) exclusive Higgs boson productions in $p\bar{p}$ collisions.

The feynman diagram of CEP dijet and CEP Higgs productions are shown in Figure 2.10. In leading order perturbative QCD, the colorless exchange from each proton is represented by an exchange of two gluons. The coupling of the gluons to the protons is described by the unintegrated parton densities of the proton. These unintegrated parton densities are two-dimensional probability density functions, depending on two gluon momentum fractions x_1, x_2. They are extracted from the vector meson production data at HERA [34]. It is generally believed that one of the two gluons attached to each proton is hard whereas the other one is soft and provides a color screening to the hard gluon so that there is no overall color flow between the scattering protons. The exclusivity of the event is assured by applying the Sudakov form factor which prohibits radiation of additional gluons in higher orders of the perturbative QCD in the event and reduces the cross section significantly.

Since both protons are intact and lose only a tiny momentum fraction, no orbital momentum is transferred in the z direction of the beam, $J_z = 0$ to a great approximation. The consequence is that the production of quark jets in particular is suppressed by a factor m_q^2/M_{jj}^2, and decreases as the mass of the dijet system M_{jj} grows. m_q represents the quark mass implying that the CEP dijet production is large for heavy quarks. Since the two gluons exchange the vacuum quantum numbers, the produced system has to carry a positive C and P-parity. This provides a useful experimental determination of the properties of the central object. By observing the CEP process, the quantum numbers of the produced object are unambiguously known. This represents a great motivation to study Central Exclusive Production at the LHC because, if it exists and is observed through the CEP mechanism, the information about C and P-parities are automatically fixed (provided that the background is not too high) contrary to the conventional methods which rely on measuring angular distributions and demand a large amount data to be collected.

The production rates of a Higgs boson at the Tevatron are too low for the Higgs to be observable. However, the CDF Collaboration has measured the exclusive dijet cross section using the dijet mass fraction (DMF) measurement [35]. The dijet mass fraction is defined as a ratio of the dijet invariant mass R_{JJ} over the total produced mass in the final state except the outgoing protons M_X, such as $R_{jj} = M_{jj}/M_X$. The total energy lost by the scattered protons is used to produce the central object in exclusive events. Hence we expect an additional signal at large $R_{jj} = 1$ if exclusive events exist.

At LHC energies, the CEP is an important part of the forward physics program. However, the cross section prediction suffers from theoretical uncertainties. These include: form and range of integration of the Sudakov form factor which is responsible for vertex corrections and suppression of additional gluon radiation, contribution of soft component to unintegrated gluon distributions which is known with con-

siderable uncertainties, and also lack of knowledge of the soft survival probability factor. Understanding the CEP of dijets at the Tevatron is therefore important to constrain CEP models and reduce their uncertainties when extrapolated to the LHC. For this reason, the CDF method to extract the exclusive dijet signal was tested in Chapter 5 of this thesis. Recently, the observation of the central exclusive charmonium χ_c production was reported at the Tevatron [36] and also provides useful data for constraining the current models.

2.15.1 Central exclusive Higgs boson production

The discovery of the SM Higgs boson in CEP is probably not possible due to the small production rates (a conservative estimate is $\approx 3\,\text{fb}$ for a Higgs mass $m_h = 120\,\text{GeV}$ [38]). But once it is observed in the central detector and its mass is roughly determined, a precise measurement of the Higgs properties can be carried out by tagging the intact protons in the forward detectors, searching the signal in a specific mass window. These detectors are currently in consideration as a future upgrade of the ATLAS and CMS experiments at the LHC and are discussed in Chapter 6. When even a few CEP Higgs events are observed, the quantum numbers of the Higgs boson are fixed, since only the scalar production 0^{++} is allowed. Moreover, the mass of the boson can be measured with the $\sim$ GeV precision with the forward detectors.

If the Higgs mass m_h is in the range $140\,\text{GeV} < m_h < 200\,\text{GeV}$, the WW^+ decay mode is the simplest channel to observe the SM Higgs in semi- or fully-leptonic decays of the electroweak bosons. It was found that about 3 signal events would be observed with $30\,\text{fb}^{-1}$ with a signal to background ratio about one.

For smaller masses the only considerable channel is $h \to b\bar{b}$, which is more challenging. If b jets can be tagged in the central detector, the CEP gg dijet background can be suppressed. Moreover, the CEP $b\bar{b}$ production is suppressed with respect to the Higgs production due to the $J_z = 0$ selection rule, and also due to spin and color suppression factors. However, another background stemming from high number of proton-proton interactions occurring in one bunch crossing, in which non-diffractive $b\bar{b}$ dijet event is overlaid with two single diffractive protons giving a hit in the forward detectors, is large. This background is reduced by registering also the proton arrival time, constraining the collision position and matching it to the vertex position reconstructed in the central detector.

In Beyond Standard Model theories like the Minimal Super Symmetric Model (MSSM) where three neutral h, H, A and two charged H^+, H^- Higgs bosons are present, the Higgs production cross sections are largely enhanced for certain parameters of the MSSM, yielding a clear signal over the mentioned dominant overlaid background [45]. The detection of scalar Higgs in $h, H \to b\bar{b}, \tau\tau$ decays is possible. Moreover, since the pseudo-scalar production is forbidden in CEP, the quantum numbers and the mass can be measured even when m_A is close to m_h or m_H, which can occur for some MSSM parameters (high $\tan\beta$).

2.16 Two-photon exchanges

Exclusive processes can also be initiated by the exchange of two photons. Their interaction yields a system X which is separated by large rapidity gaps in forward region from outgoing protons $pp \to p(\gamma\gamma)p \to p \oplus X \oplus p$, see Figure 2.11. Both protons leave the interaction intact, scattered at very small angles $\lesssim 100\,\mu\text{rad}$. The γp coupling depends on the proton electromagnetic structure, which has been

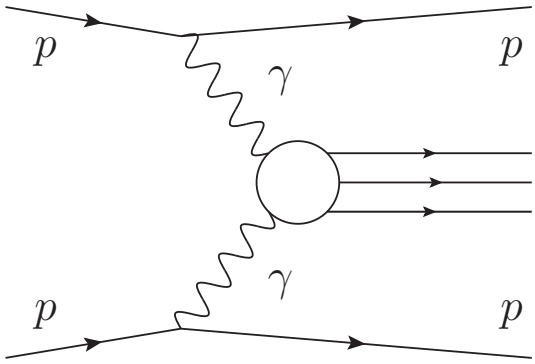

Figure 2.11: Sketch diagram showing the two-photon production of a central system. Unaltered protons leave the interaction at very small angles $\lesssim 100\,\mu$rad and the central system is produced alone in the central detector without any proton remnants.

known in detail for a long time. The production cross sections are calculable within Quantum Electrodynamics and are known very precisely.

Since the exchanged photons are almost real due to the form factor Q^2-dependence, the total cross section is factorized into the effective photon-photon luminosity $\mathrm{d}L^{\gamma\gamma}/\mathrm{d}W$ and the cross section of a particular sub-process as

$$\frac{\mathrm{d}\sigma}{\mathrm{d}\Omega} = \int \frac{\mathrm{d}\sigma_{\gamma\gamma\to X}(W)}{\mathrm{d}\Omega} \frac{\mathrm{d}L^{\gamma\gamma}}{\mathrm{d}W} \mathrm{d}W \tag{2.40}$$

The photon-photon luminosity can be calculated in the Equivalent Photon Approximation [46] and is described in detail in Chapter 4.

The only major uncertainty on the two-photon cross section is due to the fact that a soft rescattering between outgoing protons exists, which spoils the exclusive signature of the clean two-photon event. In this case, the protons are broken and a large region in rapidity is filled with proton remnants. However, the probability that a two-photon event survives is quite large. The soft survival probability is predicted to be around 0.9 (0.75) at the LHC (Tevatron) [38].

Not such a long time ago, a two-photon signal in hadron-hadron collision was first observed at the Tevatron. In particular, the CDF Collaboration recorded isolated electron-positron pairs [43] with large rapidity gaps produced in $pp \to pl^+l^-p$ through $\gamma\gamma \to l^+l^-$. The obtained agreement between the two-photon dilepton production cross section measurement with the theoretical prediction proved that the definition of exclusive process at CDF was well understood and could in turn be applied for the CEP of two photons [44]. The production cross sections are, however, small at the Tevatron. The real merit of the two-photon physics will not be before the LHC where the high center-of-mass energy implies high rates for a range of physics processes.

As it was reviewed in [47], the LHC program of photon-induced interactions includes the two-photon production of lepton pairs that will be used for the independent luminosity measurement, two-photon production of W and Z pairs as a mean to investigate anomalous triple and quartic gauge couplings, two-photon production of supersymmetric pairs, associated WH photoproduction, and anomalous single top photoproduction. Last but not least, the dimuon two-photon production will be used for calibration and an independent alignment of the forward detectors. This method will be also studied in Chapter 6 for the ATLAS 220 m forward detector.

2.16.1 Pomeron-photon interactions

Single photon exchange can occur also in conjunction with the pomeron exchange. The hybrid $\gamma\mathbb{P}$ production yields quasi-exclusive events with one clean rapidity gap on the side of the photon exchange and a smaller gap due to the pomeron remnants. The heavy $q\bar{q}$ quarkonium states such as $pp \to p\Upsilon p$ through $\gamma\mathbb{P} \to \Upsilon$ decaying into two leptons has a clean signature observable already with a low luminosity of 100 pb [48].

Bibliography

[1] C. Amsler *et al.* [Particle Data Group], Phys. Lett. B **667**, 1 (2008).

[2] T. D. Lee and C. N. Yang, Phys. Rev. **104** (1956) 254.

[3] C. S. Wu, E. Ambler, R. W. Hayward, D. D. Hoppes and R. P. Hudson, Phys. Rev. **105** (1957) 1413.

[4] J. Horejsi, *Fundamentals of electroweak theory*, Prague, Czech Republic: Karolinum Press (2002).

[5] S. L. Glashow, Nucl. Phys. **22** (1961) 579; A. Salam and J. C. Ward, Phys. Lett. **13** (1964) 168; S. Weinberg, Phys. Rev. Lett. **19** (1967) 1264.

[6] F. J. Hasert *et al.* [Gargamelle Neutrino Collaboration], Phys. Lett. B **46**, 138 (1973).

[7] G. Arnison *et al.* [UA1 Collaboration], Phys. Lett. B **122**, 103 (1983); M. Banner *et al.* [UA2 Collaboration], Phys. Lett. B **122**, 476 (1983).

[8] R. J. Davis, D. S. Harmer and K. C. Hoffman, Phys. Rev. Lett. **20** (1968) 1205.

[9] R. K. Ellis, W. J. Stirling and B. R. Webber, *QCD and collider physics*, Cambridge University Press, 1996.

[10] M. Kobayashi and T. Maskawa, Prog. Theor. Phys. **49**, 652 (1973).

[11] A. Donnachie and P. V. Landshoff, Nucl. Phys. B **244** (1984) 322; Phys. Lett. B **296**, 227 (1992) [arXiv:hep-ph/9209205].

[12] A. Hebecker, Phys. Rept. **331** (2000) 1 [arXiv:hep-ph/9905226].

[13] E. Predazzi, arXiv:hep-ph/9809454.

[14] S. Abatzis *et al.* [WA91 Collaboration], Phys. Lett. B **324** (1994) 509.

[15] V. Barone, E. Predazzi, *High-Energy Paricle Diffraction*, Springer-Verlag, Berlin, 2002.

[16] R. Bonino *et al.* [UA8 Collaboration], Phys. Lett. B **211** (1988) 239; A. Brandt *et al.* [UA8 Collaboration], Phys. Lett. B **297** (1992) 417.

[17] T. Ahmed *et al.* [H1 Collaboration], Phys. Lett. B **348** (1995) 681.

[18] M. Derrick *et al.* [ZEUS Collaboration], Z. Phys. C **68** (1995) 569 [arXiv:hep-ex/9505010]; M. Derrick *et al.* [ZEUS Collaboration], Phys. Lett. B **356** (1995) 129 [arXiv:hep-ex/9506009].

[19] G. Ingelman, P.E.Schlein, *Phys.Lett.* **B152** (1985) 256.

[20] A. Aktas *et al.* [H1 Collaboration], Eur. Phys. J. C **48**, 715 (2006) [arXiv:hep-ex/0606004].

[21] Z. Kunszt and W. J. Stirling, arXiv:hep-ph/9609245.

[22] A. Berera and D. E. Soper, Phys. Rev. D **53** (1996) 6162 [arXiv:hep-ph/9509239].

[23] J. C. Collins, Phys. Rev. D **57**, 3051 (1998) [Erratum-ibid. D **61**, 019902 (2000)] [arXiv:hep-ph/9709499].

[24] A. Aktas *et al.* [H1 Collaboration], Eur. Phys. J. C **48**, 749 (2006) [arXiv:hep-ex/0606003].

[25] J. F. Owens, Phys. Rev. D **30**, 943 (1984).

[26] C. E. DeTar, S. D. Ellis and P. V. Landshoff, Nucl. Phys. B **87**, 176 (1975); J. L. Cardy and G. A. Winbow, Phys. Lett. B **52** (1974) 95; J. C. Collins, L. Frankfurt and M. Strikman, Phys. Lett. B **307** (1993) 161 [arXiv:hep-ph/9212212].

[27] B. Abbott *et al.* [D0 Collaboration], Phys. Lett. B **531** (2002) 52 [arXiv:hep-ex/9912061].

[28] F. Abe *et al.* [CDF Collaboration], Phys. Rev. Lett. **79** (1997) 2636.

[29] A. A. Affolder *et al.* [CDF Collaboration], Phys. Rev. Lett. **84** (2000) 5043.

[30] A. A. Affolder *et al.* [CDF Collaboration], Phys. Rev. Lett. **88** (2002) 151802 [arXiv:hep-ex/0109025].

[31] K. Goulianos, Diffraction at CDF, talk at "12th International Conference on Elastic and Diffractive Scattering (Blois Workshop) - Forward Physics and QCD," arXiv:0712.3633 [hep-ph], p. 137.

[32] K. Goulianos, arXiv:hep-ph/0407035.

[33] J. Pumplin, D. R. Stump, J. Huston, H. L. Lai, P. M. Nadolsky and W. K. Tung, JHEP **0207** (2002) 012 [arXiv:hep-ph/0201195];
A. D. Martin, W. J. Stirling, R. S. Thorne and G. Watt, arXiv:0901.0002 [hep-ph].

[34] I. P. Ivanov, arXiv:hep-ph/0303053.

[35] T. Aaltonen *et al.* [CDF Collaboration], Phys. Rev. D **77** (2008) 052004 [arXiv:0712.0604 [hep-ex]].

[36] T. Aaltonen *et al.* [CDF Collaboration], Phys. Rev. Lett. **102** (2009) 242001 [arXiv:0902.1271 [hep-ex]].

[37] J. R. Cudell, A. Dechambre, O. F. Hernandez and I. P. Ivanov, Eur. Phys. J. C **61**, 369 (2009) [arXiv:0807.0600 [hep-ph]].

[38] V. A. Khoze, A. D. Martin and M. G. Ryskin, Eur. Phys. J. C **23** (2002) 311 [arXiv:hep-ph/0111078].

[39] For an overview see: A. Achilli, R. Hegde, R. M. Godbole, A. Grau, G. Pancheri and Y. Srivastava, Phys. Lett. B **659** (2008) 137 [arXiv:0708.3626 [hep-ph]].

[40] L. Frankfurt, C. E. Hyde-Wright, M. Strikman and C. Weiss, Phys. Rev. D **75** (2007) 054009.

[41] E. Gotsman, E. Levin, U. Maor, E. Naftali and A. Prygarin, arXiv:hep-ph/0511060.

[42] V. A. Khoze, A. D. Martin and M. G. Ryskin, Eur. Phys. J. C **18** (2000) 167 [arXiv:hep-ph/0007359].

[43] A. Abulencia *et al.* [CDF Collaboration], Phys. Rev. Lett. **98** (2007) 112001.

[44] T. Aaltonen *et al.* [CDF Collaboration], Phys. Rev. Lett. **99** (2007) 242002.

[45] S. Heinemeyer, V. A. Khoze, M. G. Ryskin, W. J. Stirling, M. Tasevsky and G. Weiglein, Eur. Phys. J. C **53** (2008) 231 [arXiv:0708.3052 [hep-ph]].

[46] V. M. Budnev, I. F. Ginzburg, G. V. Meledin and V. G. Serbo, Phys. Rept. **15** (1974) 181.

[47] M. G. Albrow *et al.* [FP420 R&D Collaboration], arXiv:0806.0302 [hep-ex].

[48] S. Ovyn, [CMS Collaboration], "Exclusive dilepton and ϒ production with CMS: A feasibility study," CERN-CMS-CR-2008-036.

The LHC Accelerator and the ATLAS Detector

3

The Large Hadron Collider (LHC) [1] is a multi-purpose accelerator located on the Swiss-French border at CERN (European Organization for Nuclear Research)[1]. It is designed to accelerate and collide protons of $\sqrt{s} = 14\,\text{TeV}$ energy with instantaneous luminosities of $\mathscr{L} = 10^{34}\,\text{cm}^{-2}\text{s}^{-1}$ (for comparison, the Tevatron, the current world most powerful accelerator, collides beams at a center-of-mass energy $\sqrt{s} = 2\,\text{TeV}$ with an instantaneous luminosity $\mathscr{L} = 3 \times 10^{32}\,\text{cm}^{-2}\text{s}^{-1}$). Like RHIC, the LHC is also capable of colliding heavy ion Pb-Pb of center-of-mass energy 5.5 TeV per nucleon pair. Along the ring, two multi-purpose experiments ATLAS and CMS are built and three experiments in addition for a dedicated physics programs: ALICE for heavy ion collision studies, LHCb to explore the B-physics in detail and TOTEM experiment to measure the total p-p cross section with a high, 1% precision.

In this chapter, we first describe the accelerator chain and then detail the main detector subsystems of the ATLAS experiment.

3.1 The LHC

The LHC ring has a circumference of 27 km and is divided into 8 independent sectors. The tunnel houses 1232 superconducting bending dipole magnets producing a magnetic field strength of 8.33 T. Magnets operate at 1.9 K and are cooled by super-fluid liquid helium. The ingenious design of a dipole is such that the magnetic field keeps protons traveling clockwise and counter-clockwise on orbit at the same time. Protons are accelerated by radio-frequency cavities installed in sector 4. The focusing and defocussing quadrupole or sextupole magnets, and other magnetic elements are used to keep particles on closed orbits and to collide them at the interaction points (IP) of the LHC experiments.

The proton acceleration to the nominal 7 TeV energy is performed in six steps with the use of the CERN accelerating facilities. First, the hydrogen atom is dissociated in the Duoplasmatron and positively charged protons are injected into RF cavities and accelerated to 750 keV. The beam is then transmitted to the Linear Accelerator (LINAC) which increases the energy to 50 MeV. Next, the Proton Synchrotron Booster (PBS) accelerates the protons to 1.4 GeV before sending them to the Proton Synchrotron (PS) which rises the proton energy to 25 GeV. In the Super Proton Synchrotron (SPS), the

[1]The acronym originally stood, in French, *Conseil Européene pour la Recherche Nucléaire*. It was retained even though the name changed to the current one in 1954.

energy of the beam is increased to 450 GeV and the beam is ready to be injected into the LHC. Finally, the proton beams circulating in both directions of the LHC are brought to the energy of 7 TeV by radio-frequency cavities placed in sector 4. The time needed to fill the LHC accelerator at 450 GeV is about 16 minutes. The ramp-up time of the magnets to 7 TeV and ramp-down time from maximal energy back to 450 GeV is 10 minutes each.

In the highest luminosity runs, the beam is composed of 2808 bunches, each having 10^{11} protons. The time spacing between bunches is fixed already at the Proton Synchrotron to 25 ns which makes almost 8 m because the accelerated protons travel nearly at the speed of light. The bunch length is 7.55 cm and its transverse size in ATLAS and CMS (interaction points one and five) is 16.7 μm.

3.1.1 Luminosity lifetime

The luminosity is not constant in time but decreases as the intensity and emittance[2] decreas over time. The largest degradation effect is due to beam-beam collisions in the particle experiments. The intensity or the instantaneous luminosity as a function of time can be easily computed [2]. The luminosity of the machine is given as a function of the beam intensity N, number of bunches per beam k and the revolution frequency f as

$$\mathscr{L} = \frac{kf}{4\pi\sigma_x\sigma_y}N^2 = A\cdot N^2 \tag{3.1}$$

The transverse horizontal and vertical profiles of the beam are denoted σ_x, and σ_y, respectively. If two opposite beams are collided at some small colliding angle, the luminosity (3.1) is somewhat reduced. The reduction factor generally depends on the collision angle and bunch length. Here we will assume that the bunches collide head on. However, the collision half crossing angle is 142.5 μrad in the vertical plane at IP 1 (ATLAS) and in the horizontal one in IP 5 (CMS). Note that, if the beam parameters do not change during operation, the instantaneous luminosity scales as $\sim N^2$ of the beam intensity.

The decay of the luminosity depends on the total proton-proton cross section σ_{tot} and the number of interaction points N_{ip}

$$\mathrm{d}N(t) = -\mathscr{L}(t)\cdot\sigma_{\text{tot}}\cdot N_{\text{ip}}\cdot\mathrm{d}t \tag{3.2}$$

Using (3.1), we rewrite it as

$$\frac{\mathrm{d}N(t)}{N^2(t)} = -A\cdot\sigma_{\text{tot}}\cdot N_{\text{ip}}\cdot\mathrm{d}t \tag{3.3}$$

and easily solve it with the initial condition $N(0) = N_0$ fixing the initial number of protons to the initial beam intensity and the number of bunches. We get

$$N(t) = \frac{N_0}{1 + N_0\cdot A\cdot\sigma_{\text{tot}}\cdot N_{\text{ip}}\cdot t} \tag{3.4}$$

Assuming that the beam parameters hidden in A do not change as a function of time, we may write the time dependence in terms of an initial beam luminosity $\mathscr{L}_0 = A\cdot N_0^2$. Introducing the initial decay time of the beam intensity

$$\tau \equiv \frac{N_0}{k\cdot\mathscr{L}_0\cdot\sigma_{\text{tot}}\cdot N_{\text{ip}}} \tag{3.5}$$

[2]The emmitance is an important parameter of the machine which specifies the size of the spacial and momentum phase space of the beam particles.

the beam intensity as a function of time reads

$$N(t) = \frac{N_0}{1+t/\tau} \tag{3.6}$$

and the degradation of luminosity is given by

$$\mathscr{L}(t) = \frac{\mathscr{L}_0}{(1+t/\tau)^2} \tag{3.7}$$

Since all bunches of the beam are used in the collisions with even probability, the luminosity decay time is divided by the number of bunches k in formula (3.5). Consequently, the number of protons in each bunch $N(t)$ decreases at about the same rate.

Taking the nominal LHC beam parameters: initial luminosity $\mathscr{L}_0 = 10^{34}\,\mathrm{cm}^{-2}\mathrm{s}^{-1}$ with initial beam intensity $N_0 = 1.15\,10^{11}$ protons per bunch, 2808 bunches per beam, and assuming the total cross section $\sigma_{\mathrm{tot}} = 100\,\mathrm{mb} = 10^{-25}\,\mathrm{cm}^2$ and two high luminosity experiments $N_{\mathrm{ip}} = 2$, the beam lifetime (N/e) and the luminosity lifetime ($\mathscr{L}_0/\mathrm{e}$) are

$$\tau_b = (e-1)\tau \approx 77\,\mathrm{h} \tag{3.8}$$

$$\tau_L = (\sqrt{e}-1)\tau \approx 29\,\mathrm{h} \tag{3.9}$$

In practice, there are other processes contributing to the luminosity decay (Toucheck effect, scattering of particles on residual beam gas, intrabeam scattering) such that the realistic estimated luminosity lifetime of the machine is somewhat smaller $\tau_L = 14.9\,\mathrm{h}$ [1]. The decrease of the instantaneous luminosity as a function of time is depicted in Figure 3.1 which shows that the luminosity does not fall below 4×10^{33} during 12 hours. The overall collider efficiency depends on the run length and the turnaround time which is the time needed to stop the circulating beams, inject and stabilize new beams for collisions. The anticipated run length is 12 h (5.5 h) for a turnaround time 7 h (1.2 h), respectively.

3.1.2 Multiple interactions

The number of interactions per bunch crossing depends on the details of the beam parameters: beam profile, number of protons in the bunch etc. The machine division usually reports the instantaneous luminosity with the details of the beam and collision running scenario taken into account. Together with the collision rate, it can be used to predict the mean number of interactions per bunch crossing. For instance, let us take the nominal instantaneous luminosity $\mathscr{L} = 10^{34}\,\mathrm{cm}^{-2}\mathrm{s}^{-1}$. The number of interactions per second is simply obtained from the total pp cross section: $N = \sigma_{\mathrm{tot}} \times \mathscr{L}$. The mean number of interactions per bunch crossing is then

$$\mu = \sigma_{\mathrm{tot}} \times \mathscr{L}/f \tag{3.10}$$

where f is the average collision frequency. Note that the average collision frequency can differ from the nominal collision rate 40 MHz. That is because not all of the 3564 RF beam buckets around the ring where bunches could be placed are filled. The average time between two collisions therefore scales to 31.7 ns corresponding to the mean collision frequency $f = 31.5\,\mathrm{MHz}$. Assuming again the total cross section $\sigma_{\mathrm{tot}} = 100\,\mathrm{mb} = 10^{-25}\,\mathrm{cm}^2$, we obtain ≈ 32 multiple interactions per bunch crossing. As shown in Figure 3.1, the luminosity after 12 hours of running is about $4\times10^{33}\,\mathrm{cm}^{-2}\mathrm{s}^{-1}$ which corresponds to ≈ 13 interaction per bunch crossing.

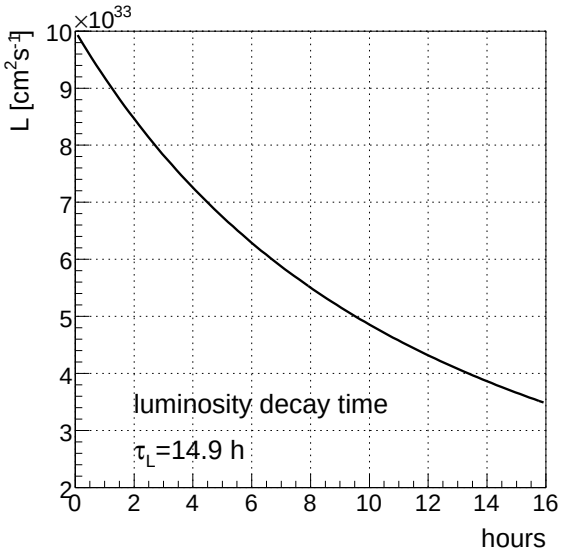

Figure 3.1: Luminosity decay as a function of time for the initial peak luminosity $\mathscr{L}_0 = 10^{34}\,\mathrm{cm}^{-2}\mathrm{s}^{-1}$ and nominal beam parameters with two high luminosity experiments and $\sigma_{\mathrm{tot}} = 100\,\mathrm{mb}$ assumed. The luminosity lifetime is $\tau_L = 14.9\,\mathrm{h}$ [1].

$\sqrt{s} = 10\,\mathrm{TeV}$

bunch spacing	50 ns	50 ns	50 ns
# of bunches	144	288	432
$\mathscr{L}[10^{30}\,\mathrm{cm}^{-2}\mathrm{s}^{-1}]$	48.3	96.5	145
μ	2.22	2.23	2.23

Table 3.1: The running scheme for the physics pilot runs of $\sim$ 10 months in total in 2009-2010 at $\sqrt{s} = 10\,\mathrm{TeV}$. μ is the mean number of interactions per bunch crossing calculated with the assumption of the total cross section at this energy $\sigma_{\mathrm{tot}} = 75\,\mathrm{mb}$.

For later discussion, it is useful to estimate how much of the collected luminosity after the start-up of the machine will have no more than one proton interaction. At [3], the up-to-date schedule for early running is given. The physics run beam setups are summarized in Table 3.1. We see that during the pilot run of approximately 10 months, the mean number of proton collisions per bunch-bunch crossing is $\mu = 2.23$. A fraction of $\sim 27\%$ of the collisions will have exactly one interaction per crossing (calculated as a conditional probability of having exactly one event out of n, when $n \geq 1$ and assuming a Poisson distribution of the occurred event with a mean μ, i.e. $\mathrm{P}(n=1)/\mathrm{P}(n \geq 1) = \mu \mathrm{e}^{-\mu}/(1-\mathrm{e}^{-\mu})$). Taking an average luminosity $\mathscr{L} = 100 \times 10^{30}\,\mathrm{cm}^{-2}\mathrm{s}^{-1}$ and an integrated luminosity of $130\,\mathrm{pb}^{-1}$ corresponding to 10 months of running with (a rather low) 50% efficiency, we obtain $\sim 30\,\mathrm{pb}^{-1}$ of effective luminosity with a very clean signal not populated by an overlaid background due to multiple interactions.

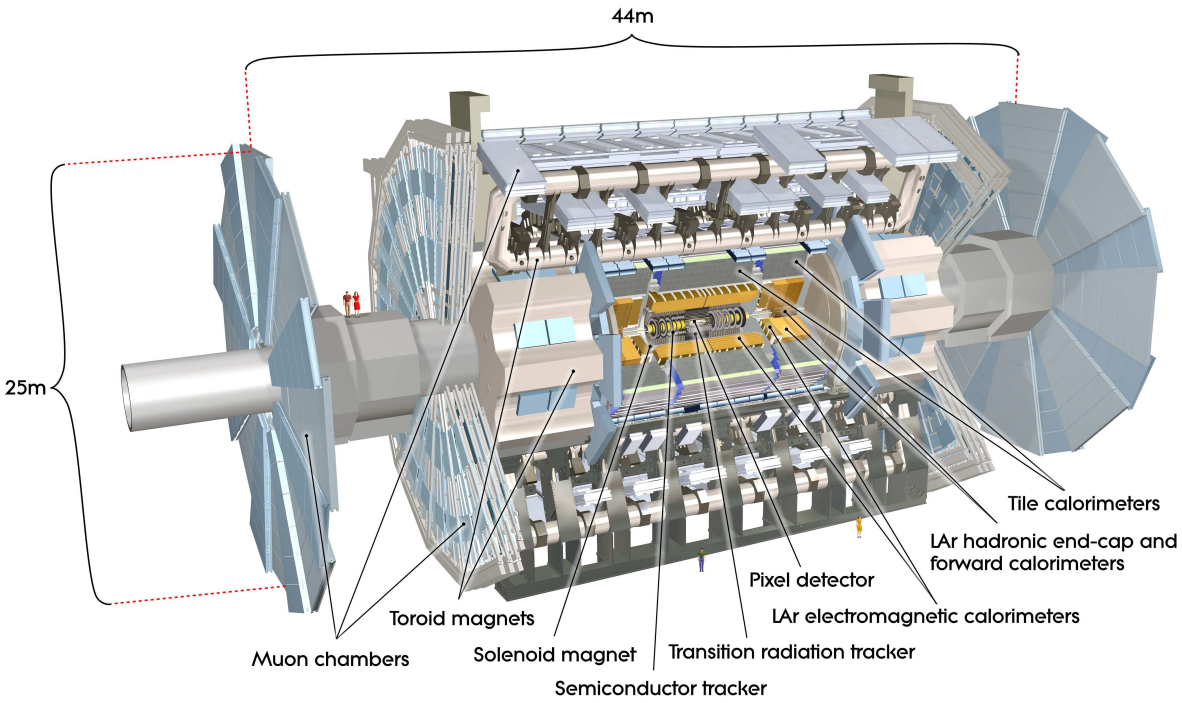

Figure 3.2: The cut-away view of the ATLAS detector with its major subdetectors.

3.2 ATLAS central detector

The ATLAS (A Toroidal LHC ApparatuS) detector [4] layout is shown in Figure 3.2. Going from the point of interaction outwards, it is composed of the inner detector system, electromagnetic and hadronic calorimeters and muon spectrometer which is located on the outer shell from the center and defines the ATLAS spacial dimensions.

The inner detector is contained in a 5.5 m long cylinder of diameter 1.5 m and the whole detector is placed in a solenoid magnetic field of 2 T.

A high granularity liquid-argon (LAr) electromagnetic (EM) sampling calorimeter, with excellent performance in terms of energy and position resolutions, covers the pseudorapidity range $|\eta| < 3.2$. The LAr technology is also used for the hadronic end-caps which share the same cryostat as the EM end-caps. The same cryostat also contains the LAr forward calorimeter which covers the highest pseudorapidity regions up to $|\eta| = 4.9$. The central hadronic calorimeter which is farther from the collision point where less radiation hard technique can be used is provided by iron scintillator-tile calorimeter. It is sub-divided into a long central barrel and two extended barrel cylinders, one on each side of the barrel.

Concerning the dimensions, the LAr calorimeters are embedded in a cylinder with an outer radius 2.25 m and spans ± 6.65 m along the z beam axis. The scintillator-tile hadronic calorimeter is contained within a concentric cylinder of radius 4.2 m and up to ± 6.1 m from the detector nominal center.

The magnetic system of ATLAS is based on an inner thin superconducting solenoid surrounding the inner detector, and large three air-core superconducting toroidal magnets placed around the calorimeters with an eight-fold azimuthal symmetry. The toroidal magnet composed of a barrel toroid (BT) and two

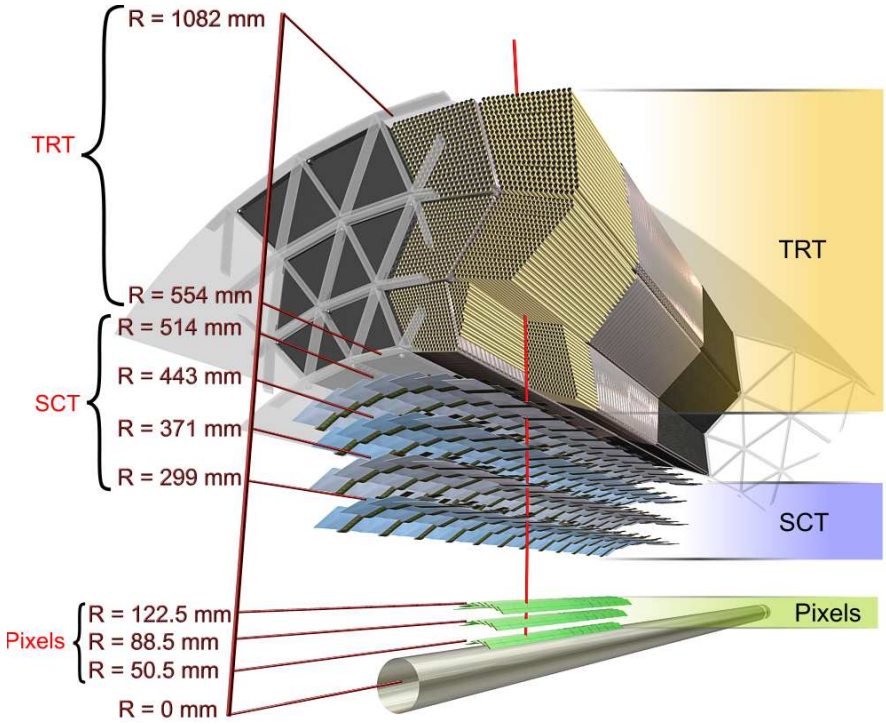

Figure 3.3: The ATLAS inner detector which consists of three systems: pixel detectors, silicon tracker (SCT) and transition radiation tracker (TRT).

end-cap toroids (ECT) generates a magnetic field for the muon spectrometer of large bending power over a big volume. The overall dimensions of the magnet system are 26 m in length and 20 m in diameter. The peak magnetic fields of the BT and ECT are 3.9 and 4.1 T, respectively. The open structure of the toroid system minimizes multiple-scattering effects and an excellent muon resolution is thereby achieved with three precision muon tracking chambers.

The ATLAS orthogonal coordinate system $(\vec{x}, \vec{y}, \vec{z})$ is defined such that $\vec{x}$ points inwards the LHC ring, $\vec{y}$ upwards, and $\vec{z}$ is chosen to form a right-handed triplet of vectors. Azimuthal angle ϕ is defined as a right-handed rotation around $\vec{z}$ measured from $\vec{x}$.

The detector overall length and height are about 46 m and 26 m, respectively, and it weights about 7000 tons. A more detailed description of ATLAS sub-detectors and their typical physics performance follows.

3.2.1 Inner detector

The high luminosity runs at the LHC will have a very large track density which demands a very high granularity of the inner detector [5] in order to precisely reconstruct charged particle tracks. The layout of the inner detector is shown in Figure 3.3. It combines high-resolution semiconductor detectors in the inner detector radii with numerous low precision continuous tracking gaseous detectors in the outer radii, both contained in the central solenoid which provides a nominal magnetic field of 2 T. The system is located in front of the calorimeters which measure the particle total energy. To achieve the desired calorimeter performance, the bulk of material in the inner detector had to be minimized.

The highest granularity is provided by the pixel detectors which are practically attached to the beam pipe. The number of pixel layers is limited because of their high cost. Due to a high radiation environment close to the collision point, the lifetime of the pixel detector is limited and the detector will have to be replaced, after some time depending on the radiation exposure (the 2014 shutdown is in consideration for the replacement when also an additional pixel layer, the so called insertable *b*-layer, should be installed in front of the current pixel detector). The pixel detector is surrounded by the silicon central tracker (SCT) with silicon strip layers tilt from each other to reconstruct track hits. Typically, a track crosses three pixel layers and eight strip layers (4 spacial points). The outer part of the inner tracker consists of straw tube transition radiation tracker (TRT) filled with a xenon-based gas mixture. Even though the TRT has a smaller resolution it adequately contributes to the high precision measurements performed by the inner tracker combining large number of measurements (typically 36) at higher average radius where tracks are better separated by the magnetic field. The relative measurement precision of pixel/SCT and TRT detectors is therefore comparable.

The layout provides a full tracking coverage over $|\eta| < 2.5$. The measurement of the impact parameter (transverse distance to the beam axis at the point of closest approach) is used for vertexing which is important for heavy flavor physics and τ tagging. The large number of points measured in TRT is used for the detection of photon and neutral vector meson conversions. The latter is an important signature of the CP violation in the B^0 system. Moreover, the e/π separation can be achieved by the detection of the transition-radiation photons emitted by relativistic electrons. The expected precision for the whole detector is

$$\begin{aligned} \sigma_{R-\phi}(\mu\mathrm{m}) &= 13 \oplus \frac{62}{p_T\sqrt{\sin\theta}} \\ \sigma_z(\mu\mathrm{m}) &= 39 \oplus \frac{90}{p_T\sqrt{\sin\theta}} \end{aligned} \tag{3.11}$$

in the plane perpendicular to the beam *z* axis and in the longitudinal *z* direction.

3.2.2 Calorimeter system

The ATLAS calorimetry is detailed in Figure 3.4. When viewed from the central to forward pseudorapidities, it consists of an electromagnetic calorimeter covering a pseudorapidity range $|\eta| < 3.2$, a hadronic barrel calorimeter covering $|\eta| < 1.7$, hadronic end-cap calorimeter covering $1.5 < |\eta| < 3.2$, and forward calorimeter covering $3.1 < |\eta| < 4.9$. To account for a particle energy loss in dead material upstream of the calorimeter, the EM calorimeter is preceded by a presampler detector.

The calorimeters use two different techniques: scintillating-tile technique in barrel hadronic calorimeter and the LAr technique in the rest of the system. The latter is more radiation hard and is more suitable for detectors which are close to the beam pipe.

The EM calorimeter which is divided into a barrel and two end-caps uses lead/liquid argon as the absorber/active ionization material. Like the central solenoid and the inner detector, the barrel is placed in a barrel cryostat. The hadronic barrel calorimeter (TileCal) is divided into three sections: the central barrel and two extended end-cap calorimeters. It is based on a sampling technique with plastic scintillators (tiles) embedded in the iron absorber. Two end-cap cryostats, one on each side of the detector, house the LAr EM end-cap, LAr hadronic end-cap, as well as the forward hadronic calorimeter. The hadronic detector uses copper/LAr technology with parallel plate geometry, and the forward calorimeter uses copper and tungsten as the absorber and LAr as the active medium.

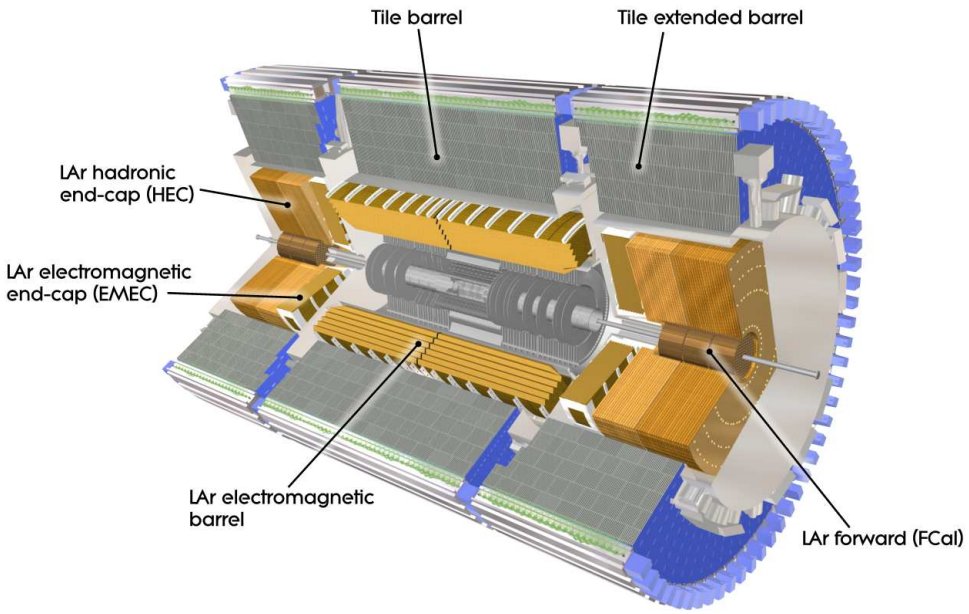

Figure 3.4: The ATLAS calorimeter system.

The pseudorapidity coverage, granularity, and longitudinal segmentation of the EM and hadronic calorimeters is detailed in Table 3.2. We can summarize that the typical granularity of the EM calorimeter in $\eta \times \phi$ varies between $(0.003 - 0.05) \times 0.1$ for pseudorapidities $|\eta| < 2.5$, and is about 0.1×0.1 for $2.5 < |\eta| < 3.2$. For the hadronic calorimeter the granularity decreases from 0.1×0.1 at central pseudorapidities to 0.2×0.2 in the forward calorimeter.

3.2.3 Electromagnetic calorimeter

The EM calorimeter is divided into a barrel part ($|\eta| < 1.475$) and two end-caps ($1.375 < |\eta| < 3.2$). The barrel is physically divided into two half-barrels separated by a 6 mm gap at $z = 0$. Each end-cap is composed of two coaxial wheels: the outer wheel covers the region $1.375 < |\eta| < 2.5$, and the inner wheel the region $2.5 < |\eta| < 3.2$. The EM calorimeter is a lead LAr detector with accordion-shaped Kapton electrodes and lead absorber plates. The accordion geometry creates a complete ϕ coverage without cracks. The lead absorber thickness was optimized as a function of η to achieve a good performance in energy resolution. The total thickness of the EM calorimeter in terms of radiation length is $24 X_0$ in the barrel and $26 X_0$ in the end-caps.

Over the high precision measurement range $|\eta|$<2.5 which overlaps with the inner detector acceptance, the EM calorimeter has three segmentations of high granularity. For the rest of the acceptance $2.5 < |\eta| < 3.2$, the calorimeter has two samplings and a coarser lateral granularity. Nevertheless, this is sufficient to meet the physics requirements on jet reconstruction and measurement of missing transverse energy $\not{E}_T$. There are about 190000 calorimeter cells in the EM calorimeter, all pointing towards the interaction region.

The total dead material seen by an incident particle before the calorimeter iron face is approximately $2.3 X_0$ at $\eta = 0$ and increases with pseudorapidity because of the particle trajectory angle. In the region

EM CALORIMETER	**Barrel**	**End-cap**	
Coverage	$\|\eta\| < 1.475$	$1.375 < \|\eta\| < 3.2$	
Longitudinal segmentation	3 samplings	3 samplings	$1.5 < \|\eta\| < 2.5$
		2 samplings	$1.375 < \|\eta\| < 1.5$
			$2.5 < \|\eta\| < 3.2$
Granularity ($\Delta\eta \times \Delta\phi$)			
- Sampling 1	0.003×0.1	0.025×0.1	$1.375 < \|\eta\| < 1.5$
		0.003×0.1	$1.5 < \|\eta\| < 1.8$
		0.004×0.1	$1.8 < \|\eta\| < 2.0$
		0.006×0.1	$2.0 < \|\eta\| < 2.5$
		0.1×0.1	$2.5 < \|\eta\| < 3.2$
- Sampling 2	0.025×0.025	0.025×0.025	$1.375 < \|\eta\| < 2.5$
		0.1×0.1	$2.5 < \|\eta\| < 3.2$
- Sampling 3	0.05×0.025	0.05×0.025	$1.5 < \|\eta\| < 2.5$
PRESAMPLER	**Barrel**	**End-cap**	
Coverage	$\|\eta\| < 1.52$	$1.5 < \|\eta\| < 1.8$	
Longitudinal segmentation	1 sampling	1 sampling	
Granularity ($\Delta\eta \times \Delta\phi$)	0.025×0.1	0.025×0.1	
HADRONIC TILE	**Barrel**	**Extended barrel**	
Coverage	$\|\eta\| < 1.0$	$0.8 < \|\eta\| < 1.7$	
Longitudinal segmentation	3 samplings	3 samplings	
Granularity ($\Delta\eta \times \Delta\phi$)			
- Samplings 1 and 2	0.1×0.1	0.1×0.1	
- Samplings 3	0.2×0.1	0.2×0.1	
HADRONIC LAr		**End-cap**	
Coverage		$1.5 < \|\eta\| < 3.2$	
Longitudinal segmentation		4 sampling	
Granularity ($\Delta\eta \times \Delta\phi$)			
		0.1×0.1	$1.5 < \|\eta\| < 2.5$
		0.2×0.2	$2.5 < \|\eta\| < 3.2$
FORWARD CALORIMETER		**Forward**	
Coverage		$3.1 < \|\eta\| < 4.9$	
Longitudinal segmentation		3 samplings	
Granularity ($\Delta\eta \times \Delta\phi$)		$\sim 0.2 \times 0.2$	

Table 3.2: Pseudorapidity coverage, granularity and longitudinal segmentation of the ATLAS calorimeters [4].

$|\eta| < 1.8$, the EM calorimeter is preceded by a presampler, which is used to correct for the energy lost by electrons and photons before reaching the EM calorimeter. The presampler consists of an active LAr layer of thickness 1.1 cm (0.5 cm) in the barrel (end-cap) region. In the transition region between the barrel and end-cap where two cryostats are aside, the amount of dead material is large (about $7X_0$). In this region, the presampler is accompanied by a scintillator slab inserted in the crack between the barrel and end-cap cryostats. This region $1.37 < |\eta| < 1.52$ is not used for precision physics measurement because of the large bulk of material up-stream of the EM calorimeter.

The signals from the EM calorimeters are sent to preamplifiers. The bipolar shaping is performed and sampled every 25 ns. The corresponding samples (typically five points) are used to extract the deposited energy, and also serve for the ATLAS first level trigger.

The EM calorimeter performance was measured with electron test beam of energies up to 300 GeV. The linearity defined as a ratio of the reconstructed over the beam electron energy was found to be better than 1%. The energy resolution of the EM barrel at $\eta = 0.9$ was measured to be [6]

$$\frac{\sigma(E)}{E} = \frac{10\%}{\sqrt{E\,[\mathrm{GeV}]}} \oplus \frac{0.39\,\mathrm{GeV}}{E} \oplus 0.3\% \tag{3.12}$$

where the numeric coefficients are the sampling, noise, and constant terms, respectively.

3.2.4 Hadronic calorimeters

The hadronic calorimeter is a system with the largest pseudorapidity coverage of all sub-systems in the central detector. It consists of the hadronic barrel (TileCal) covering $|\eta| < 1.7$, the hadronic end-cap extending to $1.5 < |\eta| < 3.2$, while the range $3.1 < |\eta| < 4.9$ is covered by the forward calorimeter (FCAL). An important parameter in the design of the hadronic calorimeter is its thickness since it should absorb all energy of the hadronic showers, keeping the rate of punch-throughs into the muon system to a minimum (punch-through occurs in events with very energetic hadronic showers in which part of the hadronic energy leaks out of the hadronic calorimeter. These events can have fake $\not{E}_T$ and a large number of hits in the muon system). On the other hand, the calorimeter thickness should be kept limited to reduce multiple scattering of muons in the calorimeter and thus maintain a good muon momentum resolution. The total thickness of the hadronic calorimeter is 11λ (in nuclear interaction length units) at $\eta = 0$, including 1.5λ from the outer support preceding the calorimeter. This setup has been shown both by measurements and simulation to be sufficient to reduce the number of particles other than muons (and neutrinos) to a manageable level. The large and complete η coverage guarantees a good missing transverse energy $\not{E}_T$ measurement, which is crucial for a broad set of physics signatures, and most importantly for SUSY particle searches.

3.2.4.1 Tile calorimeter

The large hadronic barrel calorimeter [7] is a non-compensating[3] sampling calorimeter using iron as the absorber and plastic scintillating tiles as the active medium. The tiles are placed radially and staggered in depth. The iron to scintillator ratio is 4.7 : 1 in volume. The opposite sides of the scintillating tiles

[3]Non-compensating calorimeter means that the response to the hadronic shower h is smaller than for electromagnetic shower e of the same initial energies, $e/h < 1$. It is due to π^0 which are formed in hadronic showers but decay mostly into two photons.

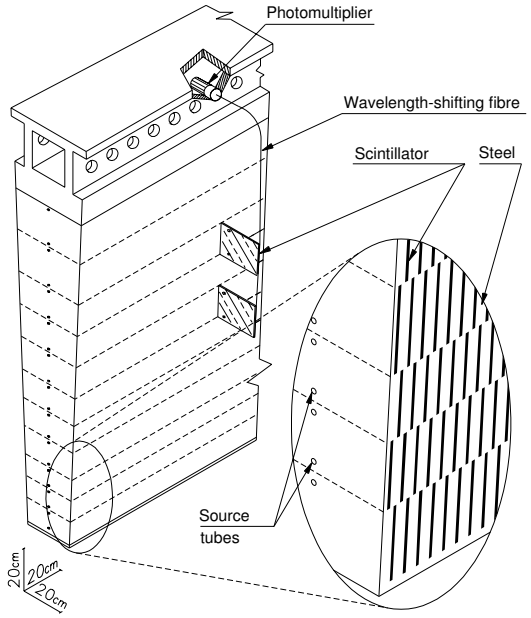

Figure 3.5: Detail of a TileCal module in which tile plastic scintillators are sandwiched with iron absorbers. The photomultipliers at the top of the modules collect scintillating light via wavelength-shifting fibers.

are read out by wavelength shifting (WLS) fibers into two separate photomultipliers (PMTs). The scintillating tiles and the absorber plates are grouped into 64 modules shown in Figure 3.5, which build the cylindrical wheels of the central and extended barrels.

Radially, the tile calorimeter extends from an inner radius of 2.28 m to an outer radius of 4.25 m. It has three longitudinal segmentations of similar granularity, which are approximately 1.4, 4.0, and $4.8\,\lambda$ interaction length thick at $\eta = 0$. In η, the readout cells built by grouping fibers into PMTs create pseudo-projective towers pointing to the interaction region. The total number of channels is about 10000. A very fast readout of the scintillating detectors is used in front-end electronics to perform an analog sum of a subset of channels, forming trigger towers for the ATLAS first level trigger.

Between the barrel and extended barrel end-caps, there is a gap of 68 cm, which is needed for the inner detector and LAr calorimetry cables, electronics and services. The gap region $1.0 < \eta < 1.6$ is instrumented with special Intermediate Tile Calorimeter (ITC) modules made of iron scintillator sandwiches, and with thin scintillator counters where the free space is limited. The ITC allows to correct for lost energy in dead material in the crack region.

The TileCal performance was studied in a test beam with single pions of energy between 20 and 350 GeV. The energy resolution was found

$$\frac{\sigma(E)}{E} \frac{52\%}{\sqrt{E[\mathrm{GeV}]}} \oplus 5\% \tag{3.13}$$

3.2.4.2 Liquid-argon hadronic end-cap calorimeters

The hadronic end-cap (HEC) calorimeters are copper LAr detectors with parallel geometry. The 8.5 mm space between consecutive copper plates is filled with three parallel electrodes, splitting the gap into four

drift spaces. Each of the HEC consists of two independent wheels of an outer radius 2.03 m. In addition, each wheel is divided into two longitudinal segments.

To maintain a good coverage over the η region at the transition between the hadronic end-cap and the forward calorimeter where the bulk of HEC material is smaller due to geometry, the EM end-cap reaches up to $|\eta| = 3.2$ to overlap with the forward calorimeter whose acceptance starts at $|\eta| = 3.1$.

The HEC resolution for single pions of energy from 5 to 200 GeV was measured in a test beam and found to be [8]

$$\frac{\sigma(E)}{E} = \frac{71\%}{\sqrt{E[\text{GeV}]}} \oplus 6\% \tag{3.14}$$

3.2.4.3 Liquid-argon forward calorimeter

The forward calorimeter (FCAL) acts as a combined electromagnetic and hadron calorimeter. Being exposed to beam remnants which are emitted from the interaction point, the calorimeter has to cope with particularly high levels of radiation. It is shifted by 1.2 m in the transverse direction from the front face of the EM end-cap to reduce the number of scattered neutrons which would otherwise populate the inner detector. It is placed in the same end-cap cryostat as the EM and hadronic end-caps. This limits the space for the installation of about 9.5 interaction lengths of material, and high density absorbers have to be used so as to limit the width and depth of showering, reduce the leakage from the FCAL into neighbouring calorimeters and decrease radiation background in the muon spectrometer.

FCAL is composed of three sections. The first one is made of copper, while the other two are made of tungsten. In each section, the calorimeter consists of a metal matrix, with regularly spaced longitudinal channels. These channels are filled with concentric tubes of diameter 5.8 mm with a central rod. The tube and the rod create electrodes that collect a ionization signal from an active LAr medium which is filled in the gap between them.

The energy resolution in the forward region is [9]

$$\frac{\sigma(E)}{E} = \frac{100\%}{\sqrt{E[\text{GeV}]}} \oplus 10\% \tag{3.15}$$

i.e. worse compared to the rest of the calorimeter system.

3.2.5 Muon spectrometer

Muons leave hits in the inner detector and deposit energy in the calorimeters before reaching the muon system which is located at the outward part of the ATLAS detector. The typical muon energy loss in the calorimeter depends slightly on the energy: it is about 2.5 GeV(4 GeV) for a muon of an energy 10 GeV(1 TeV) [10] (see Figure 3.7). The momentum and charge of a muon are determined from the curvature of a muon track formed in the magnetic field provided by the toroidal magnet integrated in the muon system. The presence of a high p_T muon is a signature of many Standard Model or Beyond Standard Model physics processes which can be relatively easily measured and triggered on. The required physics performance of the muon spectrometer is to measure a 1 TeV muon with a precision of $p_T = 10\%$ (corresponding to a sagitta 0.5 mm measured better than 50 μm).

Before entering the muon spectrometer, muons have to pass a large amount of material corresponding to about 100 X_0 radiation lengths. This is in contrast to $1-2\,X_0$ of material preceding the presampler as shown in Figure 3.7 (right). The energy losses in various sub-systems are parameterized and taken

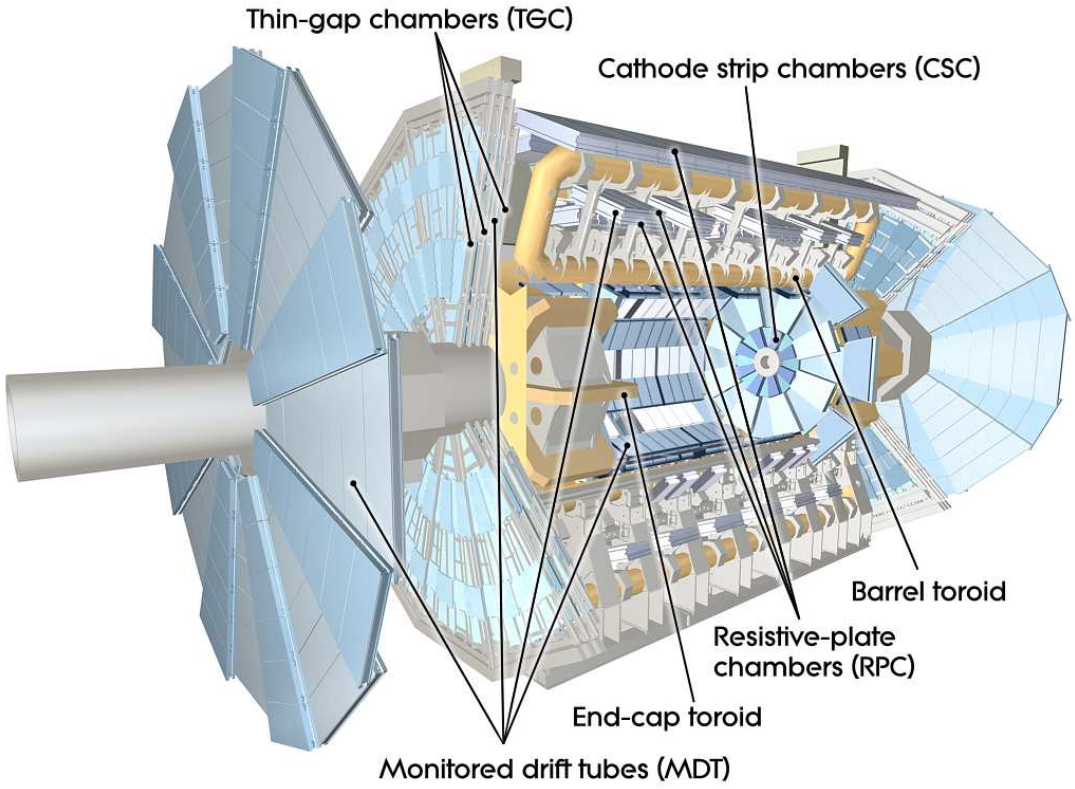

Figure 3.6: View of the ATLAS muon system.

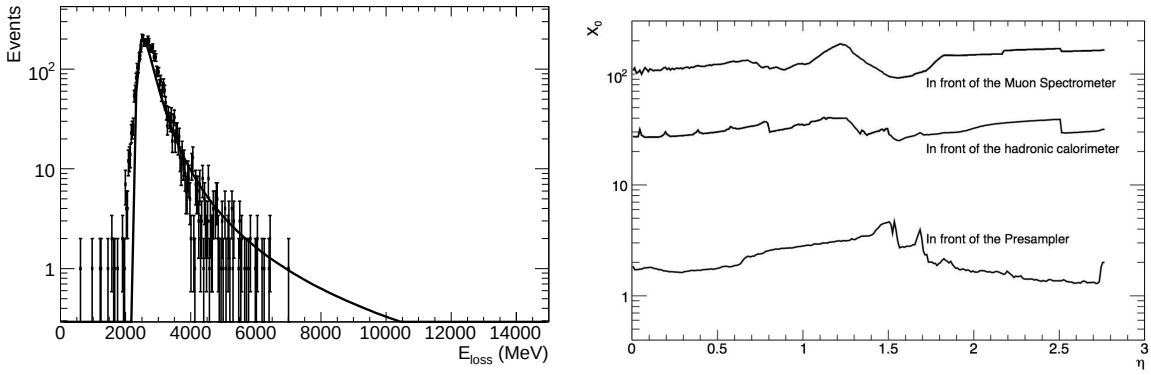

Figure 3.7: Distribution of the energy loss of 10 GeV muons passing through the calorimeters ($|\eta| < 0.15$) (left), and cumulative material traversed by a particle (in radiation lengths X_0) before entering the muon spectrometer as a function of $|\eta|$ (right) [10].

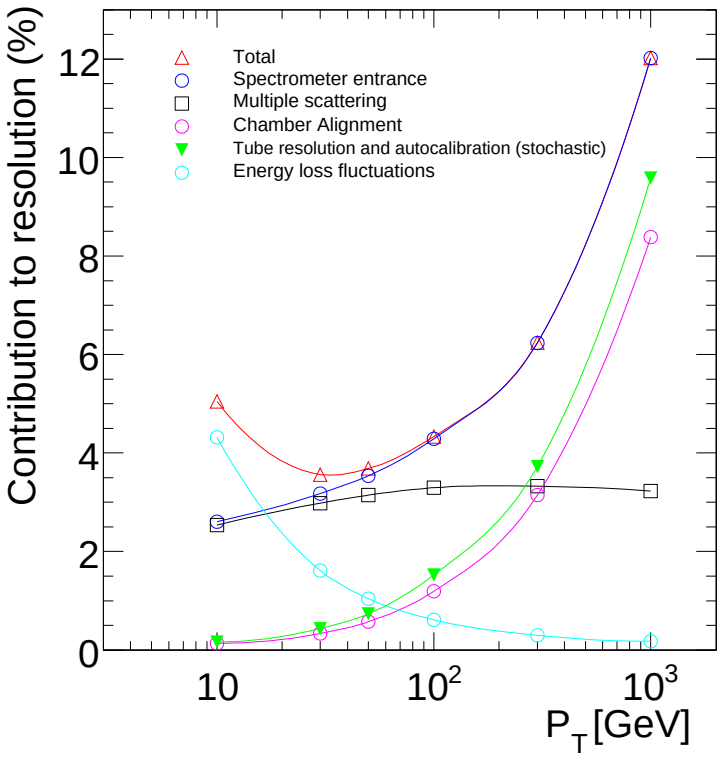

Figure 3.8: Contributions to the momentum resolution for muons reconstructed in the muon spectrometer as a function of transverse momentum for $|\eta| < 1.5$. The alignment curve is for an uncertainty of 30 μm in the chamber positions [10]. Three effects compete in the muon resolution: at low p_T the energy loss in the calorimeter is important (decreasing line with circles) whereas the effect of multiple scattering is flat over a large range of p_T. At high p_T the intrinsic resolution of the muon detector and its alignment are the leading effects.

into account by the muon reconstruction algorithms. In addition, the inner detector muon track information can be combined with the measurement in the muon spectrometer to give the overall good performance.

The ATLAS muon spectrometer [11, 12] consists of an air-core toroid magnetic system which is 25 m long, and has an inner and outer radius 4.7 m and 10 m, respectively. Its eight independent coils are installed symmetrically around the ATLAS calorimeters, each providing a magnetic field of about 0.5 T. The muon track reconstruction is provided by three barrel chambers located at radii 5, 7.5, and 10 m from the interaction point at central pseudorapidities $|\eta| < 1.0$ while two end-caps, one at each side, consisting of four large disks 7.4, 10.8, 14, and 21.5 m from the ATLAS center along the z axis cover the forward region.

The muon detection system can be divided into two classes according to their purpose: precision chambers are used to obtain high momentum resolution whereas very fast chambers are used for the trigger. Together with the toroid magnet, the muon spectrometer can be used to detect muons in a standalone mode without any additional information from inner detectors or other triggers. The precision tracking is provided by Monitored Drift Tubes (MDTs) in the barrel and most of the end-cap. It consists

	TRIGGER CHAMBERS		PRECISION CHAMBERS	
Technology	RPC	TGC	MDT	CSC
Time resolution	< 5 ns	< 7 ns	500 ns	< 7 ns
Spacial resolution	5-10 mm		80 μm	60 μm

Table 3.3: Design parameters of the different muon spectrometer sub-systems.

of aluminium tubes of 30 mm diameter with a central tungsten wire filled with argon to provide a track position resolution of 80 μm (35 μm chamber resolution in R). High pseudorapidities $2.0 < |\eta| < 2.7$ are covered by the Cathode Strip Chambers (CSCs) which have a larger granularity. CSC are multi-wire proportional chambers of spacial resolution 60 μm.

At $\eta = 0$, there is a gap in the spectrometer acceptance to have an access for services to the solenoid, calorimetry and inner detector. The region where a muon track can be missed corresponds to the range of $|\eta| < 0.08$. Another drop in efficiency occurs for $\phi \approx -1.2$ rad and $\phi \approx -1.9$ rad at $|\eta| < 1.2$ where the support of the whole ATLAS detector prevents the installation of muon chambers.

Muons of transverse momentum ranging from 3 GeV to 3 TeV can be identified with high efficiency. Their transverse momentum has to be at least $p_T = 2.5$ GeV to make it to the muon spectrometer through the bulk of material located upstream. The p_T resolution at low p_T is dominated by muon energy loss in the calorimeter and multiple scattering effects. Track of high p_T muons become more difficult to reconstruct as the track sagitta becomes smaller. The chamber alignment and intrinsic resolution become the dominant effect in the high muon p_T reconstruction. The contribution of all competing effects in the muon momentum resolution is shown in Figure 3.8 as a function of the muon transverse momentum.

To achieve a good muon resolution, the relative position of muon chambers is required to be known with high precision. Due to the large size of the system, it is not possible to stabilize the dimensions and positions of the chambers at the required 300 μm level. The chamber positions and deformations have to be constantly monitored. The system is instrumented with an optical laser system that is used to control deviations and deformation of large chambers. The alignment of small chambers relies on straight muon tracks which overlap with the large sectors. High-momentum muon tracks are also used for the relative alignment of the muon spectrometer, calorimeters and inner detector.

The time for muons to reach the muon system located on the outer shell of ATLAS is larger than the nominal LHC bunch spacing of 25 ns. The spectrometer is therefore equipped with special very fast triggers. They provide high-p_T muon identification up to $|\eta| = 2.4$. The muon trigger system consists of Resistive Plate Chambers (RPC) $|\eta| < 1.05$ in the barrel and Thin Gap Chambers (TGC) in the forward region. These systems also provide the muon position measurement in the orthogonal plane to that obtained from the precision tracking MDT chambers (up to $|\eta| = 2.7$, more than what is available for triggers). The design performance of time and spacial resolution for the different muon sub-systems is summarized in Table 3.3. The goal of the muon spectrometer is to identify the bunch crossing of the interaction with a detected muon. The required momentum resolution is

$$\frac{\sigma(p_T)}{p_T} = 10\% \tag{3.16}$$

for 1 TeV muons.

3.2.6 MBTS

The Minimum Bias Trigger Scintillator (MBTS) is a detector of sixteen counters installed on either side of ATLAS, on the inner face of the end-cap calorimeter cryostat. Each set of counters is segmented in eight units in ϕ and two units in η. They are located about 3.6 m from the interaction point in the z direction. The inner radii wheels cover a rapidity region $2.82 < |\eta| < 3.84$ and the outermost one covers $2.09 < |\eta| < 2.82$. The detector is used for triggering on minimum bias events (events in which any interaction occurred, either soft or characterized by some hard scale) but can be also employed in selecting exclusive events with large rapidity gaps requiring a veto in the MBTS detector.

3.3 ATLAS forward detectors

In addition to the central ATLAS main detector which was just described, forward detectors are installed around the interaction point IP. They are placed farther from the IP to measure forward energy flow to perform luminosity monitoring, luminosity absolute measurement, and other forward physics studies. Detectors mentioned in the following are the forward detectors which have been approved and are installed in the tunnel. Another set of forward detectors for ATLAS are in the approving stage. They are called ATLAS Forward Proton (AFP) detectors. The Chapter 6 of this thesis is dedicated to their description and performance.

3.3.1 LUCID

LUCID detector (LUminosity measurement using Cerenkov Integration Detector) is installed 17 m from the ATLAS IP [13]. The LUCID detector consists of two modules that are located in the available space between the beam pipe and the conical beam-pipe support structure. This places LUCID in the forward shielding, after the ATLAS end-cap toroids and covers the pseudorapidity range $5.4 < |\eta| < 6.1$. Its goal is to monitor the luminosity by determining an average number of interactions per bunch crossing. This is achieved by measuring the number of charged particles flying in the forward direction from the IP, and also their arrival time, in each bunch crossing. Charged particles produce Cerenkov light in one of the 200 cylindric Cerenkov counters, filled with isobutane (C_4F_{10}) as a radiator. The photomultiplier signal output time can be measured with an accuracy of 100 ps which is by far sufficient to allow bunch-by-bunch luminosity monitoring.

3.3.2 ZDC

ZDC (Zero Degree Calorimeter) [14] is a segmented calorimeter with tungsten and steel plates as an absorber and quartz strips as an active medium. The calorimeter has an electromagnetic and hadronic part corresponding to approximately $29\,X_0$ radiation length and $1.14\,\lambda$ nuclear interaction length, respectively. Two stations are placed 140 m downstream from the IP, one on each side of ATLAS. They occupy the region of a neutral particle absorber (TAN) just behind the point where the beam pipe splits into two, one pipe for each beam. Since charged particles are deflected outwards by beam magnetic elements, the ZDC calorimeter is sensitive primarily to neutral particles, detecting γ, n, and π^0, in a pseudorapidity region above $|\eta| \geq 8.3$. The range of physics goals is broad. The ZDC aids with beam tuning, luminosity monitoring and triggering on minimum bias events. The longitudinal position of a

bunch crossing can be determined with a precision of 3 cm. In ion-ion collisions, the ZDC will select ultra-peripheral collisions which give a substantial neutral particle flux in the forward region. On the other hand, the measurement of the production cross sections of pions, kaons and η mesons will constrain modeling of the atmospheric showers of incident cosmic rays which largely depends on the soft longitudinal energy flow in the pp interactions. Last but not least, the ZDC acceptance improves hermicity of the ATLAS detector in the forward region which is particularly important for diffraction.

3.3.3 ALFA

The ALFA detector (Absolute Luminosity For ATLAS) [13] is dedicated to a precise absolute determination of the delivered luminosity at IP1. The approach used by ALFA is to fit the t-distribution of elastic events in the t range where Coulomb and hadron amplitudes contribute and can be parameterized as[4]

$$\left.\frac{\mathrm{d}N}{\mathrm{d}t}\right|_{t=0} \approx \mathscr{L}\pi\left(\frac{-2\alpha_{\mathrm{EM}}}{|t|}+\frac{\sigma_{\mathrm{tot}}}{4\pi}(i+\rho)\mathrm{e}^{-b|t|/2}\right)^2 \tag{3.17}$$

With the fit, one obtains the total cross section σ_{tot}, the ratio of real and imaginary part of elastic scattering amplitude ρ, the slope of elastic events b, and the desired luminosity $\mathscr{L}$. ALFA measures elastic events in the range approximately $3\times10^{-4}<|t|<0.3$ with scintillating fibers arranged in planes which are staggered. Measuring low momentum transfers requires to place the active detectors very close to the beam[5], as close as $10\sigma = 1.2\,\mathrm{mm}$. ALFA requires dedicate low luminosity runs of so-called high β^* optics (to be discussed in Chapter 6) when the intrinsic beam divergence is significantly smaller than the smallest scattering angles to be observed. Fitting the above formula, the absolute luminosity can be determined with an uncertainty $\sim 3\%$ for 100 h long data taking [15]. The absolute luminosity reference point obtained by ALFA in a dedicated run will then be used to normalize the luminosity collected in normal physics runs.

3.4 Trigger system

When information from all the different ATLAS sub-detectors is collected, the size of one such event is typically about 1.5 MBytes. With the high LHC bunch crossing rate the amount of gathered data is far too large to be processed and stored. A mechanism has to be therefore provided to reduce the number of events to be processed from ATLAS and eventually stored and transferred to end-users for analysis.

The ATLAS trigger is based on a three level online event selection, designed to capture the physics of interest with high efficiency. It must reduce the initial bunch crossing rate of 40 MHz to $\sim 200\,\mathrm{Hz}$ ($\sim 300\,\mathrm{MB/s}$) in order to be able to save data to permanent storage which has a limited bandwidth. The three trigger systems are: Level 1 (L1) fast trigger which is hardware-based, Level 2 (L2) trigger and Event Filter (EF) (the latter two being collectively referred to as High Level Trigger or HLT) which are based on software pattern-recognition algorithms analyzing the data on dedicated large computing farms.

The Level 1 trigger is supplied with the signal identified in subsets of calorimeter and muon detectors of reduced granularity. The system has to make a decision within 2.5 μs from the time of the collision

[4] The TOTEM Collaboration aims to measure the total cross section with a luminosity independent method, using the total inelastic rate and the extrapolation of the elastic event yield at small t.

[5] σ denotes the spacial width of the beam, in this case in vertical direction.

L1 thresholds [GeV]	5	10	20	40	70	100	130	150
L1 prescales $\mathscr{L} = 10^{31}\,\mathrm{cm}^{-2}\mathrm{s}^{-1}$	2k	1k	50	3	1	1	1	1
L1 prescales $\mathscr{L} = 10^{32}\,\mathrm{cm}^{-2}\mathrm{s}^{-1}$	30k	12k	1k	50	1	1	1	1

Table 3.4: Proposed L1 jet thresholds and prescales for early running. They are adjusted so that the resulting EF pass rate is 6 Hz for luminosity 10^{31} and 13 Hz for luminosity 10^{32}.

.

to reduce the received full bunch crossing bandwidth to 75 kHz ($\sim$ 40 kHz during ATLAS startup). This task is not trivial. The muon spectrometer dimensions are so large that the time needed for a muon to arrive in the chambers is comparable with the bunch spacing of 25 ns. The collection of signal in the LAr calorimeter also extends over many bunch crossings. Before the L1 trigger decision is taken, the information from all channels is stored in pipe-line memories. The L1 calorimeter trigger decision is made upon multiplicities and energy thresholds of the following objects: Electromagnetic (EM) clusters, taus, jets, missing transverse energy ($\not{E}_T$), scalar sum of the transverse energy in the calorimeter ($\sum E_T$) and the total transverse energy of the L1 jets ($\sum E_T(\mathrm{jets})$). The input of the L1 muon trigger are muon multiplicities measured for various p_T muon thresholds.

The Level 2 trigger is based on the Region-of-Interests (RoI) already identified by the L1 trigger. Around each seed, a RoI window is constructed whose size depends on the type of the seed object. The L2 then unpacks fine-grained data within the constructed RoI window and performs a refined analysis of the L1 objects. In addition, it uses information that is not accessible at L1, most notably the reconstructed tracks from the inner detector. Information from several sub-detectors is combined to obtain a finer rejection quality. Using RoI upon the found L1 seeds in the L2 triggering is a characteristic of ATLAS; it greatly reduces the computation time of the L2 trigger and the amount of data that must be transferred. The average processing time of the L2 algorithms is 40 ms and they reduce the L1 trigger rate from 75(40) kHz to 2(1) kHz for nominal (start-up) running.

The Event Filter performs a detailed analysis of the L2 passed candidates, having the full detector information available. Unlike the L2 algorithms which have the speed priority, the selection criteria of EF use typically the same criteria as the offline analysis. The processing of the EF takes on average 1 s, and the output trigger rate is 200 Hz. Data are then written to the storage.

In the early stages of LHC running at low instantaneous luminosity $\mathscr{L} = 10^{31}\,\mathrm{cm}^{-2}\mathrm{s}^{-1}$ and low number of bunches circulating in the machine, the commissioning of the trigger will take place with smaller p_T thresholds and looser isolation criteria. Moreover, HLT triggers will operate in pass-through mode only to understand the trigger functionality thoroughly. The typical L1 single jet thresholds with their prescales are shown in Table 3.4, they were considered for running at $\sqrt{s} = 10$ TeV. The lowest single EM3 and double 2EM3 electron L1 triggers have the threshold 3 GeV. For muons, the lowest trigger single MU4 and double 2MU4 muon threshold is 4 GeV. At $\mathscr{L} = 10^{31}\,\mathrm{cm}^{-2}\mathrm{s}^{-1}$, only the EM3 is prescaled by a factor of 60, all the other electron or muon triggers are unprescaled so that the W/Z signatures will exploit the full collected luminosity [10].

3.5 Full chain analysis

The ATLAS production and analysis is performed in a data processing model called full-chain which is sourced either by pseudo events obtained from Monte Carlo simulation or by real events as collected by the ATLAS detector.

The Monte Carlo (MC) generator produces pseudo data based on phenomenological models that attempt to describe the nature of the studied physics processes. Some generators like Herwig++ [16] or Pythia [17] provide a full generation of the pp collision with the parton scattering, parton showers, fragmentation and hadronization, particle decays etc. MC generators use a large number of parameters which have been constrained from previous experiments and some of them will be reconsidered at the LHC when our understanding of the physics will be probed at higher energies. The exact setup of the MC generator for the data generation is specified via 'JobOption' files which set running parameters in a uniform format for all generators implemented in the ATLAS software. An output of the MC generator is stored in a HepMC format that includes particle momenta, particle vertices and parent-child indexing to enable the reconstruction of event production history.

Final state stable particles are passed to the Geant4 [18] simulation of the ATLAS detector. In this step, the full detector geometry with a database of sub-detector materials and layout is used to model the particle passage through all ATLAS systems as well as dead material. It models energy loss, radiation, ionization, bremsstrahlung, multiple scattering, passage through magnetic field etc. and simulates charge or energy depositions in active materials of the ATLAS detector called 'hits'. In the next step, they are converted to 'digits', which simulate the response of various ATLAS sub-detectors to passing particles, taking into account the specific detector settings such as voltage and timing.

During the detector operation, incoming data are received in a bytestream format which is similar to that of Geant4 digits. They are converted to structured c++ object representation called Raw Data Objects (RDO). The same is done in case of data coming from the MC simulation and beyond this point both types, the pseudo or real data are manipulated in the same way. Data in RDO files are then converted to high-level physics objects such as tracks, vertices, energy deposits, electrons, muons, and jets and are stored in the Event Summary Data (ESD) format. It contains the most detailed information about the event necessary for performance checks and simple physics analysis. The same reconstructed objects (tracks, jets, muons) obtained by various different algorithms are stored to be compared in performance with detailed information about actual energy deposits in various sub-detectors. Due to the large size of the ESD event, this format is not aimed to be used at large scale for end-user analysis. Instead, the ESD file format is reduced keeping only most important physics quantities such as tracks, electrons, muons, photons, jets, etc., which are important for a large set of analysis, but without a detailed information as in ESD. The reduced set of physics objects is stored in Analysis Object Data (AOD) files which are relatively small in size and are aimed for the end-user analyses.

3.6 Distributed grid computing

The total amount of produced data by the LHC experiments combined is expected to be approximately 15 Petabytes per year [20]. Such a huge amount of data has to be made available to a large physics community spread over the world to be processed and analyzed. This would certainly be a too difficult task for just one organization. CERN and its member states have therefore been developing a computing

network known as the LHC Computing Grid (LCG). It is a distributed network of computer farms spread around the world organized in a coherent way and providing resources for processing and analysis of the LHC data.

The network is divided into a tree structure of four levels. All the data collected by the LHC experiments are stored at the Tier-0 center, the first layer based in CERN. There, the first processing of data to produce ESD and AOD formats is done. The raw data will have to be reprocessed when calibration, alignment and reconstruction algorithms will be improved in future. Raw data, ESD and AOD files are copied to Tier-1 centers, which are large regional computing centers and make the second layer of LCG. Currently, there are 10 Tier-1 centers around the globe. A copy of raw data is divided among all Tier-1 centers, each having about 10% of the data. Tier-1 centers are also responsible for reprocessing the data. Further, there are many Tier-2 smaller-scales facilities which share the AOD data. At these centers, the official MC production of the experiments is performed while their result is stored in Tier-1 farms. Finally, Tier-3 are small university clusters or individual computers which access the data for physics analysis.

Bibliography

[1] O. S. Bruning, P. Collier, P. Lebrun, S. Myers, R. Ostojic, J. Poole and P. Proudlock, LHC design report. Vol. I: The LHC main ring, CERN-2004-003-V-1; `http://ab-div.web.cern.ch/ab-div/publications/LHC-DesignReport.html`, Sep. 2009.

[2] Grote, H and Herr, Werner, LHC-PROJECT-NOTE-275, 2001.

[3] H. Burghart, Proceedings of 13th International Conference on Elastic & Diffractive Scattering, to appear.

[4] ATLAS Collaboration, ATLAS: Detector and physics performance technical design report. Volume 1, CERN-LHCC-99-014, ATLAS-TDR-14, 1999.

[5] ATLAS Collaboration, ATLAS Inner Detector Technical Design Report, CERN/LHCC/97-16, 1997.

[6] ATLAS Collaboration, Liquid Argon Calorimeter, CERN/LHCC 96-41, CERN, 1996.

[7] ATLAS Collaboration, ATLAS Tile Calorimeter TDR, CERN/LHCC/96- 42, 1996.

[8] B. Dowler *et al.* [ATLAS Liquid Argon HEC Collaboration], Nucl. Instrum. Meth. A **482** (2002) 94.

[9] L. Heelan, J. Phys. Conf. Ser. **160**, 012058 (2009).

[10] G. Aad *et al.* [The ATLAS Collaboration], arXiv:0901.0512 [hep-ex].

[11] ATLAS Collaboration, ATLAS muon spectrometer: Technical design report, CERN-LHCC-97-022, 1997.

[12] ATLAS Collaboration, ATLAS magnet system: Technical design report, CERN-LHCC-97-18.

[13] ATLAS Collaboration, ATLAS Forward Detectors for Luminosity Measurement and Monitoring: Letter of Intent, CERN-LHCC-2004-010.

[14] ATLAS Collaboration, Zero Degree Calorimeters for ATLAS: Letter of Intent, CERN-LHCC-2007-001.

[15] M. Heller, Proceedings of 13th International Conference on Elastic & Diffractive Scattering, to appear.

[16] M. Bahr *et al.*, Eur. Phys. J. C **58** (2008) 639 [arXiv:0803.0883 [hep-ph]].

[17] T. Sjostrand, S. Mrenna and P. Skands, JHEP **0605** (2006) 026 [arXiv:hep-ph/0603175].

[18] S. Agostinelli *et al.* [GEANT4 Collaboration], Nucl. Instrum. Meth. A **506** (2003) 250.

[19] ATLAS Collaboration, ATLAS computing : Technical Design Report, CERN-LHCC-2005-022, 2005.

[20] C. Eck at. all, LHC computing Grid: Technical Design Report, CERN-LHCC-2005-024, 2005.

Forward Physics Monte Carlo (FPMC)

4

A realistic description of particle collisions requires to include a large range of effects. The process cross section is in general obtained by multidimensional integrals over parton densities, sub-matrix elements, fragmentation functions etc. Performing these integrals analytically or by deterministic numerical methods is difficult for their multidimensionality. It is even impossible to calculate the exact event yield prediction when detector acceptance and response are to be considered, which requires the implementation of complex kinematic constraints and the simulation of particle transport inside the detector material.

Multidimensional integrals with complicated boundaries can be evaluated using the Monte Carlo (MC) sampling technique. In addition, with the MC methods we are able to simulate the processes of interest event-by-event which is very important to understand the physics signal inside a real detector.

A vast number of Monte Carlo generators dealing with the simulation of particle scattering exist. Some of them like PYTHIA [1] or HERWIG [2] are multipurpose generators, being able to generate a large set of exchanges taking into account many details of a particular process like parton showering, hadronization, etc. Other generators are specialized for certain applications. Concerning the simulation of hard diffractive and exclusive processes, some generators already exist.

Probably the first attempt to accommodate the pomeron exchange based on the Ingelman-Schlein model (Section 2.10) in PYTHIA were done in the POMPYT Monte Carlo generator [3]. The implementation of this model inside HERWIG is in the POMWIG generator [4], which can be used to simulate diffractive events in hadron-hadron or hadron-electron scattering. With the rising interest in double pomeron exchange (DPE) and the exclusive central production (or alternatively called exclusive DPE), the DPEMC generator [5] not only implemented models for inclusive diffraction already present in POMWIG, but also other models of inclusive and exclusive diffraction. The KMR model of the central exclusive production is implemented in the ExHuME generator [6] which has to be linked to PYTHIA for hadronization.

It is evident that the simulation of the hard diffractive scattering is distributed over a large set of computer programs. FPMC (Forward Physics Monte Carlo) is an extension of the DPEMC generator and aims to accommodate all relevant models for forward physics which could be studied at the LHC. In particular, it focusses on the two-photon exchange processes which are observable at the LHC. The generation of the forward processes is embedded inside HERWIG. The great advantage of the program is that all the processes with leading protons can be studied in the same framework, using the same

hadronization model. It is dedicated to generate the following exchanges:

- two-photon exchange
- single diffraction
- double pomeron exchange
- central exclusive production

We give details about the particular models present in the following sections. The FPMC generator is used throughout this thesis for various studies. The code already developed by Boonekamp and Kucs was restructured for our purposes to allow flexible physics analyses. New pomeron structure functions measured by the H1 Collaboration were added. Two-photon production was corrected and new matrix elements to study anomalous diboson and charged Higgs pair productions in two-photon events were implemented. In this chapter, we detail the changes which have been made, without the aim to describe the complete set of production mechanisms available in FPMC.

The layout of the chapter is the following: first, some theoretical aspects of the MC event generation are reviewed, followed by the discussion on the new implementations that were carried out. Predictions of cross sections for selected processes obtained with FPMC are given.

4.1 The Monte Carlo method

Monte Carlo methods are algorithms which use a random sampling to compute their results. At the basis of each Monte Carlo generator is a pseudo-random generator, producing a random sequence $r_1, r_2, \ldots, r_n$ distributed according to a uniform probability density function (p.d.f.) $u(r)$. This simple random sequence is used to generate more complicated sequences either with the transformation method or with the von Neuman acceptance-rejection technique (both described below). Finally, the generated random numbers are used to calculate values of physical quantities that are of interest and whose distributions can be plotted. Besides the generation of random sequences, Monte Carlo methods can be effectively used as an integration algorithm. Further details on the methods described in the following can be found in [7].

4.1.1 Monte Carlo integration

Deterministic methods of numerical integration operate by taking a number of evenly spaced samples from a function, calculating Rieman sums of the function (the trapezoidal rule). In general, this works effectively for functions of few variables. However, for vector functions $\mathbb{R}^d \to \mathbb{R}$ of large dimension d, the deterministic methods can be very inefficient because their convergence is $1/n^{2/d}$ as a function of the sampling parameter n dividing the integration domain, and the computation time grows with the number of samples as n^d.

Monte Carlo methods provide a solution to reduce the exponential time-increase of the deterministic methods. The integral of a 1-dimensional function f can be estimated by drawing n random points in the domain of definition and taking an average of the function values at these points

$$\int_{\bar{x_1}}^{\bar{x_2}} f \mathrm{d}x \approx (\bar{x_2} - \bar{x_1}) \langle f \rangle \pm (\bar{x_2} - \bar{x_1}) \sqrt{\frac{\langle f^2 \rangle - \langle f \rangle^2}{n}} \tag{4.1}$$

where

$$\begin{aligned} \langle f \rangle &\equiv \frac{1}{n}\sum_{i=1}^{n} f(x_i) \\ \left\langle f^2 \right\rangle &\equiv \frac{1}{n}\sum_{i=1}^{n} f^2(x_i) \end{aligned} \tag{4.2}$$

The function is averaged over the specified range $[\bar{x_1}, \bar{x_2}]$ in which the random numbers x_i are generated and the approximation gives the exact integral value in the limit $n \to \infty$. The second term in (4.1) expresses the uncertainty on the evaluated integral and $\left\langle f^2 \right\rangle - \langle f \rangle^2$ is the variance of the function f. The uncertainty of the computation can be controlled in two ways. First, the approximation will converge as $1/\sqrt{n}$ to the true value of the integral. Secondly, the uncertainty diminishes as the variance of the function decreases. Therefore, if a sampling that better approximates the function is chosen, the convergence of the MC integration can be improved.

This improvement is achieved by the use of a weight function. A new integration variable y is introduced, such that

$$\frac{\mathrm{d}y}{\mathrm{d}x} = w(x) \tag{4.3}$$

where $w(x)$ is the weight function. The integral is now calculated according to

$$I = \int_{\bar{y_1}}^{\bar{y_2}} \frac{f(x(y))}{w(x(y))}\mathrm{d}y \approx \frac{\bar{y_2} - \bar{y_1}}{n}\sum_{i=1}^{n} \frac{f(x(y_i))}{w(x(y_i))} \tag{4.4}$$

where the sampling points are drawn randomly in the range $[\bar{y_1}, \bar{y_2}]$. The uncertainty on the integral is now evaluated in the same way but with a substitution $f(x) \to f(x)/w(x)$. Hence, choosing the appropriate weight function $w(x)$, the convergence of (4.1) can be improved. For example imagine a steeply falling function of x. Clearly it is better to sample the points according to $w(x) = 1/x$ rather than according to the uniform distribution.

The main advantage of the MC technique is found in the multidimensional function integration. The integral of the d-dimensional function $f(\mathbf{x})$ where $\mathbf{x} = (x^1, x^2, \ldots, x^d)$ is computed as

$$I \approx \frac{1}{n}\sum_{i=1}^{n} f(\mathbf{x}_i)V \tag{4.5}$$

The multidimensional volume $V = \prod_{j=1}^{d}(\bar{x_2^j} - \bar{x_1^j})$ defines the integration domain. It is important to realize that the convergence of the integral estimated in terms of the number of sampling points is still $1/\sqrt{n}$, independent of the function dimension d. This shows the real power of the MC technique.

To improve the convergence, a d-dimensional function can be introduced provided that it factorizes into the form

$$w(\mathbf{x}) = \prod_{j=1}^{d} w(x^j) \tag{4.6}$$

where each $w(x^j)$ is a weight function for dimension j.

The introduction of a weight function in (4.3) basically states that the integral is going to be calculated as the average of $f(x)/w(x)$ at points distributed according to the $w(x)$ distribution. The method, how to generate such a sequence of random points, is discussed in the next section.

4.1.2 The transformation of variables

We are interested in deriving a function $x(r)$ which, for the input of a random sequence $r_1, r_2, \ldots, r_n$ distributed according to a uniform distribution $u(r)$ in the range $[0,1]$, will yield the random numbers $x_1, x_2, \ldots, x_n$ distributed according to $h(x)$ (in the notation of the preceding section, $h(x)$ would be $w(x)$ and random sequence r_i is a special case of a sequence y_i). The function $x(r)$ can be found by comparing the cumulative distributions of $h(x)$ and $u(r)$

$$F(x(r)) = \int_{-\infty}^{x(r)} h(x')\mathrm{d}x' = \int_{-\infty}^{r} u(r')\mathrm{d}r' = r \tag{4.7}$$

The desired transformation function is obtained by solving the above formula for $x(r)$. Depending on the form of $h(x)$ in question, this may or may not be possible.

As an example, consider the probability density function $h(x) = c/x$ in the range $x \in [x_{\mathrm{xmin}}, x_{\mathrm{xmax}}]$. This type of dependence is present in many problems of high energy physics as the momentum transfer, energy or mass dependences, for instance. In order to interpret $h(x)$ as the p.d.f, we must normalize it to one, so the normalization coefficient is $c = \ln(x_{\mathrm{xmin}}/x_{\mathrm{xmax}})$. By solving the formula (4.7) for $x(r)$ one gets

$$x(r) = \left(\frac{x_{\mathrm{max}}}{x_{\mathrm{xmin}}}\right)^{r} x_{\mathrm{xmin}} \tag{4.8}$$

When a sequence r is generated according to the uniform distribution $u(r)$ and plugged into the above expression, we get a sequence which is distributed according to the $1/x$ distribution.

4.1.3 The acceptance-rejection method

For many probability distributions, the equation (4.7) however, cannot be inverted analytically. In this case, the von Neumann's acceptance-rejection technique is an alternative to generate the random sequence. The needed ingredient is to find a function $g(x)$ which completely contains the p.d.f. $h(x)$, i.e that $h(x) \leq g(x)$ holds for all x, and for which the random numbers x can be easily generated according to $g(x)/\int g(x')\mathrm{d}x'$, i.e. the transformation of variables is analytically solvable. The acceptance-rejection method then proceeds in three steps:

1. Generate a random number x according to the p.d.f $g(x)/\int g(x')\mathrm{d}x'$

2. Generate a second random number r uniformly distributed between 0 and 1

3. If $r < h(x)/g(x)$, then accept x. If not, reject x and repeat

The efficiency of the method is determined by the ratio of accepted number of events N_A to the generated number of events N_G as $\varepsilon = N_A/N_G$.

The most simple example of the envelope function $g(x)$ is a box of the width $[x_{\mathrm{min}}, x_{\mathrm{max}}]$ and of the height h_{max}, where h_{max} is the maximum value of $f(x)$ on the considered interval. However, the efficiency of the method depends on how well the function $g(x)$ approximates the function $h(x)$ in question. Of course, for peaked distributions one may rather use the $1/x$ envelope distribution, than the simple constant function h_{max}.

4.1.4 Event generation

In particle scattering, the event yield is described in terms of the differential cross section, which can be written as

$$\frac{\mathrm{d}\sigma}{\mathrm{d}x^1 \dots \mathrm{d}x^d} = f(x^1, \dots, x^d) \tag{4.9}$$

where f is a function of several kinematic variables $x^1, \dots, x^d$. The calculation of the cross section and the event generation is performed at the same time using all three mentioned methods: the MC integration, the transformation of variables and also the acceptance-rejection technique. The functions $g^j(x^j)$ in the following are the mentioned weight functions (4.3) which lead to a better convergence of the integral (it is typically $1/x$ distribution). The transformation technique is used to generate sequences according to $g^j(x^j)$. But also, the functions $g^j(x^j)$ are used as the envelope function for the acceptance-rejection technique because not all the cross sections have simple form for which the inversion of the integral (4.7) could be made.

For every event i, the kinematic variables $x_i^1, \dots, x_i^d$ are generated according to the distributions $g^j(x^j)$

$$\begin{aligned} x_i^1 : &\quad g^1(x^1) \to c^1 \\ &\quad \vdots \\ x_i^d : &\quad g^d(x^d) \to c^d \end{aligned} \tag{4.10}$$

with their appropriate normalizations $c^1, \dots, c^d$. The generated values represent a process kinematics and must satisfy momentum and energy conservation, or a user cut on the transverse momentum of the generated system for example. The weight of each event is calculated as

$$W = \frac{f(x_i^1, \dots, x_i^d)}{\prod_{j=1}^d c^j g^j(x_i^j)} \tag{4.11}$$

The event weight is basically a differential cross section for a generated specific final state kinematics $x_i^1, \dots, x_i^d$, properly reweighted so that the sum over many generated events gives the correct integrated cross section.

The next step is to decide whether the event generated according to the approximate distributions $g^j(x_i^j)$ will be kept. The decision is made with the acceptance-rejection method. The generator usually shoots a sample of a few thousand events before the actual event generation to find the maximum weight W^{max} over the whole phase space

$$W^{max} \geq \frac{f(x^1, \dots, x^d)}{\prod_{j=1}^d c^j g^j(x^j)} \quad \forall x^1, \dots, x^d \tag{4.12}$$

Then for every event, a second random number r according to a uniform distribution between $[0, 1]$ is generated. The event is retained if

$$r \cdot W^{max} < W \tag{4.13}$$

otherwise the event is rejected. In this way the true distribution of f is generated and each event event has the weight of one.

Understanding these basic points about sequence generation and weight calculation was necessary to implement new matrix elements, and the pomeron and photon fluxes.

NFLUX	Flux
9	QCD factorized model, Pomeron flux
10	QCD factorized model, Reggeon flux
12	QED flux from Cahn, Jackson; $R \sim 1.2A^{\frac{1}{3}}$
13	QED flux from Drees et al., valid for heavy ions only
14	QED flux in pp collisions, from Papageorgiou
15	QED flux in pp collisions, from Budnev et al.
16	QCD KMR flux
17	QCD factorized model, Pomeron + Reggon flux

Table 4.1: Overview of available fluxes which are implemented in the FPMC generator. The QED flux corresponds to the photon exchange. The QCD flux corresponds to the pomeron/reggeon exchange, or to the gluon exchange in the case of the CEP predicted by the KMR calculation.

4.2 Generation of diffractive and photon events

In FPMC, the diffractive and exclusive processes are implemented by modifying the HERWIG routine for the $e^+e^- \to (\gamma\gamma) \to X$ process. In case of the two-photon pp events, the Weizsäcker-Williams (WWA) formula describing the photon emission off point-like electrons is substituted by the Budnev flux which describes properly the coupling of the photon to the proton, taking into account the proton electromagnetic structure. For the central exclusive production, a look-up table of the effective gluon-gluon luminosity computed by ExHuME is implemented. In case of the pomeron/reggeon exchange, the WWA photon fluxes are turned to the pomeron/reggeon fluxes multiplied by the diffractive parton density functions.

For processes in which the partonic structure of the pomeron is probed, the existing HERWIG matrix elements of non-diffractive production are used to calculate the production cross sections. The list of particles is corrected at the end of each event to change the type of particles from the initial state electrons to hadrons and from the exchanged photons to pomerons/reggeons, or gluons, depending on the process.

All the mentioned fluxes are implemented in the `FLUX` routine. The user selects the desired production mechanism by selecting the `NFLUX` parameter. Their overview is shown in Table 4.1. The energy which is carried by the exchanged object (photon/pomeron/reggeon/gluon) from the colliding particles is driven by the parameters `WWMIN` and `WWMAX`, representing the minimal and maximal momentum fraction loss ξ of the collided hadron.

4.3 Two-photon interactions

The two-photon production was first evaluated outside the MC by means of a numerical integration. Then the photon flux was implemented in FPMC. In addition, the two-photon dilepton production was compared with the existing LPAIR generator [11] and new two-photon processes were added: H^+H^-, and anomalous WW, ZZ productions. The details of the changes are discussed below.

4.3.1 Two-photon production cross section

Two-photon production in pp collision is described in the framework of Equivalent Photon Approximation (EPA) [8]. The almost real photons (low photon virtuality $Q^2 = -q^2$) are emitted by the incoming protons producing an object X, $pp \to pXp$, through two-photon exchange $\gamma\gamma \to X$. The photon spectrum of virtuality Q^2 and energy E_γ is proportional to the Sommerfeld fine-structure constant α and reads

$$\mathrm{d}N = \frac{\alpha}{\pi}\frac{\mathrm{d}E_\gamma}{E_\gamma}\frac{\mathrm{d}Q^2}{Q^2}\left[\left(1-\frac{E_\gamma}{E}\right)\left(1-\frac{Q^2_{min}}{Q^2}\right)F_E + \frac{E_\gamma^2}{2E^2}F_M\right] \tag{4.14}$$

where E is the energy of the incoming proton of mass m_p, $Q^2_{min} \equiv m_p^2 E_\gamma^2/[E(E-E_\gamma)]$ the photon minimum virtuality allowed by kinematics and F_E and F_M are functions of the electric and magnetic form factors. They read in the dipole approximation [8]

$$F_M = G_M^2 \qquad F_E = (4m_p^2 G_E^2 + Q^2 G_M^2)/(4m_p^2 + Q^2) \qquad G_E^2 = G_M^2/\mu_p^2 = (1+Q^2/Q_0^2)^{-4} \tag{4.15}$$

The magnetic moment of the proton is $\mu_p^2 = 7.78$ and the fitted scale $Q_0^2 = 0.71\ \mathrm{GeV}^2$. Electromagnetic form factors are steeply falling as a function of Q^2. That is the reason why the two-photon cross section can be factorized into the sub-matrix element and two photon fluxes. To obtain the production cross section, the photon fluxes are first integrated over Q^2

$$f(E_\gamma) = \int_{Q^2_{min}}^{Q^2_{max}} \frac{\mathrm{d}N}{\mathrm{d}E_\gamma \mathrm{d}Q^2}\mathrm{d}Q^2 \tag{4.16}$$

up to a sufficiently large value of $Q^2_{max} \approx 2-4\,\mathrm{GeV}^2$. The result can be written as

$$\mathrm{d}N(E_\gamma) = \frac{\alpha}{\pi}\frac{\mathrm{d}E_\gamma}{E_\gamma}\left(1-\frac{E_\gamma}{E}\right)\left[\varphi\left(\frac{Q^2_{max}}{Q_0^2}\right) - \varphi\left(\frac{Q^2_{min}}{Q_0^2}\right)\right] \tag{4.17}$$

where the function φ is defined as

$$\begin{aligned}
\varphi(x) &= (1+ay)\left[-\ln(1+x^{-1}) + \sum_{k=1}^{3}\frac{1}{k(1+x)^k}\right] \oplus \frac{(1-b)y}{4x(1+x)^3} \\
&+ c\left(1+\frac{y}{4}\right)\left[\ln\frac{1+x-b}{1+x} + \sum_{k=1}^{3}\frac{b^k}{k(1+x)^k}\right] \\
y &= \frac{E_\gamma^2}{E(E-E_\gamma)} \\
a &= \frac{1}{4}(1+\mu_p^2) + \frac{4m_p^2}{Q_0^2} \approx 7.16 \\
b &= 1 - \frac{4m_p^2}{Q_0^2} \approx -3.96 \\
c &= \frac{\mu_p^2 - 1}{b^4} \approx 0.028
\end{aligned} \tag{4.18}$$

Note that the formula for the Q^2-integrated photon flux was cited incorrectly several times in literature. There is a sign error in the original paper by Budnev *et al.* [8], which we emphasized in the

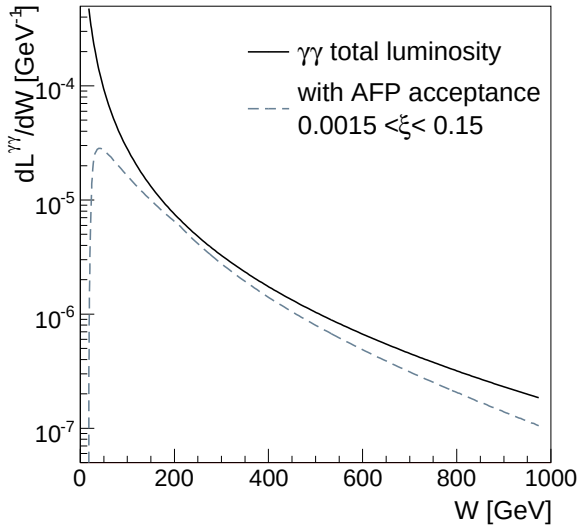

Figure 4.1: Relative effective $\gamma\gamma$ luminosity in pp collisions at 14 TeV as a function of the two-photon invariant mass. The maximal virtualities of the emitted photons are set to $Q^2_{max} = 2\,\mathrm{GeV}^2$. The dashed curve shows the photon spectrum within the ATLAS or CMS forward detector acceptance.

above formula by the circled plus sign $\oplus$ in front of the second term. Moreover, in [9] there is another typesetting error leading to wrong second and last terms.

The contribution to the integral above $Q^2_{max} \approx 2\,\mathrm{GeV}^2$ is very small. The Q^2-integrated photon flux also falls rapidly as a function of the photon energy E_γ which implies that the two-photon production is dominant at small masses $W \approx 2\sqrt{E_{\gamma 1} E_{\gamma 2}}$. Integrating the product of the photon fluxes $f(E_{\gamma 1}) \cdot f(E_{\gamma 2}) \cdot \mathrm{d}E_{\gamma 1} \cdot \mathrm{d}E_{\gamma 2}$ from both protons over the photon energies while keeping the two-photon invariant mass fixed to W, one obtains the two-photon effective luminosity spectrum $\mathrm{d}L^{\gamma\gamma}/\mathrm{d}W$.

The effective $\gamma\gamma$ luminosity is shown in Figure 4.1 as a function of the mass W in full line. The production of heavy objects is particularly interesting at the LHC when new particles could be produced in a very clean environment. The production rate of massive objects is however limited by the photon luminosity at high invariant mass. The integrated two-photon luminosity above $W > W_0$ for $W_0 = 23\,\mathrm{GeV},\ 2 \times m_W \approx 160\,\mathrm{GeV}$, and 1 TeV is respectively 1%, 0.15% and 0.007% of the luminosity integrated over the whole mass spectrum. The luminosity spectrum was calculated using the upper virtuality bound $Q^2_{max} = 2\ \mathrm{GeV}^2$ using numerical integration. The luminosity spectrum $0.0015 < \xi < 0.15$ (to be discussed later) is also shown in the figure (it is calculated in the limit of low Q^2, thus setting $E_\gamma = \xi E$).

Using the effective relative photon luminosity $\mathrm{d}L^{\gamma\gamma}/\mathrm{d}W$, the total cross section reads

$$\frac{\mathrm{d}\sigma}{\mathrm{d}\Omega} = \int \frac{\mathrm{d}\sigma_{\gamma\gamma\to X}(W)}{\mathrm{d}\Omega} \frac{\mathrm{d}L^{\gamma\gamma}}{\mathrm{d}W} \mathrm{d}W \tag{4.19}$$

where $\mathrm{d}\sigma_{\gamma\gamma\to X}/\mathrm{d}\Omega$ denotes the differential cross section of the sub-process $\gamma\gamma \to X$, dependent on the invariant mass of the two-photon system.

In FPMC, the formula (4.17) is directly plugged in the routine `FLUX`. It is normalized by the beam energy and is actually dimensionless, parameterized by the momentum fraction loss of the proton $\xi = E_\gamma/E$.

PTMIN [GeV]	cross section $\sqrt{s} = 14\,\text{TeV}$ [pb]	cross section $\sqrt{s} = 10\,\text{TeV}$ [pb]
3	48.9	41.2
5	13.5	11.1
10	2.22	1.79
50	$2.46 \cdot 10^{-2}$	$1.78 \cdot 10^{-2}$
100	$1.97 \cdot 10^{-3}$	$1.93 \cdot 10^{-3}$
Flags: `TYPEPR='EXC',TYPINT='QED',IPROC='16008',WWMIN=0.,WWMAX=1.`		

Table 4.2: Two-photon dimuon production cross sections at generator level from FPMC. The survival probability factor of 0.9 is not taken into account.

The transverse momentum of the exchanged photon is generated using the von Neuman acceptance-rejection technique because the equation (4.7) is not solvable analytically for the Budnev photon flux $\mathrm{d}N/\mathrm{d}E_\gamma \mathrm{d}Q^2$ (4.14) since it has a rather complicated Q^2-dependence. However, since the inequality

$$\frac{\mathrm{d}N}{\mathrm{d}E_\gamma \mathrm{d}Q^2} < \frac{\alpha}{\pi E_\gamma} \frac{1}{Q^2} \tag{4.20}$$

holds for all non-zero E_γ, the random sequence can be generated according to $1/Q^2$. This guarantees a high generation efficiency of the photon transverse momentum.

4.3.1.1 Two-photon dilepton production

The two-photon production of dileptons has quite a large cross section at the LHC. It is shown for $\sqrt{s} = 14\,\text{TeV}$ and $\sqrt{s} = 10\,\text{TeV}$ in Table 4.2 for several p_T thresholds. The cross sections obtained with FPMC were compared to the LPAIR generator [11] which implements the two-photon dilepton pruduction only. The agreement was better than 1%. The muon transverse momentum p_T^{lep}, rapidity y^{lep}, and the proton transverse momentum p_T^{prot} and momentum fraction loss ξ^{prot} predicted by FPMC and LPAIR[1] are shown in Figure 4.3. They agree well.

The dilepton production can create a background to other exclusive processes. Certainly, one of the most discussed topics is the search for the Higgs boson in central exclusive production. When dileptons or dijets with invariant mass equal to the Higgs mass are created through the two-photon exchange, they may mimic the signal. Except a small difference in the proton p_T spectrum, which is more peaked at zero for the two-photon events, both types of events look the same. The concern is that for these analysis, the two-photon production corresponding to a typical mass window of a Higgs boson is not negligible with respect to the searched Higgs signal.

Let us illustrate this in more detail. The mass spectrum of two-photon dimuons $W = \sqrt{s\xi_1\xi_2}$ is shown in Figure 4.2 (left). The generic acceptance of the forward detector $0.0015 < \xi < 0.15$ reduces the cross section especially at low masses. The zoom on the missing masses, between $100 < W < 200\,\text{GeV}$ is shown in Figure 4.2 (right). Requiring a typical mass window $115 < W < 125\,\text{GeV}$ and $p_T^\mu > 10\,\text{GeV}$, one obtains the effective cross section of a dimuon pair production $\sigma_{ll} = 14.7\,\text{fb}$. With the additional constraints of the forward detector acceptance and $|\eta^\mu| < 2.5$, one gets the cross section $\sigma_{ll} = 6.0\,\text{fb}$.

[1] LPAIR is a not officially released Monte Carlo generating lepton pair events produced via two-photon exchange in $pp(\bar{p})$ or ep collisions.

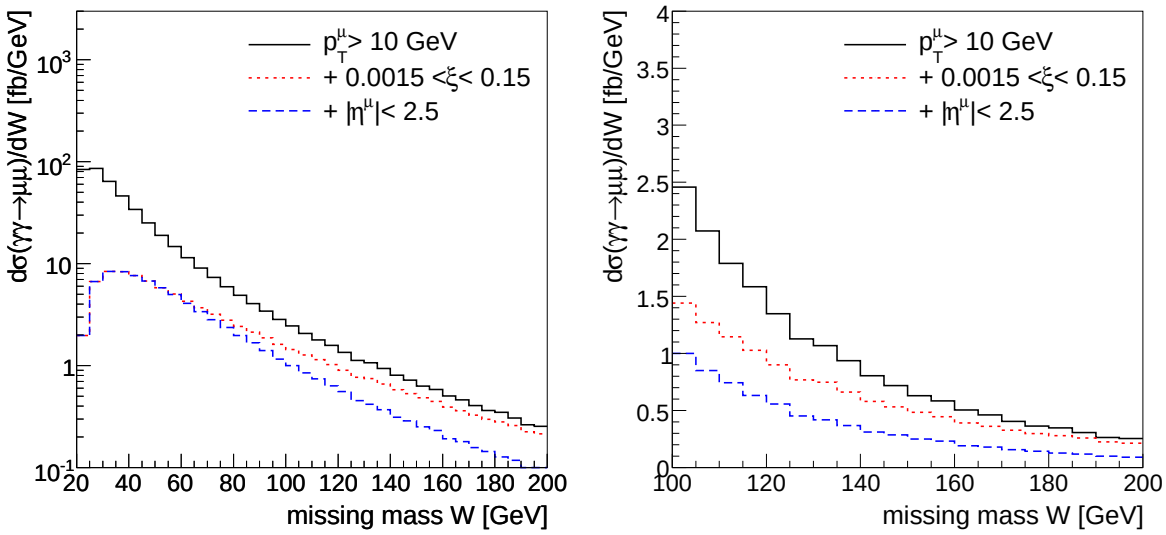

Figure 4.2: Two-photon dimuon production of dimuons plotted as a function of the proton missing mass (left) and zoomed plot for $100 < W < 200\,\text{GeV}$ (right). The full, dotted, and dashed curves correspond to a subsequent application of the following cuts: $p_T^\mu > 10\,\text{GeV}$, forward detector acceptance $0.0015 < \xi < 0.15$, and $|\eta^\mu| < 2.5$.

The cross sections are 3 times higher for dijet production due to the color factor of quarks. Although these rates have to be multiplied by the soft survival probability factor, it is large (0.9) for the two-photon events. Let us remind, that the total SM CEP Higgs cross section is about 3 fb for a Higgs mass of $m_h = 120\,\text{GeV}$. The concern is that, up to the author's knowledge, this background was not investigated at all in the Higgs analyses.

Depending on the triggering capabilities on low-p_T electrons and muons, about tens of two-photon dilepton or dimuon events could be collected with early data taking ($\mathscr{L} \approx 10\,\text{pb}^{-1}$) and the definition of exclusivity in those events could be checked.

4.3.2 Two-photon diboson production and anomalous couplings

The total two-photon SM cross section of the $pp \to pWWp$ process is 95.6 fb (for $\alpha = 1/137$). The $pp \to pZZp$ process is forbidden in the SM. The cross sections of both processes can be enhanced in the presence of anomalous triple gauge and quartic gauge boson couplings. These processes are elaborated in detail in Chapter 7 where the study of the sensitivities to the anomalous couplings is presented. Here we discuss the technical implementation of the corresponding anomalous $\gamma\gamma \to WW$ and $\gamma\gamma \to ZZ$ subprocess cross sections into FPMC.

The effective Lagrangians parametrizing these new interactions are mentioned explicitly in Equations 7.19 and 7.30. They are functions of six anomalous parameters: $\Delta\kappa^\gamma$, λ^γ for the triple gauge couplings and a_0^W/Λ^2, a_0^Z/Λ^2, a_C^W/Λ^2, a_C^Z/Λ^2 for the quartic ones. The corresponding matrix elements were obtained with the CompHEP program [12]. The Feynman rules following from the effective Lagrangians were plugged into CompHEP, which generated the C code containing two important routines: `asgn_` through which the free parameters of the model are set, and `sqme_` which returns a matrix element

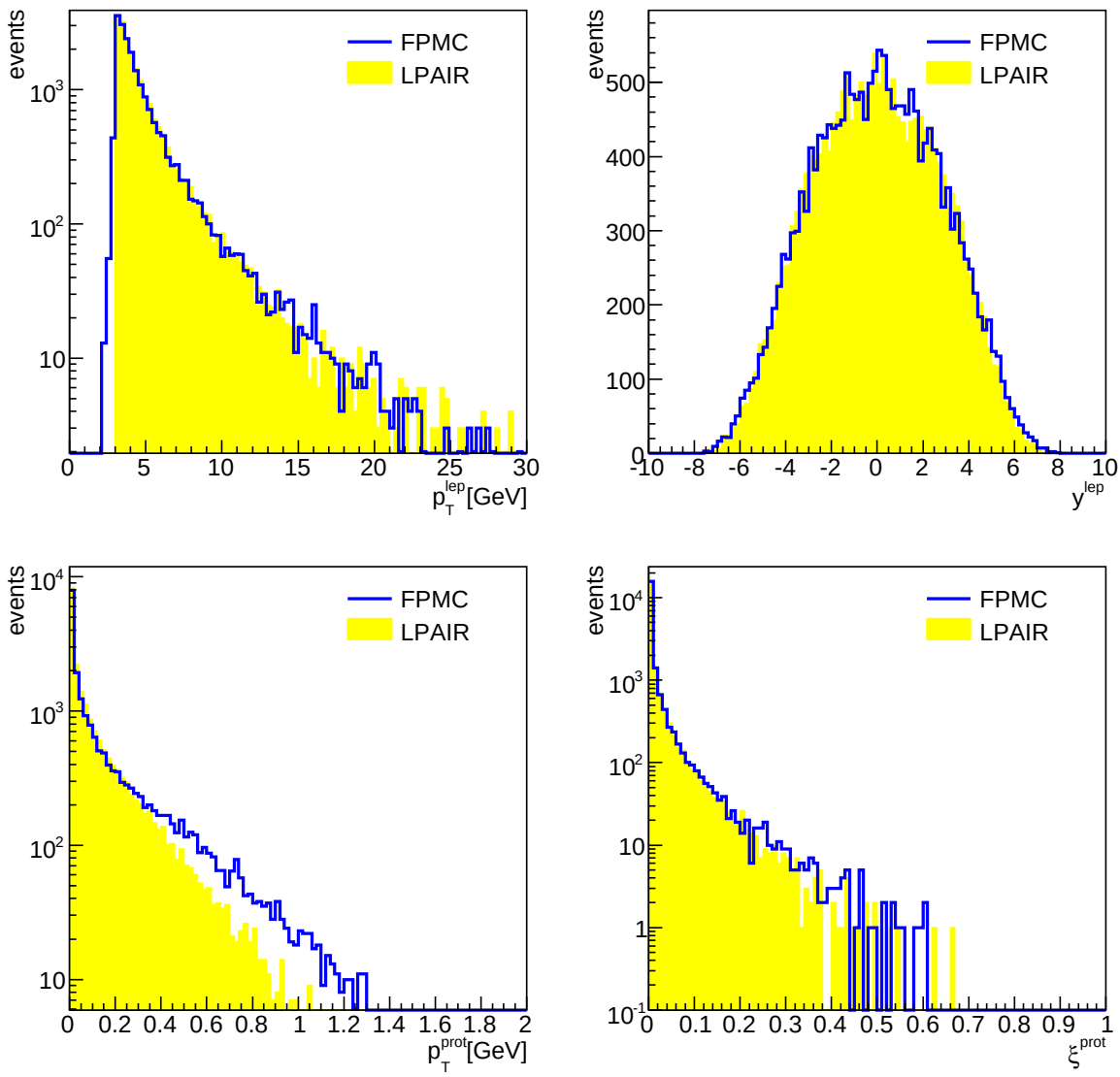

Figure 4.3: Comparison of FPMC and LPAIR predictions for the two-photon muon pair production at $\sqrt{s} = 14\,\text{TeV}$ for the following distributions: lepton transverse momentum (top-left), rapidity distribution of the lepton (top-right), transverse momentum of the scattered proton (bottom-left), and momentum fraction loss of the scattered proton (bottom-right). The small difference in the transverse momentum of the proton is attributed to the fact that the spin correlation between leptons and protons is taken into account in LPAIR but not in FPMC.

squared for the specified initial state photons and the final state bosons four-momenta [13].

The important point in the implementation of the CompHEP code into FPMC was to understand where to plug the matrix elements and how to assign the weight of the sub-process correctly. The $\gamma\gamma \to WW$ process is implemented in the `HWHQPM` routine in the standard HERWIG. This routine was extended to also enable the ZZ generation in $\gamma\gamma$ events. The WW production is switched on with a (standard) process `IPROC`=16010, the ZZ with a newly implemented `IPROC`=16015 process. The HERWIG event weight of a sub-process is the ratio of the differential cross section with respect to the momentum transfer t in nb, integrated over the polar angle φ, and divided by the sampling function and its normalization

$$W = \frac{1}{cg(t_i)} \int \frac{\mathrm{d}\sigma(t_i)}{\mathrm{d}t\mathrm{d}\varphi}\mathrm{d}\varphi \tag{4.21}$$

Such formula was already mentioned in (4.4) and (4.11). The momentum transfer t is generated according to the $1/t$ distribution. However, it is done in two steps to take into account the p_T cut on the boson momentum defined by the user. First, the variable is generated according to $1/t$ for $t_{min} < t < t_{max}$, which corresponds to the angles $0 < \theta < \pi/2$, i.e. only for half of the allowed t range. Then, a random number is drawn between $[0,1]$. In half of the cases the t variable is switched to a u Mandelstam variable and the t is calculated using $t = 2m_W^2 - s - u$. The corresponding factors added to the weight, related to the t generation, are

$$-2 \cdot \ln(t_{max}/t_{min}) \cdot \mathrm{MAX}(t,u) \tag{4.22}$$

The $\mathrm{MAX}(t,u)$ function is effectively $1/g(t_i)$ after the change of u and t variables, the logarithm is the normalization of $1/t$ p.d.f., and the factor 2 comes from the fact that the t was generated within only one half of the allowed $0 < \theta < \pi$ range.

The general differential cross section code line of the $2 \to 2$ particle scattering reads

$$\frac{\mathrm{d}\sigma}{\mathrm{d}\Omega} = \frac{1}{64\pi^2 s}\frac{\lambda^{1/2}(s,m_3,m_4)}{\lambda^{1/2}(s,m_1,m_2)}\left|\mathscr{M}\right|^2 \tag{4.23}$$

where $\mathscr{M}$ is the matrix element of the process, the triangle function is defined as

$$\lambda(x,y,z) = x^2 + y^2 + z^2 - 2xy - 2yz - 2xz \tag{4.24}$$

and m_1, m_2 and m_3, m_4 are the masses of the particles in the initial and the final states, respectively. In the case of photons $m_1 = m_2 = 0$ and vector bosons $m_3 = m_4 = m_W$, the triangular functions are s^2, and the $s^2\beta^2$, respectively, where $\beta \equiv \sqrt{1 - 4m_W^2/s}$ is the vector boson velocity in the center-of-mass frame. Using the relation for the Jacobian $\left|\mathrm{d}t/\mathrm{d}(\cos\theta)\right| = s\beta/2$, the φ integrated differential cross section reads

$$\begin{aligned}\int \frac{\mathrm{d}\sigma}{\mathrm{d}t\mathrm{d}\varphi}\mathrm{d}\varphi &= \int \frac{\mathrm{d}\sigma}{\mathrm{d}\Omega}\left|\frac{\mathrm{d}(\cos\theta)}{\mathrm{d}t}\right|\mathrm{d}\varphi \\ &= \frac{4\pi}{64\pi^2 s^2}\left|\mathscr{M}^2\right|\end{aligned} \tag{4.25}$$

Putting together equations (4.22) and (4.25), we arrive at the final formula for the weight to be assigned for WW or ZZ production from massless photons

```
FACTR=-GEV2NB*2*LOG(TMAX/TMIN)*MAX(T,U)
     *2*PIFAC/(64.*PIFAC**2)/S**2*2d0*AMP2
```

where the `GEV2NB` is 389379 nb/GeV representing the change of units, and `AMP2` is the squared amplitude obtained from CompHEP.

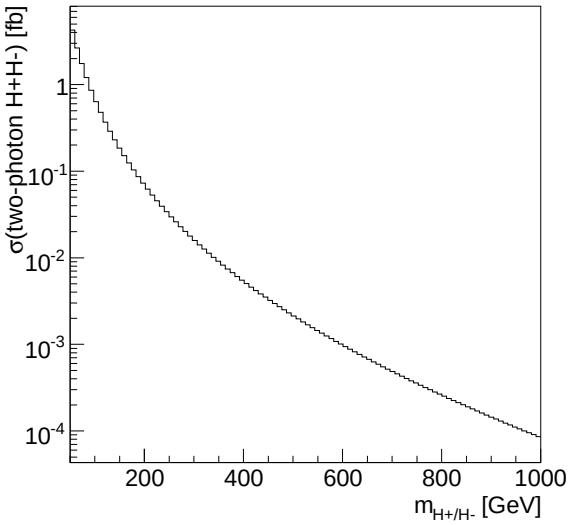

Figure 4.4: Two-photon H^+H^- total production cross section as a function of the Higgs mass m_H.

4.3.3 Two-photon Higgs production

The central exclusive SM Higgs production is discussed extensively in the forward physics community. In SUper SYmmetric (SUSY) theories, there is more than one Higgs boson. In the Minimal Super Symmetric Model (MSSM) in particular, there are five Higgs bosons: three neutral h, H, A, and two charged ones $H^{\pm}$. The charged Higgs boson pair could be produced in two-photon interactions. Its decay into τ and ν pairs is planned to be studied [14]. We therefore implemented this process in FPMC.

The charged Higgs boson production cross section is identical to that of the charged scalar pair $\gamma\gamma \to \varphi^+\varphi^-$ production, provided that the scalar mass is set to the Higgs mass. The differential cross section reads [15]

$$\frac{\mathrm{d}\sigma}{\mathrm{d}\Omega} = \frac{\alpha^2\beta}{2s}\left(1 - \frac{8m^2 s}{s^2-(t-u)^2} + \frac{32m^2s^2}{(s^2-(t-u)^2)^2}\right) \tag{4.26}$$

The implementation of this process follows the same lines as in the case of the anomalous couplings. The differential cross section was added into the same routine `HWHQPM`. The process can be selected with new process number `IPROC`=16030 and the Higgs mass is set via the `HCM` parameter.

The total cross section of the two-photon charged Higgs production is shown in Figure 4.4. It falls quickly as a function of the Higgs boson mass and the Higgs searches have to concentrate on the Higgs masses in this channel. The Higgs decaying to τ-leptons was excluded at LEP up to masses $\approx 90\,\mathrm{GeV}$, depending on the τ branching fraction [16]. For such a low mass, the two-photon total Higgs cross section is about 1 fb.

Only τ decays of the Higgs boson were implemented since it is the dominant decay channel of the low-mass (below the top mass) charged Higgs. The user can define the specific branching ratio $H \to \tau\tau^+$ corresponding to the SUSY parameter space via the variable `HCBR`.

Fit parameter	Fit A	Fit B
$\alpha_{\mathbb{P}}(0)$	1.118 ± 0.008	1.111 ± 0.007
$n_{\mathbb{R}}$	$(1.7 \pm 0.4) \times 10^{-3}$	$(1.4 \pm 0.4) \times 10^{-3}$
$\alpha'_{\mathbb{P}}$	$0.06^{+0.19}_{-0.06}\,\mathrm{GeV}^{-2}$	
$B_{\mathbb{P}}$	$5.5^{-2.0}_{+0.7}\,\mathrm{GeV}^{-2}$	
$\alpha_{\mathbb{R}}(0)$	0.5 ± 0.10	
$\alpha'_{\mathbb{R}}$	$0.3^{+0.6}_{-0.3}\,\mathrm{GeV}^{-2}$	
$B_{\mathbb{R}}$	$1.6^{-1.6}_{+0.4}\,\mathrm{GeV}^{-2}$	

Table 4.3: Diffractive structure function parameters of QCD Fit A and Fit B fits [18] appearing in (2.32) and (2.33). These structure functions are used as defaults in FPMC.

IFIT	**PDF set**	Source
10	H1 (old)	[17]
20	Zeus (old)	[17]
30	combined H1 and Zeus (old)	[17]
100	H1 Fit B	[18]
101	H1 Fit A	[18]

Table 4.4: Implemented diffractive parton density functions in FPMC. The most recent are the H1 Fits A and Fit B IFIT=101, 100.

4.4 Implementation of pomeron exchange

Diffractive parton density functions (DPDF) were measured at HERA. The outcome of the fits are the values of the pomeron and reggeon trajectories $\alpha_{\mathbb{P}}(t) = \alpha_{\mathbb{P}}(0) + t\alpha'_{\mathbb{P}}$, $\alpha_{\mathbb{R}}(t) = \alpha_{\mathbb{R}}(0) + t\alpha'_{\mathbb{R}}$ governing the corresponding flux energy dependence (2.32), and the pomeron/reggeon parton distribution functions $f_{\mathbb{P}/p}(\beta, Q^2)$, $f_{\mathbb{R}/p}(\beta, Q^2)$. Only the normalization of the product of the diffractive structure function $f_i^D(x, Q^2, x_{\mathbb{P}}, t)$ mentioned in (2.33) and of the pomeron/reggeon flux (2.32) is fixed by the QCD fits. Therefore, the normalization of the fluxes is conventionally fixed at $x_{\mathbb{P}} = x_{\mathbb{R}} = 0.003$ such that

$$x_{\mathbb{P}} \int_{t_{\mathrm{cut}}}^{t_{\mathrm{min}}} f_{\mathbb{P}/p}\, \mathrm{d}t = 1 \tag{4.27}$$

where $|t_{\mathrm{min}}| \simeq m_p^2 x_{\mathbb{P}}^2/(1 - x_{\mathbb{P}})$ is the minimum kinematically accessible value of $|t|$, m_p is the proton mass and $|t_{\mathrm{cut}}| = 1.0\,\mathrm{GeV}^2$. The normalization of the reggeon flux is defined in the same way.

The pomeron and reggeon parameters obtained in the most recent H1 QCD fits (2.33) are shown in Table 4.3. The implemented diffractive parton densities are summarized in Table 4.4 and can be selected with the `IFIT` parameter. The flux parameters are fixed in the routine `HWMODINI` where the initial parameters are set. The parton densities are used in the routine `HWSFUN` where the call to the H1 tables (the source code can be found at [18]) is made.

We can compare the pomeron and photon Budnev flux energy dependence. This is shown in Figure 4.5. The photon flux is truncated due the proton electromagnetic form factors. The pomeron flux is

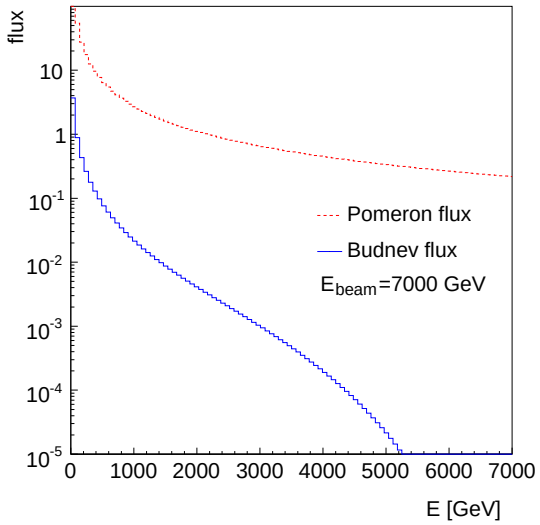

Figure 4.5: Comparision of two-photon and pomeron fluxes at the LHC as a function of photon/pomeron energy E.

$\sqrt{s} = 1.96\,\text{TeV}$

PTMIN [GeV]	SD dijets [pb]	DPE dijets [pb]
10 GeV	$180 \cdot 10^5$	$429 \cdot 10^3$
15 GeV	$29 \cdot 10^5$	$42 \cdot 10^3$
25 GeV	$23 \cdot 10^5$	$1.3 \cdot 10^3$

$\sqrt{s} = 14\,\text{TeV}$

PTMIN [GeV]	SD dijets [pb]	DPE dijets [pb]
15 GeV	$107 \cdot 10^6$	$5.2 \cdot 10^6$
25 GeV	$14 \cdot 10^6$	$5.4 \cdot 10^5$
35 GeV	$3.5 \cdot 10^6$	$1.1 \cdot 10^5$

Table 4.5: Single diffractive and double pomeron exchange dijet cross sections for various thresholds at the Tevatron and the LHC. No survival probability factor, which is expect to be 0.06, was applied.

larger by two orders of magnitude and spans up to high values of the pomeron energies. This, however, might not be reasonable because the proton will more likely break at high momentum fraction loss. The validity of the Ingelman-Schlein model is usually considered up to $\xi \approx 0.1 - 0.2$.

Predictions of the single diffractive and double pomeron exchange dijet cross sections for various jet p_T thresholds are summarized in Table 4.5. They are given assuming the pomeron exchange only since the sub-leading exchange was found to be negligible at the Tevatron. Similarly, the single diffractive W and Z production cross sections are shown in Table 4.6. All numbers are calculated with the H1 Fit B parton density functions, with the cut on the maximum momentum fraction loss of the proton $\xi_{max} = 0.1$. The rates are not corrected for the survival probability which is expected to be 0.06 at the LHC [19].

process	$\sqrt{s} = 1.96\,\text{TeV}$	$\sqrt{s} = 14\,\text{TeV}$	
$W \rightarrow$ anything+Gap	468 pb	9570 pb	IPROC=11499
$Z/\gamma \rightarrow$ anything+Gap	640 pb	6292 pb	IPROC=11399
Flags: `TYPEPR='INC',TYPINT='QCD',PART1='P',PART2='E+',WWMAX=.1`			

Table 4.6: Total single diffractive production cross section of W and Z/γ bosons at $\sqrt{s} = 14\,\text{TeV}$. No survival probability factor, which is expected to be 0.06, was applied.

4.5 Implementation of exclusive production

The implementation of the central exclusive Higgs and dijet productions is not done in terms of flux like before but rather in terms of the effective gluon-gluon luminosity. The calculation of the effective gluon-gluon luminosity in exclusive events [20] is available in the ExHuME generator. It is convenient to study the forward processes in the same framework with the same hadronization model. We therefore adopted the ExHuME calculation of the gluon-gluon luminosity in FPMC.

CEP production is implemented by means of look-up tables of the gluon-gluon luminosity calculated by ExHuME (`Lumi()` routine) as a function of the momentum fraction losses of the scattered protons ξ_1, ξ_2. It is evaluated and added to the event weight after generation of both of ξ_1, ξ_2. The rest of the event is then generated with the $gg \rightarrow q\bar{q}, gg, H$ matrix elements respecting the $J_z = 0$ selection rule. The comparison of the effective gluon-gluon luminosity included in FPMC with that calculated by ExHuME (v1.3.3) is shown in Figure 4.6.

4.5.1 Conclusion

The FPMC generator produces a large set of forward physics processes. The inclusive and exclusive productions can be studied in one framework. First, the update of the pomeron/reggeon density functions for inclusive single diffraction and double pomeron exchange was done. The main part of the work concerned the generation of two-photon processes. FPMC gives predictions of $\gamma\gamma \rightarrow WW$ and $\gamma\gamma \rightarrow ll$ which perfectly agree with those in the literature. Two-photon events are used throughout the thesis. The two-photon lepton production is used to study a possible method to align the proposed ATLAS forward detectors in Chapter 6. The implementation of new effective couplings of the photons to W/Z allowed the investigation of the sensitivities due to anomalous couplings of a photon to electroweak bosons and it will be presented in Chapter 7. Moreover, the rapidity gap reconstruction in the ATLAS calorimeter using dimuon two-photon events is presented in Chapter 8. Also, the production of charged Higgs boson pair was implemented which will be useful for Higgs searches with the forward detectors.

The program code was interfaced with the ATLAS simulation framework ATHENA. The most recent version of the program can be found at [10].

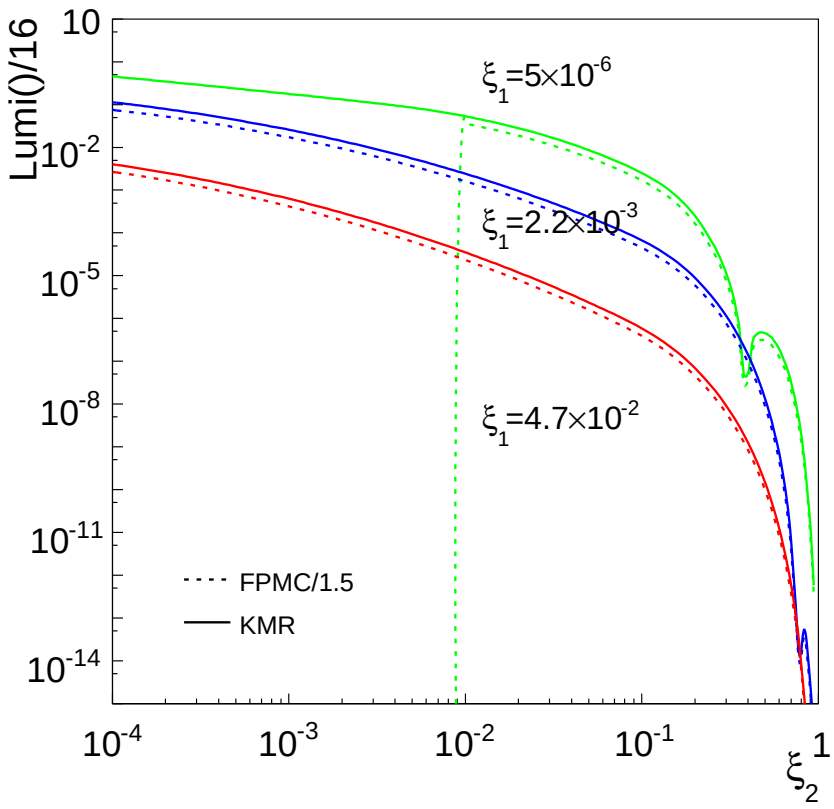

Figure 4.6: Comparison of the effective gluon-gluon luminosity implemented in FPMC in the form of looked up tables and as in ExHuMe calculation, shown for three momentum fraction losses $\xi_1 = 5\times10^{-6}$, 2.2×10^{-3}, 4.7×10^{-2}, They are exactly the same but FPMC is scaled down by a factor 1.5 for demonstration purposes. The drop in the luminosity for $\xi_2 \sim 0.02$ when $\xi_1 = 5\times10^{-6}$ is fixed, occurs for masses $\sqrt{s\xi_1\xi_2} < 3\,\text{GeV}$ which is the mass limit of the look-up tables.

Bibliography

[1] T. Sjostrand, S. Mrenna and P. Skands, JHEP **0605** (2006) 026 [arXiv:hep-ph/0603175].

[2] G. Corcella *et al.*, JHEP **0101** (2001) 010 [arXiv:hep-ph/0011363]; hep-ph/0210213.

[3] POMPYT generator for diffraction in Pytha, `http://www3.tsl.uu.se/thep/pompyt/`, Sept. 2009.

[4] B. E. Cox and J. R. Forshaw, Comput. Phys. Commun. **144**, 104 (2002) [arXiv:hep-ph/0010303].

[5] M. Boonekamp and T. Kucs, Comput. Phys. Commun. **167** (2005) 217 [arXiv:hep-ph/0312273].

[6] J. Monk and A. Pilkington, Comput. Phys. Commun. **175** (2006) 232 [arXiv:hep-ph/0502077].

[7] G. Cowan, Statistical data analysis, *Oxford, Clarendon Press*, (1998);
S. Brandt, Data Analysis, *Springer-Verlag New York Inc.*, (1999).

[8] V. M. Budnev, I. F. Ginzburg, G. V. Meledin and V. G. Serbo, Phys. Rept. **15** (1974) 181.

[9] M. Boonekamp, C. Royon, J. Cammin and R. B. Peschanski, Phys. Lett. B **654** (2007) 104 [arXiv:0709.2742 [hep-ph]].

[10] Forward Physics Monte Carlo, `www.cern.ch/fpmc`, Sep. 2009;
M. Boonekamp, V. Juranek, O. Kepka, C. Royon,
Proceedings of the workshop: HERA and the LHC workshop series on the implications of HERA for LHC physics, arXiv:0903.3861 [hep-ph], 2007.

[11] S. P. Baranov, O. Duenger, H. Shooshtari and J. A. M. Vermaseren, *In *Hamburg 1991, Proceedings, Physics at HERA, vol. 3* 1478-1482. (see HIGH ENERGY PHYSICS INDEX 30 (1992) No. 12988)*

[12] E. Boos *et al.* [CompHEP Collaboration], Nucl. Instrum. Meth. A **534** (2004) 250 [arXiv:hep-ph/0403113].

[13] T. Pierzchala, private communication on the implementation of the anomalous couplings in `CompHEP`.

[14] V. Khoze, M. Tasevsky, private communication.

[15] A.I. Akhiezer, V.B. Berestetskii, *Quantum Electrodynamics*, English translation, Interscience Publishers, 1965.;
S. J. Brodsky, T. Kinoshita and H. Terazawa, Phys. Rev. D **4**, 1532 (1971).

[16] G. Abbiendi *et al.* [OPAL Collaboration], arXiv:0812.0267 [hep-ex].

[17] C. Royon, L. Schoeffel, S. Sapeta, R. B. Peschanski and E. Sauvan, Nucl. Phys. B **781** (2007) 1 [arXiv:hep-ph/0609291].

[18] A. Aktas *et al.* [H1 Collaboration], Eur. Phys. J. C **48** (2006) 715 [arXiv:hep-ex/0606004]; source code `http://www-h1.desy.de/psfiles/papers/desy06-049_files/`, Sep. 2009.

[19] V. A. Khoze, A. D. Martin and M. G. Ryskin, Eur. Phys. J. C **18** (2000) 167 [arXiv:hep-ph/0007359].

[20] V. A. Khoze, A. D. Martin and M. G. Ryskin, Eur. Phys. J. C **23** (2002) 311 [arXiv:hep-ph/0111078].

Exclusive Diffraction at the Tevatron

5

The work presented in this chapter aims to check the existence of the exclusive dijet signal produced via Central Exclusive Production (CEP) using existing models of inclusive and exclusive productions. Although the exclusive production yields kinematically well constrained final state objects, their experimental detection is non-trivial due to the overlap with the inclusive double pomeron exchange (DPE) events. Exclusive events appear only as a small deviation from the prediction of inclusive models and need to be studied precisely. In particular, the pomeron structure as obtained from HERA is not precisely known at high momentum fraction, and specifically, the gluon in the pomeron is not well constrained. It is not clear if such uncertainty could not lead to the misidentification of the observed processes as exclusive.

The dijet mass fraction distribution (DMF) measured by the CDF Collaboration [2] is used to show that one is unable to give a satisfactory description of the data without the existence of exclusive events, even when the uncertainties associated with the pomeron structure are taken into account. We also include other approaches to explain diffraction in our study, the so called Soft color interaction model.

First, the models used in the study are briefly described, with more details given for the ones that were not mentioned in the theoretical chapter. Next, we present how the introduced models describe the measurement performed by CDF. At the end of the chapter, a prediction of how the DMF could be used to identify the exclusive events at the LHC is given. This study was published in [1].

5.1 Theoretical models

The used inclusive and exclusive DPE models are implemented in the Monte Carlo program FPMC [3]. The Soft color interaction model is embedded in the PYTHIA program [4]. A survey of the different models follows.

5.1.1 Inclusive models

The first inclusive model to be mentioned is the Ingelman-Schlein model [5]. As was already discussed in preceding chapter, the diffractive PDF measured at HERA are used to describe pomeron exchanges at the hadron collider provided that the cross sections are corrected for the survival probability factor

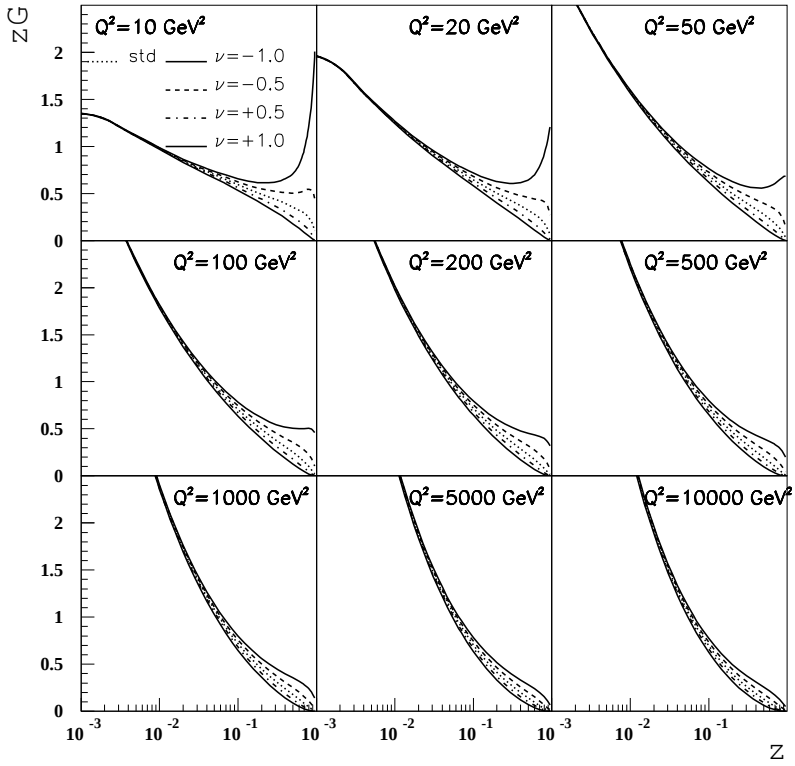

Figure 5.1: Uncertainty on the gluon density at high β (here $\beta \equiv z$). The gluon density is multiplied by the factor $(1-\beta)^{\nu}$ where ν=-1., -0.5, 0.5, 1. The default value $\nu = 0$ is the gluon density in the pomeron determined directly by a fit to the H1 F_2^D data with an uncertainty of about 0.5.

which is about 0.1 at the Tevatron and 0.03 at the LHC. This model will be referred to as “Factorized model" (FM) from now on.

On the other hand, the Boonekamp-Peschanski-Royon (BPR) inclusive model [6], is purely a non-perturbative calculation utilising only the shape of the pomeron parton density functions and leaving the overall normalization to be determined from the experiment. We confronted the prediction of DPE cross section with the observed rate at the Tevatron [7] and obtained the missing normalization factor. The obtained normalization factor is $9.3 \cdot 10^{-3}$ for the parton densities measured at HERA.

In the BPR model, the partonic content of the pomeron is expressed in terms of the distribution functions as $f_{i/\mathbb{P}}(\beta_i) \equiv \beta_i G_{i/\mathbb{P}}(\beta_i)$, where the $G_{i/\mathbb{P}}(\beta_i)$ are the true parton densities as measured by the HERA experiments, and β_i denotes the momentum fraction of the parton i in the pomeron. The integral of $f_{i/\mathbb{P}}(\beta_i)$ is normalized to 1, so that in the limit $f_{i/\mathbb{P}}(\beta_i) \to \delta(\beta_i)$ the exclusive cross section of Bialas-Landshoff model (to be discussed) is recovered.

Both models use the pomeron structure measured at HERA which is gluon dominated. In this study, we use the results of the QCD fits of the pomeron structure function data measured by the H1 collaboration [8]. The gluon density at high β, where β denotes the momentum fraction of the particular parton in the pomeron, is not well constrained from the QCD fits performed at HERA. To study this

uncertainty, we multiply the gluon distribution by the factor $(1-\beta)^{\nu}$ as shown in Figure 5.1. QCD fits to the H1 data lead to the uncertainty on the ν parameter $\nu = 0.0 \pm 0.5$ [8]. We will see in the following how this parameter influences the results on the dijet mass fraction as measured at the Tevatron.

5.1.2 Exclusive models

We used the Khoze, Martin, Ryskin (KMR) [9] model which is purely a perturbative approach of the central production as was already discussed in detail in Section 2.15.

In addition, we also investigated the Bialas-Landshoff exclusive model [10] (BL) which is based on an exchange of two “non-perturbative" gluons between a pair of colliding hadrons which connect to the hard subprocess. Reggeization of the gluon propagators is employed in order to recover the pomeron parameters which successfully describe soft diffractive phenomena, e.g. the total cross section at low energies. It should be mentioned that the so called Bialas-Landshoff exclusive model is actually an extension of the Higgs boson exclusive production calculated by Bialas and Landshoff (see first Ref. of [10]) for the dijet production. This is composed of a cross section for $q\bar{q}$ [10] and gg [11] productions.

The two models show a completely different p_T dependence of the DPE cross section. The energy dependence of the BL model is found to be weaker since the pomeron is assumed to be soft whereas it is not the case for the KMR model.

5.1.3 Soft color interaction model

The Soft color interaction model (SCI) [4, 12] assumes that diffraction is not due to a colorless pomeron exchange between the protons but due to a soft interaction of colored partons which emerged from the hard interaction. It gives a probability that each pair of these colored parton make a soft interaction. This interaction changes only the color state of the partons and not their momenta. They involve some non-perturbative soft interaction which the model tries to describe. The only parameter of the models is the probability P (to be determined from the experiment) that there will be a string connection, a color exchange between the pair of partons. The number of soft interactions will thus vary from event-to-event. In some cases, the soft color exchange creates a color singlet from the proton remnants, which is separated from the rest of the colored partons and thus gives rise to a rapidity gap. Technically, the soft interaction is implemented in PYTHIA as an intermediate step before the hadronization mechanism modeled by the Lund string model [13].

The SCI model is very successful in describing the HERA data in which the probability parameter was tuned to $P \approx 0.5$. Moreover, exactly the same model tuned at HERA describes the Tevatron diffractive data. It gives correct rates of SD processes (dijets, W, beauty and charm mesons) and also DPE dijets if the diffractive event is defined with the rapidity gap requirement. There is no need for the concept of survival probability and a correct normalisation is found between the Tevatron and HERA data without additional parameters, which is one of the biggest successes of this model.

5.2 Dijet mass fraction at the Tevatron

The dijet mass fraction turns out to be a very appropriate observable for identifying the exclusive production. It is defined as the ratio $R_{JJ} = M_{JJ}/M_X$ of the dijet system invariant mass M_{JJ} to the total mass of the final state system M_X (excluding the intact (anti)protons). If the jet algorithm has such proper-

ties that the out-of-cone effects are small, the presence of an exclusive production would manifest itself as an excess of the events towards $R_{JJ} \sim 1$; for exclusive events, the dijet mass is essentially equal to the mass of the central system because no pomeron remnant is present. The advantage of DMF is that one can focus on the shape of the distribution; the observation of exclusive events does not rely on the overall normalization which might be strongly dependent on the detector simulation and acceptance of the roman pot detector. In the following analysis, we closely follow the measurement performed by the CDF Collaboration.

5.2.1 Kinematic constraints

We mention only the cuts which are relevant for our analysis. The complete description of the measurement and the detector setup are presented in [2]. To simulate the CDF detector, we use a fast simulation interface [14], which performs a smearing of the deposited cell energy above a 0.5 GeV threshold and reconstructs jets using a cone algorithm of a radius $R = 0.7$ in the $\eta \times \phi$ plane. The properties of the event such as the rapidity gap size were evaluated at the generator particle level.

CDF uses a roman pot detector to tag the antiprotons on one side (corresponding to $\eta_{\bar{p}} < 0$). For the DMF measurement, we require the antiprotons to have a longitudinal momentum loss in the range $0.01 < \xi_{\bar{p}} < 0.12$ and we apply the roman pot acceptance obtained from the CDF Collaboration (the CDF detector acceptance is greater than 0.5 for $0.035 < \xi_{\bar{p}} < 0.095$). On the proton side, where no such device is present, a rapidity gap of the size $3.6 < \eta_{gap} < 5.9$ is required. In the analysis, further cuts are applied: two leading jets with a transverse momentum above the threshold $p_T^{jet1,jet2} > 10\,\text{GeV}$ or $p_T^{jet1,jet2} > 25\,\text{GeV}$ in the central region $|\eta^{jet1,jet2}| < 2.5$, a third jet veto cut ($p_T^{jet3} < 5\,\text{GeV}$) as well as an additional gap on the antiproton side of the size $-5.9 < \eta_{gap} < -3.6$. For the sake of brevity, the threshold for the transverse momentum of the two leading jets will be in the following denoted as p_T^{min}, if needed.

5.2.2 Reconstruction of the event kinematics

The dijet mass is computed using the jet momenta for all events passing the above mentioned cuts. In order to follow as much as possible the method used by the CDF collaboration, the mass of the diffractive system M_X is calculated from the longitudinal antiproton momentum loss $\xi_{\bar{p}}$ within the roman pot acceptance, and the longitudinal momentum loss of the proton ξ_p^{part} is determined from the generator level particles in the central detector ($-4 < \eta_{part} < 4$), such that:

$$M_X = \sqrt{s \xi_{\bar{p}} \xi_p^{part}} \tag{5.1}$$

$$\xi_p^{part} = \frac{1}{\sqrt{s}} \sum_{particles} p_T \mathrm{e}^{\eta} \tag{5.2}$$

summing over the particles with energies higher than 0.5 GeV in the final state at generator level. To reconstruct the diffractive mass, ξ_p^{part} was multiplied by a factor 1.1, obtained by fitting the correlation plot between the momentum loss of the proton at generator level ξ_p and ξ_p^{part} at particle level with a straight line (see the discussion below).

Differences in the dijet mass fraction distribution reconstructed on the particle level and as measured by the CDF Collaboration originate mainly in two issues. First, the invariant mass reconstructed from the dijet system M_{JJ} has finite resolution due to possible out-of-cone energy deposition which is

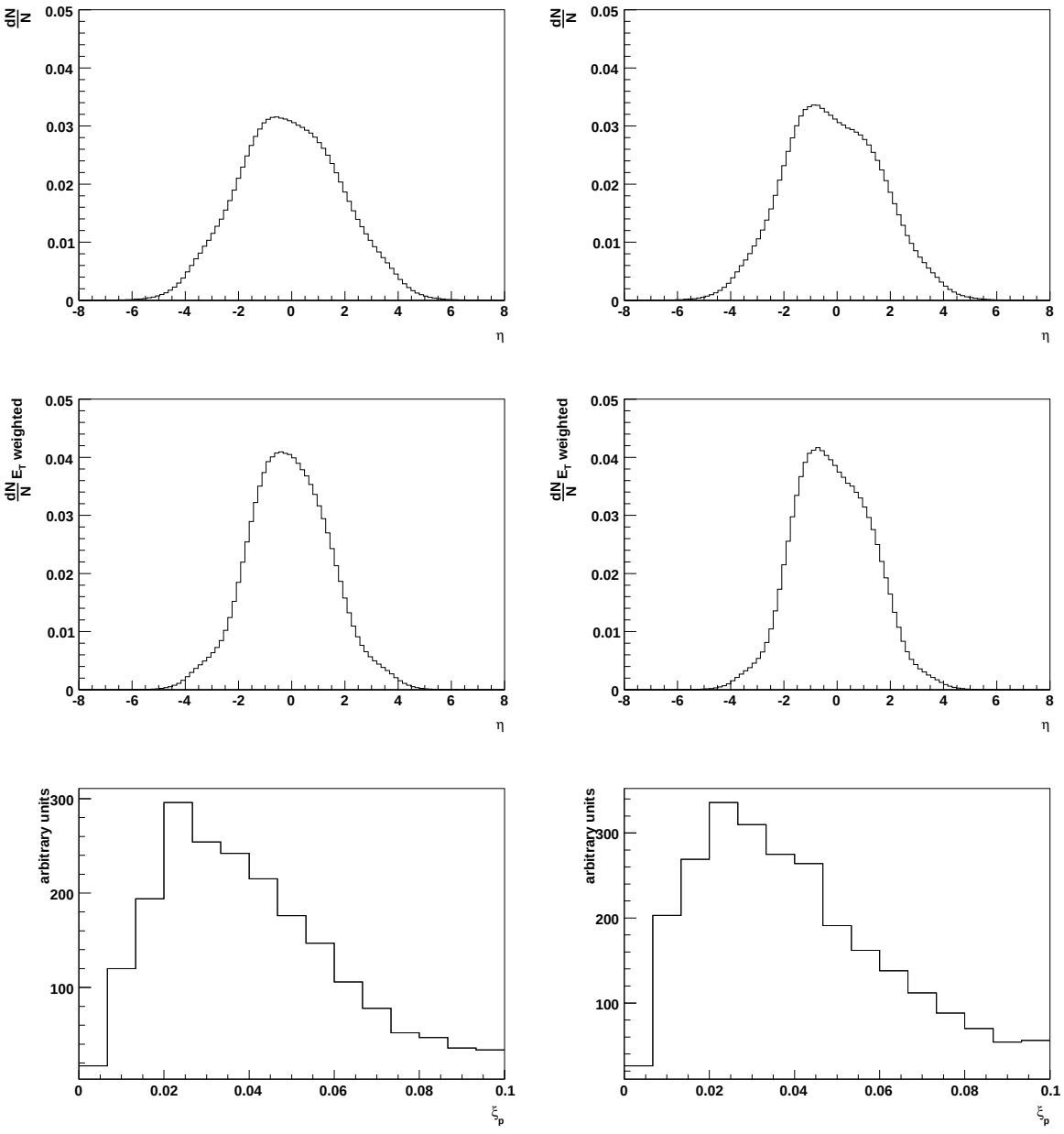

Figure 5.2: Top and middle plots: Rapidity and E_T weighted rapidity distributions of all particles produced (except the protons); Bottom plot: momentum loss of the proton in double pomeron exchange events ξ_p for FM (left) and BPR (right) inclusive models.

not clustered into the jets. Second, the energy resolution of the calorimeter towers and the detector acceptance effects the mass of the reconstructed diffractive system M_X. The R_{JJ} for exclusive events is therefore shifted to lower values.

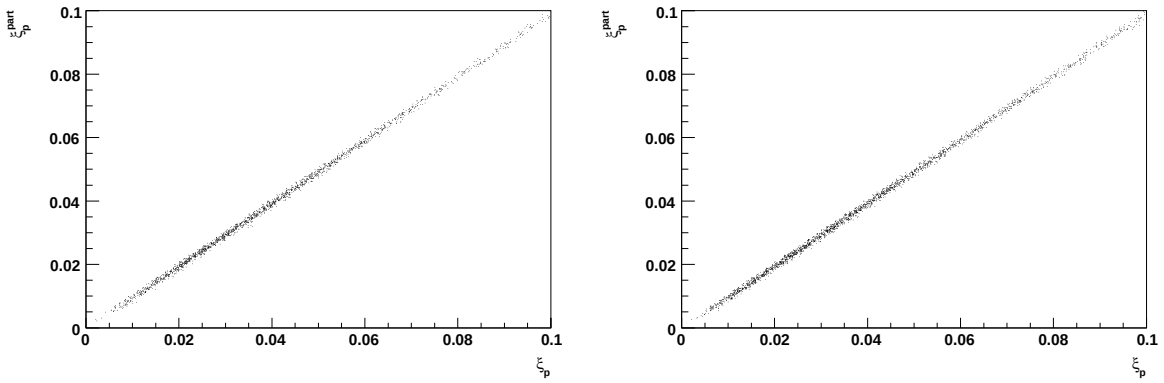

Figure 5.3: Comparison of the proton momentum loss ξ_p^{part} calculated with formula (5.2) and the proton momentum loss ξ_p at generator level.

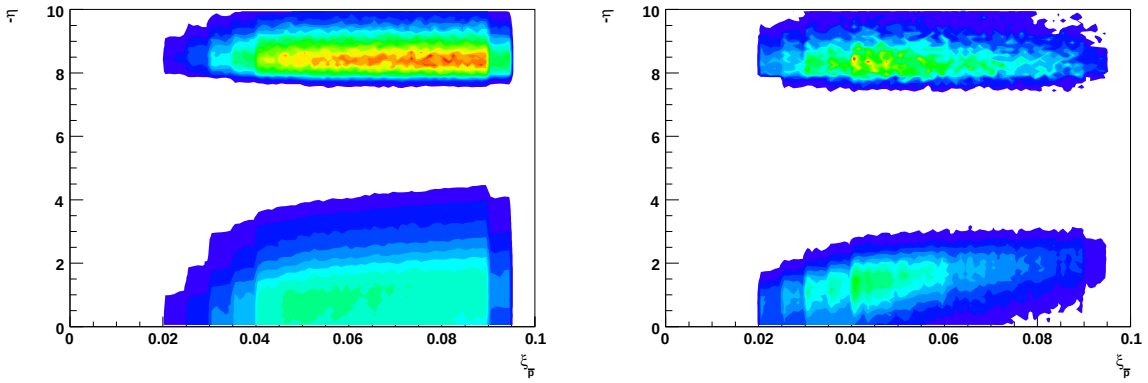

Figure 5.4: Rapidity of particles on the $\bar{p}$ side vs. $\bar{p}$ momentum loss: for the inclusive factorized model (left) and exclusive KMR model (right). Hits of scattered $\bar{p}$ are included.

5.2.3 Effects of the fast simulation

The DMF reconstruction is deeply dependent on the accuracy of the detector simulation. In order to understand the DMF observable within our fast simulation approach, we discuss some of the kinematic distributions in the following for jets with $p_T > 10\,\text{GeV}$.

- In our analysis, we defined the dijet mass fraction as a ratio of the two leading jet invariant mass M_{JJ} to the central diffractive mass M_X. We must ensure that most of the produced diffractive energy M_X is deposited in the central detector, otherwise the particular acceptance of the CDF detector would lead to a large discrepancy of the reconstructed M_X between our approach (5.2) and the CDF one. The energy flow of the particles as a function of rapidity at the generator level is shown in Figure 5.2, upper plot. The middle plot shows the energy flow weighted by the transverse momentum of the particle E_T. We see that most of the energy is deposited in the calorimeter region, i.e. for $|\eta| < 4$. In $\bar{p}$ tagged events, protons most frequently lose a smaller

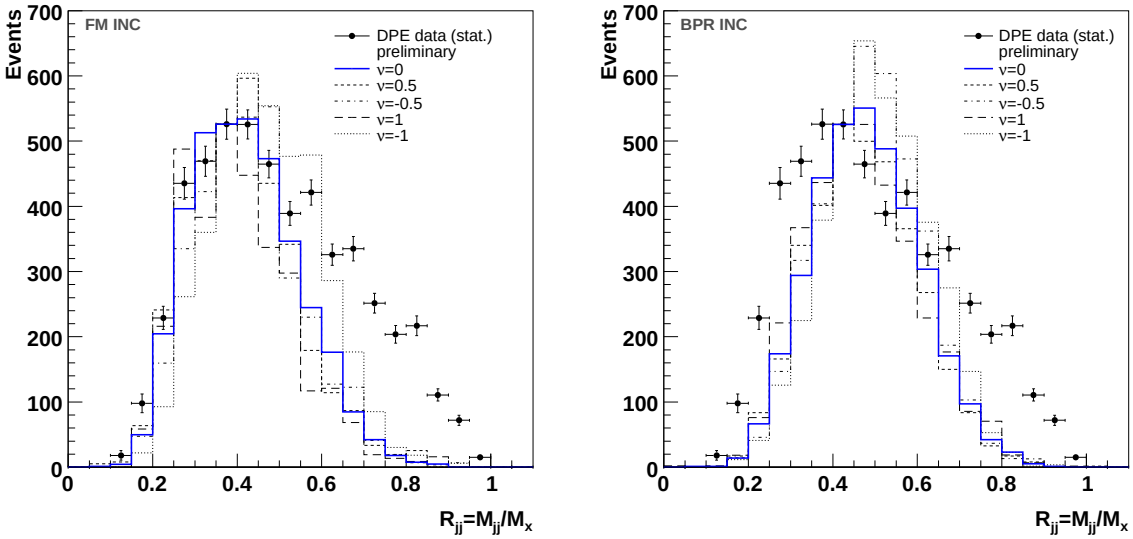

Figure 5.5: Dijet mass fraction for jets $p_T > 10\,\text{GeV}$. FM (left) and BPR (right) models, inclusive contribution. The uncertainty of the gluon density at high β is obtained by multiplying the gluon distribution by $(1-\beta)^\nu$ for different values of ν (non-solid lines).

momentum fraction (roughly $\xi_p \sim 0.025$) than the tagged antiproton for which the acceptance turns on for $\xi_{\bar{p}} > 0.035$. This can be seen from the ξ_p population plot in the bottom of Figure 5.2. Thus, a collision of a more energetic pomeron from the antiproton side with a pomeron from the proton side is boosted towards the $\bar{p}$ as it is seen on the energy flow distributions.

- A comparison between the proton momentum loss obtained from particles ξ_p^{part} calculated using formula (5.2) and the proton momentum loss at generator level ξ_p leads to the factor 1.1 mentioned in the previous section. The dependence is displayed in Figure 5.3 with the factor applied on ξ_p^{part}.

- The size of the rapidity gap approximately scales as $\Delta\eta \sim \log 1/\xi$ as a function of the momentum loss ξ. The size of the gap which increases with decreasing ξ for inclusive models can be seen in Figure 5.4. Regions of high rapidity show the $\bar{p}$ hits whereas the low rapidity region is due to the produced particles detected in the central detector; they are well separated by a rapidity gap. For exclusive events, the size of the rapidity gap is larger and does not show such a strong ξ dependence as for inclusive models.

5.2.4 Inclusive model prediction

We present first the dijet mass fraction calculated with FM and BPR models and explore the impact of the high β gluon uncertainty in the pomeron. To do so, we multiply the gluon density by the factor $(1-\beta)^\nu$, for different values of $\nu = -1, -0.5, 0, 0.5, 1$. The impact of the parameter is shown in Figures 5.5 and 5.6 for jets with $p_T > 10\,\text{GeV}$ and $p_T > 25\,\text{GeV}$, respectively. The computed distributions were normalized in shape, since the luminosity used for the dijet mass fraction measurement is not given. This should be understood in the following way: in the CDF note [2], the luminosity of the whole sample $310\,\text{pb}^{-1}$ is given which differs from the effective luminosity used for R_{JJ}. The difference is mainly due

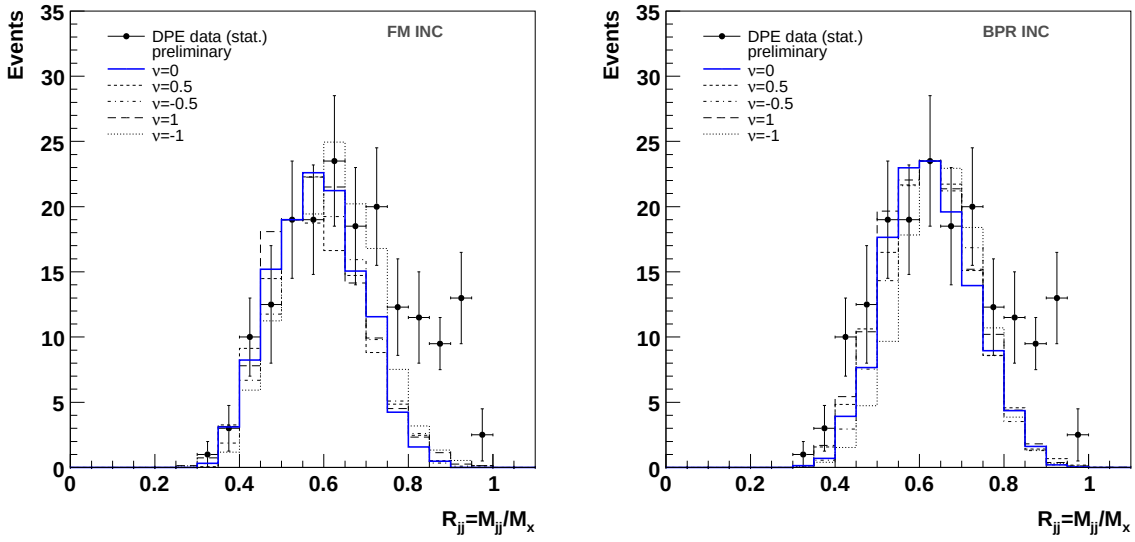

Figure 5.6: Dijet mass fraction for jets $p_T > 25\,\text{GeV}$. FM (left) and BPR (right) models, inclusive contribution. The uncertainty of the gluon density at high β is obtained by multiplying the gluon distribution by $(1-\beta)^{\nu}$ for different values of ν (non-solid lines).

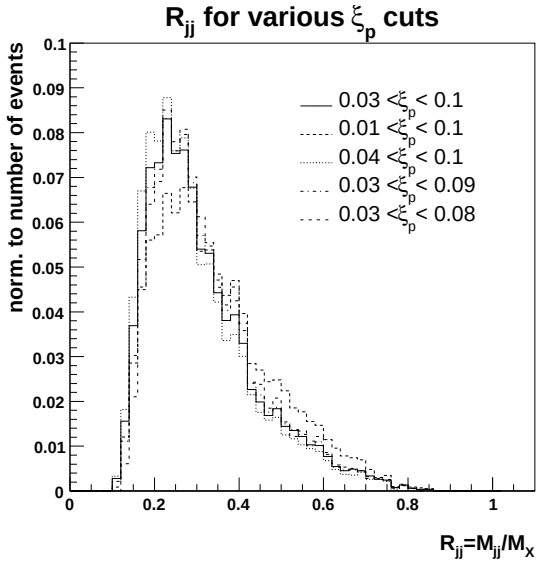

Figure 5.7: Dijet mass fraction at the generator level for $p_T^{parton1,2} > 10$ GeV, $0.03 < \xi_{\bar{p}} < 0.095$ and ξ_p cut as specified in the figure. The shape of the DMF is not much sensitive to the ξ_p cut in a reasonable range.

to multiple interactions effects. The diffractive R_{JJ} events are selected using single interactions only (gaps would be filled in overlap events) which correspond in average to a few percent of the whole data sample. However, the exact number is not given in the CDF note. On the other hand, one can compare the theoretical prediction to the shape of the cross section corrected to hadron level provided by CDF. We find that the cross sections agree up to a factor 2-3 for different jet p_T cuts. This difference can be attributed to the fast simulation which we are using. It is obvious that the size of the rapidity gap (directly related to ξ_p) is difficult to be studied without a full simulation. The factor 2-3 can be easily obtained by a small change of ξ_p since the cross section itself has $1/\xi_p$ dependence. However, it is important to notice that the shape of the dijet mass fraction does not depend strongly on the ξ_p or the size of the rapidity gap as illustrated in Figure 5.7 and therefore it does not change the conclusion about the description of the DMF using inclusive diffraction.

The interesting possible exclusive region at high R_{JJ} is enhanced for $\nu = -1$, however, not in such extent that would lead to a fair description of the observed distributions. As a consequence, the measured tail of the dijet mass fraction at high R_{JJ} cannot be explained by enhancing the gluon distribution at high β, and another contribution such as exclusive events is required.

A particular property seems to disfavour the BPR model at the Tevatron. Indeed, the dijet mass fraction is dumped at low values of R_{JJ}, especially for jets $p_T > 10\,\text{GeV}$. Since the cross section is obtained as a convolution of the hard matrix element and the distribution functions, the dumping effect is a direct consequence of the use of a multiplicative factor β in the parton density functions in the pomeron mentioned in Section 5.1.1. We will come back on this point when we discuss the possibility of a revised version of the BPR model in the following.

As we have seen, inclusive models are not sufficient to describe well the measured CDF distributions. Thus, it opens an area to introduce different types of processes/models which give a significant contribution at high R_{JJ}.

5.2.5 Exclusive models predictions

In this section, we will study the enhancement of the dijet mass distribution using exclusive DPE processes, with the aim to describe the CDF dijet mass fraction data. We examine three possibilities of the interplay of inclusive plus exclusive contributions, specifically:

1. FM + KMR
2. FM + BL exclusive
3. BPR + BL exclusive

The full contribution is obtained by fitting the inclusive and exclusive distribution to the CDF data, leaving the overall normalization N and the relative normalization between the two contributions $r^{\text{EXC/INC}}$ free. More precisely, the DMF distribution is obtained with the fit as $N(\sigma^{\text{INC}}(R_{JJ}) + r^{\text{EXC/INC}}\sigma^{\text{EXC}}(R_{JJ}))$. The fit was done for jets with $p_T^{min} = 10\,\text{GeV}$ and $p_T^{min} = 25\,\text{GeV}$, separately.

The overall normalization factor cannot be studied since the CDF collaboration did not determine the luminosity for the DMF measurement. On the other hand, the relative normalization between the inclusive and exclusive production can provide a useful information. The relative normalization allows to make predictions for higher p_T jets or for LHC energies for instance. For this sake, the relative normalizations $r^{\text{EXC/INC}}$ should not vary much between the two p_T^{min} measurements. Results are summarized

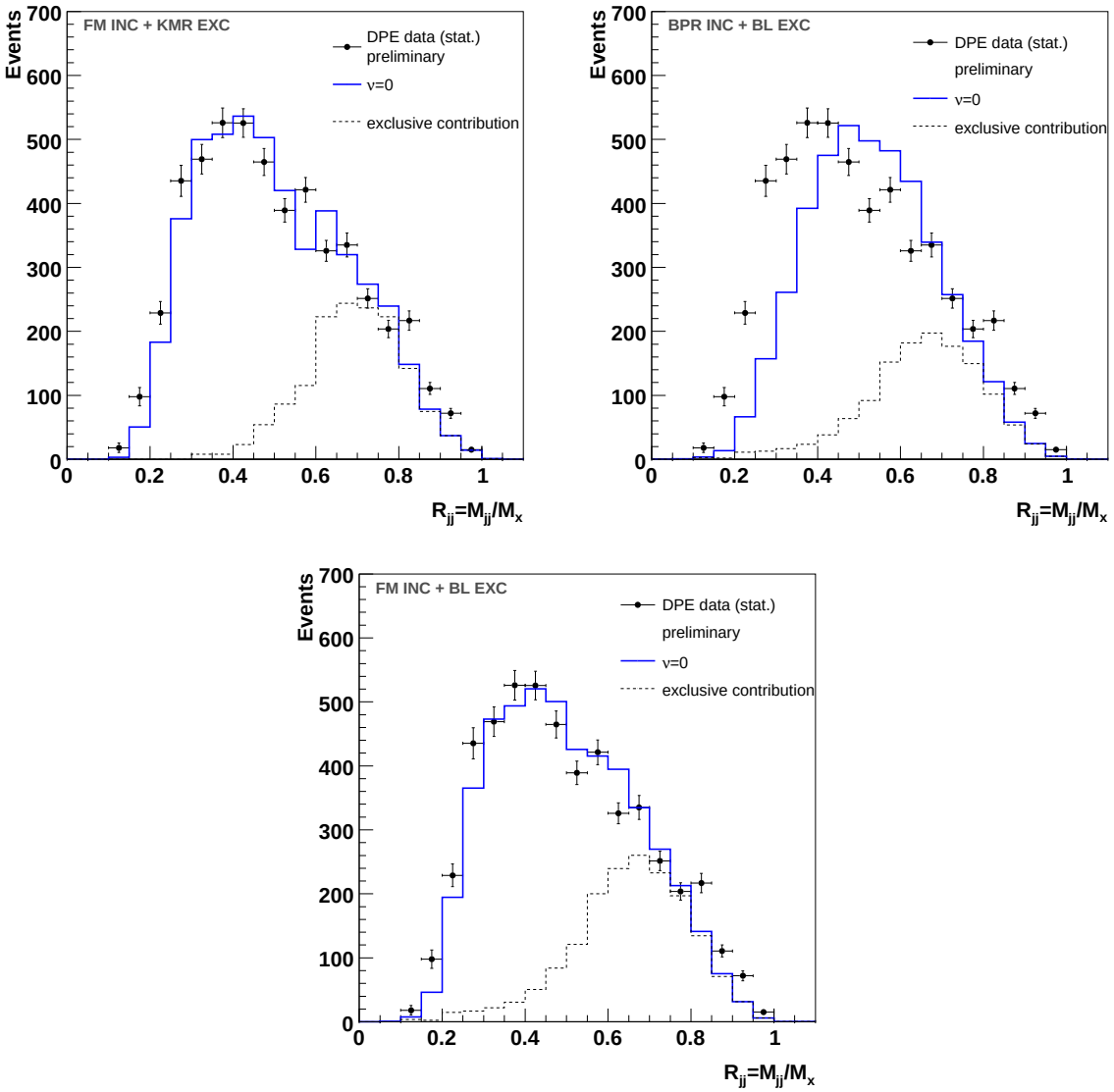

Figure 5.8: Dijet mass fraction for jets $p_T > 10\,\text{GeV}$. FM + KMR (left), BPR + BL (right), FM + BL (bottom) models. We notice that the exclusive contribution allows to describe the tails at high R_{JJ}.

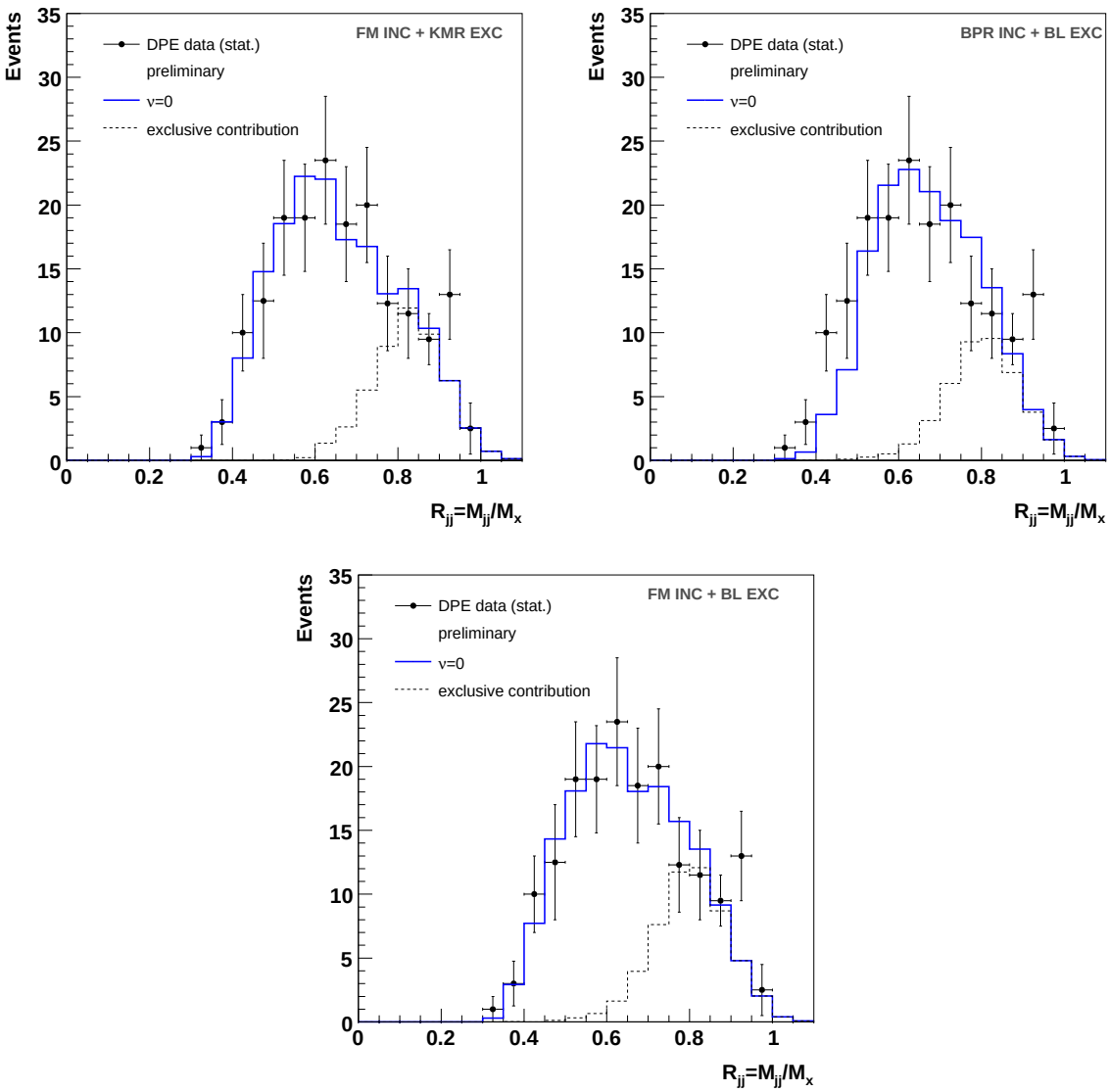

Figure 5.9: Dijet mass fraction for jets $p_T > 25\,\text{GeV}$. FM + KMR (left), BPR + BL (right), FM + BL (bottom) models. We note that the exclusive contribution allows to describe the tails at high R_{JJ}.

contributions	$r^{\mathrm{EXC/INC}}(10)$	$\sigma^{\mathrm{INC}}(10)$[pb]	$\sigma^{\mathrm{EXC}}(10)$[pb]
FM + KMR	2.50	1249	238
FM + BL exc	0.35	1249	1950
BPR + BL exc	0.46	2000	1950
	$r^{\mathrm{EXC/INC}}(25)$	$\sigma^{\mathrm{INC}}(25)$[pb]	$\sigma^{\mathrm{EXC}}(25)$[pb]
FM + KMR	1.0	7.39	3.95
FM + BL exc	0.038	7.39	108
BPR + BL exc	0.017	40.6	108

Table 5.1: Cross sections for inclusive diffractive production σ^{INC}, exclusive cross section σ^{EXC} to be rescaled with a relative additional normalization between inclusive and exclusive events $r^{\mathrm{EXC/INC}}$ for $p_T > 10\,\mathrm{GeV}$ and $p_T > 25\,\mathrm{GeV}$ jets and for different models (see text). Note that the fit to the data is parameterized as $N(\sigma^{\mathrm{INC}}(R_{JJ}) + r^{\mathrm{EXC/INC}}\sigma^{\mathrm{EXC}}(R_{JJ}))$.

in Table 5.1. We give the inclusive σ^{INC} and the exclusive cross sections σ^{EXC}, obtained directly from the models, and the relative scale factor needed to describe the CDF data to be applied to the exclusive contribution only. While the relative normalization changes as a function p_T^{min} by an order of magnitude for the exclusive BL model, it tends to be rather stable for the KMR model (the uncertainty on the factor 2.5 might be relatively large since we do not have a full simulation interface and the simulation effects tend to be higher at low jet transverse momentum). Finally, in Figures 5.8 and 5.9, the fitted distributions are depicted for $p_T^{min} = 10, 25\,\mathrm{GeV}$ jets, respectively.

The Tevatron data are well described by the combination of FM and KMR model. We attribute the deviation from the smooth distribution of the data to the imperfection of our fast simulation interface. On the contrary, the BPR model is disfavoured because it fails to describe the low R_{JJ} region. The R_{JJ} distribution is shifted towards higher values due to the β_i factor in the parton density $f_{i/\mathbb{P}}(\beta_i)$ used by the BPR model. This factor was introduced to maintain the correspondence between the inclusive and exclusive model in the limit $f_{i/\mathbb{P}}(x_i) \to \delta(x_i)$. On the contrary, this assumption leads to properties in contradiction with CDF data. Using the BPR model without this additional normalization factor leads to a DMF which is in fair agreement with data. Indeed, we show in Figure 5.10 the predictions of the "modified" model (i.e. defined as $f_{i/\mathbb{P}}(\beta_i) \equiv G_{i/\mathbb{P}}(\beta_i)$) for $p_T > 10\,\mathrm{GeV}$ and $p_T > 25\,\mathrm{GeV}$ jets. We see that the low R_{JJ} region is described well and that fitting the prediction of the exclusive KMR model with the BPR model yields roughly the same amount of exclusive events as using the factorizable models. We will not mention further this "modified" version of the BPR model since it gives similar results as the factorizable models.

The exclusive BL model leads to a quite reasonable description of the DMF shape for both p_T^{min} cuts in combination with FM. However, it fails to grasp the shape of the exclusive cross section measured as a function of the jet minimal transverse momentum p_T^{min}. To illustrate this, in Figure 5.11 we present the CDF data for exclusive cross section corrected for detector effects compared with the predictions of both exclusive models after applying the same cuts as in the CDF measurement, namely: $p_T^{jet1,2} > p_T^{min}$, $|\eta^{jet1,2}| < 2.5$, $3.6 < \eta_{gap} < 5.9$, $0.03 < \xi_{\bar{p}} < 0.08$. The BL exclusive model shows a much weaker p_T dependence than the KMR model and is in disagreement with data.

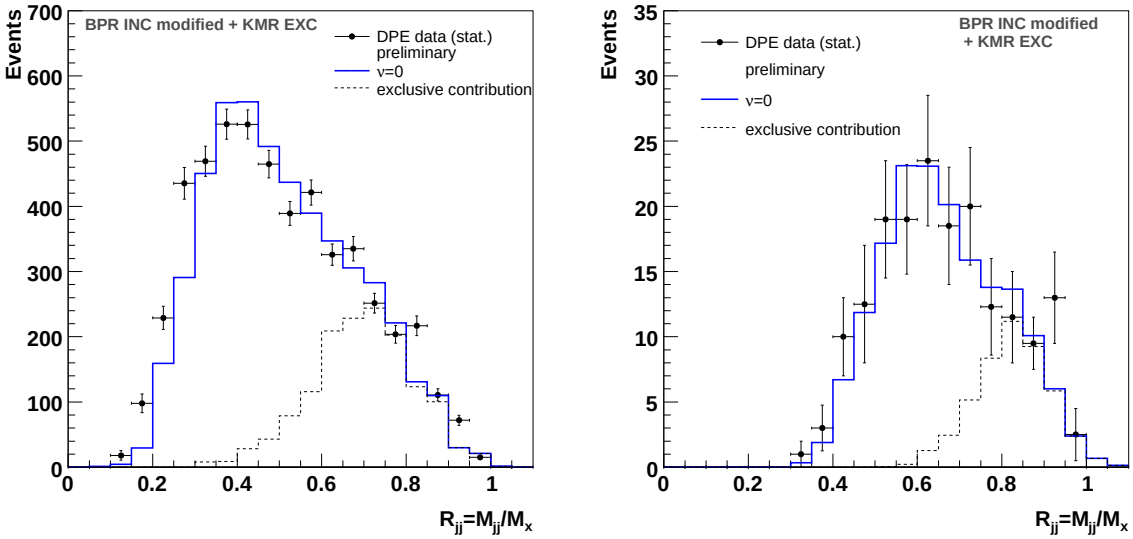

Figure 5.10: Dijet mass distribution at the Tevatron calculated with the "modified" parton densities in BPR model (see text) for 10 GeV (left) and 25 GeV (right) jets, KMR exclusive model included.

Let us note that the cross section of exclusive events measured by the CDF collaboration is an indirect measurement since it was obtained by subtracting the inclusive contribution using an older version of the gluon density in the pomeron measured at HERA. In that sense, the contribution of exclusive events using the newest gluon density from HERA might change those results. However, as we noticed, modifying the gluon density even greatly at high β by multiplying the gluon distribution by $(1-\beta)^{\nu}$ does not change the amount of exclusive events by a large factor, and thus does not modify much the indirect measurement performed by the CDF collaboration.

To finish the discussion about the pomeron like models, it is worth mentioning that these results assume that the survival probability has no strong dependence on β and ξ. If this is not the case, we cannot assume that the shape of the gluon distribution as measured at HERA could be used to make predictions at the Tevatron. However, this is a reasonable assumption since the survival probability is related to soft phenomena occurring during hadronization, effects which occur at a much longer time scale than the hard interaction.

5.2.6 Prospects of future measurements at the Tevatron

In this section, we list some examples of observables which could be used to better identify the exclusive contribution in DMF measurements at the Tevatron. We present the prediction as a function of the minimal transverse momentum of the two leading jets p_T^{min}. Since the BPR model does not describe the DMF at low R_{JJ}, we choose to show only the FM prediction in combination with both, KMR and BL exclusive models.

The same roman pot acceptance and restriction cuts as in the CDF measurement were used, specifically, $0.01 < \xi_{\bar{p}} < 0.12$, $p_T^{jet1,2} > p_T^{min}$, $|\eta^{jet1,2}| < 2.5$, $3.6 < |\eta_{gap}| < 5.9$. Moreover, we adopted a normalization between inclusive and exclusive events as obtained for the $p_T > 25\,\text{GeV}$ analysis in the previous section because we are less sensitive to the imperfections of the fast simulation interface for

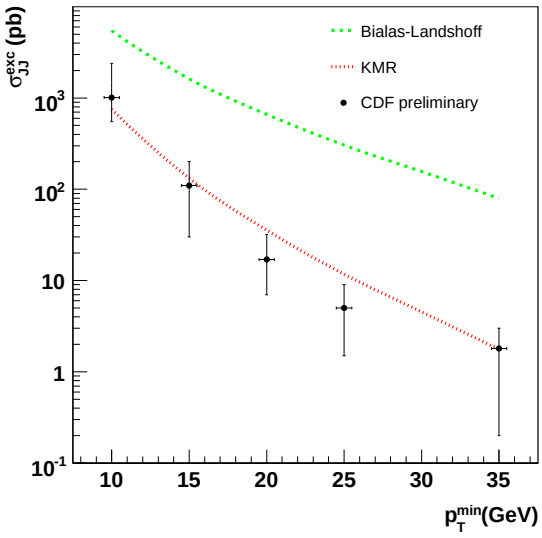

Figure 5.11: Exclusive cross section as a function of the minimal transverse jet momentum p_T^{min} measured by the CDF collaboration and compared to the prediction of the KMR and BL exclusive models. We note that the BL model overestimates the CDF measurement while the KMR model is in good agreement.

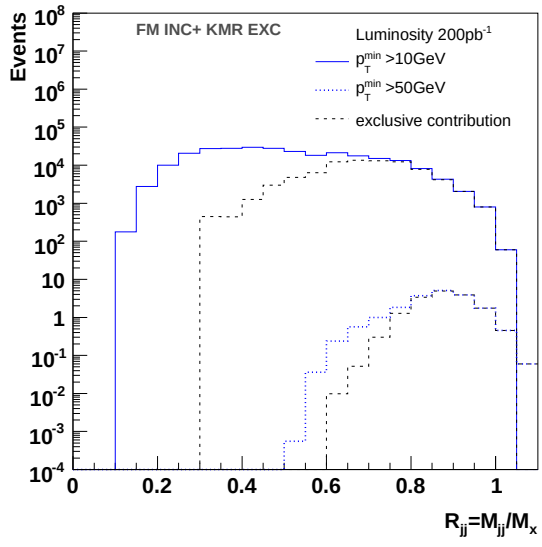

Figure 5.12: Dijet mass fraction for two values of minimal transverse jet momentum p_T^{min} at the Tevatron. We note that the relative exclusive contribution is higher at high p_T^{min}.

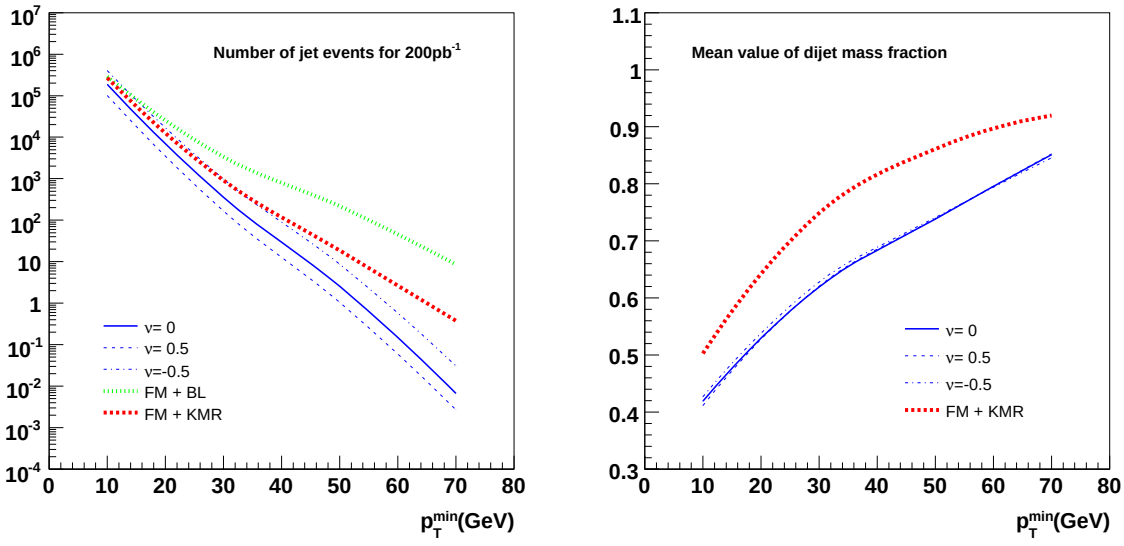

Figure 5.13: Number of jet events and mean of the dijet mass fraction as a function of the minimal jet p_T^{min}. We note that the ideal value of p_T^{min} to enhance the exclusive contribution is of the order of 30-40 GeV which leads to a high enough production cross section as well as a large effect of the exclusive contribution on the dijet mass fraction.

higher p_T jets. Figure 5.12 illustrates the DMF distribution for two separate values of minimum jet p_T^{min}. The character of the distribution is clearly governed by exclusive events at high p_T^{min}.

Figure 5.13 shows the rate of DPE events. In addition to the curves denoting the inclusive contribution with the varied gluon density for $\nu = -0.5, 0, 0.5$, the full contribution for both exclusive models is shown. For the FM model which is in better consistency with accessible data, the measurement of the DPE rate does not provide an evident separation of exclusive contribution from the effects due to the pomeron uncertainty since the noticeable difference appears when the cross sections are too low to be observable. It is possible, however, to examine the mean of the DMF distribution. As seen in Figure 5.13, this observable disentangles well the exclusive production with the highest effect between 30 and 40 GeV. It should be noted that the assumed luminosity $200\,\mathrm{pb}^{-1}$ is the effective luminosity with only one interaction per bunch crossing.

In what has been discussed so far, we assumed pomeron-like models for inclusive diffraction. The next section focuses on the prediction of a soft color interaction model in which there is no relation to the pomeron.

5.2.7 Soft color interaction model

The Soft color interaction model uses a different approach to explain diffractive events. In this model, diffraction is due to special color rearrangement in the final state as we mentioned earlier. It is worth noticing that in this model, the CDF data are dominated by events with a tagged antiproton on the $\bar{p}$ ($\eta_{\bar{p}} < 0$) side and a rapidity gap on the p side. In other words, in most of the events, there is only one single antiproton in the final state accompanied by a bunch of particles (mainly pions) flowing into the beam pipe. This is illustrated in Figure 5.14 (right) which shows the rapidity distribution of produced

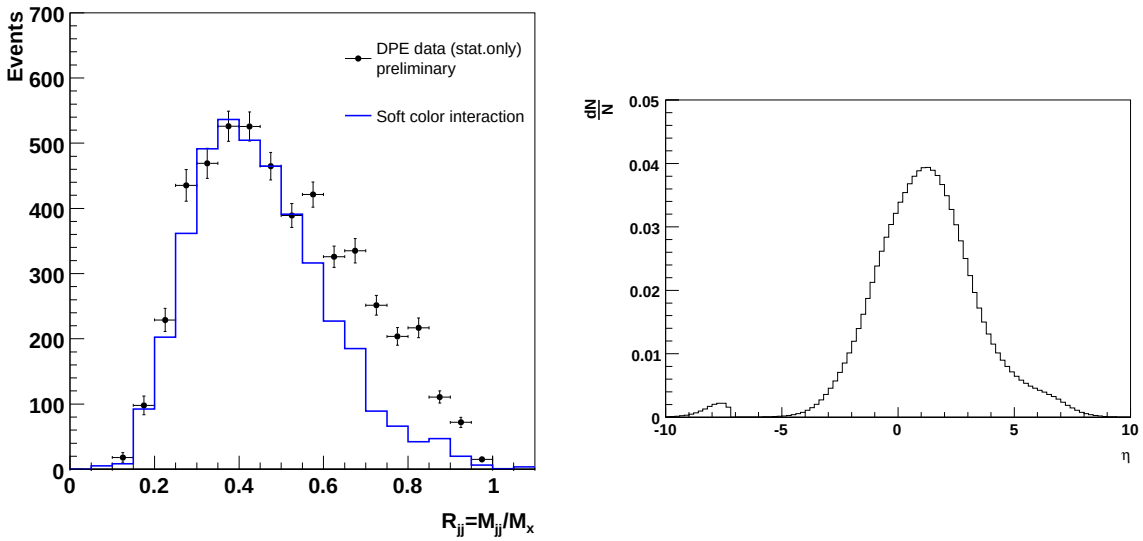

Figure 5.14: Dijet mass fraction at the Tevatron for jets $p_T > 10\,\text{GeV}$ (left) and the η distribution of produced particles (right) for the Soft color interaction model.

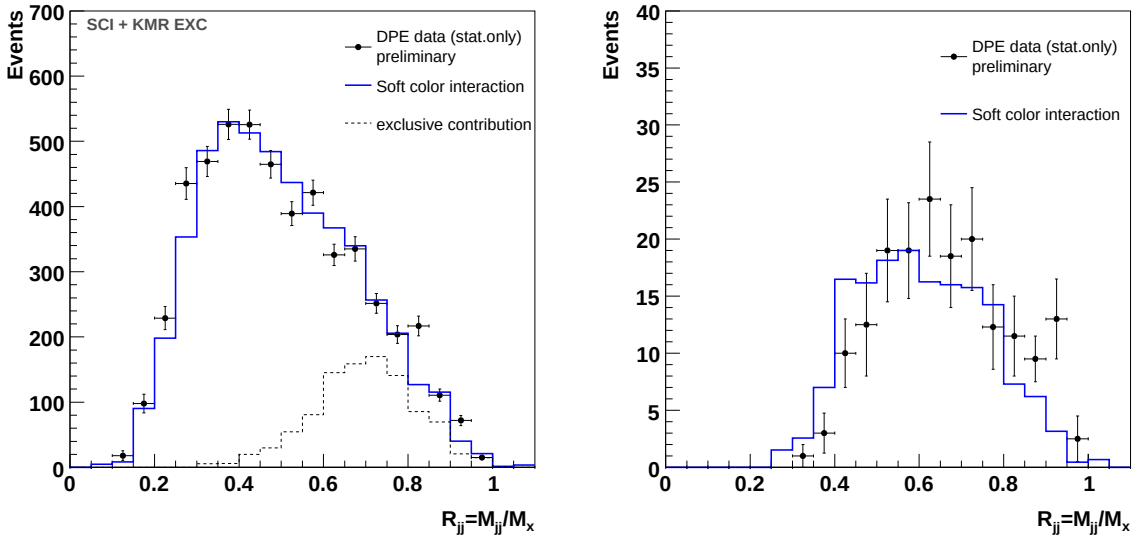

Figure 5.15: Dijet mass fraction at the Tevatron for jets $p_T > 10\,\text{GeV}$ for the SCI model and KMR exclusive model (left), and for jets $p_T > 25\,\text{GeV}$ for the SCI model only (right).

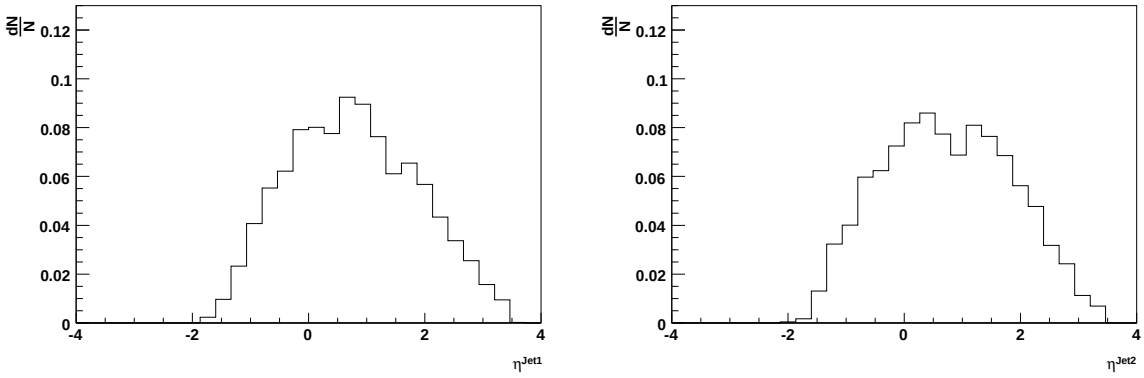

Figure 5.16: Rapidity distribution of a leading jet (left) and a second leading jet (right) in the SCI model when calculating the dijet mass fraction.

particles and we notice the tail of the distribution at high rapidity. We should not omit to mention that on the other hand, the probability to get two protons intact is extremely small. Thus, the central exclusive events with double proton tags are rare in the SCI model.

After applying all CDF cuts mentioned above, the comparison between SCI and CDF data on R_{JJ} is shown in Figures 5.14 (left) and 5.15. While it is not possible to describe the full dijet mass fraction for a jet with $p_T > 10\,\text{GeV}$, it is noticeable that the exclusive contribution is found to be lower than in the case of the pomeron inspired models. Indeed, performing the same independent fit of SCI and KMR exclusive contribution one finds that only 70 % of the exclusive contribution needed in the case of pomeron inspired models is necessary to describe the data. For jets with $p_T > 25\,\text{GeV}$, no additional exclusive contribution is needed (within uncertainties) to describe the measurement which can be seen in Figure 5.15. Most events are asymmetric in the sense that only the antiproton is strictly intact and there is a flow of particles in the beam pipe on the other side. This should influence the rapidity distribution of jets in the detector. As shown in Figure 5.16, the rapidity distribution is boosted towards high values of rapidity and not centered around zero like for pomeron inspired models and CDF data. Moreover, the cross section for $p_T > 10\,\text{GeV}$ jets is in the SCI model $\sigma^{\text{SCI}} = 167\,\text{pb}$, only about 13% of the cross section predicted by the pomeron inspired models which however give a correct prediction of a large range of observables including DPE cross sections. Therefore, such properties disfavour the SCI model. However, it would be worth to study and modify the SCI model since the probability to observe two protons in the final state (and/or two gaps) should be higher than the square probability of observing one proton (and/or one gap) only (single diffraction) as it was seen by the CDF collaboration [16]. The SCI models quite remarkably describe a whole range of ep and pp processes, both single diffractive and double pomeron exchange, if the diffractive events are selected using the rapidity gap requirement. On the other hand, it was already pointed out by the authors [12], that the model underestimates the production rates when the leading (anti)proton is tagged, which we are using in the case of DMF. In this case, the cross section is more sensitive to details in the model, such as the remnant treatment.

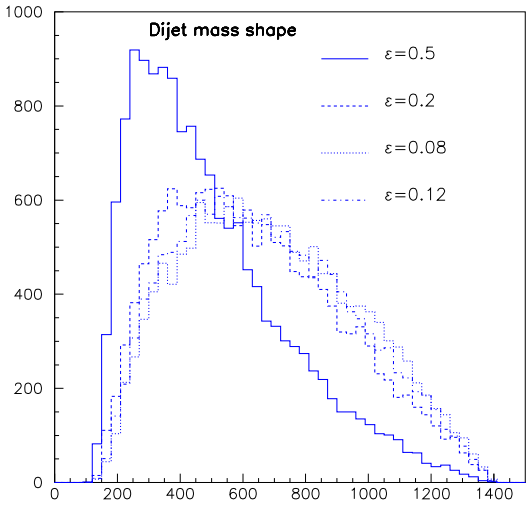

Figure 5.17: Sensitivity of the dijet mass fraction to different values of the pomeron intercept $\alpha_{\mathbb{P}} = 1+\varepsilon$. The figure shows the number of events for $p_T^{jet} > 150\,\text{GeV}$ for a luminosity $10\,\text{fb}^{-1}$.

5.3 Dijet mass fraction at the LHC

To make the predictions of the DMF at the LHC we assume that the factorization breaking between HERA and the LHC comes only from a survival probability factor which is about 3%. Since the inclusive BPR and BL exclusive models showed to be disfavored at the Tevatron, we use only the FM and KMR models. As in the previous sections, we also include a study of the uncertainty on the gluon density enhancing the high β gluon with a factor $(1-\beta)^{\nu}$. Nevertheless, new QCD fits using single diffractive or double pomeron exchange data will have to be performed to fully constrain the parton densities and the pomeron flux at the LHC.

The flux depends on the pomeron intercept $\alpha_{\mathbb{P}}$ whose impact on the DMF distribution at LHC energies is shown in Figure 5.17. The pomeron intercept is parameterized as $\alpha_{\mathbb{P}} = 1+\varepsilon$ and the prediction is made for four values of $\varepsilon = 0.5, 0.2, 0.12, 0.08$. The HERA pomeron structure function analysis [8] shows that the “hard pomeron" intercept value is close to $\alpha_{\mathbb{P}} = 1.12$.

DPE events in this analysis were selected applying the roman pot acceptance on both sides from the interaction point $0.01 < \xi < 0.1$, and using a fast simulation of the CMS detector [15] (the results would be similar using the ATLAS simulation) and asking two leading jets with $p_T >= 100, 200, 300, 400\,\text{GeV}$.

The dijet mass fraction as a function of different p_T is visible in Figure 5.18. The exclusive contribution manifests itself as an increase in the tail of the distribution which can be seen for 200 GeV jets (left) and 400 GeV jets (right), respectively in Figure 5.19. Exclusive production slowly turns on with the increase of the jet p_T which is demonstrated in Figure 5.20 where the number of expected DPE events is shown. However, with respect to the uncertainty on the gluon density this appearance is almost negligible.

The exclusive production at the LHC plays a minor role for low p_T jets. Therefore, measurements e.g for $p_T < 200\,\text{GeV}$ where the inclusive production is dominant could be used to constrain the gluon

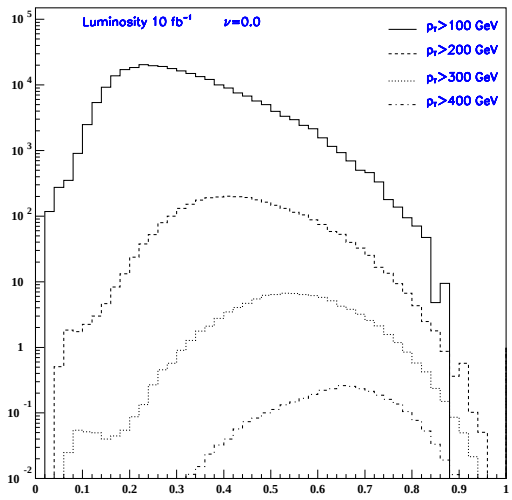

Figure 5.18: Dijet mass fraction at the LHC as a function of the jet minimal transverse momentum p_T^{min}, FM inclusive model.

density in the pomeron. Afterwards, one can look at the high p_T jet region to extract the exclusive contribution from the tail of the DMF.

5.4 Conclusion

The aim of this chapter was to investigate whether we can explain the excess of events at the high dijet mass fraction measured at the Tevatron without the exclusive production. The result is actually twofold.

Concerning the pomeron induced models ("Factorized model" and Bialas-Landshoff inclusive models) we found that the uncertainty on the high β gluon density in the pomeron has a small impact at high R_{JJ}. Therefore, an additional contribution is needed to describe the CDF data with these models. We examined the exclusive KMR model and Bialas-Landshoff exclusive model predictions for the role of the additional contribution and found that the best description of data is achieved by the combination of the Factorized inclusive model (or the modified inclusive Bialas-Landshoff one) and the KMR exclusive model. The exclusive contribution at the Tevatron can be magnified requesting higher p_T jets and studying specific observables like the mean of the dijet mass fraction, for example. Though, one of the limitations of using high p_T jets is due to the rate of DPE events which falls logarithmically allowing measurements for jets up to approximately 40 GeV. The Bialas-Landshoff exclusive model seems to be disfavoured by Tevatron data since it shows a softer jet p_T dependence and predicts unphysical large DPE rates at LHC energies.

In the case of the Soft color interaction model which is not based on pomeron exchanges, the need to introduce an additional exclusive production is less obvious. For low p_T jets the amount of exclusive events to describe the data is smaller than in case of the Factorized model, but for high p_T jets no additional contribution is necessary. This draws a new question: whether the double pomeron exchange

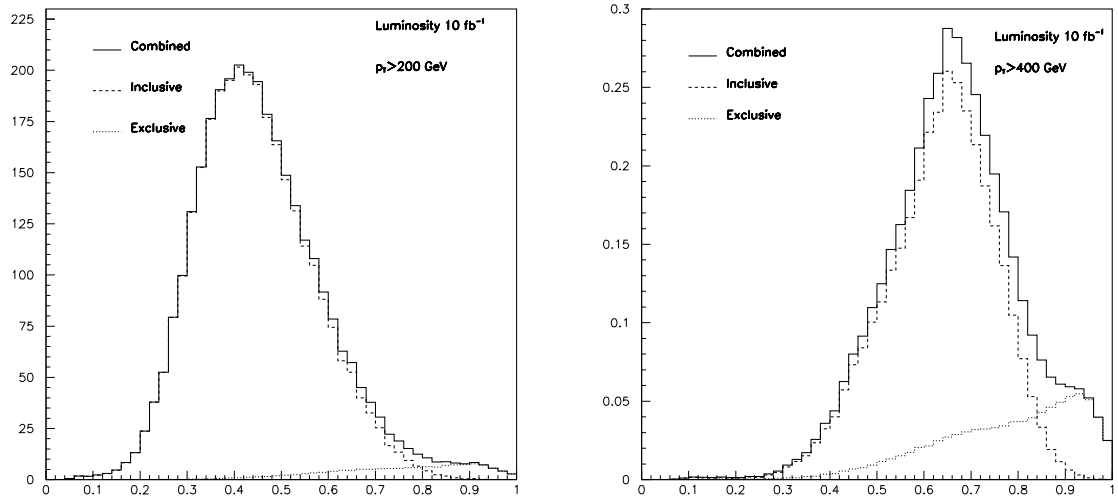

Figure 5.19: Dijet mass fraction at the LHC for jets $p_T > 200\,\text{GeV}$ and $p_T > 400\,\text{GeV}$, respectively, FM inclusive + KMR exclusive models.

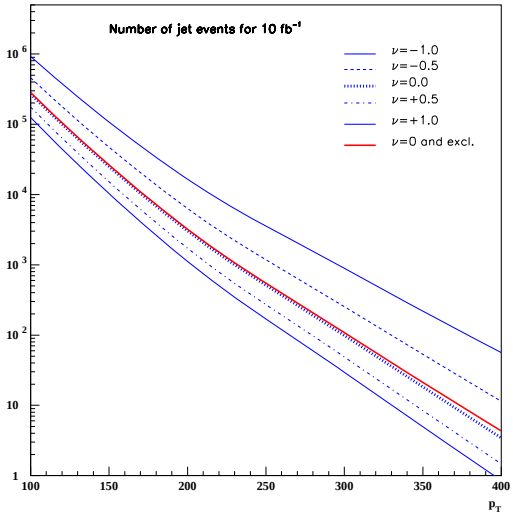

Figure 5.20: Number of DPE events at the LHC as a function of the minimal transverse momentum p_T^{min} of the two leading jets. FM inclusive + KMR exclusive models. The gluon variation is displayed for different ν values.

events could be explained by a special rearrangement of color only? When one proton is tagged, the DMF data are in this model dominated by single diffractive events. Selecting DPE in this leading proton sample with the gap requirement on the other side gives about factor 8 smaller rates than those measured by CDF. Thus, it indicates that the modeling of remnants recombination into the proton which could be tagged might not be precise and would have to be reconsidered in order to describe correctly the leading proton data at the Tevatron and perhaps also the double pomeron exchange data with the intact proton in the future at the LHC.

Bibliography

[1] O. Kepka and C. Royon, Phys. Rev. D **76** (2007) 034012 [arXiv:0704.1956 [hep-ph]].

[2] T. Aaltonen *et al.* [CDF Collaboration], Phys. Rev. D **77** (2008) 052004 [arXiv:0712.0604 [hep-ex]].

[3] M. Boonekamp and T. Kucs, Comput. Phys. Commun. **167** (2005) 217.

[4] R. Enberg, Pythia SCI Monte Carlo program, `http://www.isv.uu.se/thep/MC/scigal/`, Sept. 2009.

[5] G. Ingelman, P.E.Schlein, *Phys.Lett.* **B152** (1985) 256.

[6] M. Boonekamp, R. Peschanski, C. Royon, *Phys. Rev. Lett.* **87** (2001) 251806;
M. Boonekamp, R. Peschanski, C. Royon, *Nucl. Phys.* **B669** (2003) 277, Err-ibid **B676** (2004) 493.

[7] A. A. Affolder *et al.* [CDF Collaboration], Phys. Rev. Lett. **84** (2000) 5043.

[8] C. Royon, L. Schoeffel, S. Sapeta, R. B. Peschanski and E. Sauvan, Nucl. Phys. B **781** (2007) 1 [arXiv:hep-ph/0609291].

[9] V.A. Khoze, A.D. Martin, M.G. Ryskin, *Eur. Phys. J.* **C19** (2001) 477, Err-ibid **C20** (2001) 599;
V.A. Khoze, A.D. Martin, M.G. Ryskin, *Eur. Phys. J.* **C23** (2002) 311;
V.A. Khoze, A.D. Martin, M.G. Ryskin, *Eur. Phys. J.* **C24** (2002) 581;
V. A. Khoze, A. D. Martin and M. G. Ryskin, Eur. Phys. J. **C48** (2006) 467;
V. A. Khoze, A. D. Martin and M. G. Ryskin, Phys. Lett. B **650** (2007) 41 [arXiv:hep-ph/0702213].

[10] A. Bialas, P. V. Landshoff, *Phys. Lett.* **B256** (1990) 540;
A. Bialas, W. Szeremeta, *Phys. Lett.* **B296** (1992) 191;
A. Bialas, R. Janik, *Zeit. für. Phys.* **C62** (1994) 487.

[11] A. Bzdak, *Acta Phys. Polon.* **B35** (2004) 1733.

[12] A. Edin, G. Ingelman and J. Rathsman, Z. Phys. C **75** (1997) 57;
R. Enberg, G. Ingelman, A. Kissavos, N. Timneanu, *Phys. Rev. Lett.* **89** (2002) 081801;
R. Enberg, G. Ingelman and N. Timneanu, Phys. Rev. D **64** (2001) 114015.

[13] B. Andersson, G. Gustafson, G. Ingelman and T. Sjostrand, Phys. Rept. **97** (1983) 31.

[14] Fast simulation of the CDF and DØ detectors, SHW package.

[15] CMSIM, fast simulation of the CMS detector, CMS Collab., Technical Design Report (1997);
TOTEM Coll., Technical Design Report, CERN/LHCC/99-7;
ATLFAST, fast simulation of the ATLAS detector, ATLAS Coll., Technical Design Report, CERN/LHC C/99-14.

[16] CDF Coll., *Phys. Rev. Lett.* **91** (2003) 011802.

ATLAS Forward Proton Detectors and Alignment

6

The forward physics program of the ATLAS experiment will be remarkably broadened when FP220 and FP420 proton tagging detectors are installed 220 m and 420 m from the ATLAS interaction point (IP), in addition to the existing LUCID, ZDC and ALFA detectors which were discussed in Section 3.3. In fact, physics applications of the AFP (ATLAS Forward Proton) detectors consisting of FP220 and FP420 is orthogonal to that of the already existing forward detectors. The aim is to detect scattered protons originating in soft and hard diffractive, and exclusive processes. In this chapter, we discuss the forward detectors which are proposed as an upgrade of the ATLAS central detector. First, the main physics motivations for the new detectors are given, followed by some details on the detector system and proton tracking through the LHC beam line. The central part of the chapter describes the results of our work on the investigation of the alignment and calibration method of FP220 using two-photon dimuon events detected in the central detector.

6.1 AFP principal and physics application

The AFP detectors use the LHC magnet optics as a giant spectrometer. A proton which loses a small amount of energy at the IP is deflected at small angle, moves slower than the LHC bunches, and is consequently transported by the LHC optics outside the beam envelope. The AFP detectors consist of four independent stations installed at 220 m and 420 m on either side of the ATLAS detector. Each of them houses several layers of 3D silicon detectors used to reconstruct both position and angle of the protons tracks, and timing detectors measuring the time of the proton arrival. By inverting the proton transport through the LHC magnetic field, the measured proton track information is used to reconstruct the kinematics of the scattered proton at the interaction point. The kinematic variables are: the fractional momentum loss

$$\xi = \frac{|\vec{p}_b| - |\vec{p}|}{|\vec{p}_b|} \tag{6.1}$$

the momentum transfer square

$$t = (p_b - p)^2 \approx -p_T^2 \tag{6.2}$$

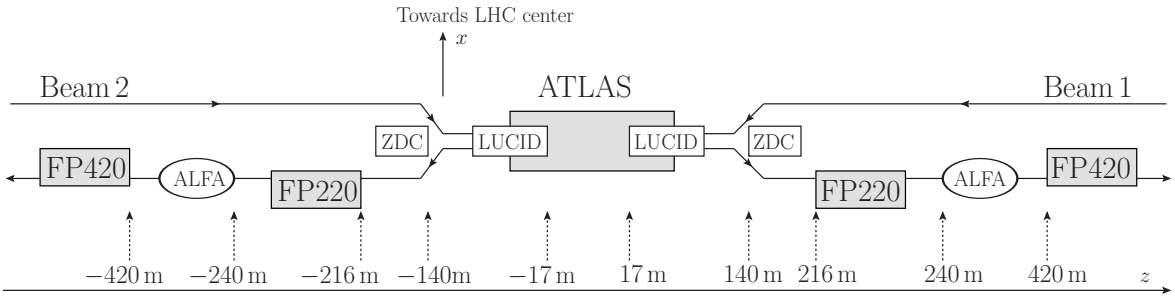

Figure 6.1: Layout of AFP detectors: FP220 and FP420 placed at 216 m and 420 m from the ATLAS nominal beam crossing point. Other ATLAS forward detectors are shown: LUCID installed 17 m and ALFA located 240 m from the ATLAS IP.

of the scattered proton (p_b is the four-momentum of the beam protons) which is to a good approximation proportional to the squared proton transverse momentum when ξ is small, and the polar angle

$$\cos\phi = p_x/p_T \tag{6.3}$$

In the processes with two intact scattered protons, the reconstructed fractional momentum losses ξ_1, ξ_2 measured in the forward AFP detectors on positive and negative sides of ATLAS determine the diffractive mass W. With the so called missing mass method we have a relation

$$W = \sqrt{s\xi_1\xi_2} \tag{6.4}$$

where $\sqrt{s} = 14\,\text{TeV}$ is the center-of-mass beam energy which holds in the limit $W \gg m_p$ when the proton mass can be neglected. The acceptances of the forward detectors in terms of these variables are approximately $0.002 < \xi < 0.02$ for the FP420 station and $0.01 < \xi < 0.2$ for the closer FP220. This implies a wide acceptance on the mass of the central object spanning from $\sim 80\,\text{GeV}$ up to masses beyond 1 TeV. The t coverage is up to several GeV^2. The exact acceptance depends on the closest approach of the active detectors to the beam. It also depends on the position and apertures of the machine collimator elements, which are designed to capture scattered non-beam protons to prevent superconducting magnets from quenching. As a consequence, they may also absorb part of the scattered diffractive protons coming from the interaction point.

There are two units with active detectors for each detector station: for FP220 at $s = 216\,\text{m}$ and $s = 224\,\text{m}$, and for FP420 at $s = 420\,\text{m}$ and $s = 424\,\text{m}$ from the interaction point, for both beam 1 and 2. Beam 1 circulates clock-wise in the direction from IP 1 to IP2. Beam 2 circulates in opposite direction from IP1 to IP 8. The particular choice of the detector positions was constrained by the actual available space in the tunnel and was optimized in the detector acceptance for protons coming from diffractive and exclusive events. The detector station layout is depicted in Figure 6.1, where other forward detectors of ATLAS are shown as well.

6.1.1 Trigger system

The detector performance depends on the capability of triggering on the interesting events. The trigger can be successfully implemented at FP220 by grouping together a defined number of subsequent silicon strips with a very fast readout and sending it to the central Level 1 trigger processor of ATLAS. Since the

L1 trigger decision has to be made within 2.5 μs and all the information from the detector subsystems has to be collected within 1.9 μs from the time of the collision, it is impossible to include the hit information from the FP420 detector. The time needed for light to travel from the IP to the FP420 forward detector and back is 2.8 μs. However, to trigger on events of desired missing mass, it is possible to cut on ξ_1 from FP220 at L1 asking ξ_2 to be in FP420 acceptance and using formula (6.4). For High Level Triggers, the information from both FP220 and FP420 can be used since the L2 decision is taken within 40 ms.

6.1.2 Timing detectors

Proton tagging is not a new technique. It has already been successfully operated by previous experiments UA8, and CDF in hadron-hadron collisions and by H1 in electron-proton scattering. What is novel at the LHC is the high number of multiple interactions which will occur at the same time. Contrary to the current experiments, it is not sufficient to simply select events with exactly one reconstructed vertex for forward physics studies because the probability to have just one collision occurring in the bunch crossing is small at high LHC luminosities. Moreover, due to multiple interactions (up to 32 multiple interactions per bunch crossing can be present, see Section 3.1.2) a fake signal-like event can be registered in which non-diffractive events are overlaid with two soft single diffractive events leaving hits in the forward detectors. Those events represent a background for forward physics studies and must be rejected.

The method to reject overlap events is to verify that the detected protons originated in the same vertex as the system observed in the central detector. This is done by measuring the proton arrival time at the forward detectors. Scattered protons move almost at the speed of light and the position of the vertex is then essentially given by the time difference between the proton hits on both sides of the AFP timing detectors. Combining this information from the reconstructed vertex in the inner detector, the contribution of the overlaid background can be greatly reduced (for instance, the trigger of the dijet background to the central exclusive production of Higgs boson decaying $H \to b\bar{b}$ can be reduced by a factor of 40).

It should be noted, however, that even a femtosecond timing cannot remove the overlaid background completely. There is always a small contribution due to the large size of the LHC bunches in longitudinal direction $\sim 20-30$ cm. Two interactions might occur during the bunch crossing at exactly the same position: first when the two bunches meet head-on and second, in the tail of the bunches when bunches are about to separate. Since the time of the interaction is not known, this type of overlaid background is indistinguishable. The timing of the interaction would be needed to remove that background.

6.1.3 Application

The physics which can be studied using forward detectors was essentially summarized in Chapter 2. It covers single diffraction and double pomeron exchanges, the measurement of the diffractive structure function, and the investigation of the factorization breaking in diffractive and exclusive events. The central exclusive production of Higgs boson in the Standard Model or in Super Symmetric Models (Section 2.15) are leading processes of interest, but also the two-photon and pomeron-photon physics makes an important part of the program. A complete summary of the forward physics at the LHC with the proton taggers is described in [1].

6.1.4 Project status

A proposal in form of a LOI (Letter Of Intent) has been presented to the ATLAS community in Feb. 2009. The ATLAS decision to accept the detectors will be taken in October 2009.

6.2 Experimental system

The detector instrumentation in the FP220 and FP420 stations is essentially the same. However, the integration of the stations in the vicinity of the beam pipes requires a completely new approach at 420 m. The LHC elements (dispersion suppressors and arc elements) are placed in a continuous cryostat from the Q7 quadrupole installed 270 m downstream from the IP, all the way to the Q7 quadrupole of the next IP. At about 420 m from the IP, there is a free drift space, but the cold-beam pipes and other cryogenic equipments are contained in the so called Connection Cryostat (CC) about 14 m long, and the installation of the near-beam detectors is not possible. A New Connection Cryostat (NCC) was therefore developed to replace the (CC) which provides a warm beam-pipe section and a cryogenic bypass. The passage of the cryogenic lines was arranged to be as far away as possible to leave adequate space for the near-beam detectors.

At 220 m, the installation is relatively simple, since the beam pipes are warm and can be accessed without further difficulties.

6.2.1 Hamburg beam pipe

Because of the limited available space at 420 m due to the cryogenic bypass, the traditional Roman Pot technique cannot be used. Moreover, as it will be shown below, the scattered protons from diffractive and exclusive events are deflected inward the LHC ring, and the active detectors have to be placed in a limited space between the two beam pipes (the nominal distance between the beam pipe axes is 194 mm, and their radius is 5.4 cm).

A new concept of the detector integration in the so called moving beam pipe pioneered at DESY [1] is therefore adopted. The sensitive detectors are mounted directly on the beam pipe at two rectangular pockets. The ends of the moving beam pipe are connect to the fixed beam pipes by a set of bellows, allowing the displacement of the detectors between data taking and parked positions. Since the moving beam pipe operates on open air without the requirement of a vacuum, the mechanical and optical control of the actual detector position can be implemented. The system integration in one detector unit for FP420 is shown in Figure 6.2.

In addition, the same integration within the moving beam pipe, but without the need of cryogenic bypass and the NCC (shown below the support table and on the side of the beam pipe in Figure 6.2) is used for FP220.

6.2.2 Silicon detectors

In order to detect protons originating from the IP and to get a good acceptance for masses around $\approx 100\,\mathrm{GeV}$, the detector edge at 420 m has to approach the beam axis as close as 5 mm. At 220 m, the expected detector approach is 2-3 mm. Aiming to operate at the highest LHC luminosities, one of the important requirements on the detector performance is therefore their radiation hardness.

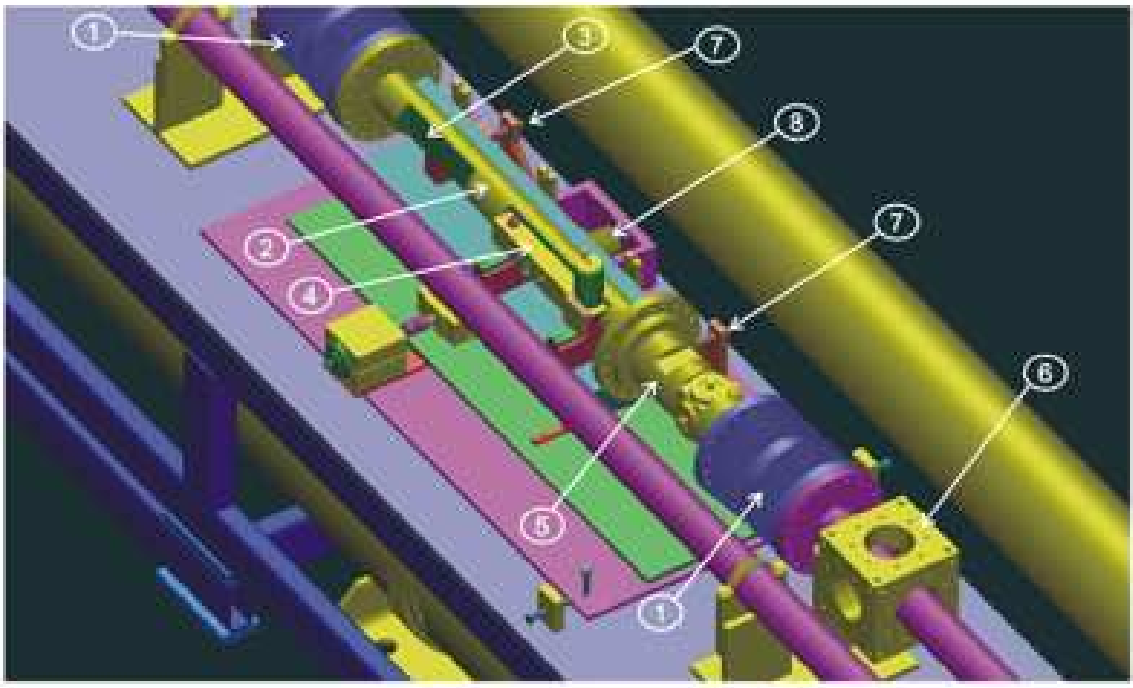

Figure 6.2: Top view of one detector unit. Bellows (1) connect the fixed beam pipe to the moving beam pipe (2). Pockets (3) and (4) house the 3D silicon and timing detectors. Two Beam Position Monitors are installed: (5) moving BPM and (6) fixed BPM. In addition, the position measurement (7) and emergency spring systems (8) are shown.

The second requirement is related to the desired mass resolution. It was found that the proton track position and angle has to be measured with the precision of $10\,\mu$m and $2\,\mu$rad in the horizontal direction at FP420 in order to obtain a resolution of 3-5 GeV for a range of missing mass $40 < W < 250\,$GeV when both FP220 and FP420 detectors are used. Since two tracking stations are 8 m and 4 m apart at 220 m and 420 m respectively, a detector resolution of $10\,\mu$m is also required for the good track angular reconstruction.

The proton tracks are measured by the 3D silicon detectors which fulfil the above mentioned criteria. Micro-machining techniques allow to cross the detector thickness with narrow (5-25 μm) holes orthogonal to the surface, spaced by $50\,\mu$m, and filled with *p* or *n*-type conducting media, in order to produce a transverse electric field. Particle passing between these electrods excite electrons. The typical small inter-electrode distance allows a fast charge collection and implies the radiation hardness of the detector. Another advantage of the 3D silicon technology is that similar micro-machining techniques allow to produce edges where the amount of dead silicon is significantly reduced. This is an important point since the active parts of the detectors have to be as close as possible to the beam. The active detector area is $25 \times 5\,$mm at FP420 and $20 \times 20\,$mm at FP220.

We also mentioned that a new radiation hard readout front-end electronics was developed to be placed directly under the 3D silicon sensors.

6.2.3 Timing detectors

Timing detectors are an important part of the forward detector used to reject protons which come from overlap events. They are composed of a radiator in which the Čerenkov light is produced by the passing proton, and a device which collects and amplifies the produced light signal. The micro-channel plate tubes (MCP-PMT) represent a compact new technique to detect the Čerenkov light with a large gain and 5 ps time resolution on the photon arrival time. Two time-of-flight counter techniques are being considered for AFP. In GASTOF (Gas Time Of Flight), the light is produced in a gas radiator C_4F_8O, pressured at 1.3 bar. A thin concave mirror at the back reflects the light to a MCP-PMT. On the other hand, artificial quartz bars are used as radiators in the so called QUARTIC detectors. Using GASTOF and QUARTIC is complementary, and therefore both timing detectors are planned to be used in each detector station. However, it must be kept in mind that the time measurement using the QUARTIC is a destructive for the proton.

6.2.4 Detector alignment system

In addition to a good precise detector resolution, it is necessary to have also a reliable online monitoring system to control the detector position with respect to the beam. Each forward detector unit will be equipped with two sets of Beam Position Monitors (BPM). Two of them will be mounted on the fixed beam pipe, and the other two will be attached directly on the movable pipe.

To determine the detector position with respect to the beam, the measured beam position by BPMs will be transfered to the detector by measuring the distances of the BPMs and the detector with respect to an alignment wire stretched along the whole system at each station unit. A special Wire Positioning Sensor (WPS) can measure this distance with a sub-micron precision.

The largest uncertainty on the alignment using BPMs comes from the temperature dependence whose systematic error was estimated to be $\sim 15-20\,\mu$m. Studying the in-situ BPM performance and performing cross calibrations between surrounding BPMs might help to reduce the alignment systematics.

6.3 Particle transport in the beam line

After the description of the forward detector systems, we focus on the particle transport inside the LHC magnetic elements which is needed to obtain the proton hits in the detector station downstream from the IP. First, the beam parameters like emittance, beam width, etc. are discussed, and then proton hits from physics processes are shown. We focus mainly on the FP220 detectors.

Particle motion around a closed orbit is called betatron motion. The particle motion is described in a Frenet-Serret coordinate system which is an orthonormal curvilinear right handed coordinate system $(\vec{x}, \vec{y}, \vec{s})$ at each point of the reference orbit. The local $\vec{s}$ axis is the tangent of the reference orbit pointing in the particle velocity. The two other axes are perpendicular to the reference orbit: $\vec{x}$ lies in the bend plane and points outwards from the center of the ring, and $\vec{y}$ is perpendicular to the bend plane and form the right-handed system with the other vectors.

The particle kinematics is determined by its horizontal and vertical positions $[x, y]$ with respect to the reference orbit, and by the gradients x', y' in $\vec{x}$ and $\vec{y}$ directions. The particle trajectory in magnetic elements of the beam lattice is described by Hamilton's equations of motion. A very profound discus-

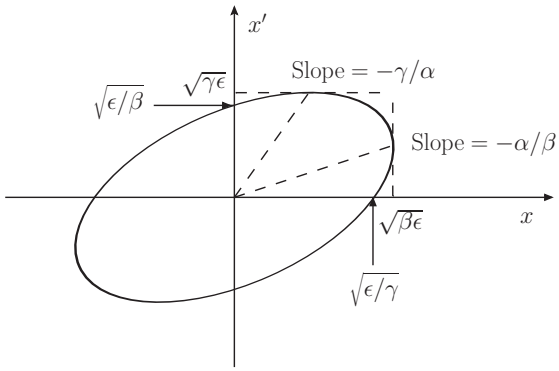

Figure 6.3: The Courant-Snyder invariant ellipse. The area enclosed by the ellipse is equal to $\pi\varepsilon$, where ε is the emittance. α, β, and γ are betatron amplitude functions. The maximum spacial amplitude of betatron motion is $\sqrt{\beta\varepsilon}$, and the maximum transverse beam divergence is $\sqrt{\gamma\varepsilon}$. The same ellipse can be drawn for the y, y' phase space [2].

sion of the accelerator physics can be found in [2]; here only the most important points necessary to understand the particle transport in the beam line are presented.

The main beam lattice elements are dipole and quadrupole magnets, even though many other optical elements exist that help to correct the beam trajectory and focus beams in the interaction points of the experiments.

- Dipole magnets have a magnetic field perpendicular to the beam particle direction and are used to guide charged particles along a desired orbit. From the Lorentz force law, the bending angle θ between the positions s_1 and s_2 inside a magnetic field B is given by

$$\theta = \frac{e}{p_0} \int_{s_1}^{s_2} B \cdot \mathrm{d}l \tag{6.5}$$

  for a particle of positive charge e having a momentum p_0.

- Quadrupole magnets are used to focus/defocus the beam (i.e. change the transverse size of the bunches). The magnetic field inside a quadrupole magnet is such that if the beam is being focused in the x direction, it is being defocused in the y direction at the same time. Particle bunches are therefore carried around the ring, being periodically focused and defocused in the horizontal and vertical planes.

6.3.1 Emittance

If the accelerator is composed of linear elements such as dipoles and quadrupoles, the beam space and momentum phase space occupied by the particles of the beam are constant. The size of the phase space is called emittance and it is an important parameter of the accelerator. Dipole and quadrupole magnets can focus and defocus the beam and change either the space or momentum distribution of beam particles, but cannot change the emittance which is conserved as a consequence of the Liouville's theorem. To adjust the emittance, special techniques like radiation damping or stochastic cooling have to be used.

6.3.2 Beam width

The beam particle evolution in the phase space is characterized by the Courant-Snyder ellipse whose shape changes from point to point around the reference orbit, but whose area is fixed and equal to the emittance. Betatron amplitude functions $\alpha(s)$, $\beta(s)$, $\gamma(s)$ characterize the solution of the equation of motion in the beam lattice, and determine the maximum spacial amplitude of the betatron motion $\sqrt{\beta\varepsilon}$ and the maximum (angular) divergence $\sqrt{\gamma\varepsilon}$, see Figure 6.3. Since $\gamma = (1+\alpha^2)/\beta$ holds for the solution, the transverse beam divergence is smaller at a location with a large $\beta(s)$ value, i.e. when particles travel in parallel paths. The term β^* means a value of the $\beta(s)$ function at the interaction point. It is usually used to define the beam lattice parameters as required by the LHC experiments. As mentioned, the large β^* optics means small divergence of the beam enabling forward experiments like TOTEM and ALFA to detect scattered protons at very small angles with near-beam detectors. The nominal running β^* is small 0.55 m [3] in order to reduce the transverse size of the beam as much as possible and thus achieve the highest luminosities (see also (3.1)).

The normalized emittance ε_n is sometimes used instead of the emittance. They are related by

$$\varepsilon_n = \gamma_r \beta_r \varepsilon \tag{6.6}$$

where γ_r, β_r are the usual Lorentz relativistic variables (and they are not related to the betatron amplitude functions). In order to reach the nominal luminosity of $\mathscr{L} = 10^{34}\,\mathrm{cm}^{-2}\mathrm{s}^{-1}$ with $\beta^* = 0.55\,\mathrm{m}$, the normalized emittance must be $\varepsilon_n = 3.75\,\mu\mathrm{m}$ with the number of bunches 2808, each having 1.15×10^{11} of protons [3].

The beam particles execute a betatron motion around an ideal closed orbit which passes through the centers of LHC magnets. Since the beam bunch has a finite size, its constituent particles have their own slightly different orbits. Also, a particle with a momentum p different from the nominal beam has its own off-momentum closed orbit, $D(s)\delta$, where $D(s)$ is the dispersion function at position s and $\delta = (p-p_b)/p_b$ is the fractional momentum deviation. The fractional momentum deviation depends on the beam preparation and the value is $\delta = 1.1\times10^{-4}$ for the LHC. If the dispersion function is large at certain position, the transverse size of the beam is determined not only by the betatron function $\beta(s)$, but also the dispersion has to be taken into account. In this general case, the beam envelope is calculated as

$$\sigma^2(s) = \sigma_b^2(s) + \sigma_d^2(s) \equiv \beta(s)\varepsilon + (D(s)\delta)^2 \tag{6.7}$$

where σ_b and σ_d are the maximum amplitudes of the bunch particles due to betatron motion and the particle space deviation due to the momentum spread.

6.3.3 Mad-X project

Mad-X (Methodical Accelerator Design) [4] is a computer program which implements all the beam magnetic elements as installed in the LHC tunnel and calculates the charged particle trajectories along the ring. The user has to provide a corresponding magnet layout which can be obtained from the LHC beam division and the beam parameters among which the most important ones are the beam emittance, the number of bunches per beam, the number of protons in a bunch and of course the beam energy. Particle position and momentum, betatron functions, beam dispersions, etc. can be obtained at desired observations points.

The optics of the LHC can be used in two different modes, thin and thick. In the thick optics mode, the particle is tracked through the optics lenses taking into account the element size and magnetic inhomogeneities inside the magnets. In the thin optics mode, an approximation is made. The effect of the magnet is applied only at the center of the magnets. The thin optics approximation works well if particle deviations from the ideal orbit are small. In the following, we use the version of the thin optics V6.500 and compare it with the thick optics V6.500 occasionally.

Comparisons of the thin and thick optics in Mad-X of the proton tracks at 220 m from the IP for both beams are shown in Figure 6.4 for the horizontal displacement x and slopes θ_x, and in Figure 6.5 for the vertical displacement y and slope θ_y. The difference between both optics is apparent for beam 1, whereas the thin optics well approximate the particle transport for beam 2. The difference is mainly pronounced in track angles. In fact, from Figure 6.4 we observe that already for small angles at the IP, the particle tracks at FP220 have an opposite orientation in the two approaches (the track points outwards in thick optics, but points inwards when using the thin optics). The difference grows with the initial scattering angle θ at the IP. On the other hand, the track position is not much affected. We also note that the same comparison was done for another tracking program called FPTrack [5]. It agrees very precisely with the predictions based on the thick Mad-X optics.

Although it will be necessary to have as precise simulation of the LHC beam lattice as possible for the real data analysis, the moderate differences of the simulation do not play a significant role for the design of the forward detectors and the alignment discussed below. The thin optics will be used predominantly here since it was the only code available to us at that time.

It is interesting to note that the deviation of the diffractive proton is basically provided by two dipole elements which separate beam 1 and beam 2 from each other at 140 m from the interaction point. Protons which have zero t and some non-zero ξ would travel in the beam lattice composed of quadrupoles only along the straight line and would not be deviated outside the beam envelope.

6.3.4 Diffractive proton hits in FP220

Let us investigate the track hits in the forward detectors created by the diffractive protons characterized by a fractional momentum loss ξ, a momentum transfer t, and by an azimuthal angle ϕ. The protons are transported from the position (x_0, y_0, z_0) of the ATLAS IP to the detector positions at 216 m and 224 m. In Figure 6.6 (left), the proton hits in FP220 are shown for beam 1 in steps of ξ, for two values of $t = 0, -0.05\,\mathrm{GeV}^2$, and several azimuthal angles ϕ. The displacement in horizontal and vertical direction is measured from the position of the beam which has coordinates $[0, 0]$. The hit pattern follows a horizontal and vertical displacement in the transverse plane. The horizontal coordinate is more sensitive to ξ than the vertical one. Proton hits in the second station are shifted and the track angle can be measured.

Note that the deviation of the physics protons is in positive x direction. From the definition of the Frenet-Serret coordinate system, it follows that the positive axis points outwards of the LHC ring. As shown in the AFP layout Figure 6.1, beam 1 is the outer beam pipe. Hence the diffractive protons scatter outside from the two beams. This is important since protons can be detected by installing active detectors in the free space at the side of the beam line.

The same scatter diagram is shown again in Figure 6.6 (right) comparing thick and thin optics trackings. The difference is small, but it increases as the scattered protons lose more energy characterized by larger ξ and travel farther from the ideal orbit tuned for beam particles.

For beam 2 the diffractive hit pattern is similar. Diffractive protons scatter also outwards. As shown

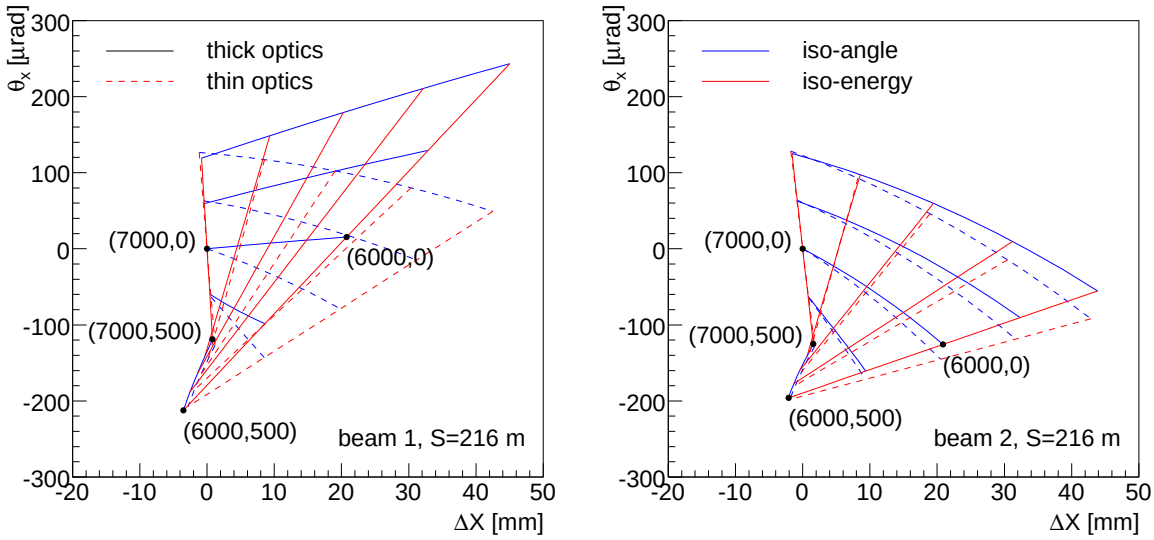

Figure 6.4: Comparison of thick (full line) and thin optics (dashed) in Mad-X for the proton displacement and slope in x direction at 216 m from the IP and for beam 1 (left) and beam 2 (right). Numbers in parentheses (E, θ_x) denote the initial scattered proton energy and scattering angle in x. Lines running vertically correspond to the protons with the same initial angle (iso-angle), whereas the horizontal ones denote protons of the same energy (iso-energy).

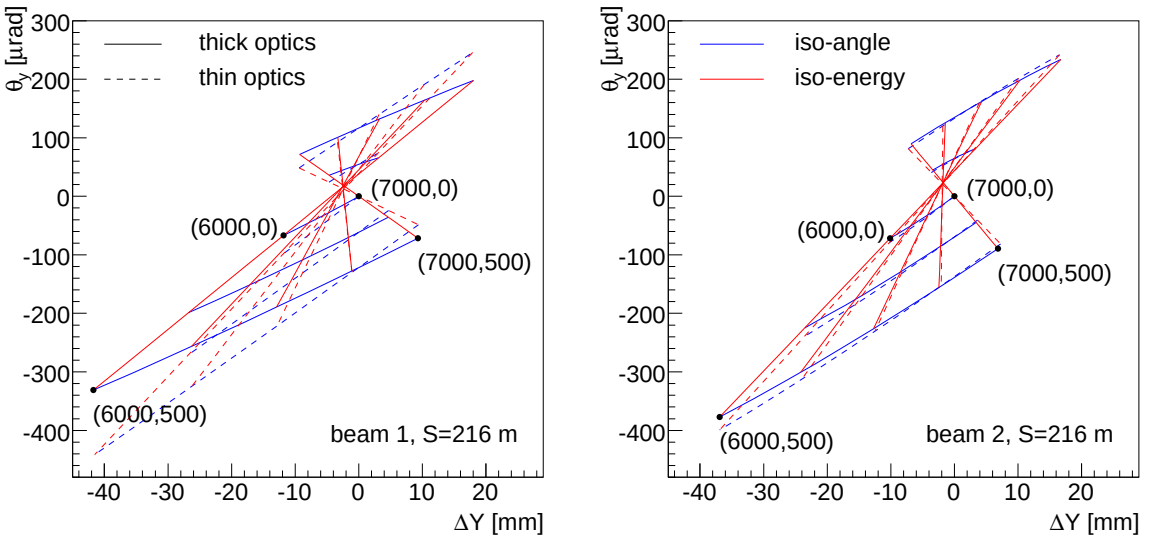

Figure 6.5: Comparison of thick (full line) and thin optics (dashed) in Mad-X for the proton displacement and slope in y direction at 216 m from the IP for beam 1 (left) and beam 2 (right). Numbers in parentheses (E, θ_y) denote the initial scattered proton energy and scattering angle in y. Lines running vertically correspond to the protons with the same initial angle (iso-angle), whereas the horizontal ones denote protons of the same energy (iso-energy).

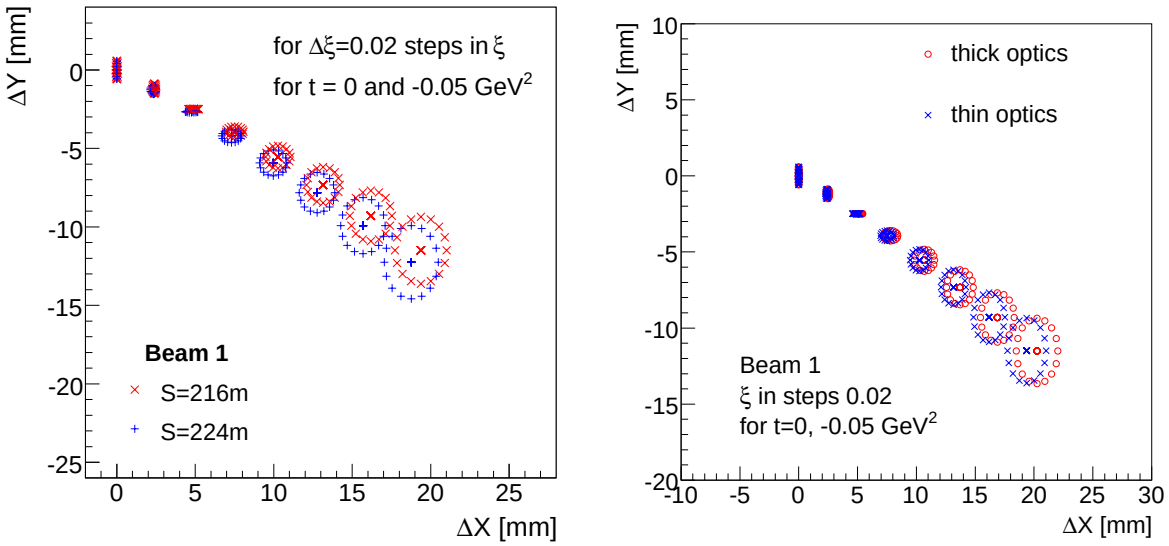

Figure 6.6: Hits of diffractive protons at the FP220 detector for ξ in steps of $\Delta\xi = 0.02$ and for $t = 0, -0.05\,\mathrm{GeV}^2$ with a ϕ dependence creating circles in the $X \times Y$ transverse plane (courtesy of A. Kupčo) (left). Comparison of thin and thick Mad-X optics for diffractive proton hits at $s = 216\,\mathrm{m}$ (right).

in Figure 6.6, the range of the fractional momentum loss up to $\xi = 0.14$ is covered with detectors which have a small area of $2 \times 2\,\mathrm{cm}$ as previously mentioned. Even such small detectors can give an acceptance to events with high fractional momentum losses.

6.3.5 Diffractive proton hits in FP420

The difference between FP220 and FP420 positions is illustrated in Figure 6.7 where the hit pattern is shown for two-photon dimuon events. Due to the beam focusing by the quadrupole magnets, particles deflect inwards at 420 m between the two beam pipes, where the detectors have to be placed in a limited space (14 cm). The small overlap between the stations at FP220 and FP420 is visible for tracks with x coordinate $x < -20\,\mathrm{mm}$.

6.3.6 Beam parameters at FP220 and FP420

The closest possible approach of the detectors to the beam is given by the safety considerations of the machine. It is determined in terms of the beam width. As we have seen, the diffractive protons are deflected in the horizontal direction mainly. In Table 6.1 the betatron $\beta(s)$ and dispersion $D(s)$ functions are given and the corresponding beam width is calculated according to formula (6.7).

The beam optics of beam 1 and 2 are very similar as they yield alike betatron functions. The FP220 and FP420 positions are, however, quite different. The beam can be up to ~ 15 (depending on the exact position) times wider in x direction at FP420 than at FP220. The momentum dispersion impact on the beam size at FP220 is only about 10% of the maximum betatron amplitude and it is often neglected. At FP420 on the other hand, the dispersion gives a non-negligible contribution to the beam spacial distribution.

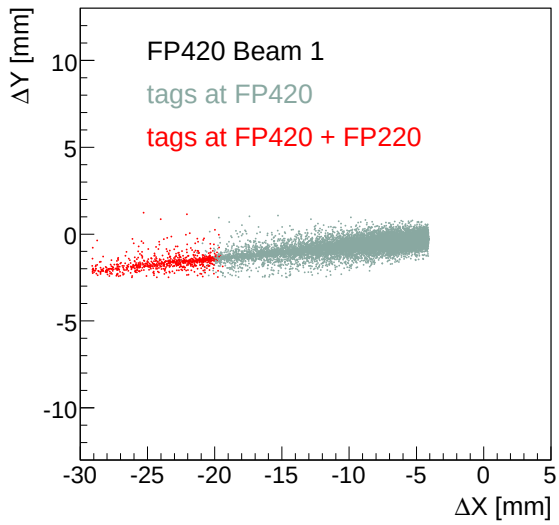

Figure 6.7: Proton hits from two-photon dimuon events with $p_T^{\mu} > 8\,\text{GeV}$ at FP420 for beam 1. The detector was placed at 4 mm from the beam at FP420 and 1.5 mm from the beam at FP220. The small overlap is visible for events which arrive at distances $|\Delta X| > 20\,\text{mm}$.

From the physics point of view, the closer the approach to the beam, the better is the acceptance for diffractive and exclusive events. This is always in competition with the machine safety requirements which do not allow devices to be placed too close in order not to disrupt the beam operation. The generally considered safe distance at which detectors can be installed is [6]

$$d = 2 \cdot \sigma_d + 15 \cdot \sigma_b \tag{6.8}$$

It is useful to remember that at FP220 this requirement means a real distance of 1.5 mm and 1.9 mm for beam 1 and 2, respectively. For FP420, the allowed operation distance is about 4.2 mm. We must note, however, that these approaches do not determine the effective acceptance, since some space has to be accounted for a thin metal window in the moving beam pipe pockets ($\sim 500\,\mu$m) and also a thermal safety offset for 3D silicon detector installation inside the pocket (few hundreds of microns).

6.3.7 Detector acceptance

The impact of the detector positions on the missing mass acceptance is shown in Figure 6.8 for two cases. On the left, the acceptance for double tagged events in FP420 on either side of ATLAS illustrates that if the detectors are operated as close as 5 mm from the beam, the acceptance on missing mass $W = \sqrt{s\xi_1\xi_2} > 100\,\text{GeV}$ is not degraded. On the right side, the missing mass acceptance is shown for coincidences in FP220 and FP420 detectors. For low masses of the SM Higgs boson mass $\sim 120\,\text{GeV}$, the acceptance drops quickly as a function of the closest approach of the FP220 detector. Therefore it is desirable to place the detector as close as possible to the beam (if there is no QUARTIC timing detector which would destroy the protons).

Beam 1:				
$s = 216\,\mathrm{m}$	$\beta_x = 18.4\,\mathrm{m}$	$D_x = -0.11\,\mathrm{m}$	$\sigma_b = 96.2\,\mu\mathrm{m}$	$\sigma_d = 12.1\,\mu\mathrm{m}$
$s = 224\,\mathrm{m}$	$\beta_x = 8.7\,\mathrm{m}$	$D_x = -0.14\,\mathrm{m}$	$\sigma_b = 66.1\,\mu\mathrm{m}$	$\sigma_d = 15.4\,\mu\mathrm{m}$
$s = 420\,\mathrm{m}$	$\beta_x = 132.0\,\mathrm{m}$	$D_x = 1.61\,\mathrm{m}$	$\sigma_b = 257.2\,\mu\mathrm{m}$	$\sigma_d = 177.1\,\mu\mathrm{m}$
$s = 424\,\mathrm{m}$	$\beta_x = 148.4\,\mathrm{m}$	$D_x = 1.71\,\mathrm{m}$	$\sigma_b = 273.1\,\mu\mathrm{m}$	$\sigma_d = 188.1\,\mu\mathrm{m}$
Beam 2:				
$s = 216\,\mathrm{m}$	$\beta_x = 31.2\,\mathrm{m}$	$D_x = -0.12\,\mathrm{m}$	$\sigma_b = 125.2\,\mu\mathrm{m}$	$\sigma_d = 13.2\,\mu\mathrm{m}$
$s = 224\,\mathrm{m}$	$\beta_x = 12.4\,\mathrm{m}$	$D_x = -0.12\,\mathrm{m}$	$\sigma_b = 78.9\,\mu\mathrm{m}$	$\sigma_d = 13.2\,\mu\mathrm{m}$
$s = 420\,\mathrm{m}$	$\beta_x = 112.2\,\mathrm{m}$	$D_x = 1.79\,\mathrm{m}$	$\sigma_b = 237.4\,\mu\mathrm{m}$	$\sigma_d = 197\,\mu\mathrm{m}$
$s = 424\,\mathrm{m}$	$\beta_x = 127.9\,\mathrm{m}$	$D_x = 1.91\,\mathrm{m}$	$\sigma_b = 253.6\,\mu\mathrm{m}$	$\sigma_d = 210\,\mu\mathrm{m}$

Table 6.1: Horizontal betatron β_x and dispersion D_x functions for the FP220 and FP420 detector positions. The last two columns show the maximal betatron amplitude σ_b and the beam size in the horizontal direction due to the momentum spread of beam particles σ_d. Both variables determine the spacial beam size.

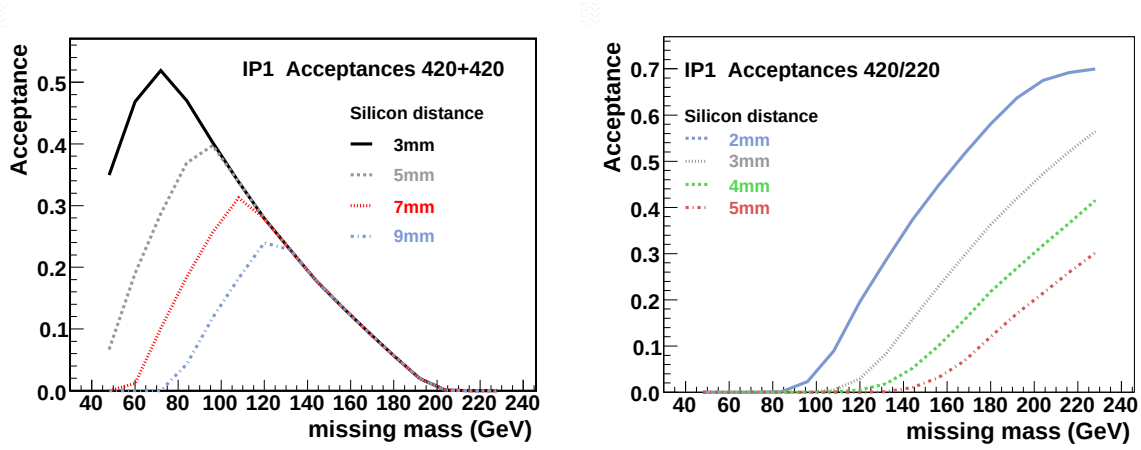

Figure 6.8: Acceptance as a function of the missing mass $W = \sqrt{s\xi_1\xi_2}$ when protons are detected in FP420 detectors upstream and downstream (left), and for the cases where protons are tagged in FP220 and FP420 (right). For the latter scenario, the FP420 detector is placed 5 mm from the beam, whereas the FP220 detector position was set at different distances (courtesy of P. Bussey).

6.3.8 Transport parameterization

In order to have a fast reconstruction of the scattered proton kinematics from the detector hits at FP220, we use the proton transport parameterization [8] which approximate the Mad-X transport by analytic formulae, valid for diffractive protons. In this method, the scattered proton of four-momentum $P = (E, p_x, p_y, p_z)$ is described in terms of three variables: proton energy, and two orthogonal angles x'_0, y'_0:

$$E = \sqrt{m^2 + \vec{p}^2} \qquad x'_0 = \frac{p_x}{p_z} \qquad y'_0 = \frac{p_y}{p_z} \tag{6.9}$$

where m is the proton mass.

The vertex position (x_0, y_0, z_0) can vary from event-to-event. The parameterization therefore provides a mapping from $(E, \alpha_0, \alpha'_0, z_0) \to \alpha, \alpha'$, where $\alpha = [x, y]$ are the track hits at 216 m, $\alpha' = [x', y']$ are the track directions (in the curvilinear coordinate system) and α_0, α'_0 their counterparts at the IP. It can be written as

$$\alpha = A_\alpha + \alpha'_0 B_\alpha + \alpha_0 C_\alpha + \alpha'_0 z_0 D_\alpha + z_0 F_\alpha \tag{6.10}$$

$$\alpha' = A_{\alpha'} + \alpha'_0 B_{\alpha'} + \alpha_0 C_{\alpha'} + \alpha'_0 z_0 D_{\alpha'} + z_0 F_{\alpha'} \tag{6.11}$$

where all the capital letters are polynomials of the proton energy E, up to E^4 term. It was found that the accuracy of the parameterization with respect to the true Mad-X tracking is about 1 μm on the track hit position and 50 nrad on the angle which should be sufficient with respect to the typical resolutions of the 3D silicon detectors (10 μm and 2 mrad).

6.3.9 Fast proton reconstruction

The inverse procedure of the scattered proton kinematics reconstruction from the proton tracks at the detector stations can be done only with additional assumptions since the proton transport is a surjective mapping. With the assumption that the collision took place exactly at the center of ATLAS, $x_0 = y_0 = z_0 = 0$ and due to the fact that both equations (6.11) describe the transport of the same particle, the above chain of equations can be rewritten as

$$(x - A_x - F_x z_0 - x_0 C_x) \cdot (B_{x'} + z_0 D_{x'}) - (x' - A_{x'} - F_{x'} z_0 - x_0 C_{x'}) \cdot (B_x + z_0 D_x) = 0 \tag{6.12}$$

Solving this equation numerically for E, we reconstruct the scattered proton energy which can be in turn used to calculate the track slope at the IP x'_0, y'_0. Note that the x and y directions are decoupled so that a similar equation as (6.12) can be written for the y coordinate. However, since the sensitivity to ξ is smaller in the y direction, the precision of the reconstruction would be worse. Also, we have to make sure that (6.12) has only one solution in a reasonable domain of E. For two-photon events (discussed below), the function (6.12) has only one zero in the range $5000 < E < 7200$ GeV.

6.4 Alignment method using $\gamma\gamma \to \mu\mu$ for FP220

The reconstruction of the scattered proton kinematics relies on the knowledge of the proton track distance from the beam and on the track direction. The detector system position will be monitored with the BPM system with the estimated resolution $10 - 20\,\mu$m. However, it is also important to calibrate the detectors with protons coming from a well defined physics process in which the proton kinematics

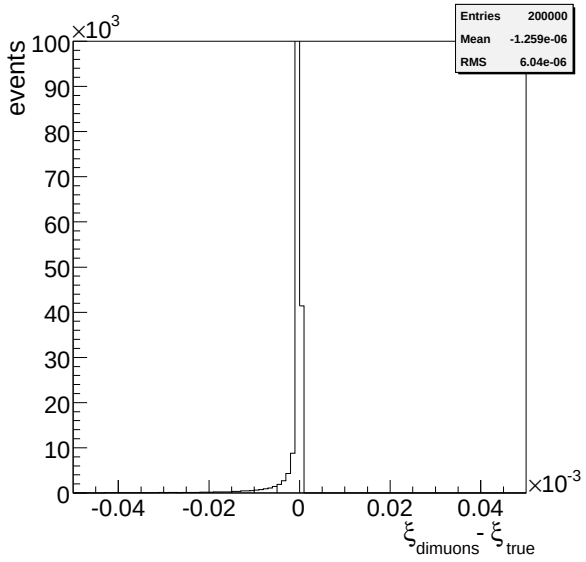

Figure 6.9: Effect of the zero-p_T approximation (6.15) on the proton ξ reconstruction (6.14) with respect to the generator true value in dimuon two-photon events with $p_T^\mu > 8\,\text{GeV}$ at 14 TeV.

could be obtained from the central detector and matched to that measured at AFP. This will not only cross-check the detector alignment, but also verify that the beam optics used for the proton transport corresponds to the real up-to-date layout of the machine magnets. In principal, even if the alignment of the detectors with respect to the beam is perfect, small differences between the tracking optics and the LHC magnets will imply small shifts in the reconstructed missing mass. The energy correction for the energy reconstruction could be obtained using the calibration with physics processes.

In this section, we investigate the capability of the two-photon dimuon production $\gamma\gamma \to \mu\mu$ for the alignment of the detector station at FP220. Since FP420 is sensitive to lower masses, hundreds of events can be collected during one physics store. Such a sample was shown to be sufficient to perform a standard calibration and alignment of the stations in every physics store. At the closer station FP220, the situation is more difficult. As we already know, the two-photon production drops quickly as a function of the produced mass and a large portion of the two-photon events is not observed with the FP220 detector because it is sensitive to higher missing masses. Nevertheless, our aim is to determine the reconstruction precision of the scattered proton kinematics using two-photon events and time needed to align the detector stations to the desired 10 μm precision in the horizontal direction.

6.4.1 Alignment strategy

In the following, we assume that a dimuon (or dielectron) pair was measured in the central detector. The kinematics between the scattered protons and the dileptons is precisely calculable in the case of the exclusive production. The fractional momentum losses of the two scattered protons ξ_1, ξ_2 can be expressed as

$$\xi_1 = X_{12}\exp(y) \quad \xi_2 = X_{12}\exp(-y) \tag{6.13}$$

where the total rapidity of the dilepton system is $y = y_{l1} + y_{l2}$. The variable

$$X_{12} = \frac{1}{\sqrt{s}} \left[M^2 + (\vec{p}_{1T} + \vec{p}_{2T})^2 \right]^{1/2} \tag{6.14}$$

is related to the dilepton invariant mass M and to the sum of the scattered protons transverse momenta $\vec{p}_{1T}, \vec{p}_{2T}$. The center-of-mass energy of the collision is s.

In two-photon processes, the proton form factors truncate the Q^2-dependence of the photon fluxes. Consequently, the transverse momenta of the scattered protons are quite small. For instance, from Figure 4.3 we see that less than 10% of the dimuon events have the proton transverse momentum $p_T^{\text{prot}} > 0.3\,\text{GeV}$. Hence, for not so small M, the transverse momenta of the protons can be neglected. We denote the transition

$$X_{12} \to X_{12} = \sqrt{\frac{M^2}{s}} \tag{6.15}$$

as the zero-p_T approximation.

The effect of the approximation (6.15) is shown in Figure 6.9 for two-photon dimuon events with $p_T^{\mu} > 8\,\text{GeV}$. The corresponding shift in the ξ distribution is of the order of 2×10^{-6}. If one of the protons is tagged and the leptons are detected in the central detector, the mass of the system M is constrained by kinematics, and is not arbitrary small. The bias of the zero-p_T approximation then decreases. The approximation is also justified by the fact that ξ cannot be reconstructed better then 10^{-4} (for $\xi \approx 0.01$) in a single measurement when the detector resolution and the beam uncertainties are taken into account.

Note that only one proton has to be measured in order to use this method, allowing independent alignment of stations in the positive and negative directions. Requiring only one proton tag at FP220 saves a large portion of the two-photon signal, since the non-detected proton on the opposite side can carry any momentum which gives a sufficient mass to produce two leptons in the central detector.

Another consequence of the small virtuality of the exchanged photons is that the produced dileptons have nearly the same transverse momentum p_T^{μ}. Their azimuthal angle separation is close to $\Delta\phi \equiv \phi_1 - \phi_2 \approx \pi$ (i.e. they have zero acoplanarity). This property can be used to select the two-photon dilepton signal.

In the following, we focus on the alignment using dimuon pairs only, however, the same method could also be used for electrons.

The two-photon events were produced with the FPMC generator (see the discussion in Chapter 4). The output was interfaced with the ATLAS full simulation and the scattered protons were tracked with the Mad-X program.

6.4.2 Proton hits for two-photon dimuon events

When protons are tracked from the IP to the FP220 station, they create a pattern shown in Figure 6.10. Only a small fraction of events falls in the acceptance of the forward detectors. The hit pattern forms a straight line in the $\Delta X \times \Delta Y$ plane inside the detector acceptance. Both horizontal and vertical displacements are sensitive to the fractional momentum loss and these events could not only be used for the alignment in the horizontal direction, but also in the vertical one. However, in the vertical direction the sensitivity to ξ is smaller.

The correlation between the ΔX coordinate of the proton hits and the proton ξ is depicted in Figure 6.11 for both beams. The precise acceptance in ξ depends linearly on the detector closest approach.

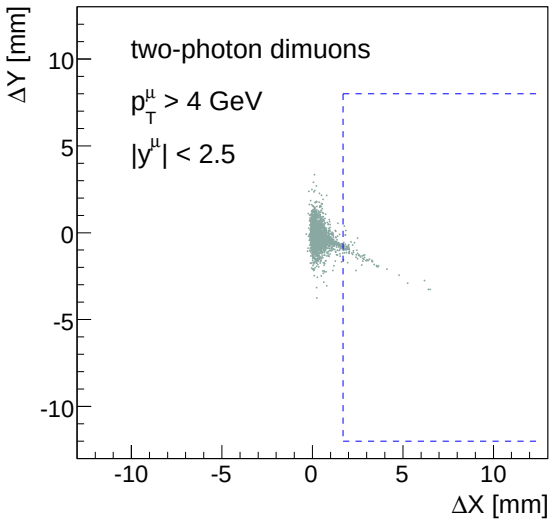

Figure 6.10: Proton hits of dimuon events in the FP220 station, beam 1. The sample was simulated using $p_T^\mu > 4\,\text{GeV}$ and muons were required to be within the acceptance of the central detector $|\eta| < 2.5$. The dashed area illustrates the acceptance of the active silicon detector. The particle transport was performed using Mad-X.

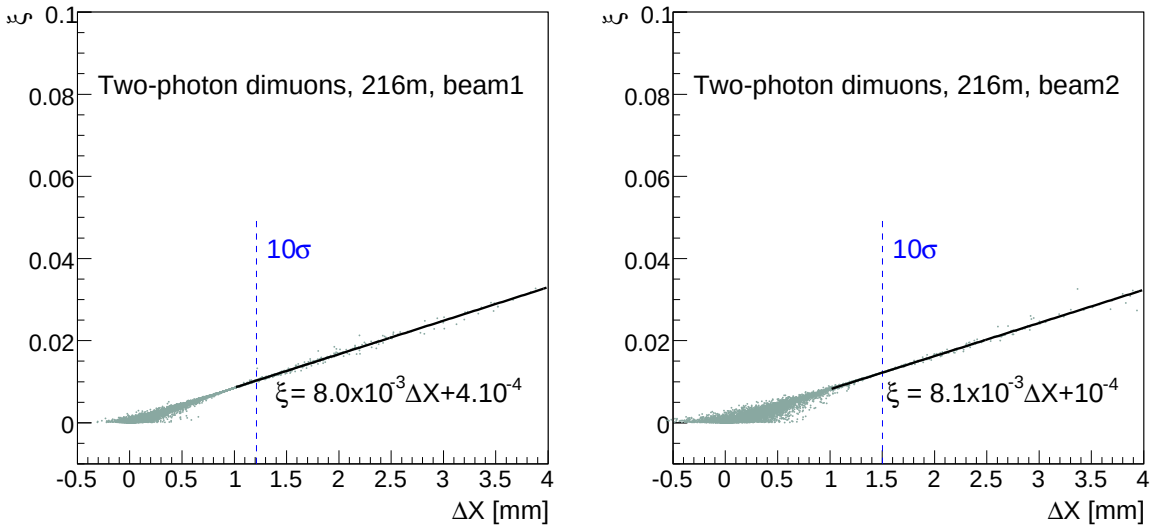

Figure 6.11: Correlation between the fractional momentum loss of the proton ξ and the corresponding hit distance ΔX from the nominal beam in FP220 stations in two-photon dimuon events simulated in the same way as in Figure 6.10. The results are shown for beam 1 (left) and beam 2 (right). The dashed line gives the detector approach at $10\sigma + 250\,\mu\text{m}$ which corresponds to $\approx 1.2\,\text{mm}$ for beam 1 and $\approx 1.5\,\text{mm}$ for beam 2. The particle transport was simulated using Mad-X.

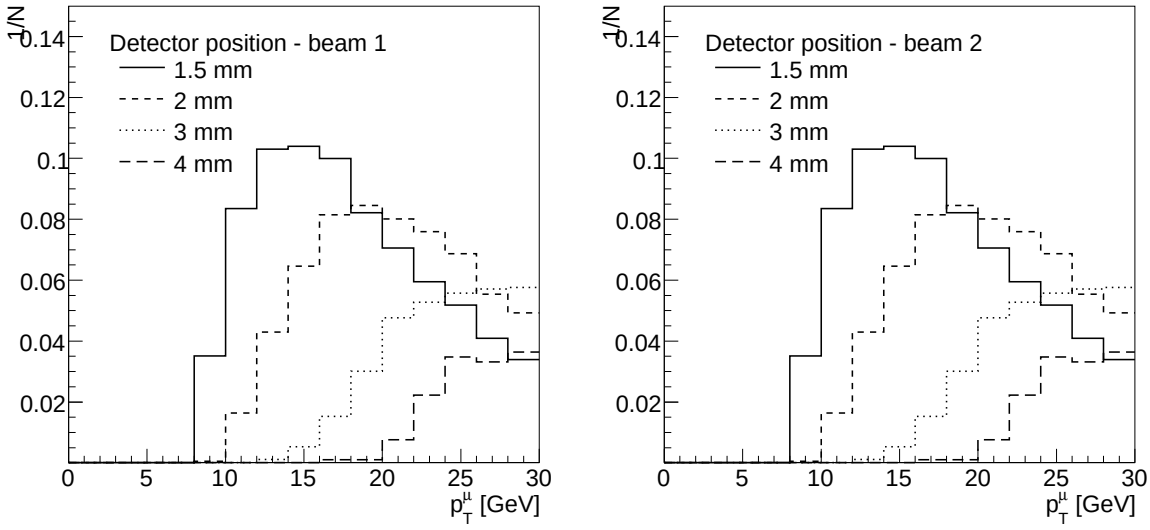

Figure 6.12: Effect of the FP220 distance of approach to the beam on the muon transverse momentum p_T^μ>8 GeV. With the theoretical most closest approach of 1.5 mm, only muons with p_T^μ above 10 GeV are selected because they are required to be within the $|\eta^\mu| < 2.5$ acceptance of the central detectors.

For two-photon events, the correlation can be parameterized by a linear function as

$$\begin{aligned} \text{beam 1}: \quad \xi &= 8.0\times10^{-3}\Delta X + 4\times10^{-4} \\ \text{beam 2}: \quad \xi &= 8.1\times10^{-3}\Delta X + 1\times10^{-4} \end{aligned} \tag{6.16}$$

where the displacement ΔX is in mm. The lower edges of the acceptance are $\xi_{min} = 0.01, 0.015, 0.02$ for the detector positions $\Delta X = 1.2, 1.8,$ and 2.4 mm, respectively for the beam 1. Numbers for beam 2 are similar.

Tagging one of the protons in FP220 and requiring the muons to be detected in the muon spectrometer or in the inner detector system ($|\eta|$<2.5) induces a kinematic constraint on the other proton momentum, the produced mass and also on the muon transverse momenta. This effect is shown in Figure 6.12 for several detector positions: 1.5, 2, 3 and 4 mm from the beam. Even for the closest allowed operation position of 1.5 mm tolerated by the LHC safety requirements (6.8), the measured muon p_T^μ is not smaller than 10 GeV in the tagged events. For a more realistic position of the detector at 2 mm, the threshold is about 15 GeV. We therefore concentrate on studying dimuon samples with $p_T^\mu > 10$ GeV only, applying a cut on the muon transverse momentum directly at the generator level.

In the following sections, we first describe the reconstruction of the fractional momentum loss using the forward detectors and the ξ reconstruction using dimuons in the central detector. Both methods will be combined afterwards to study the alignment of the FP220.

6.4.3 Proton ξ reconstruction

The proton reconstruction is performed using the fast proton kinematics unfolding method described in Section 6.3.9. Several effects determine the reconstruction resolution. They are related to the beam and detector uncertainties summarized in Table 6.2. First, the proton-proton collision can occur anywhere

Beam uncertainties	Value
beam transverse size	16.6 μm
angular spread in X	30.2 μrad
angular spread in Y	30.2 μrad
energy spread	0.77 GeV

detector resolution	Value
in horizontal X direction	10 μm
in vertical Y direction	50 μm

Table 6.2: Beam uncertainties during the nominal LHC operation [3] and the 3D silicon detector resolutions for each unit.

in the interaction region of the size $\sigma_t/\sqrt{2} = 11.7\,\mu$m, where σ_t=16.6 μm is the transverse size of each beam. This effect is difficult to be corrected for since the impact parameter of the track of a particle with $p_T \approx 10$ GeV cannot be measured with a precision better then 15 μm with the inner detector (see (3.11)). Second, due to the momentum dispersion of particles inside LHC bunches, there is a small angular spread of 30.2 μrad in the transverse plane of the colliding proton pair with respect to the nominal beam z direction. Finally, the protons have an energy spread around the nominal value 7000 GeV parameterized by a gaussian distribution of variance 0.77 GeV. On the other hand, the detector resolution is given by the detector layout of the 3D silicon detectors and the number of active layers. The resolution in horizontal and vertical directions was obtained from simulations for the proposed detector layout and was found to be $\sigma_x = 10\,\mu$m in the horizontal direction and $\sigma_y = 50\,\mu$m in the vertical one [9].

The reconstructed ξ distribution from the proton tracks at FP220 in fully simulated events (discussed below) with two muons $p_T^\mu > 10$ GeV in the central detector is shown in Figure 6.13. The resolution of the reconstructed fractional momentum loss is shown in Figure 6.14. On the left, the contributions of various beam and detector uncertainties are shown. The largest contribution to the resolution is due to the non-zero beam transverse size. At higher ξ values, the finite detector resolution becomes more important. The deterioration of the resolution is mainly due to the resolution on the track angle reconstruction. On the other hand, the slightly worse resolution at very small ξ is a consequence of the track position smearing. Energy and angular beam smearings correspond to about 20% of the total resolution. It should be also mentioned that the error on ξ due to the reconstruction from the fast parameterization mentioned in Section 6.3.9 was found to be of the order of 10^{-9} in terms of ξ, and hence negligible.

In Figure 6.14 (right), the overall resolution on ξ from the forward detector is shown, $\Delta\sigma_\xi(\text{prot}) = 4.3 \times 10^{-4}$. The mean shift in the reconstructed value is very small with respect to the true value, and there is no significant bias.

Having studied the reconstruction of the fractional momentum loss from the FP220 detectors, we now turn to investigate the ξ reconstruction using the dimuon pairs in the central detector.

6.4.4 Muon simulation

In order to obtain realistic estimates of the method precision, the two-photon dimuon events were generated, simulated, and reconstructed in the ATLAS full simulation framework, version 14.5.0. Data sets were produced privately with the FPMC generator. The `Staco` muon objects were obtained from the `StacoMuonCollection` container.

The low-p_T^μ muon reconstruction using the muon spectrometer is more difficult since part of the

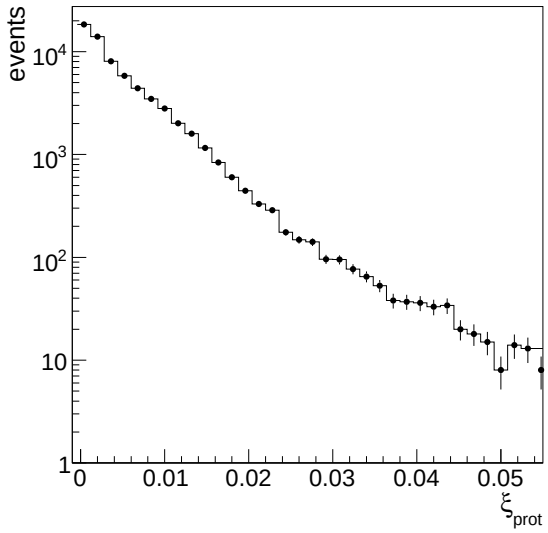

Figure 6.13: Fractional momentum loss ξ reconstructed at FP220, beam 1, requesting muons $p_T^\mu > 10\,\text{GeV}$ reconstructed in the central detector. The error bars reflect the statistical uncertainty $1/\sqrt{N}$. The reconstruction is performed without the acceptance of the detector.

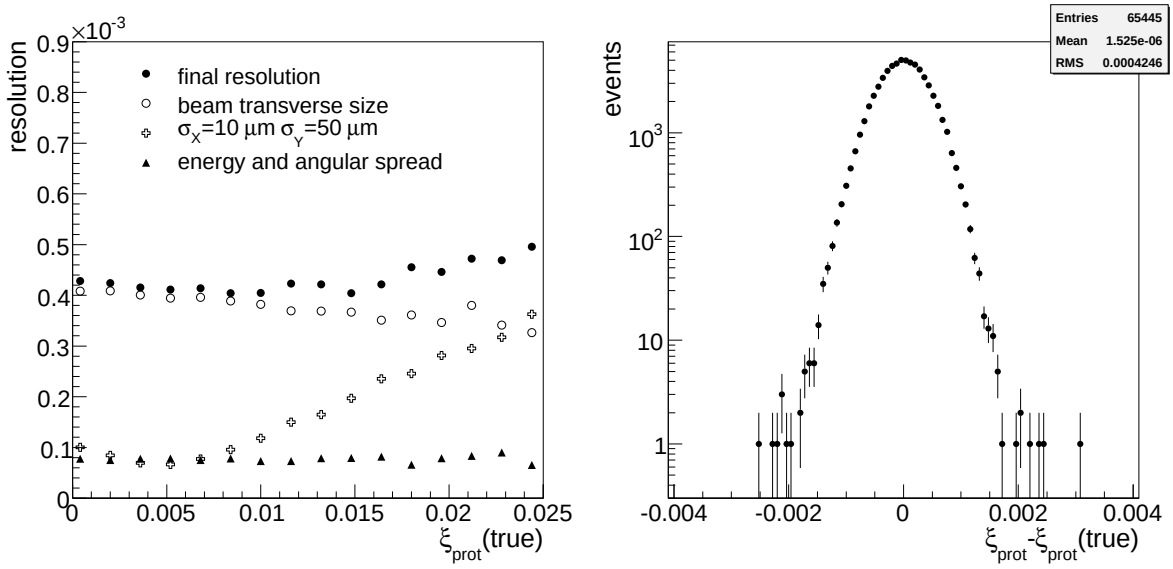

Figure 6.14: Contributions to the resolution with ξ reconstructed in dimuon events with $p_T^\mu > 10\,\text{GeV}$ at $s = 216\,\text{m}$ without taking into account the detector acceptance of the proton taggers. The largest contribution comes from the finite beam transverse size, but at high ξ_{prot} the detector smearing becomes also important. The error bars on the left reflect the statistical uncertainty.

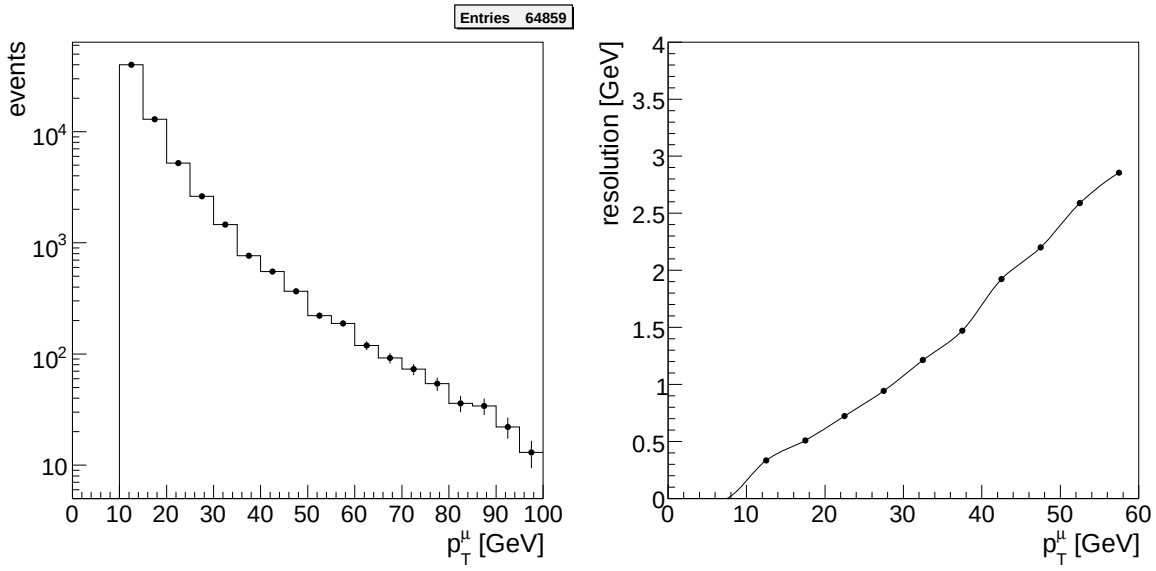

Figure 6.15: Transverse momentum (left) and resolution (right) of the leading muon.

muon energy is lost in the preceding calorimeters (about 2.5 GeV for a 10 GeV muon). The inner detector measurement is used for low p_T^μ muons since their track curvatures inside the inner detector solenoid field allow a precise reconstruction. The information from both sub-systems is combined, yielding a better p_T^μ resolution for $30 < p_T^\mu < 200$ GeV than the one from individual sub-systems. It is about 2.5% for p_T^μ=30 GeV.

6.4.5 Event selection

Dimuon events are selected requiring both muon transverse momenta $p_T^\mu > 10$ GeV. The leading muon p_T^μ distribution is shown in Figure 6.15 (left). In order to evaluate the muon reconstruction resolution, the reconstructed muons are matched to the nearest true muon at generator level. The distance R is calculated according to $R = \sqrt{(\Delta\eta)^2 + (\Delta\phi)^2}$. The resolution of the transverse momentum reconstruction is depicted in Figure 6.15 (right). The observed resolution is about 2-4% for small p_T^μ and is in good agreement with the combined muon algorithm performance presented in [10]. The dimuon events are produced predominantly at central pseudorapidities. The η resolution of $\sigma_\eta = 8 \times 10^{-4}$. The azimuthal angle is reconstructed precisely with a typical ϕ resolution found to be $\sigma_\varphi = 0.35\,\mu$rad.

The main source of uncertainties on the fractional momentum loss of the proton calculated from the dimuon pair kinematics according to (6.15) is the invariant mass of the pair. The mass distribution is shown in Figure 6.16 (left). As expected, it falls quickly due to the mass dependence of the effective photon-photon luminosity spectrum. The uncertainty on the invariant dimuon mass is shown in Figure 6.16 (right). The resolution is about 2% for masses around 40 GeV, and is better for lower masses.

The resolution on the fractional momentum loss calculated from the muons is depicted in Figure 6.17 (left) as a function of ξ_μ, and integrated over ξ_μ on the right. We note that the resolution is about 2-4% for small ξ_μ and is dominated by the dimuon mass resolution as it should be since it is calculated according to (6.14) and the uncertainty on the pseudorapidity is small. For very small values of ξ_μ,

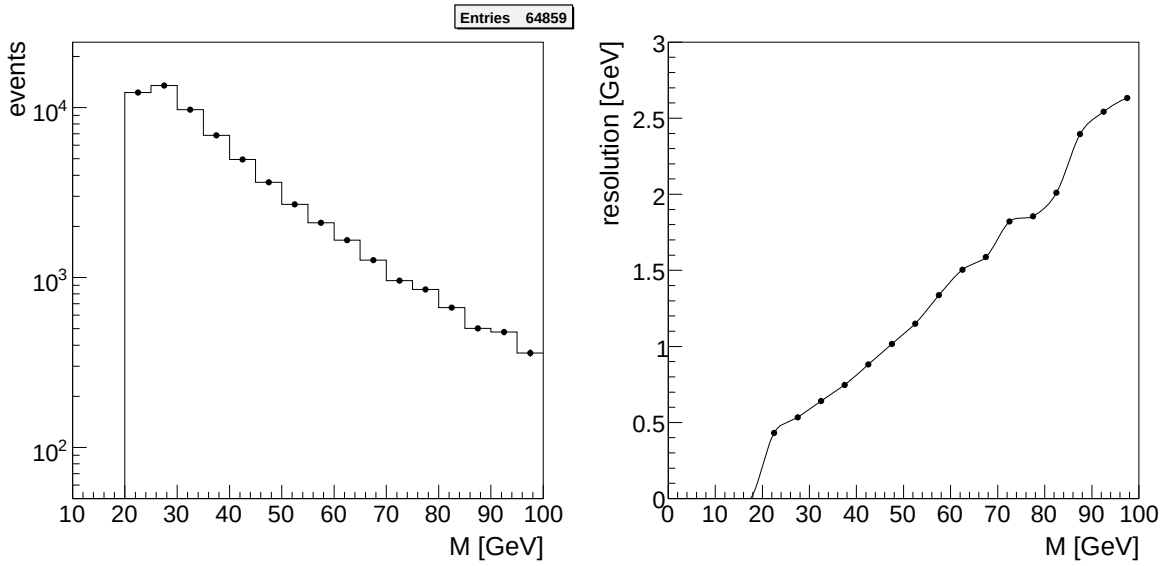

Figure 6.16: Mass of the dimuon pair (left) and its resolution (right).

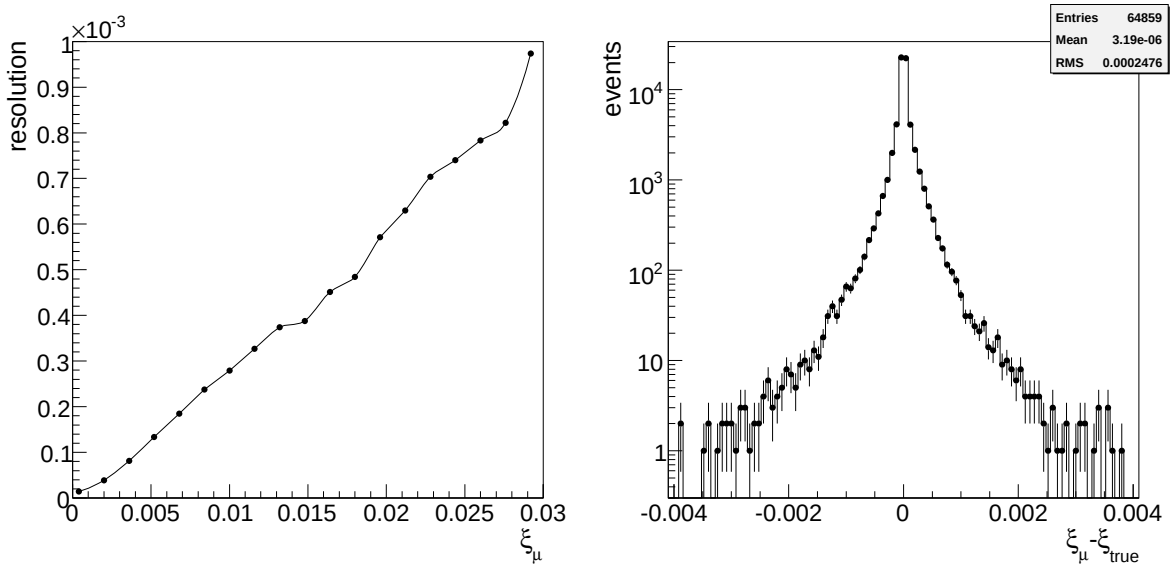

Figure 6.17: Resolution on the fractional momentum loss ξ_μ reconstructed from muons as a function of ξ_μ (left). On the right, the overall resolution is shown.

the theoretical precision of the reconstruction using dimuons is better than the one from the forward detectors which is deteriorated due to beam smearing effects. However, we must remember that the acceptance of FP220 does not span below $\xi \lesssim 0.015$ due to the minimal safety distance. In fact, the precision on the ξ reconstruction using both methods is about the same with the FP220 detector at a distance of 1.5 mm from the beam and with the muon system. For farther detector positions, the resolution on ξ calculated from the dimuon pair worsens which will have an effect on the forward detector alignment.

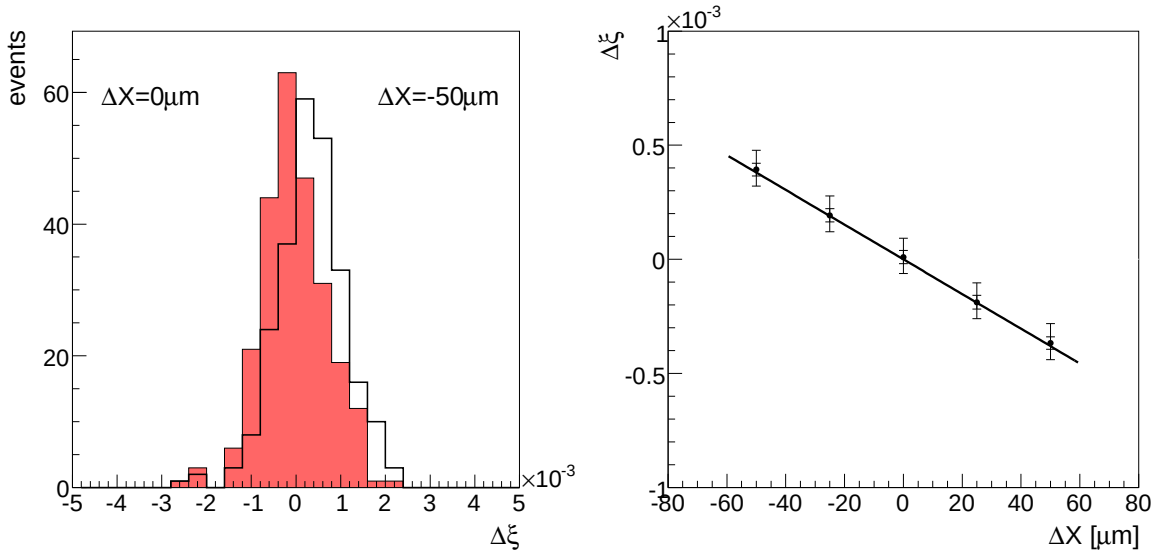

Figure 6.18: Difference between the fractional momentum loss reconstructed from the FP220 station and from dimuon pairs $\Delta\xi \equiv \xi_{\text{prot}} - \xi_{\mu}$ for nominal detector position and a shifted position by $-50\,\mu$m (left). On the right, the mean shift is depicted for several detector displacements $\Delta X = -50, -25, 0, 25, 50\,\mu$m. The smaller error bars represent the uncertainty on the mean of $\xi_{\text{prot}} - \xi_{\text{true}}$ for 250 events. The larger error bars describe the uncertainty on the mean of $\Delta\xi$ calculated for 250 events.

6.4.6 Alignment of the forward detector system

Having analyzed the ξ reconstruction using both the central and forward detectors, we can now use the information obtained from the dimuon pairs to align the forward detectors. A shift in detector position will lead to the anti-correlation between ξ reconstructed from dimuons and the one from the forward stations. The analysis is performed for three detector positions: 1.5, 2, and 3 mm from beam 1. Since the properties of beam 2 are similar to beam 1 at 220 m from the IP, the alignment of the FP220 stations in beam 2 is expected to be similar.

Anticipating the fact that dimuon samples will have to be collected over a long time period, we have to take the BPM resolution into account. The BPM information will be used to correct the detector position with respect to the beam from store-to-store. For this reason, we worsen our detector resolution by a factor of two. The detector smearing in the horizontal direction is therefore $\sigma_{\text{x}} = 20\,\mu$m.

First, it is useful to estimate at which precision a shift in ξ has to be known in order to claim the alignment precision of $10\,\mu$m. From (6.16) we know that $10\,\mu$m corresponds approximately to the shift in reconstructed fractional momentum loss $\Delta\xi \approx 8 \times 10^{-5}$. The uncertainty on the mean $\langle\Delta\xi\rangle$ of the variable $\Delta\xi \equiv \xi_{\text{prot}} - \xi_{\mu}$ corresponding to the shift in the detector position, decreases as $\sigma_{\Delta\xi}/\sqrt{N}$ with the number of observed events N, where $\sigma_{\Delta\xi}$ is the collected sample variance.

The $\Delta\xi$ distribution is shown in Figure 6.18 (left) for the nominal detector position (shaded region) and a detector position displaced by $\Delta X = -50\,\mu$m for 250 observed events with a detector placed at 1.5 mm. When the detector is displaced, the mean of the distribution is clearly shifted to positive values since the reconstructed proton track hit x coordinate is larger, implying also higher values of reconstructed ξ_{prot}. In the same figure on the right, the shift in $\Delta\xi$ is shown for several detector mis-

distance from beam	$\langle\Delta\xi\rangle$	$\sigma_{\Delta\xi}$	slope a [μm^{-1}]: $\Delta\xi = a\cdot\Delta X$
1.5 mm	1.6×10^{-5}	4.6×10^{-4}	-7.6×10^{-6} (10%)
2 mm	4.7×10^{-5}	5.2×10^{-4}	-7.5×10^{-6} (10%)
3 mm	-1.5×10^{-5}	6.1×10^{-4}	-6.6×10^{-6} (19%)

Table 6.3: Mean $\langle\Delta\xi\rangle$ and variance $\sigma_{\Delta\xi}$ of the difference in ξ as reconstructed in FP220 and inside ATLAS $\Delta\xi \equiv \xi_{\text{prot}} - \xi_{\mu}$ for three detector positions: 1.5, 2, and 3 mm from beam 1 and zero misalignment. The obtained slope of the linear correlation function between $\Delta\xi = a\cdot\Delta X$ is also shown. The values in parentheses denote the errors obtained from the fit of a.

positions. The correlation between ΔX and $\Delta\xi$ is linear as expected from Figure 6.11. Projecting the point error bars using the linear function on the ΔX axis we see that 250 dimuon two-photon events are more than sufficient to determine the detector position with the needed accuracy if the detector is placed at 1.5 mm from the beam.

The means and variances of $\Delta\xi$ are summarized in Table 6.3 for three possible detector positions: 1.5, 2, and 3 mm. We notice that the variances $\sigma_{\Delta\xi}$ increase as the detectors are placed farther from the beam. This is due to the fact that by tagging protons at larger distances we request heavier central masses. These masses are reconstructed with smaller absolute precision as shown in Figure 6.16, and correlate less well with ξ_{prot} measured in the forward detectors.

It must be mentioned that in order to obtain a good correlation between ξ_{prot} and ξ_{μ}, events with $\xi_{\mu} < 0.005$ originating in the simulation imperfections are rejected. In addition, only events which show a compatible fractional momentum loss reconstructed by both methods $\Delta\xi \equiv |\xi_{\text{prot}} - \xi_{\mu}| < 0.006$ are retained. The second requirement is important especially for far detector positions from the beam and helps to remove a bias due to obviously wrongly reconstructed dimuon events. The efficiencies of these cuts were 99% for the position 1.5 mm and 96% for the 3 mm one.

The fit results of the slope a determined from the correlation $\Delta\xi = a\cdot\Delta X$ as shown in Figure 6.18 are also given in Table 6.3. It allows to translate the uncertainties on $\Delta\xi$ in terms of the detector displacement. From

$$N = \left(\frac{\sigma_{\Delta\xi}}{a\Delta X}\right)^2 \tag{6.17}$$

we determine the needed number of events to align the detectors with a precision 10 μm. For the three mentioned configurations of the detector position 1.5, 2, and 3 mm, the number of needed events is $\approx 40, 50$, and 90. To be conservative, we conclude that about hundred events is necessary to be observed to gain the desired alignment of 10 μm.

6.4.7 Cross section estimates

The effective cross section of the single tagged events in FP220 with a dimuon pair $p_T^{\mu} > 10$ GeV in the central detector was calculated for various detector distances from the beam. The detector size of 2×2 cm is large enough to contain all dimuon signal from its active edge, so that the closest approach of the detector to the beam is the only parameter to be considered.

The cross section is shown in Figure 6.19. As expected, it falls rapidly as a function of the distance from the beam. The corresponding values for 1.5, 2 and 3 mm positions are: 89, 42, and 14 fb. It should

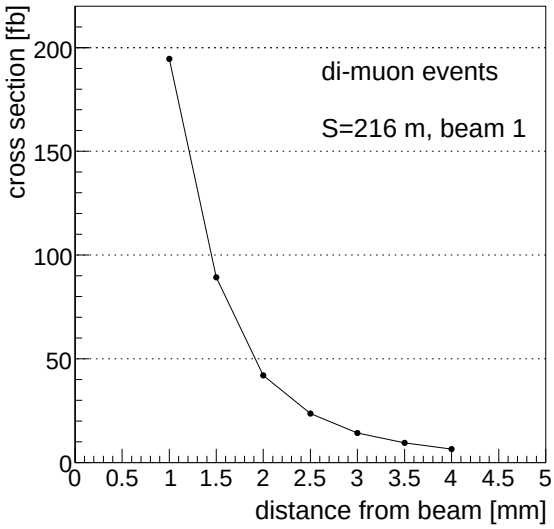

Figure 6.19: Effective cross section of dimuon events with $p_T^{\mu} > 10\,\text{GeV}$ as a function of the detector front edge distance from the beam.

be noted that they are corrected for the soft survival probability factor which is 0.9 for two-photon events. Assuming an average running luminosity $\mathscr{L} = 10^{33}\,\text{cm}^{-2}\text{s}^{-1} = 10^{-6}\,\text{fb}^{-1}\,\text{s}^{-1}$, for one running day of $10^5\,\text{s}$ (which is quite conservative), we obtain one day integrated luminosity of $0.1\,\text{fb}^{-1}$. The sample of one 100 events would therefore be collected in 12, 24, and 70 days.

6.4.8 Conclusion

Quite a long time is needed to collect the dimuon samples which means that the BPM information will have to be used in order to register the beam position from the 3D silicon detectors. This correction will have to be applied for each sample collected in individual LHC stores. We attempted to mimic the effect of these additional position measurements by worsening the detector resolution by a factor of 2. However, it is clear that understanding the BPM alignment system in-situ as well as having a practical experience with the beam position determination are important ingredients to enable the vast physics program offered by the forward detectors. The number of events needed to be collected is about 100 for the position of the detectors between 1.5-3 mm. In the most optimist case, the needed sample will be collected in two weeks. In the worst one, it will take about two months.

It should be stressed that the application of the dimuon events does not only concern the alignment, but also the absolute calibration of the reconstructed missing mass. Two-photon events will be used for the absolute mass scale determination over a long period of time. The precision will depend on beam position monitoring performed by BPMs, since the beam position might fluctuate from store-to-store, and has to be monitored.

As there is not (yet) a unique physics process for the alignment and calibration during every LHC store as in the case of FP420, the alignment of the FP220 will have to be combined using various techniques in the same time and perform cross checks between them. For instance, the BPMs can be aligned and cross-calibrated with the BPMs of the LHC. Concerning the physics processes for the calibration,

exclusive dijets are thought to give some constraints on the detector alignment. Also, reconstructing the W mass in single diffractive events using the missing transverse energy and the outgoing lepton might be useful as already demonstrated by the CDF Collaboration. Last but not least, the alignment between FP220 and FP420 could be done using tracks which pass through both detectors. The number of these tracks will be high due to the large cross sections of soft single diffractive events. But we should keep in mind that since the measurement of the proton arrival time using the QUARTIC timing detector is destructive for the proton, this relatively simple method of inter-alignment of the two forward detectors might not be be possible. It would require dedicate runs in which the movable beam pipe with QUARTIC detector would not be inserted.

Bibliography

[1] M. G. Albrow *et al.* [FP420 R and D Collaboration], arXiv:0806.0302 [hep-ex].

[2] S. Y. Lee, Accelerator physics, *Singapore, Singapore: World Scientific (1999).*

[3] O. S. Bruning, P. Collier, P. Lebrun, S. Myers, R. Ostojic, J. Poole and P. Proudlock, LHC design report. Vol. I: The LHC main ring, CERN-2004-003-V-1; `http://ab-div.web.cern.ch/ab-div/publications/LHC-DesignReport.html`, Sep. 2009.

[4] W. Herr, F Schmidt, CERN-AB-2004-027-ABP, Mad-X documentation at `http://mad.web.cern.ch/mad/`, August 2009.

[5] P. Bussey, FPTrack Programme, `http://ppewww.physics.gla.ac.uk/~bussey/FPTRACK/`

[6] K. Potter, private communication. See also `http://indico.cern.ch/materialDisplay.py?contribId=6&materialId=slides&confId=49945`, 1.9.2009.

[7] Atlas Forward Proton Collaboration, Letter Of Intent, to appear.

[8] R. Staszewski and J. Chwastowski, Nucl. Instrum. Meth. A **609** (2009) 136 [arXiv:0906.2868 [physics.ins-det]].

[9] P. Ruzicka, private communication.

[10] G. Aad *et al.* [The ATLAS Collaboration], arXiv:0901.0512 [hep-ex].

Weak Boson Coupling in Two-photon Events

7

Two-photon physics will be a significant enhancement of the LHC physics program. It allows us to study the Standard Model in a unique way at the hadron collider through exchange of photons. This chapter focuses on two applications of the diboson production in two-photon events. First we propose a measurement of the $pp \to pWWp$ cross section with the use of forward detectors to tag the escaping intact protons. Later, we explore the sensitivities to anomalous quartic $WW\gamma\gamma$, $ZZ\gamma\gamma$ (QGC) and anomalous triple $WW\gamma$ (TGC) gauge couplings. Since the cross section is highly increased when anomalous couplings are considered, the study of QGC sensitivities is divided into two parts: first, the sensitivities achievable with low integrated luminosity ($\sim 10\,\mathrm{pb}^{-1}$) collected in a couple of months after the start-up of the LHC are derived and second, the sensitivities at high luminosity using forward detectors are presented. The work was presented in two papers [1, 2].

7.1 Boson interactions in the standard model

The process that we intend to study is the W pair production induced by the exchange of two photons. It is a completely QED process in which the decay products of the W bosons are measured in the central detector and the scattered protons leave intact down the beam pipe at very small angles, contrary to inelastic collisions. Since there is no proton remnants the process is purely exclusive; only W products populate the central detector.

The fact that the central object is produced exclusively provides an additional information available to pin-down the signal from the large QCD background, emerging from inelastic collisions with a broken proton in the final state. Forward detectors which are capable of detecting unaltered protons are necessary to study single/double pomeron exchanges, central exclusive production, two-photon exchange and pomeron-photon fusion as summarized in Chapter 2 (see also [3]). Moreover, if such detectors can detect events with large momentum fraction loss of the proton, they allow innovative type of studies in which a high mass object ($\sim$ TeV) is created in the central detector and one can measure this created mass quite precisely with the forward detectors (with a resolution of few GeV). The idea is that the created energy is high enough to open up some channels of new physics beyond the SM which can be investigated using the measured missing mass. Two-photon exchange provides us a ground to study new processes in very well constrained kinematic conditions. The central exclusive Higgs production

has drawn recently most of the interest to study the Higgs production at low mass $\approx 120\,\mathrm{GeV}$, which is otherwise difficult to be detected using the conventional methods. But in fact, forward detectors can be used to look for any new high mass object produced with a pure inclusive trigger with a large missing mass measured in the forward detectors.

As was already introduced, the electroweak boson production in two-photon interactions is of particular interest. As we know, the electroweak part of the standard model Lagrangian prescribes the interactions between bosons as a result of the underlying gauge symmetry $\mathrm{SU}(2)_L \times \mathrm{U}(1)_Y$. It was proposed in late 1960s by Weinberg and Salam that the left-handed components of the fermion fields should be $\mathrm{SU}(2)$ doublets and their right-handed components singlets. Imposing the local gauge invariance, such choice leads automatically to the desired Vector - Axial structure of the charged weak current. Embedding electromagnetic and weak interaction into one framework is achieved by requiring the unifying condition which relates the electromagnetic e and weak g coupling constants by

$$e = g \sin\theta_W \tag{7.1}$$

where θ_W is a non-zero weak mixing angle parameterizing the orthogonal transformation between the gauge and physical fields (see also a discussion in the introduction following formula (2.9)). This condition implies a very important relation between the Fermi coupling G_F of the old four-fermion weak interaction and the W boson mass

$$m_W = \left(\frac{\pi\alpha}{G_F\sqrt{2}}\right)^{1/2} \frac{1}{\sin\theta_W} \tag{7.2}$$

which provided the prediction of the W mass before its actual discovery (α is the fine-structure constant).

After the gauge fields are rotated with (2.9) and the physical spectrum of $\gamma, W^{\pm}, Z$ is identified in the Lagrangian, the interactions between boson γ, W and Z can be written down. Considering the interactions with at least one photon, three-boson $WW\gamma$, and four-boson $WW\gamma\gamma$ and $WWZ\gamma$ interactions exist

$$\mathscr{L}_{WW\gamma} = -ie(A_\mu W^-_\nu \overset{\leftrightarrow}{\partial^\mu} W^{+\nu} + W^-_\mu W^+_\nu \overset{\leftrightarrow}{\partial^\mu} A^\nu + W^+_\mu A_\nu \overset{\leftrightarrow}{\partial^\mu} W^{-\nu}) \tag{7.3}$$

$$\mathscr{L}_{WW\gamma\gamma} = -e^2(W^-_\mu W^{+\mu} A_\nu A^\nu - W^-_\mu A^\mu W^+_\nu A^\nu) \tag{7.4}$$

$$\mathscr{L}_{WWZ\gamma} = g^2 \sin\theta_W \cos\theta_W (-2W^-_\mu W^{+\mu} A_\nu Z^\nu + W^-_\mu Z^\mu W^+_\nu A^\nu + W^-_\mu A^\mu W^+_\nu Z^\nu) \tag{7.5}$$

where the asymmetric derivative has the form $X \overset{\leftrightarrow}{\partial^\mu} Y = X\partial^\mu Y - Y\partial^\mu X$.

The production of Z bosons via two-photon exchange is forbidden in the lowest order perturbation theory because neither the Z boson nor the photon carries an electric or weak charge. On the other hand, the W-boson can be produced in pairs. In this case, both the triple gauge $WW\gamma$ (with $s-$ and $t-$channel exchange) and the quartic gauge $WW\gamma\gamma$ boson interactions must be included as shown in Figure 7.1.

The total cross section of the $pp \to pWWp$ which proceeds through two-photon exchange is effectively calculated as a convolution of the two-photon luminosity and the total cross section $\gamma\gamma \to WW$, where the two photons are basically on-shell. Results will be shown later, but now we discuss the properties of the sub-process $\gamma\gamma \to WW$ in some detail and show how the SM fine-tuned couplings ensure a good behavior of the theory in the high energy limit.

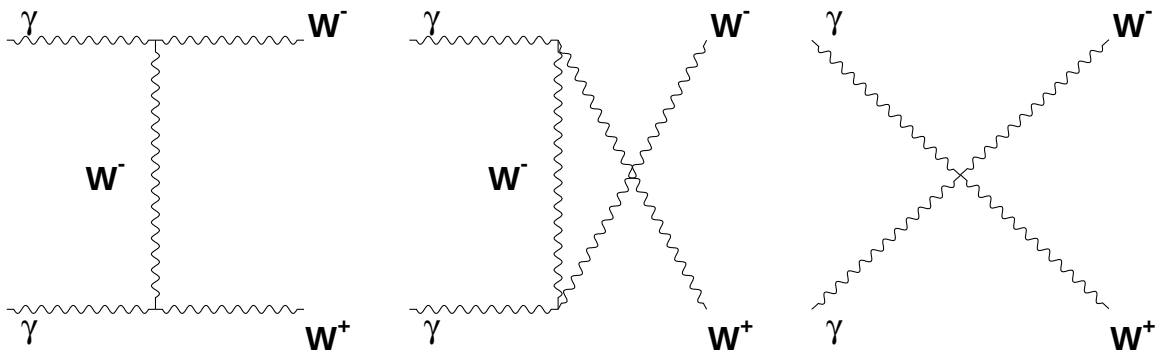

Figure 7.1: Feynman diagrams of SM processes that contribute to the $\gamma\gamma \to WW$ scattering amplitude in the lowest order perturbation series with a coupling e^2. The trilinear couplings of strength e are involved in diagrams a) and b) and the direct quartic coupling of strength e^2 in diagram c).

7.1.1 Tree level unitarity and divergence cancelation

In the $\gamma\gamma \to WW$ process, the fundamental property of divergence cancelation in the SM at high energy is directly incorporated. The SM model is a renormalizable theory. A necessary condition for the renormalizibility of the theory into all orders is the so called "tree unitarity" demanding that the unitarity is only minimally (logarithmically) violated in any fixed order of the perturbation series [4, 5]. More precisely the tree level unitarity means that any n-point tree level amplitude M^n_{tree} of the process $1+2 \to 3+4+\cdots+n$ grows for the fixed non-zero angles in the high energy limit $E \to \infty$ not faster than $M^n_{tree} = O(E^{4-n})$ (here E is some typical energy of the considered process, the center-of-mass energy of the particles 1+2 for instance). This requirement is sometimes denoted as the “asymptotic softness of the tree level amplitudes”. For the binary process of W pair production in particular, the tree level unitarity implies that the scattering amplitude $\gamma\gamma \to WW$ should be a constant or vanish in the high energy limit. In the SM, this condition is indeed satisfied. We are going to detail how different processes interplay in order to give a constant matrix element for a $\gamma\gamma \to WW$ process.

When the tree-level scattering amplitudes of the $s-$ and $t-$ channels a) and b) in Figure 7.1 are calculated using standard techniques of the quantum field theory formalism, the result includes terms growing as a function of the process energy. Formally, the different terms correspond to different polarizations of the final state W bosons.

The polarization vectors of the massive spin 1 particle (such as W or Z boson) plane wave $B_\mu = \varepsilon_\mu e^{ikx}$ are labeled, for a given four-momentum k, as $\varepsilon^\mu(k,\lambda)$ with $\lambda = 1,2,3$. Their normalization is conventionally fixed by

$$\varepsilon(k) \cdot \varepsilon^*(k) = -1 \tag{7.6}$$

The polarizations can be defined in such a way that two of the vectors lie in the plane perpendicular to $\vec{k}$

$$\begin{aligned} \varepsilon^\mu(k,1) &= \left(0, \vec{\varepsilon}^{(1)}(\vec{k})\right) \\ \varepsilon^\mu(k,2) &= \left(0, \vec{\varepsilon}^{(2)}(\vec{k})\right) \end{aligned} \tag{7.7}$$

where the $\vec{\varepsilon}^{(\lambda)}$, $\lambda = 1,2$ are two linearly independent vectors, and the third vector points along vector

momentum $\vec{k}$

$$\varepsilon^{\mu}(k,3) = \Big(\frac{|\vec{k}|}{m}, \frac{k_0}{m}\frac{\vec{k}}{|\vec{k}|}\Big) \tag{7.8}$$

and $k_0 = \sqrt{\vec{k}^2 + m^2}$. $\varepsilon^{\mu}(k,1), \varepsilon^{\mu}(k,2)$ are usually denoted as *transverse polarization* vectors whereas $\varepsilon^{\mu}(k,3)$ corresponds to the *longitudinal polarization* vector.

Thus in the high energy limit $|\vec{k}| \gg m$, the longitudinal polarization behaves as the four-momentum itself

$$\varepsilon^{\mu}(k,3) = \frac{k^{\mu}}{m} + O\Big(\frac{m}{|\vec{k}|}\Big) \tag{7.9}$$

whilst the transverse polarizations behave as a constant because they are bound by the Euclidean norm (7.6).

The amplitude of the $\gamma\gamma \to WW$ can be schematically written as

$$\mathscr{A}(\gamma\gamma \to WW) = e^2(X + Y \cdot E + Z \cdot E^2) \tag{7.10}$$

where e^2 is the electromagnetic constant (cf. (7.3) and (7.4)) and Z, Y, Z are constants independent of the center-of-mass energy $E = \sqrt{s}/2$ of the two-photon system. The constant term in the amplitude for $\gamma\gamma \to WW$ scattering represents the case in which both Ws are transversally polarized, the linear term to the case in which at least one of the boson is longitudinally polarized, and finally, the quadratic divergence corresponds to the case when both Ws are longitudinally polarized. Such ill high energy behavior of the scattering amplitude is cured by taking also the direct coupling diagram c) in Figure 7.1 into account. Its leading quadratically and sub-leading linearly divergent terms behave in exactly the same way as those non-direct ones, except that they come with an opposite sign. The divergence of the amplitude is thus canceled for any combination of the external W boson polarizations.

The cross section is therefore constant in the high energy limit. The leading order differential formula for the $\gamma\gamma \to WW$ process is a function of the Mandelstam variables s,t,u and the mass of the vector boson W [6]

$$\frac{\mathrm{d}\sigma}{\mathrm{d}\Omega} = \frac{3\alpha^2\beta}{2s}\left\{1 - \frac{2s(2s+3M_W^2)}{3(M_W^2-t)(M_W^2-u)} + \frac{2s^2(s^2+3M_W^4)}{3(M_W^2-t)^2(M_W^2-u)^2}\right\} \tag{7.11}$$

where $\beta = \sqrt{1-4M_W^2/s}$ is the velocity of the W bosons. For $s \to \infty$ the total cross section is $\sigma_{\mathrm{tot}} = 80.8\,\mathrm{pb}$.

To finish the theoretical discussion concerning the W-pair production from two photons, it is worth mentioning that an alternative of the electroweak unification exists, based on the tree level unitarity only. In fact, the SM model can be completely derived without any reference to the underlying $\mathrm{SU}(2)_L \times \mathrm{U}(1)_Y$ symmetry, which seems a rather bizzare postulate at first look. The SM, i.e. the unified theory of the electroweak interactions with heavy intermediate boson W, Z and also with an additional scalar particle which couples to the gauge bosons as well as to the fermions, can be built upon the condition that all possible tree-level amplitudes fulfill the tree unitarity. We will not go into technical details but rather only sketch the procedure. Consider an example from the old four-fermion theory of weak interaction. The Lagrangian with four-fermions direct coupling predicts rising cross sections (of the $e\nu$ process for instance) violating the tree-level unitarity in the high energy limit (simply due to the dimension 6 of the Lagrangian in terms of a typical mass). If one introduces the W boson coupled to two fermions, the four-fermion interaction is then carried out by the W boson exchange and the wrong high energy

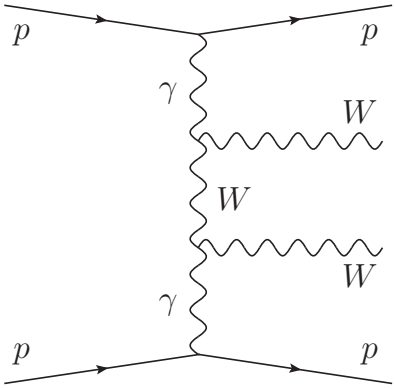

Figure 7.2: Diboson production through the two-photon exchange. Unaltered protons leave the interaction scattered at small angles $\lesssim 100\,\mu$rad.

behavior is cured. But since W bosons carry an electric charge they must also couple to the photon as $WW\gamma$. We have seen that having only the triple gauge coupling causes again problems in the high energy limit if one of the W bosons is longitudinally polarized. The leading and sub-leading divergences are removed when a direct quartic coupling $WW\gamma\gamma$ is introduced in the theory with a coupling exactly tuned in order to cancel the divergence. If we continue to examine the high energy behavior of all the newly added terms, introducing a vector boson Z and also a scalar particle, we will find that all possible interactions that we can construct in our theory at the lowest order behave well at high energies (and also solving the so-called Adler-Bell-Jackiw (ABJ) axial anomaly). Spectacularly, this procedure converges to exactly the same structure of the SM as the one emerging from the requirement of the local gauge symmetry $\mathrm{SU}(2)_L \times \mathrm{U}(1)_Y$ giving us a strong confidence in the legitimacy of the electroweak sector of the standard model [7] at least at the accessible energies.

Measuring the $\gamma\gamma \to WW$ scattering process at the LHC is therefore interesting not only because we can use the hadron-hadron machine as the photon-photon collider with a clean collision environment without beam remnants, but also because it provides a very clear test of the Standard Model consistency in a rather textbook process.

7.2 $pp \to pWWp$ signal process

The total cross section of the exclusive process $pp \to pWWp$ where the interaction proceeds through exchange of two quasi-real photons shown in Figure 7.2 is 95.6 fb. It is obtained in the Equivalent Photon Approximation (EPA) framework (the complete formula is presented in Chapter 4) integrating the two-photon effective luminosity (4.19) and the sub-process cross section (7.11) over all accessible two-photon masses $W_{\gamma\gamma}$ and also over photon virtualities from the kinematic minimum $Q^2_{min} \equiv m_p^2 E_\gamma^2/[E_b(E_b - E_\gamma)]$ (E_γ is the photon energy, E_b the beam energy, and m_p^2 the mass of the proton) up to a chosen maximum $Q^2_{max} = 2\,\mathrm{GeV}$. The actual value of the high limit Q^2_{max} is of low relevance because the Q^2 is naturally truncated by the electromagnetic proton form factors (4.15). Since the virtuality of the photon is very close to zero, the electromagnetic coupling appearing in the interaction Lagrangians (7.3) and (7.4) is evaluated at the scale $Q^2 = 0$; the electromagnetic fine-structure constant therefore takes the value $\alpha = 1/137$. Note that the above mentioned total cross section is different from the

usually presented value of 108 fb ([10, 11] for example) by about 10%. This is due to the fact that the authors considered the fixed electromagnetic coupling 1/129, at the scale of the W mass. So both results are compatible provided that one does the scaling $95.6 \times 137^2/129^2 = 108$. However, the photon virtuality should be taken as the scale and not the mass of the W. In Landau gauge, the invariant charge is driven by the self-energy insertion into the photon propagator only (and not by the vertex correction) [8]. In the propagator we have to take the photon virtuality as the scale, which is very small. The total cross section is therefor $\sigma = 95.6\,\text{fb}$. This value has to be corrected for the survival probability factor 0.9.

The cross section is rather modest in comparison to the inelastic production which is about three orders of magnitude higher (at $\sqrt{s} = 14\,\text{TeV}$, the NLO W^+W^- cross section is 111.6 pb, produced via quark-anti-quark annihilation $q\bar{q} \to W^+W^-$ ($\sim 95\%$) and also via gluon-gluon fusion $gg \to W^+W^-$ ($\sim 5\%$)). A substantial amount of luminosity has to be therefore collected to have a significant WW sample. It can only be accumulated when running at high LHC instantaneous luminosities $\mathscr{L} = 10^{33} - 10^{34}\,\text{cm}^{-2}\text{s}^{-1}$. Under such running conditions, the two-photon events must be selected with the forward proton tagging detectors. We will omit the technical details here concerning the acceptance of the Atlas Forward Physics (AFP) detectors. They were already discussed in the preceding Chapter 6. In fact, the acceptance on the momentum fraction loss ξ is assumed to be $0.0015 < \xi < 0.15$ which agrees with the coverage of the FP220 and FP420 detectors to be installed at a distance of 220 and 420 m around the ATLAS interaction point.

A shortcoming of the data taking at high luminosity is the number of multiple interactions occurring at the same time as the process of interest. As discussed in Section 3.1.2, up to 32 interactions per bunch crossing can occur at the same time at $\mathscr{L} = 10^{34}\,\text{cm}^{-2}\text{s}^{-1}$ and the number does not decrease below 13 interactions per bunch crossing during a typical physics run. Two protons from 2 single diffractive minimum bias events can give a hit in the forward detectors on positive and negative side, while the third standard inelastic event could mimic the two-photon signal in the central detector. In this case, the protons detected in the forward detectors are not related at all to the hard event producing the W pair. To reject this type of background the timing detectors will be used. They measure the arrival time of the two protons on each side with a $5-10\,\text{ps}$ precision constraining the vertex position from which the protons come within $10\,\text{ps}/\sqrt{2} \times c = 2.1\,\text{mm}$ (where c is the velocity of the scattered protons, close to the speed of light). Matching this information to the reconstructed vertex position determined by the inner tracker, the overlaid background can be suppressed almost completely (for example a suppression of about a factor 40 can be achieved with $5-10\,\text{ps}$ timing resolution on the $b\bar{b}$ background for Exclusive Higgs Production). Note however that even a femtosecond timing cannot remove the overlaid background completely. There is always a small contribution due to the large size of the LHC bunches in longitudinal direction $\sim 20-30\,\text{cm}$. Two interactions might occur during the bunch crossing at exactly the same position: first when the two bunches meet head-on and second, in the tail of the bunches when bunches are about to separate. Since the time of the interaction is not known, this type of overlaid background is indistinguishable. A timing of the interaction would be needed to remove that background.

The W boson decays hadronically ($\sim 68\%$) or leptonically ($\sim 32\%$). Since the two-photon cross section is small, the hadronic or semi-leptonic decays in which at least one jet is present could be mimicked by the QCD dijets or non-diffractive WW production, overlaid with other minimum bias interactions leading to a proton hit in the forward detectors. Studying the WW production in those channels would therefore require a more subtle analysis. For simplicity, we focus on the WW decays

only into electrons or muons in the final state. This in turn means that also only the leptonic decays of the τ lepton ($\sim 35\%$) are considered. About $\sim 6\%$ of the total WW cross section is retained for the analysis. About 1800 events are produced with two leptons in the final states for $30\,\text{fb}^{-1}$, an integrated luminosity which corresponds approximately to 3 years of running. We will see further that taking into account the forward detector acceptance, and the electron/muon reconstruction efficiencies, the expected number of events drops down to 50 events.

In the following we assume that the background due to multiple interaction is negligible with the use of timing detectors and consider only fully leptonic W decays to simplify the study.

7.3 Diffractive and $\gamma\gamma$ dilepton background

The clean two-leptonic signature of the two boson signal process

- $\gamma\gamma \to W^+W^- \to l\bar{l}\nu\bar{\nu}$

could be mimicked by several background processes which all have two intact protons in the final state. They are the following:

1. $\gamma\gamma \to l\bar{l}$ - two-photon dilepton production
2. DPE$\to l\bar{l}$ - dilepton production through double pomeron exchange
3. DPE$\to W^+W^- \to l\bar{l}\nu\bar{\nu}$ - diboson production through double pomeron exchange

Two-photon dilepton production is described within the EPA formalism. Because the kinematic threshold $2 \times m_l$ is much lower than for diboson events, the effective photon-photon luminosity is probed at small $W_{\gamma\gamma}$ masses where it is large and the total production cross section is high, 13.5 pb (for a pair of leptons of one family, $p_T^{lep} > 5\,\text{GeV}$). The leptons are produced exactly back-to-back due to the intrinsically tiny transverse momentum of the exchanged photons. The Double Pomeron Exchange (DPE) production of dileptons and dibosons is described within the factorized Ingelman-Schlein model where the hard diffractive scattering is interpreted in terms of the colorless pomeron with a partonic structure. Cross sections are obtained as a convolution of the hard matrix elements with the diffractive parton density functions measured at HERA (see Section 2.10.1 for a discussion about the extraction of diffractive densities at HERA and Section 4.4 about their implementation inside FPMC). Dileptons in DPE are produced as Drell-Yan pairs, probing the quark structure of the pomerons. The exchange is carried out through γ^* or Z^*. Contrary to the two-photon exclusive case where only scattered protons and leptons in the central detector are present, in DPE events, pomeron remnants accompany the interacting partons. They give a significant boost to the lepton pair in the transverse plane resulting in a non-negligible azimuthal decorrelation $\Delta\phi$ between the leptons. Finally, the diboson production in DPE is very similar to the actual $\gamma\gamma \to WW$ signal except that the mass distribution of the WW system is not as strongly peaked towards small values. The DPE dilepton and diboson total production cross section at the generator level are 743 pb (all lepton families) and 211 fb (all decay modes), respectively.

The experimental signature of the two-photon or DPE interaction in which two scattered protons continue to travel down the beam pipe and can be tracked in forward detectors can be lost by additional soft interactions between the outgoing protons. These soft QCD exchanges (occuring either before or after the hard interaction) of low momentum transfer cause the break-up of the proton. As a result, only

process	total cross section	flag
$\gamma\gamma \to WW$	86 fb	`YWWMAX=1.`
$\gamma\gamma \to ll$ ($p_T^{lep1} > 5\,\text{GeV}$)	36 pb	`PTMIN=5.`
DPE$\to ll$	7.4 pb	`EMMIN=10, YWWMAX=0.2`
DPE$\to WW$	6.2 fb	`YWWMAX=0.2`

Table 7.1: Total cross sections for SM $\gamma\gamma \to WW$ signal and background processes at 14 TeV including the gap survival probability factor (0.9 for QED and 0.03 for DPE processes). The process specific flags for the FPMC event generation are shown in the last column: `EMMIN` is the minimum Drell-Yan invariant mass and `YWWMAX` is the maximum allowed momentum fraction loss ξ of the protons.

some fraction of the exclusive or diffractive events will have two intact protons and two rapidity gaps in the final state. As was already mentioned in Section 2.14, the survival probabilities for the QED two-photon processes and QCD diffractive and central exclusive processes are distinctively different. Following the calculation in Ref. [12] the QED survival probability factor is 0.9 whereas the QCD survival probability is about 0.03 at the LHC. The mentioned total cross sections have to be therefore multiplied by these survival probability factors yielding cross sections of the signal and background shown in Table 7.1. The dilepton production creates the largest background, three orders of magnitude higher than the desired $\gamma\gamma \to WW$ signal.

The characteristic properties of the two-photon and DPE productions are visible in Figure 7.3. Here the leptons=(e/μ) are required to be within the generic central detector acceptance $p_T^{lep1,2} > 10\,\text{GeV}$, $|\eta^{lep}| < 2.5$. The p_T distributions (left) are peaked towards 0. Since the leptons are predominantly produced at central pseudo-rapidity this reflects the steepness of the two-photon luminosity dependence as a function of $W_{\gamma\gamma}$. In the DPE dilepton spectrum one can identify the Z^* resonance around $p_T^{lep1} = 45\,\text{GeV}$. The diboson spectrum on the other hand slowly increases until the WW channel is totally kinematically open and then decreases due to the drop of the effective photon-photon or pomeron-pomeron luminosity. On the right side of Figure 7.3, the momentum fraction loss ξ distribution shows again that the two-photon production is dominant at low mass. The momentum fraction tail of the DPE is truncated at $\xi = 0.2$ which is about the limit of the validity of the factorized pomeron model. The acceptance of the AFP detectors is shown as well. It provides us an access of two-photon masses up to $\sqrt{s} \times \xi_{max} = 14\,\text{TeV} \times 0.15 = 2.1\,\text{TeV}$.

The most natural distinction of the diboson signal is the missing transverse energy ($\not{E}_T$) in the event due to the undetected two neutrinos, see Figure 7.4 (left). It provides a very effective suppression not only of the two-photon dileptons where leptons are produced back-to-back in the central detector with no intrinsic $\not{E}_T$, but suppresses also the DPE dilepton background, even though some of the energy to pomeron remnants is not seen in the calorimeter. It can be due to either a limited η coverage of the calorimeter or due to a minimum energy readout threshold in the system which the pomeron remnants do not pass. Both cases mimic $\not{E}_T$.

Another way to distinguish the diboson signal is to use the missing mass $W = \sqrt{\xi_1 \xi_2}$ reconstructed in forward detectors which is shown in Figure 7.4 (right). The dilepton production is dominant at low mass in both two-photon and DPE exchanges, but has also a non-negligible contribution at high mass. The azimuthal angle $\Delta\phi$ between the two leading leptons is depicted in Figure 7.5. Dilepton events are more back-to-back than the diboson ones.

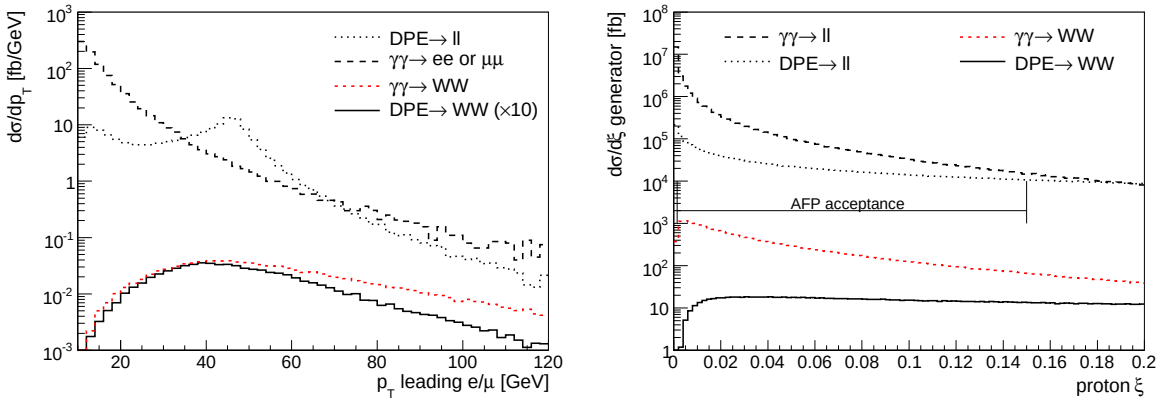

Figure 7.3: Transverse momentum of the leading e or μ (left) and the momentum fraction loss ξ (right) distributions for processes which have two leptons as well as two forward intact protons in the final state. The signal $\gamma\gamma \to WW$ is outraged by the ll two-photon and DPE production.

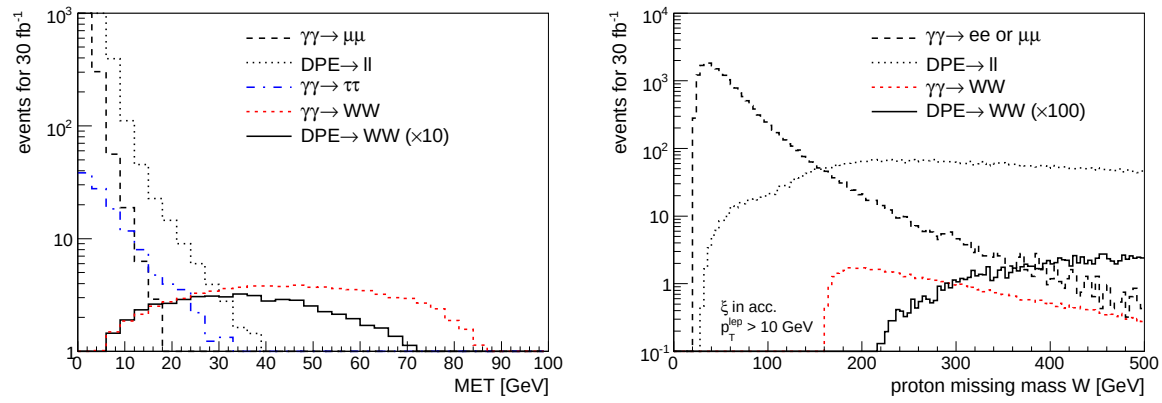

Figure 7.4: Missing transverse $\not{E}_T$ energy (left) and reconstructed W missing mass in the forward detectors (right) for the two-photon WW signal and background processes. The WW signal has a production threshold at $2m_W$ and has a large $\not{E}_T$ due to the undetected neutrinos.

All the above mentioned signal and background processes are generated using FPMC [13] (see Chapter 4). The output of the generator was interfaced with the fast simulation of the ATLAS detector in the standalone ATLFast package for ROOT [14]. The aim was to examine the general properties of all backgrounds in a fast way to define the strategies for early data measurements with the emphasis on the two-photon dilepton and anomalous coupling studies. Effects of the charge or jet mis-identifications are not considered here but will be evaluated with the real data.

We will now discuss how to select the signal $\gamma\gamma \to WW$ events from the mentioned background.

7.4 Measurement of the $pp \to pWWp$ process

It is necessary to use forward detectors to search for $pp \to pWWp$ production at high luminosity. After tagging the protons with a momentum fraction $0.0015 < \xi_{1,2} < 0.15$, the signal is selected with $\not{E}_T >$

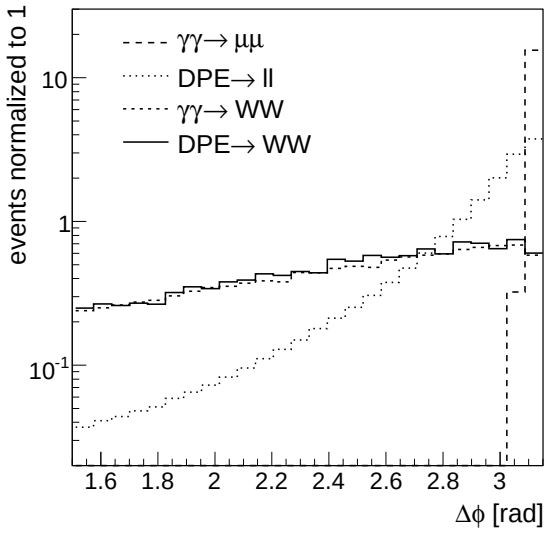

Figure 7.5: $\Delta\phi$ between two leading leptons. Dilepton events are more back-to-back than diboson events. DPE dileptons is less peaked because of the presence of the pomeron remnants which gives a transverse boost to the Drell-Yan system.

20 GeV measured in the central detector and a missing mass $W > 2m_W$ measured in forward proton detectors. Both cuts are natural for the diboson production. Events which are removed by the missing mass requirement are also removed by $\not{E}_T > 20\,\text{GeV}$. Although the missing mass cut is redundant it can reduce the background due to multiple interaction which we do not consider here and therefore it is useful to retain it. The $\gamma\gamma \to ll$ production where leptons are produced back-to-back is completely removed requesting the azimuthal angle between the two observed leptons $\Delta\phi < 2.7\,\text{rad}$.

The remaining background is composed of the DPE$\to ll$ ($\sim 80\%$) and DPE $\to WW$ (20%). We handle it by requesting the transverse momentum of the leading lepton $p_T^{lep1} > 25\,\text{GeV}$ and the missing mass smaller than $W < 500\,\text{GeV}$, see Figure 7.6. This leaves us with the cross section $1.69 \pm 0.01\,\text{fb}$ for the signal (the shown uncertainty reflects the statistical uncertainty of the calculation). In summary, the following requirements are used:

$$p_T^{lep1} > 25\,\text{GeV},\ p_T^{lep2} > 10\,\text{GeV},\ 0.0015 < \xi < 0.15,\ \not{E}_T > 20\,\text{GeV},\ 160 < W < 500\,\text{GeV},\ \Delta\phi < 2.7\,\text{rad} \tag{7.12}$$

The successive effects of all mentioned constraints is given in Table 7.2 where the number of events is shown for $30\,\text{fb}^{-1}$. In three years, one expects about 50.8 ± 0.2 signal events and 1.7 ± 0.1 background events. It is interesting to notice that this measurement can be successfully carried out even if the AFP acceptance does not reach its design maximum acceptance range $\xi_{max} = 0.15$. The number of expected events for $\xi_{max} = 0.1$, and $\xi_{max} = 0.05$ are 47 ± 0.2, 32 ± 0.2 for $30\,\text{fb}^{-1}$. The corresponding total backgrounds are 1.5 ± 0.1 and 0.74 ± 0.08, respectively.

7.4.1 Trigger

The trigger menus of ATLAS are designed in a way to have the least possible prescales on leptons produced in electroweak bosons W/Z decays. The L1 and HLT triggers can be operated without prescales

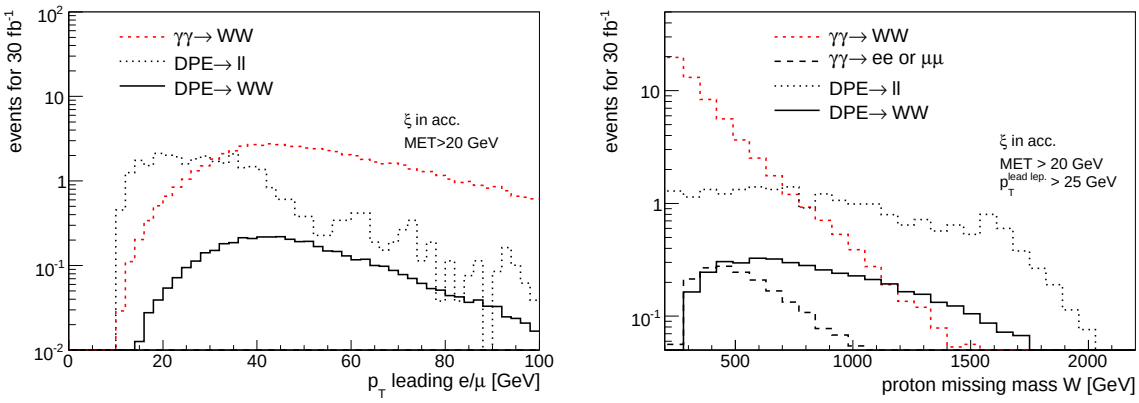

Figure 7.6: Signal $\gamma\gamma \to WW$ and background before the cut on the leading lepton transverse momentum p_T>25 GeV (left) and before the cut on the missing mass $W < 500\,\text{GeV}$ (right). Both of the constraints are aimed to suppress the DPE$\to ll$ production which plays the role of most important background for the measurement.

cut / process	$\gamma\gamma \to ee$	$\gamma\gamma \to \mu\mu$	$\gamma\gamma \to \tau\tau$	DPE$\to ll$	DPE$\to WW$	$\gamma\gamma \to WW$
gen. $p_T^{lep1} > 5\,\text{GeV}$	364500	364500	337500	295200	530	1198
$p_T^{lep1,2} > 10\,\text{GeV}$	24896	25547	177	17931	8.8	95
$0.0015 < \xi < 0.15$	10398	10535	126	11487	5.9	89
$\not{E}_T > 20\,\text{GeV}$	0	0.86	14	33	4.7	78
$W > 160\,\text{GeV}$	0	0.86	8.3	33	4.7	78
$\Delta\phi < 2.7\,\text{rad}$	0	0	0	14	3.8	61
$p_T^{lep} > 25\,\text{GeV}$	0	0	0	7.5	3.5	58
$W < 500$	0	0	0	1.0	0.67	51
$\xi < 0.1$	0	0	0	0.85	0.54	47
$\xi < 0.05$	0	0	0	0.40	0.25	32

Table 7.2: Background rejection to select $\gamma\gamma \to WW$ events for $\mathscr{L}$=30 fb^{-1}. The overall final signal is 51, 47, 32 signal events for the upper limit of the forward detector acceptance $\xi_{max} = 0.15$, 0.1, and 0.05, respectively, whereas the background is as low as 1.7, 1.4, 0.65 events. The statistical uncertainty on the expected number of events is at most 15% and is the largest for DPE$\to ll$. The Monte Carlo statistical uncertainty of events which could have fluctuated to 0 for two-photon productions after all cuts with the probability corresponding to 5σ for Gaussian distribution was found ~ 0.1 and is neglected with respect to the considered background.

ξ_{max}	signal [fb]	background [fb]	$S/\sqrt{B+1}$	$\mathscr{L}$=5 fb^{-1}	$\mathscr{L}$=10 fb^{-1}
0.05	1.69	0.06		7.5	14
0.1	1.57	0.05		7.1	13
0.15	1.07	0.02		5.1	9.1

Table 7.3: Signal and total background cross sections for $\gamma\gamma \to WW$, and the $S/\sqrt{B+1}$ ratio for luminosities 5 and 10 fb^{-1} as a function of the forward detector acceptance $0.0015 < \xi < \xi_{max}$ after all cuts mentioned in the text.

up to luminosities $\mathscr{L} = 2 \times 10^{33}\,\text{cm}^{-2}\text{s}^{-1}$ with thresholds of 20 GeV for single muons, and 18 GeV at the L1 and 22 GeV at the HLT for single electrons. For higher luminosities, the trigger menus will have to be studied and tuned. The FP220 can be included in the L1 trigger, whereas the FP420 will be included in the HLT triggers only due to their farther position from the IP. However, for the analysis concerning the leptonic decays of W/Z, it is not necessary to trigger on the scattered protons in the forward detectors because the events will be registered using the standard trigger system of ATLAS.

7.4.2 Results

The 5σ discovery of the $pp \to pWWp$ process could be achieved with about 5 fb^{-1} of data in the leptonic mode only. The signal significance is calculated as the P-value α, i.e. as the probability to find the number of observed events or more from the background alone, see (7.38) at the end of this chapter.

For 5 fb^{-1}, the confidence $1-\alpha$ expressed in numbers of standard deviations for the Gaussian distribution reads 5.3, 5.8, 6.2 for $\xi_{max} = 0.15, 0.1, 0.05$, respectively. correspond The number of signal and background events for 5 fb^{-1} and 10 fb^{-1} together with the value of the confidence level, is given in Table 7.3.

It should be noted that the process $pp \to pWWp$ can be discovered even with lower luminosity if one takes the full-leptonic and semi-leptonic decays of the two final states W into account. In [1] we considered a simplified analysis studying the two-photon WW production and the DPE$\to WW$ background only assuming that the overlaid background due to multiple interactions is removed with timing detectors. Events with at least one lepton above $p_T^{lep1} > 30$ GeV in addition to both proton tags in forward detectors $0.0015 < \xi_{1,2} < 0.15$ were selected. The full-hadronic W decays were rejected in order to remove the high QCD dijet background. It turned out that the process can be discovered already with 400 pb^{-1} of integrated luminosity by observing 11 signal events and 0.9 background yielding a confidence 5.8. Signal and background cross sections after the mentioned cuts are summarized in Table 7.4 with the corresponding signal-to-background ratios. The higher sensitivity to the two-photon WW production is of course due to the higher cross section when one takes into account the semi-leptonic decays. In this case, however, a new background arises from the central exclusive production of two quarks which was not studied. If one of the quarks radiates a W boson, the W+jet+jet final state mimics the semi-leptonic WW decays in two-photon production. This background process is planned to be included in future releases of FPMC to allow a complete study of the two-photon WW production even in the semi-leptonic decay mode [16].

ξ_{max}	signal [fb]	background [fb]	$S/\sqrt{B}$ $\mathscr{L}$=200 pb^{-1}	$S/\sqrt{B+1}$ $\mathscr{L}$=1 fb^{-1}
0.05	13.8	0.16	4.8	12
0.10	24.0	1.0	7.6	17
0.15	28.3	2.2	5.9	16

Table 7.4: Signal and background cross sections for $\gamma\gamma \to WW$ production with at least one lepton $p_T > 30\,\text{GeV}$ in the final state, and $S/\sqrt{B+1}$ ratios for two luminosities ($200\,\text{pb}^{-1}$ and $1\,\text{fb}^{-1}$) as a function of the forward detector acceptance $0.0015 < \xi < \xi_{max}$. The presence of at least one reconstructed lepton is required as mentioned in the text.

7.5 Anomalous coupling of W and Z to photon

The process $pp \to pWWp$ has been shown to be observable at the LHC. We are now in the position to use it to test some Beyond Standard Model (BSM) theories. The two-photon production of dibosons is very suitable to test the electroweak theory because it involves the trilinear and four-linear boson couplings which can be both probed with the same process. The test is based on deriving the sensitivities to parameters (coupling strengths) of new auxiliary interaction Lagrangians added to the SM, to simulate low energetic effects of some BSM theories whose typical scales (i.e the typical new particle masses) are beyond the reach of the LHC energies.

In this section we introduce the parameterization of a general BSM theory effect for the quartic couplings, show the cross section predictions and compare it with the considered background. This prescription will be used later to derive the sensitivities to parameters of the new Lagrangian terms.

7.5.1 Effective quartic couplings operators

As was already mentioned, the boson self-interaction in the SM is completely derived from the underlying $\text{SU}(2)_L \times \text{U}_Y(1)$ local symmetry. New vector boson fields are added to the Lagrangian to guarantee the invariance under this symmetry and their self-interactions emerge from the vector boson kinetic terms.

The vector boson masses are, however, more deeply linked with the Higgs field and the vacuum symmetries. The symmetry O(4) of the Higgs potential $V(\Phi) = -\mu^2\Phi^\dagger\Phi + \lambda(\Phi^\dagger\Phi)^2$ in (2.5) (recall that in the SM, the Higgs field is a complex doublet equivalent to four real fields) is in fact larger than the required $\text{SU}(2) \times \text{U}(1)$. It is known that the symmetry O(4) is locally isomorphic to $\text{O}(4) \simeq \text{SU}(2) \times \text{SU}(2)$. When the symmetry is spontaneously broken and one particular vacuum Φ_U is chosen, the vacuum symmetry is reduced. The vacuum is invariant under $\text{SU}(2)$ only. The weak isospin generators $\vec{\tau}/2$ corresponding to the broken symmetry constitute a triplet with respect to the vacuum symmetry sub-group. Very interestingly, this vacuum symmetry controls the value of the ρ parameter

$$\rho = \frac{M_W^2}{M_Z^2 \cos^2\theta_W} \tag{7.13}$$

and is usually called the custodial $\text{SU}(2)_C$ symmetry. The SM value of the parameter is $\rho = 1$ and it was very well confirmed experimentally (taking $m_W = 80.396 \pm 0.025$, $m_Z = 91.1876 \pm 0.021$, and $\sin^2\theta_W = 0.231 \mp 0.00023$ as in [9], we obtain $\rho = 1.011 \pm 0.001$ so it is known with a precision better

than 1%). In models with higher Higgs multiplets, ρ can significantly differ from 1. We will assume that this symmetry holds also in more general theory which we are about to parameterize and construct new effective Lagrangian terms in such a way to obey the deeper $SU(2)_C$ symmetry which is tightly linked with the precisely measured value of the ρ parameter.

The boson self-interactions in the SM (including their kinetic terms) can be conveniently represented by $-\frac{1}{4}W_{\mu\nu}\cdot W^{\mu\nu}$ where the vector

$$\vec{W}_\alpha = \begin{pmatrix} \frac{1}{\sqrt{2}}(W_\alpha^+ + W_\alpha^-) \\ \frac{i}{\sqrt{2}}(W_\alpha^+ - W_\alpha^-) \\ Z_\alpha/\cos\theta_W \end{pmatrix} \tag{7.14}$$

is a triplet of the custodial $SU(2)_C$ symmetry. The field tensor for W bosons appearing in the product is $\vec{W}_{\mu\nu} = \partial_\mu\vec{W}_\nu - \partial_\nu\vec{W}_\mu + g\vec{W}_\mu \times \vec{W}_\nu$.

In the following, the parameterization of the quartic couplings based on [17] is adopted. We concentrate on the lowest order dimension operators which have the correct Lorentz invariant structure and obey the $SU(2)_C$ custodial symmetry in order to fulfill the stringent experimental bound on the ρ parameter. Also, the $U(1)_Q$ gauge symmetry for those operators which involve photons is required.

There are only two four-dimension operators:

$$\begin{aligned} \mathscr{L}_4^0 &= \frac{1}{4}g_0 g_W(\vec{W}_\mu\cdot\vec{W}^\mu)^2 \\ \mathscr{L}_4^C &= \frac{1}{4}g_C g_W(\vec{W}_\mu\cdot\vec{W}_\nu)(\vec{W}^\mu\cdot\vec{W}^\nu) \end{aligned} \tag{7.15}$$

They are parameterized by the corresponding couplings g_0 and g_C. Using the explicit form of the $SU(2)_C$ triplet (7.5.1) we see that these Lagrangians do not involve photons. Clearly, it is not possible to construct any operator of dimension 5 since an even number of Lorentz indices is needed to contract the field indices. Thus the lowest order interaction Lagrangians which involve two photons are dim-6 operators. There are two of them:

$$\mathscr{L}^0 = -\frac{\pi\alpha}{4\Lambda^2}a_0 F_{\alpha\beta}F^{\alpha\beta}(\vec{W}_\mu\cdot\vec{W}^\mu) \tag{7.16}$$

$$\mathscr{L}^C = -\frac{\pi\alpha}{4\Lambda^2}a_C F_{\alpha\mu}F^{\alpha\nu}(\vec{W}^\mu\cdot\vec{W}^\nu) \tag{7.17}$$

parameterized with new coupling constants a_0, a_C, and the fine-structure constant $\alpha = e^2/(4\pi)$. The new scale Λ is introduced so that the Lagrangian density has the correct dimension four and is interpreted as the typical mass scale of new physics. Expanding the above formula using the definition of the $SU(2)_C$ triplet and expressing the product

$$\vec{W}_\mu\cdot\vec{W}_\nu = 2\left(W_\mu^+W_\nu^- + \frac{1}{2\cos^2\theta_W}Z_\mu Z_\nu\right) \tag{7.18}$$

we arrive at the following expression for the effective quartic Lagrangian

$$\begin{aligned} \mathscr{L}_6^0 &= \frac{-e^2}{8}\frac{a_0^W}{\Lambda^2}F_{\mu\nu}F^{\mu\nu}W^{+\alpha}W_\alpha^- - \frac{e^2}{16\cos^2\theta_W}\frac{a_0^Z}{\Lambda^2}F_{\mu\nu}F^{\mu\nu}Z^\alpha Z_\alpha \\ \mathscr{L}_6^C &= \frac{-e^2}{16}\frac{a_C^W}{\Lambda^2}F_{\mu\alpha}F^{\mu\beta}(W^{+\alpha}W_\beta^- + W^{-\alpha}W_\beta^+) - \frac{e^2}{16\cos^2\theta_W}\frac{a_C^Z}{\Lambda^2}F_{\mu\alpha}F^{\mu\beta}Z^\alpha Z_\beta \end{aligned} \tag{7.19}$$

In the above formula, we allowed the W and Z parts of the Lagrangian to have specific couplings, i.e. $a_0 \to (a_0^W, a_0^Z)$ and similarly $a_C \to (a_C^W, a_C^Z)$. From the structure of $\mathscr{L}_6^0$ in which the indices of photons and W are decoupled, we see that this Langrangian can be interpreted as the exchange of a neutral scalar particle whose propagater does not have any Lorentz index.

A such Lagrangian density conserves $C-$, $P-$, and $T-$parities separately and hence represents the most natural extension of the SM. The invariance can be seen right away using the definitions of the discrete symmetries

$$\begin{aligned} CW_\mu C^{-1} = -W_\mu^+ \qquad & CA_\mu C^{-1} = -A_\mu \\ PB_\mu(\vec{x},t)P^{-1} \quad = \quad & B^\mu(-\vec{x},t) \\ TB_\mu(\vec{x},t)T^{-1} \quad = \quad & B^\mu(\vec{x},-t) \end{aligned} \tag{7.20}$$

where $B^\mu = W^\mu, A^\mu$.

The current best experimental 95% c.l. limits on the above anomalous parameters come from the OPAL Collaboration where the quartic couplings were measured in $e^+e^- \to W^+W^-\gamma$, $e^+e^- \to \nu\bar{\nu}\gamma\gamma$ (for $WW\gamma\gamma$ anomalous couplings), and $e^+e^- \to q\bar{q}\gamma\gamma$ (for $ZZ\gamma\gamma$ couplings) at center-of-mass energies up to 209 GeV. The corresponding 95% confidence level limits on the anomalous coupling parameters were found [18]

$$\begin{aligned} -0.007\,\text{GeV}^{-2} < \quad & a_0^Z/\Lambda^2 \quad < 0.023\,\text{GeV}^{-2} \\ -0.029\,\text{GeV}^{-2} < \quad & a_C^Z/\Lambda^2 \quad < 0.029\,\text{GeV}^{-2} \\ -0.020\,\text{GeV}^{-2} < \quad & a_0^W/\Lambda^2 \quad < 0.020\,\text{GeV}^{-2} \\ -0.052\,\text{GeV}^{-2} < \quad & a_C^W/\Lambda^2 \quad < 0.037\,\text{GeV}^{-2} \end{aligned} \tag{7.21}$$

On the other hand, there has not been any direct constraint on the anomalous quartic couplings reported from the Tevatron so far.

7.5.2 Coupling form factors

The WW and ZZ two-photon cross sections rises quickly at high energies when any of the anomalous parameters are non-zero, as illustrated in Figure 7.7. It was mentioned at the beginning of this chapter that the tree-level unitarity uniquely restricts the $WW\gamma$ and in turn the $WW\gamma\gamma$ couplings to the SM values at asymptotically high energies. This implies that any deviation of the anomalous parameters a_0^Z/Λ^2, a_C^Z/Λ^2, a_0^W/Λ^2, a_C^W/Λ^2 from the SM zero value will eventually violate unitarity. Therefore, the cross sections have to be regulated by a form factor which vanishes in the high energy limit to construct a realistic physical model of the BSM theory. At LEP where the center-of-mass energy was rather low, the wrong high-energy behavior did not violate unitarity; however, it must be reconsidered at the LHC. We therefore modify the couplings as introduced in (7.19) by form factors that have the desired behavior, i.e. they do not modify the coupling at small energies but suppress it when the center-of-mass energy $W_{\gamma\gamma}$ increases such as

$$a \to \frac{a}{(1+W_{\gamma\gamma}^2/\Lambda^2)^n} \tag{7.22}$$

The exact form of the form factor is not imposed but rather only conventional and the same holds for the value of the exponent n. Λ^2 corresponds to the scale where new physics should appear and where the new type of production would regularize the divergent high energy behavior of the Lagrangians (7.19).

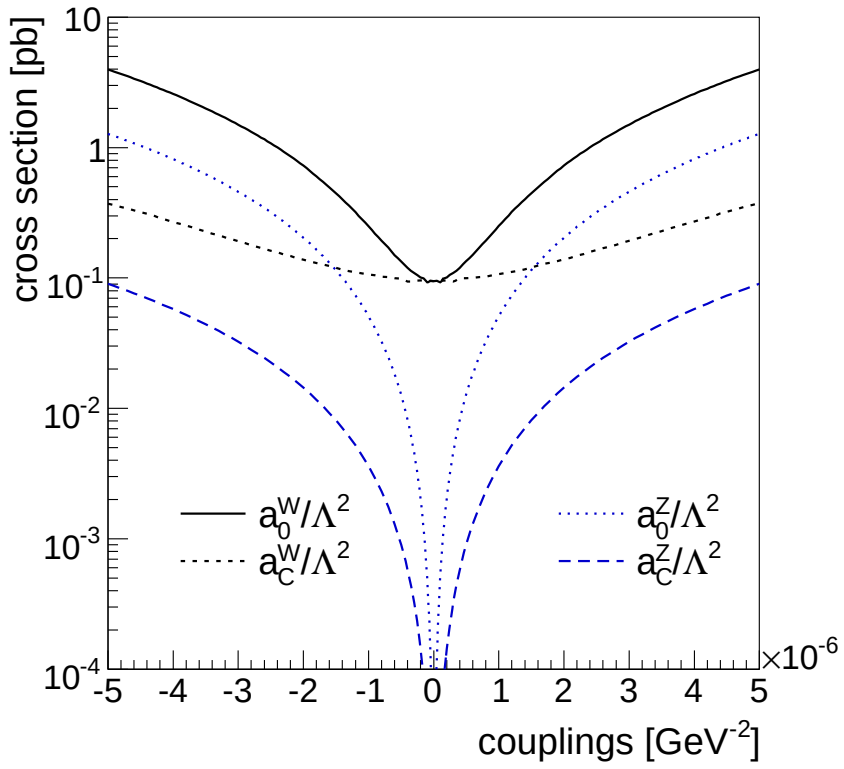

Figure 7.7: Enhancement of the $pp \to pWWp$ and $pp \to pZZp$ cross section at $\sqrt{s} = 14\,\text{TeV}$ with quartic-boson anomalous couplings a_0^W, a_C^W, and a_0^Z, a_C^Z from the SM values 95.6 fb and 0, respectively. The survival probability factor is not included.

The unitarity violation in $\gamma\gamma \to WW$ process was investigated in the recent study [10]. First, the scattering amplitude $\mathscr{A}$ of the $\gamma\gamma \to WW$ exchange was decomposed as a sum of partial wave amplitudes

$$a_J(\sqrt{s}) = \frac{1}{32}\int_{-1}^{1} \mathrm{d}(\cos\theta)\mathscr{A}(\sqrt{s},\cos\theta,a_0,a_C)P_J(\cos\theta) \tag{7.23}$$

where $P_J(\cos\theta)$ are the Legendre polynomials depending on the polar angle in the $\gamma\gamma$ center-of-mass. The unitarity condition of the J scattering amplitude reads

$$\beta \sum_{\lambda_1,\lambda_2} |a_J(\sqrt{s})|^2 \leq \frac{1}{4} \tag{7.24}$$

where $\beta = \sqrt{1-4m_W^2/s}$ is the velocity of a W boson in the center-of-mass frame and the λ_1, λ_2 indices denote the W polarization states. It was found that the scalar wave $J = 0$ is dominant, which we can easily understand since it produces Ws with longitudinal polarizations without any spin flip. For relevant values of a_0^W which are to be probed at the LHC, it was found that the unitarity is violated around $W_{\gamma\gamma} = 2\,\text{TeV}$ for the form factor exponent $n = 2$. We therefore adopt this type of form factor for the following study, i.e. the form factor

$$a \to \frac{a}{\left[1+(W_{\gamma\gamma}/2\,\text{TeV})^2\right]^2} \tag{7.25}$$

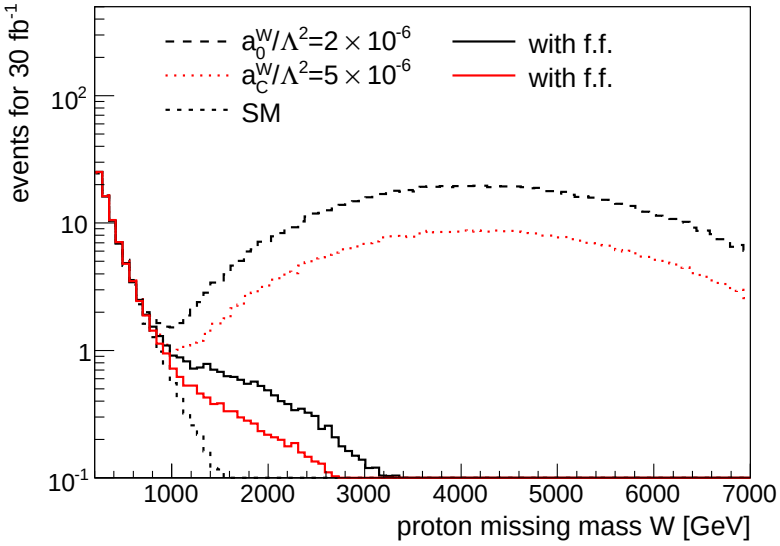

Figure 7.8: Missing mass distribution showing the effect of the form factor (7.22) on the cross section. The signal due to the anomalous coupling appears for masses $W > 800\,\text{GeV}$. Both leptons are in the detector acceptance and above $p_T > 10\,\text{GeV}$.

is introduced for all quartic couplings $a = a_0^W/\Lambda^2, a_0^Z/\Lambda^2, a_C^W/\Lambda^2, a_C^Z/\Lambda^2$.

7.5.2.1 Total cross section for quartic couplings

We are ready to study the phenomenological consequences of the new terms in the Lagrangian. The anomalous effective model was implemented in the FPMC generator (see Section 4.3.2). This allowed us to compare the studied signal due to anomalous couplings directly with all the backgrounds that leave the proton intact and create two leptons, electrons or muons, in the central detector.

As shown in Figure 7.7, the anomalous couplings in $pp \to pWWp$ and $pp \to pZZp$ processes augment the cross section from their SM values 95.6 fb and 0. It is the highest for a_0^W/Λ^2, whereas it is the smallest for a_0^Z/Λ^2. Note that the distribution is symmetric so the sensitivity to positive and negative values of the coupling is the same. The suppression of the cross section due to the form factors is shown in Figure 7.8. It is important to stress that this effect is large and it has to be taken into account when deriving the sensitivities to the anomalous couplings. In the opposite case, we would quote the results for a model which does not have a good physical interpretation already at LHC energies and would be meaningless.

7.5.3 High p_T effect

In Figure 7.9, the p_T distributions of the signal due to quartic couplings and the background are superimposed. As expected, the signal due to anomalous coupling appears at high transverse momentum, or at high masses. The general strategy of the analysis is therefore to select high p_T leptons together with an exclusivity requirement which allows to collect clean two-photon events with unaltered protons in the final state. Since the cross section enhancement due to anomalous couplings is very large, the test of

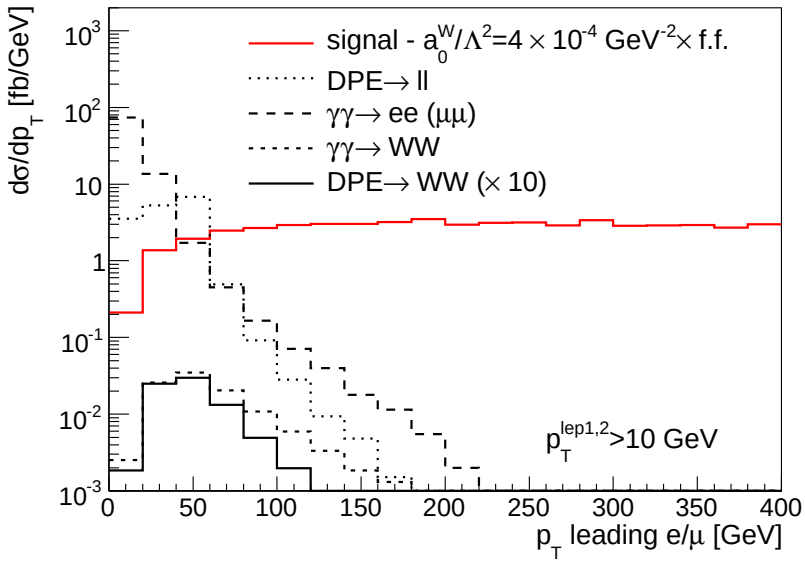

Figure 7.9: Contributions of various background processes to the signal with anomalous coupling $a_0^W/\Lambda^2 = 3\times10^{-4}\,\mathrm{GeV}^{-2}$ with the coupling form factors taken into account at generator level. The signal due to the anomalous coupling manifest itself at high transverse lepton momenta

anomalous parameters could be carried out even at low luminosities.

After this theoretical introduction we first focus on deriving the sensitivities using the low luminosity runs without forward detectors and then proceed to the same discussion at high luminosity runs including the forward detectors.

7.6 Sensitivities to anomalous QGC at low luminosity

Since the project to install forward detectors is still under development and awaits for its approval within ATLAS, the tagging of the scattered protons will not be possible at the start of the LHC. On the other hand, one can use a different technique to identify the exclusive two-photon events. Since there will be no (or few) multiple interaction present during early running, the exclusive events can be selected by requesting two leptons in the detector and nothing else. This in practice means requesting low number of tracks, less or equal than 2 for the full-leptonic decays of WW, and no hadronic activity in the calorimeter above noise level. Requesting no hadronic activity is achieved by registering only the cells with energies above a specified energy threshold which is optimized in order to obtain the best resolution in reconstructing the size of the empty regions in the calorimeter. A dedicated discussion of the definition of rapidity gaps devoid of particles in the calorimeter will be covered in Chapter 8.

Assuming that the integrated luminosity without multiple interactions ranges from $10\,\mathrm{pb}^{-1} - 100\,\mathrm{pb}^{-1}$ which we have discussed in Section 3.1.2, we perform the sensitivity study to anomalous parameters based on the exclusivity requirement. It is foreseen to operate the LHC at a somewhat lower center-of-mass energy $\sqrt{s} = 10\,\mathrm{TeV}$ than the nominal one. In Table 7.5 the total cross sections for all background processes (including the SM two-photon WW production) are summarized for this running scenario. The sensitivities are derived with a simple counting experiment to distinguish the signal due to anomalous

process	total cross section	flag
$\gamma\gamma \to WW$	86 fb	`YWWMAX=1.`
$\gamma\gamma \to ll$ ($p_T^{lep1} > 5\,\text{GeV}$)	32.0 pb	`PTMIN=5.`
DPE$\to ll$	4.9 pb	`EMMIN=10, YWWMAX=0.2`
DPE$\to WW$	3.9 fb	`YWWMAX=0.2`

Table 7.5: Total cross sections for SM processes which consitute the background to the quartic anomalous signal at $\sqrt{s} = 10\,\text{TeV}$ multiplied by the gap survival probability factor (0.9 for QED and 0.03 for DPE processes). Process specific flags for the FPMC event generation are shown in the last column: `EMMIN` is the minimum Drell-Yan invariant mass and `YWWMAX` is the maximum allowed momentum fraction loss ξ.

couplings from the background. The signal selection is treated in different ways for WW and ZZ.

7.6.1 Rejecting background for WW signal

The requirement of $n_{tracks} \leq 2$ removes the DPE background (the expected number of events for $\mathscr{L} = 10\,\text{pb}^{-1}$ is 0.251 ± 0.002 for DPE$\to ll$ and $5.5 \cdot 10^{-5} \pm 1.4 \cdot 10^{-6}$ for DPE$\to WW$) and also the non-diffractive WW background. This cut might be modified in real data but the idea is simple. Hadrons either originating in non-diffractive events or due to pomeron remnants show many tracks and we require 2 leptons and no other reconstructed object. The leading lepton p_T dependence in Figure 7.10 shows the signal and background: $\gamma\gamma \to WW, WW \to ee$ or $\mu\mu$. The final sample is selected with $p_T^{lep1} > 160\,\text{GeV}$ where the contribution from the background is negligible. The missing $\not{E}_T > 20\,\text{GeV}$ was applied as well even though our background was already low. This only ensures that the expected background is kept at 0 level (this holds for the $100\,\text{pb}^{-1}$ luminosity as well) and any observed events passing these stringent requirements can be interpreted as a signal due to anomalous couplings. To summarize, all the applied cuts are

$$p_T^{lep1} > 160\,\text{GeV},\ p_T^{lep2} > 10\,\text{GeV},\ n_{tracks} \leq 2,\ \not{E}_T > 20\,\text{GeV} \tag{7.26}$$

7.6.2 Rejecting background for ZZ signal

The ZZ signal is background free because two leptons of the same charge are created when both Zs decay leptonically. The requirement which was used to select the ZZ signal was either to have ≥ 2 leptons of the same charge, or ≥ 3 leptons. Leptons (e, μ) have to have a transverse momentum $p_T^{lep} > 25\,\text{GeV}$. In addition, no jet can be seen in the event. Such requirements are sufficient to reject all two-photon or DPE exchange background. The charge misidentification can play a role in this scenario. For electrons and muons of $p_T = 500\,\text{GeV}$ (which is about where the ZZ signal dominates) the probability that the charge will be wrongly reconstructed in ATLAS is about 1% [19] and the effect is rather small (the charge misidentification probability for muons is smaller for $p_T < 2\,\text{TeV}$ than for electrons). The fraction of events with two leptons of the same charge is about 0.5. All our ZZ signal is at high mass and the cut $p_T^{lep1} > 160\,\text{GeV}$ can be used without affecting the signal. Being away from the Z and W pole might be a useful additional constrain in a real analysis helping to suppress the background due to multiple

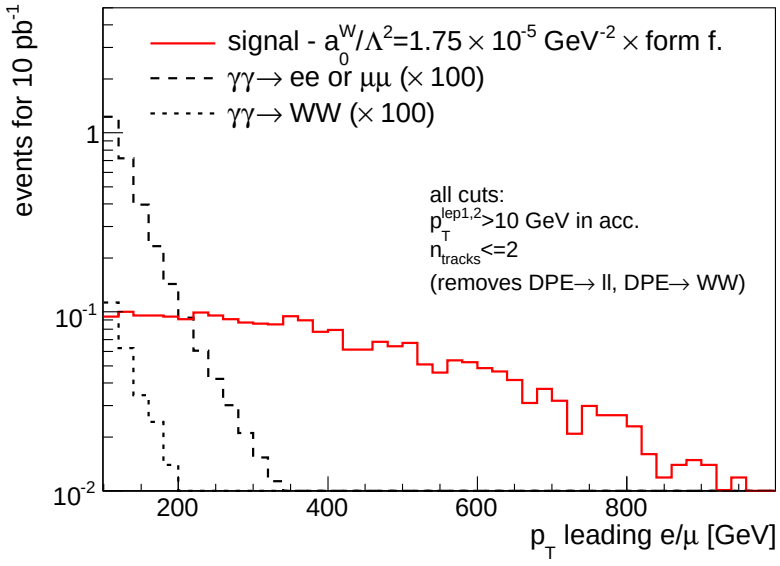

Figure 7.10: p_T distribution of the leading leptons for signal and two-photon background (scaled by 100) at low luminosity using $\mathscr{L} = 10\,\mathrm{pb}^{-1}$ after all cuts. The other DPE background was rejected completely with $n_{tracks} \leq 2$.

events for $10\,\mathrm{pb}^{-1}$

cut / process	$\gamma\gamma \to ee$	$\gamma\gamma \to \mu\mu$	$\gamma\gamma \to \tau\tau$	DPE$\to ll$	DPE$\to WW$	$\gamma\gamma \to WW$
$p_T^{lep1,2} > 10\,\mathrm{GeV}$	9.2	9.0	0.062	3.3	0.0016	0.022
$n_{tracks} \leq 2$	9.2	9.0	0.053	0.25	$5.5 \cdot 10^{-5}$(26%)	0.021
$p_T^{lep1} > 160\,\mathrm{GeV}$	$1.5 \cdot 10^{-3}$	$1.6 \cdot 10^{-3}$	$2.3 \cdot 10^{-5}$	0	0	0
$\not{E}_T > 20\,\mathrm{GeV}$	$1.0 \cdot 10^{-7}$(38%)	$2.3 \cdot 10^{-4}$	$2.2 \cdot 10^{-5}$	0	0	0

Table 7.6: Suppression of the number of background events for $\mathscr{L}$=$10\,\mathrm{pb}^{-1}$ at low luminosity with no multiple interaction. All non-zero values have a statistical precision better than 1% except when the relative uncertainty is specified in parentheses explicitly.

interactions at higher instanteneous luminosity which will be dominant at smaller transverse momenta. All cuts are:

$$(n_{lep} \geq 2,\ 2\,\text{of same charge}) \text{ or } n_{lep} \geq 3,\ n_{tracks} \leq 2,\ p_T^{lep1} > 160\,\mathrm{GeV},\ p_T^{lep2} > 25\,\mathrm{GeV},\ n_{jet} = 0 \quad (7.27)$$

7.6.3 Results at low luminosity

The expected number of signal events for $\mathscr{L} = 10\,\mathrm{pb}^{-1}$ is depicted in Figure 7.11 after all mentioned requirements. In this case, only one of the anomalous parameters is varied while the others are kept to their SM values, i.e. to zero. The event yield was calculated for a set of values of anomalous parameters and interpolated using the SPLINE interpolation method. The quality of the interpolation was checked and was found in good agreement when additional points, not used for the interpolation,

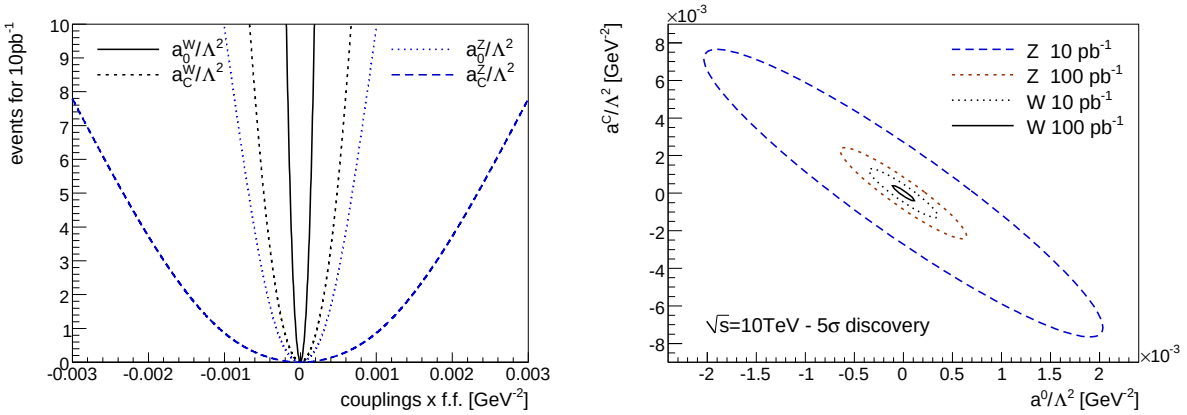

Figure 7.11: Number of events for the signal (left) due to different anomalous couplings after all the cuts (see text) for $\mathscr{L}$=10 pb^{-1}, and 5σ discovery contours (right) for all the WW and ZZ quartic couplings at $\sqrt{s} = 10$ TeV for $\mathscr{L}$=10 pb^{-1}and $\mathscr{L}$=100 pb^{-1}.

were added. This allowed us a fast calculation of the sensitivities for which the signal cross section has to be determined for many parameters.

The limits on the anomalous parameters were calculated according to formula (7.39), where in this case the mean value of the background is $\mu_b = 0$. The formula was solved numerically for the significance α corresponding to 95%, 3σ, and 5σ as for a variable distributed according to gaussian distribution. The resulting exclusion sensitivities are shown in Table 7.7 where also limits without taking into account the coupling form factors are mentioned. We see that the effect of the form factor is important and accounts approximately to a factor 5 difference. With 10 times higher luminosity it is possible to improve the parameter limits by another factor 3 or so as demonstrated in Table 7.8.

Of course we can ask the question how the limits look like when two of the parameters are varied at the same time. Since the analysis is different for W and Z events, the limits are investigated in the two dimensional plane $a_0 \times a_C$ for W and Z production separately. The 5σ discovery limits make elliptic contours as shown in Figure 7.11 (right) because the cross section has a valley in the $a_0 \times a_C$ plane. The longer axis of the valley is in the second and fourth quadrants where $a_0 \times a_C < 0$, which means that the two Lagrangian terms either for W or Z coupling in (7.19) interfere and partially compensate each other.

Let us now make a comparison with the current best quartic parameter limits (7.21) as they were measured by the OPAL collaboration. It is important to note that even with a limited amount of collected data, the limits on the parameters can be improved by more than a factor of 100 for all parameters except a_C^Z where the improvement is only a factor of 20. It makes of course such a measurement very interesting. For tens of pb^{-1} we would detect tens of $\gamma\gamma \to ll$ events which should give us the confidence that the events with two leptons and nothing else, the exclusive events, are well selected. Using the same techniques, one should look for high p_T dileptons for relevant anomalous signal in data.

7.7 Sensitivities at high luminosity

At high luminosity, the situation is particularly different. As it was already advertised, the exclusivity requirement of having a small number of tracks as reconstructed objects and nothing else in the detector

		limits $[10^{-5}\,\mathrm{GeV}^{-2}]$			
	form factor	$\lvert a_0^W/\Lambda^2\rvert$	$\lvert a_C^W/\Lambda^2\rvert$	$\lvert a_0^Z/\Lambda^2\rvert$	$\lvert a_C^Z/\Lambda^2\rvert$
95% c.l	$\Lambda_{cut}=\infty$	1.7	6.6	13	47
	$\Lambda_{cut}=2\,\mathrm{TeV}$	10	35	52	180
3σ evidence	$\Lambda_{cut}=\infty$	2.5	9.0	18	65
	$\Lambda=2\,\mathrm{TeV}$	14	50	73	250
5σ discovery	$\Lambda_{cut}=\infty$	4.0	14	28	100
	$\Lambda_{cut}=2\,\mathrm{TeV}$	22	74	100	300

Table 7.7: 95% c.l. interval, 3σ evidence, and 5σ discovery potential on the $WW\gamma$ anomalous quartic parameters using $\mathscr{L}$=10 pb^{-1} of data without multiple interactions, and with or without the form factors applied.

		limits $[10^{-5}\,\mathrm{GeV}^{-2}]$			
	form factor	$\lvert a_0^W/\Lambda^2\rvert$	$\lvert a_C^W/\Lambda^2\rvert$	$\lvert a_0^Z/\Lambda^2\rvert$	$\lvert a_C^Z/\Lambda^2\rvert$
95% c.l	$\Lambda_{cut}=\infty$	0.55	2.1	4.0	16
	$\Lambda_{cut}=2\,\mathrm{TeV}$	3.3	11	17	59
3σ evidence	$\Lambda_{cut}=\infty$	0.76	2.9	5.6	22
	$\Lambda=2\,\mathrm{TeV}$	4.6	15	24	82
5σ discovery	$\Lambda_{cut}=\infty$	1.2	4.6	8.8	33
	$\Lambda_{cut}=2\,\mathrm{TeV}$	7.3	24	37	125

Table 7.8: 95% c.l. interval, 3σ evidence, and 5σ discovery potential on the $WW\gamma\gamma$ anomalous quartic parameters using $\mathscr{L}$=100 pb^{-1} of data without multiple interactions, and with or without the form factors applied.

can no longer be used because of the high number of multiple interactions occurring at the same time. We assume that the intact protons are tagged with the forward detectors and the timing of the protons is measured to suppress the overlaid background. In practice, it will be still possible to request a limited number of high p_T objects at high instantaneous luminosity but the exact selection has to be studied with data. The background suppression to WW and ZZ signal is again treated separately.

7.7.1 Rejecting background for WW signal

At high luminosity, the forward detector acceptance (high cut on $\xi < 0.15$) removes the highest mass events and the signal due to anomalous coupling which appears at high masses is not observed. The background is then a bigger issue. We have to define better tuned cuts than at low luminosity where the number of expected events for the background was small.

The WW events which give a hit in both forward detectors are first selected with $\not{E}_T > 20\,\mathrm{GeV}$. The $\not{E}_T$ dependence is depicted in Figure 7.12 (left) for the signal $a_0^W/\Lambda^2 = 2\times10^{-6}\,\mathrm{GeV}^{-2}$ and the background. Note that the signal is barely distinguishable from the SM $\gamma\gamma\to WW$ process. On the other hand, processes in which lepton pairs are created directly through $\gamma\gamma$ or DPE exchange are greatly sup-

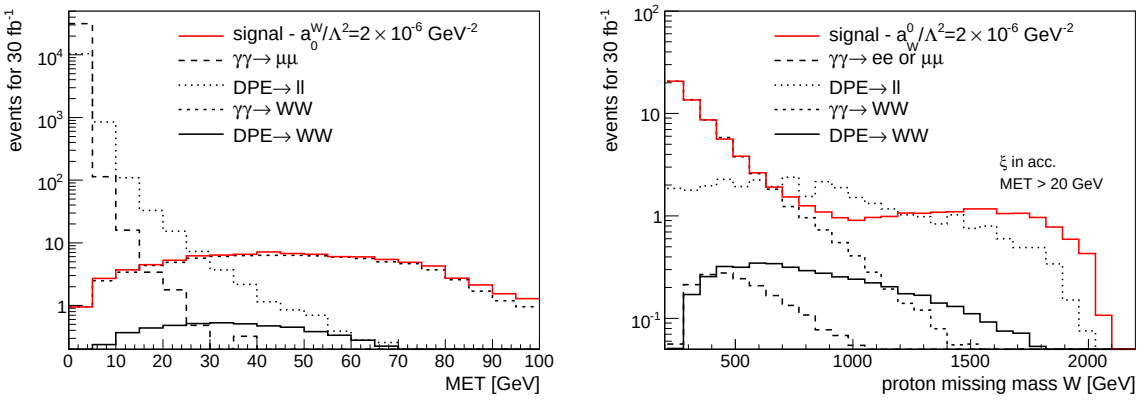

Figure 7.12: Missing transverse energy distribution $\not{E}_T$ in the AFP detector acceptance cut (left) and proton missing mass (right) in the AFP acceptance and after the cut on $\not{E}_T > 20\,\text{GeV}$ cut for signal and all backgrounds with $\mathscr{L}$=30 fb^{-1}.

pressed. The next cut focuses on the high diphoton mass $W_{\gamma\gamma}$ where the signal is preferably enhanced. In Figure 7.12 (right) we see that the signal due to anomalous coupling is well selected if the reconstructed missing mass in the forward detectors is $W > 800\,\text{GeV}$. It was verified that such selection applies for all anomalous parameters in question in a very similar way, i.e. that the $W > 800\,\text{GeV}$ retains the interesting signal for a wide range of anomalous parameters. To summarize, the following cuts are used to select the anomalous signal at high luminosity

$$p_T^{lep1} > 160\,\text{GeV},\, p_T^{lep2} > 10\,\text{GeV},\, 0.0015 < \xi < 0.15,\, \not{E}_T > 20\,\text{GeV},\, W > 800\,\text{GeV},$$
$$M_{ll} \notin \langle 80, 100 \rangle\,,\, \Delta\phi < 3.13 \tag{7.28}$$

The most dominant background which remains is the DPE$\rightarrow ll$ production. A large part of this background is removed by requesting the angle between reconstructed leptons $\Delta\phi < 3.13$ as illustrated in Figure 7.13 (top). This removes also the potential two-photon dileptons. However, the $\Delta\phi$ cut cannot be arbitrarily relaxed because we would remove part of the signal as well. Finally, the p_T^{lep} distribution after all mentioned constrains is shown on the bottom of Figure 7.13 (bottom). The remaining background is composed not only from the expected $\gamma\gamma \rightarrow WW$ production but also from DPE$\rightarrow ll$ by about an equal amount.

The successive effect of all cuts and their rejection power of the background is summarized in Table 7.9 where the number of events is shown for $\mathscr{L} = 30\,\text{fb}^{-1}$. The total number of background events is thus reduced to 0.90 ± 0.05.

7.7.2 Rejection background for ZZ signal

The rejection of the possible non-diffractive background which is the only background follows the same strategy as at low luminosity. In addition, we have to consider the forward detector acceptance. The complete set of used cuts is

$$(n_{lep} \geq 2,\ 2\,\text{of same charge}) \text{ or } n_{lep} \geq 3,\, 0.0015 < \xi < 0.15,\, p_T^{lep1} > 160\,\text{GeV},\, p_T^{lep2} > 25\,\text{GeV},\, n_{jet} = 0 \tag{7.29}$$

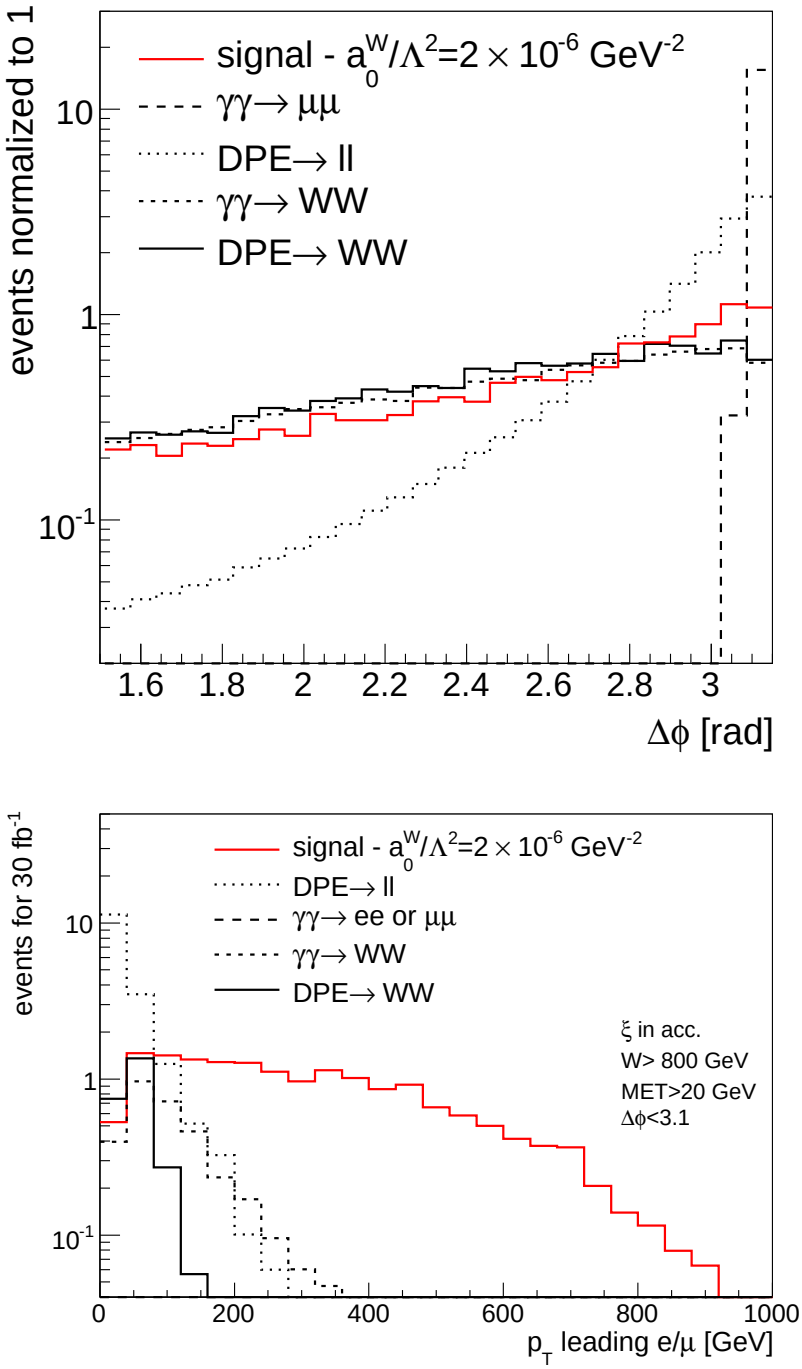

Figure 7.13: Angle between detected leptons (top) and p_T distribution of the leading lepton (bottom) after all cuts as mentioned in the text for signal and background. The events are normalized for $\mathscr{L}$=30 fb^{-1}.

	events for $30\,\mathrm{fb}^{-1}$					
cut / process	$\gamma\gamma \to ee$	$\gamma\gamma \to \mu\mu$	$\gamma\gamma \to \tau\tau$	$\gamma\gamma \to WW$	DPE$\to ll$	DPE$\to WW$
gen. $p_T^{lep1} > 5\,\mathrm{GeV}$	364500	364500	337500	1198	295200	530
$p_T^{lep1,2} > 10\,\mathrm{GeV}$	24895	25547	177	99	18464	8.8
$0.0015 < \xi < 0.15$	10398	10534	126	89	11712	6.0
$\not{E}_T > 20\,\mathrm{GeV}$	0	0.86	14	77	36	4.7
$W > 800\,\mathrm{GeV}$	0	0.27	0.15	3.2	16	2.5
$M_{ll} \notin < 80, 100 >$	0	0.27	0.15	3.2	13	2.5
$\Delta\phi < 3.13$	0	0	0.10	3.2	12	2.5
$p_T^{lep1} > 160\,\mathrm{GeV}$	0	0	0	0.69	0.20	0.024

Table 7.9: Rejection of the background by the successive application of the selection cuts. The number of events is normalized to $\mathscr{L} = 30\,\mathrm{fb}^{-1}$ of integrated luminosity. The lepton index lep corresponds to electrons or muons. The DPE$\to ll$ was generated with a minimum Drell-Yan mass 10 GeV. The largest statistical uncertainty is 7% for DPE$\to ll$ after all cuts.

	events for $30\,\mathrm{fb}^{-1}$	
cut / couplings (with f.f.)	$\left\|a_0^W/\Lambda^2\right\| = 5.4 \cdot 10^{-6}\ \mathrm{GeV}^{-2}$	$\left\|a_C^W/\Lambda^2\right\| = 20 \cdot 10^{-6}\ \mathrm{GeV}^{-2}$
$p_T^{lep1,2} > 10\,\mathrm{GeV}$	202	200
$0.0015 < \xi < 0.15$	116	119
$\not{E}_T > 20\,\mathrm{GeV}$	104	107
$W > 800\,\mathrm{GeV}$	24	23
$M_{ll} \notin < 80, 100 >$	24	23
$\Delta\phi < 3.13$	24	22
$p_T^{lep1} > 160\,\mathrm{GeV}$	17	16

Table 7.10: Selection of the signal by the successive application of the cuts. The number of events is given for integrated luminosity of $\mathscr{L} = 30\,\mathrm{fb}^{-1}$. The lepton index lep correspond to electrons or muons.

7.7.3 Limits - high luminosity

The procedure to derive limits for the anomalous parameters proceeds in the same way as before. The number of events after all cuts as a function of the anomalous parameters, see Figure 7.14 (left), is used to calculate the exclusion upper limits according to formula (7.39). The results are summarized in Tables 7.11 and 7.12 for $\mathscr{L} = 30\,\mathrm{fb}^{-1}$ and $\mathscr{L} = 200\,\mathrm{fb}^{-1}$, respectively.

Comparing obtained the values with the OPAL limits (7.21) we see that the improvement which can be obtained with a collected luminosity $30\,\mathrm{fb}^{-1}$ corresponding approximately to three years of running with the forward detectors, we can constrain the anomalous quartic coupling better by a factor of 5000 for all couplings except a_C^Z/Λ^2 where the improvement is about a factor 5 worse. With the full $\mathscr{L}$=200 fb^{-1} luminosity, the improvement reaches about a factor of 10000.

		limits $[10^{-6}\,\mathrm{GeV}^{-2}]$			
	form factor	$\lvert a_0^W/\Lambda^2\rvert$	$\lvert a_C^W/\Lambda^2\rvert$	$\lvert a_0^Z/\Lambda^2\rvert$	$\lvert a_C^Z/\Lambda^2\rvert$
95% c.l	$\Lambda_{cut}=\infty$	1.2	4.2	6.0	27
	$\Lambda_{cut}=2\,\mathrm{TeV}$	2.6	9.4	9.4	35
3σ evidence	$\Lambda_{cut}=\infty$	1.6	5.8	7.4	33
	$\Lambda_{cut}=2\,\mathrm{TeV}$	3.6	13	11	43
5σ discovery	$\Lambda_{cut}=\infty$	2.3	9.7	9.6	43
	$\Lambda_{cut}=2\,\mathrm{TeV}$	5.4	20	15	55

Table 7.11: 95% c.l. interval, 3σ evidence, and 5σ discovery potential on the $WW\gamma\gamma$ and $ZZ\gamma\gamma$ anomalous quartic parameters using $\mathscr{L}$=30 fb^{-1} of data without multiple interactions, and with or without the form factors applied.

		limits $[10^{-6}\,\mathrm{GeV}^{-2}]$			
	form factor	$\lvert a_0^W/\Lambda^2\rvert$	$\lvert a_C^W/\Lambda^2\rvert$	$\lvert a_0^Z/\Lambda^2\rvert$	$\lvert a_C^Z/\Lambda^2\rvert$
95% c.l	$\Lambda_{cut}=\infty$	0.7	2.4	2.3	10
	$\Lambda_{cut}=2\,\mathrm{TeV}$	1.4	5.2	3.7	14
3σ evidence	$\Lambda_{cut}=\infty$	0.85	3.0	2.9	13
	$\Lambda=2\,\mathrm{TeV}$	1.8	6.7	4.6	17
5σ discovery	$\Lambda_{cut}=\infty$	1.2	4.3	3.7	17
	$\Lambda_{cut}=2\,\mathrm{TeV}$	2.7	9.6	5.9	22

Table 7.12: 95% c.l. interval, 3σ evidence, and 5σ discovery potential on the $WW\gamma\gamma$ and $ZZ\gamma\gamma$ anomalous quartic parameters using $\mathscr{L}$=200 fb^{-1} of data without multiple interactions, and with or without the form factors applied. 95% c.l. limit, 3σ evidence, and 5σ discovery potential correspond to the values of the couplings outside of the quoted intervals.

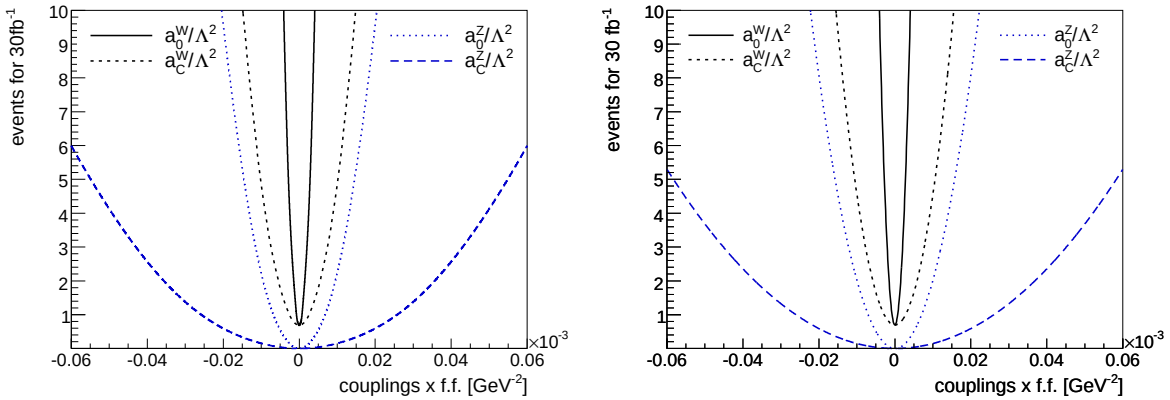

Figure 7.14: Number of events for signal (left) due to different values of anomalous couplings after all cuts (see text) for $\mathscr{L}$=30 fb^{-1}, and 5σ discovery contours (right) for all the WW and ZZ quartic couplings at $\sqrt{s}=14\,\mathrm{TeV}$ for $\mathscr{L}$=30 fb^{-1}and $\mathscr{L}$=200 fb^{-1}.

7.8 Anomalous triple gauge $WW\gamma$ coupling

The investigation of the triple gauge $WW\gamma$ couplings is perhaps less interesting than the quartic ones because they have already been quite well constrained at LEP. Nevertheless, we carry out a similar analysis for the TGC as well. In this section, the effective Lagrangian involving trilinear boson couplings with a photon will be introduced and used to study the sensitivities to the coupling parameters in two-photon events. Note that the lowest dimensional triple gauge boson operator $ZZ\gamma$ is of dimension six, the effect of this coupling will not be studied here.

First, the effective Lagrangians describing the triple gauge couplings are introduced. Next, the total cross section is evaluated. Finally, we define the signal selection strategies for each of the triple anomalous parameters and determine the sensitivites.

7.8.1 Effective triple gauge boson operators

The most general form of an effective Lagrangian $\mathscr{L}_{WW\gamma}$ involving two charged vector bosons W and one neutral vector boson has only seven terms which have the correct Lorentz structure (see [15] for details). This is because only seven out of the nine helicity states of the W pair production can be reached with the spin-1 vector boson exchange. The other two states have both W spins pointing in the same direction with an overall spin 2.

Further more, only three out of the seven operators preserve the P,C and T discrete symmetries separately. We restrict ourselfs to study this subset of operators. They are the following

$$\mathscr{L}/g_{WW\gamma} = i(W^+_{\mu\nu}W^\mu A^\nu - W_{\mu\nu}W^{+\mu}A^\nu) + i\kappa^\gamma W^+_\mu W_\nu A^{\mu\nu} + i\frac{\lambda^\gamma}{M_W^2}W^+_{\rho\mu}W^\mu{}_\nu A^{\nu\rho} \tag{7.30}$$

where the tensor is $W_{\mu\nu} = \partial_\mu W_\nu - \partial_\nu W_\mu$, $g_{WW\gamma} = e$ is the trilinear coupling in the SM model whose strength is fixed by the charge of the W, and κ^γ and λ^γ are the anomalous parameters, and their values are 1 and 0 in the SM, respectively. They can be related to the magnetic μ_W and electric Q_W moments of the W^+ by

$$\begin{aligned} \mu_W &= \frac{e}{2m_W}(1+\Delta\kappa^\gamma+\lambda^\gamma) \\ Q_W &= \frac{e}{m_W^2}(\Delta\kappa^\gamma-\lambda^\gamma) \end{aligned} \tag{7.31}$$

where $\Delta\kappa^\gamma \equiv \kappa^\gamma - 1$ describes the deviation of the parameter from the SM value. (it is straight forward to verify that (7.30) gives the SM trilinear Lagrangian (7.3) for $\kappa^\gamma = 1$ and $\lambda^\gamma = 0$. Our convention differs from the one in [15] by a factor of -1).

The current best 95% c.l. limits on anomalous couplings come from the combined fits of all LEP experiments [20].

$$-0.098 < \Delta\kappa^\gamma < 0.101 \quad -0.044 < \lambda^\gamma < 0.047 \tag{7.32}$$

The CDF collaboration presented the most stringent constraints on $WW\gamma$ coupling measured at hadron colliders [21]

$$-0.51 < \Delta\kappa^\gamma < 0.51 \qquad -0.12 < \lambda^\gamma < 0.13 \tag{7.33}$$

analyzing the $W\gamma$ events in parton-parton interactions. Even though the LEP results are more precise than the results from the hadron collider, there is always a mixture of γ and Z exchanges present in the process $e^+e^- \to WW$ from which the couplings are extracted. The two-photon WW production has the advantage that pure $W-\gamma$ couplings are tested and no SM Z exchange is present.

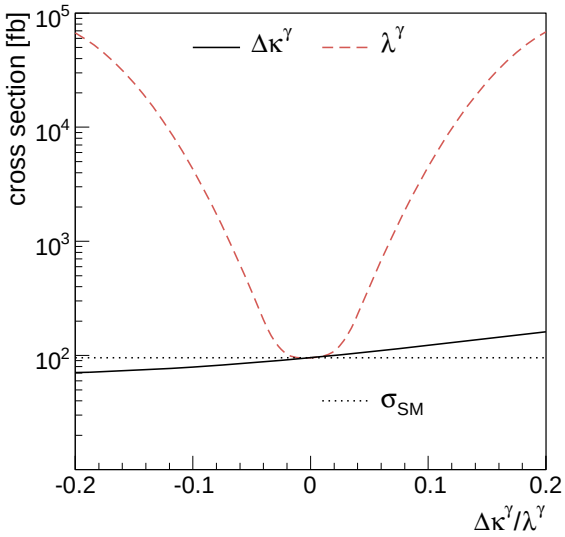

Figure 7.15: The enhancement of the total cross section with the triple-boson anomalous couplings $\Delta\kappa^\gamma$, λ^γ. The rise of the cross section due to λ^γ is well pronounced whereas the dependence on $\Delta\kappa^\gamma$ is modest (the tail for large negative $\Delta\kappa^\gamma$ where cross section increases is not shown).

7.8.2 Total cross section

The effect of the two anomalous couplings is different. The total cross section is much more sensitive to the anomalous coupling λ^γ. As shown in Figure 7.15, the SM cross section $\sigma_{SM} = 95.6\,\text{fb}$ is a global minimum with respect to the λ^γ parameter. For $\Delta\kappa^\gamma$ the minimum also exists but for large negative values which have already been excluded by experiments. The last term proportional to λ^γ in (7.30) does not have a dimensionless coupling. With simple dimensional consideration we see that the $\gamma\gamma \to WW$ scattering amplitude which has to be dimensionless will have the form $\sim \frac{s^2}{M_W^4}$ and will therefore be quickly rising as a function of the two-photon mass $M_{\gamma\gamma}$. This is seen in Figure 7.16 where the cross section is shown as a function of the momentum fraction loss of the proton. $\Delta\kappa^\gamma$ enhances the overall normalization of the distribution (left) whereas λ^γ gives rise to the ξ tail (right) as anticipated.

7.8.3 Coupling form factors

The rise of the cross section for anomalous TGC at high energy leads again to the violation of unitarity. The enhancement of the cross section has to be again regulated by appropriate from factors. We apply the same form factors as already mentioned for the quartic couplings (7.22). This ensures that we can compare our results to those which were obtained in standard non-diffractive channels

7.8.4 Signal selection

The limits obtained at LEP and the Tevatron are already very stringent, more than in the case of quartic anomalous couplings. Let us however remind that triple and genuine quartic couplings are not related in any way. Hence, the analysis which has been performed above for the quartic couplings has its own importance irrespective of the triple ones. The production cross sections corresponding to the current

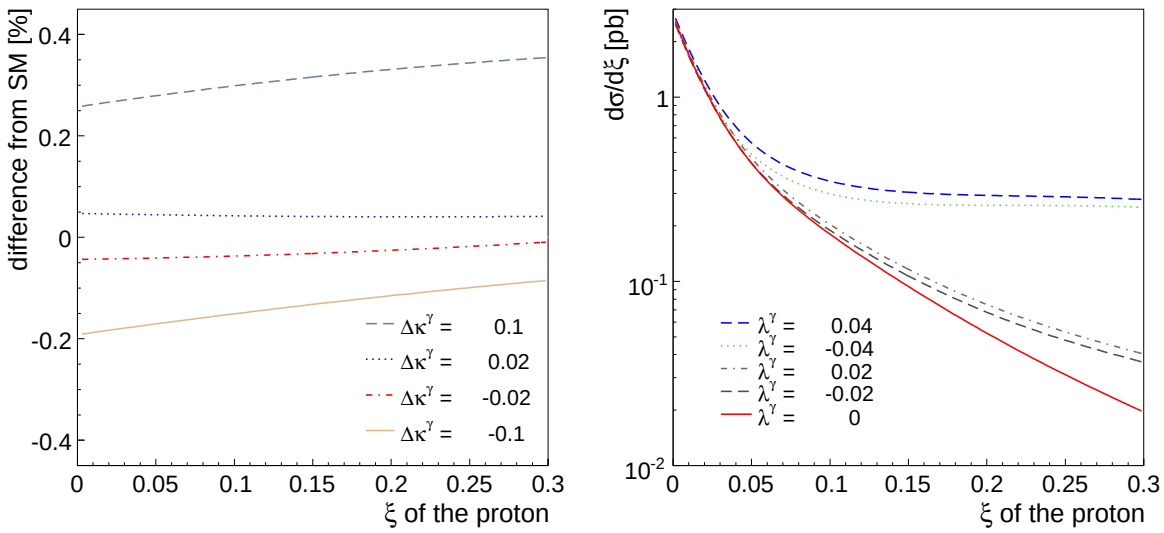

Figure 7.16: ξ dependence of the two-photon WW cross section for different values of $\Delta\kappa^\gamma$ (left) and λ^γ (right) (SM values are 0). For λ^γ, the cross section is enhanced at high ξ which is at the edge of the forward detector acceptance ($\xi = 0.15$). On the contrary, varying $\Delta\kappa^\gamma$ in the interesting range ($-0.05 < \Delta\kappa^\gamma < 0.05$) changes mainly the normalization and not the shape of the ξ distribution.

limits for $\Delta\kappa^\gamma$ and λ^γ are too small to yield any improvement with the limited collected luminosity during the pilot physics runs at the LHC. The only option to gain an improvement is to consider the high luminosity scenario with forward detectors.

The signal selection follows closely two already defined strategies. Since $\Delta\kappa^\gamma$ changes only the normalization, the signal at low $W_{\gamma\gamma}$ masses has to be retained. Therefore the selection of the signal is the same as it was optimized for the measurement of the SM $pp \to pWWp$ cross section (Section 7.4). On the contrary, the signal due to λ^γ parameters appears at high mass with high p_T objects created in the central detector. We can simply use the signal selection requirements designed for the quartic couplings discussed in (Section 7.7.1). For clarity, we use the following cuts for $\Delta\kappa^\gamma$:

$$p_T^{lep1} > 25\,\text{GeV},\ p_T^{lep2} > 10\,\text{GeV},\ 0.0015 < \xi < 0.15,\ \not{E}_T > 20\,\text{GeV},\ 160 < W < 500\,\text{GeV} \quad (7.34)$$

$$\Delta\phi < 2.7\,\text{rad} \quad (7.35)$$

and for λ^γ:

$$p_T^{lep1} > 160\,\text{GeV},\ p_T^{lep2} > 10\,\text{GeV},\ 0.0015 < \xi < 0.15,\ \not{E}_T > 20\,\text{GeV},\ W > 800\,\text{GeV},$$
$$M_{ll} \notin \langle 80, 100\rangle\,,\ \Delta\phi < 3.13 \quad (7.36)$$

The expected backgrounds for $\mathscr{L} = 30\,\text{fb}^{-1}$ are 1.5 ± 0.1 for $\Delta\kappa^\gamma$ and 0.90 ± 0.05 for $\Delta\kappa^\gamma$ as discussed in sections 7.4 and 7.7.1. The successive application of all mentioned requirements for $\Delta\kappa^\gamma$ and λ^γ signal is detailed in Table 7.13.

7.8.5 Results - leptonic channel

The limits are calculated according to formula (7.39) and are summarized in Table 7.14 for 30 and $200\,\text{fb}^{-1}$. Comparing these values with the current limits from the Tevatron, we see that the improvement

events for $30\,\text{fb}^{-1}$		events for $30\,\text{fb}^{-1}$	
cut	$\Delta\kappa^\gamma = 0.3$ (with f.f.)	cut	$\lambda^\gamma = 0.1$ (with f.f.)
$p_T^{lep1,2} > 10\,\text{GeV}$	194	$p_T^{lep1,2} > 10\,\text{GeV}$	168.
$0.0015 < \xi < 0.15$	179	$0.0015 < \xi < 0.15$	119
$\not{E}_T > 20\,\text{GeV}$	158	$\not{E}_T > 20\,\text{GeV}$	107
$W > 160\,\text{GeV}$	158	$W > 800\,\text{GeV}$	25
$\Delta\phi < 2.7\,\text{rad}$	118	$M_{ll} \notin < 80, 100 >$	25
$p_T^{lep1} > 25\,\text{GeV}$	112	$\Delta\phi < 3.13$	24
$W < 500$	98	$p_T{}^{lead.e/\mu} > 160\,\text{GeV}$	19

Table 7.13: Selection of the $\Delta\kappa^\gamma$ and λ^γ signal by the successive application of the cuts. The number of events is given for integrated luminosity $\mathscr{L} = 30\,\text{fb}^{-1}$.

		$\mathscr{L} = 30\,\text{fb}^{-1}$		$\mathscr{L} = 200\,\text{fb}^{-1}$	
	Form factors	$\Delta\kappa^\gamma$	λ^γ	$\Delta\kappa^\gamma$	λ^γ
95% c.l	$\Lambda = 2\,\text{TeV}$	[-0.25, 0.16]	[-0.052, 0.049]	[-0.096, 0.057]	[-0.023, -0.027]
3σ evidence	$\Lambda = 2\,\text{TeV}$	[-0.39, 0.25]	[-0.066, 0.064]	[-0.136, 0.087]	[-0.037, 0.038]
3σ evidence	$\Lambda = 2\,\text{TeV}$	[-0.67, 0.40]	[-0.088, 0.094]	[-0.26, 0.16]	[-0.053, 0.049]

Table 7.14: 95% c.l., 3σ evidence, and 5σ discovery potential on the $WW\gamma$ anomalous parameters for a luminosity of $\mathscr{L}$=$30\,\text{fb}^{-1}$ and $200\,\text{fb}^{-1}$ using the AFP forward detectors with coupling form factors applied.

	$\Delta\kappa^\gamma$	λ^γ
$W\gamma, (p_T^\gamma)$	[-0.11, 0.05]	[-0.02, 0.01]
$WW, (M_T)$	[-0.056, 0.054]	[-0.052, 0.100]

Table 7.15: 95% c.l. limits on the $WW\gamma$ coupling parameters obtained from fitting the p_T^γ and $M_T(WW)$ distributions in $W\gamma$ and WW final states in inelastic production in ATLAS, and calculated for $\mathscr{L}$=$30\,\text{fb}^{-1}$ and for the form factors $\Lambda = 2\,\text{TeV}$, $n = 2$ [19].

is about by a factor of 2 with $30\,\text{fb}^{-1}$of collected luminosity.

Let us also compare the results to those obtainable in the conventional ATLAS analysis without forward detectors. $WW\gamma$ anomalous couplings are probed by fitting the p_T^γ spectrum of the photon distribution to the NLO expectation using the combined sample of $W(e\nu)\gamma$ and $W(\mu\nu)\gamma$ events or by fitting the transverse mass distribution $M_T(WW)$ of the boson pair, reconstructed from the two observed leptons and the missing transverse energy [19]. The corresponding 95% c.l. limits obtained for $\mathscr{L} = 30\,\text{fb}^{-1}$, with the same form factor assumption as before (7.22) are shown in Table 7.15. The presented analysis using forward detectors has about a factor 2 worse precision than the analysis in non-diffractive studies and would therefore be a complementary measurement.

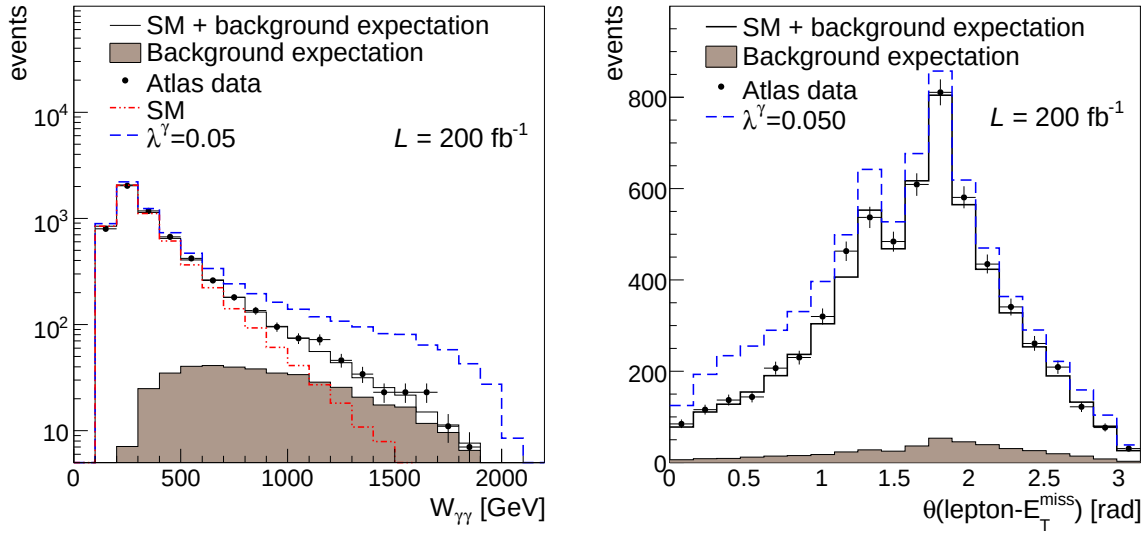

Figure 7.17: Distributions of the $\gamma\gamma$ photon invariant mass $W_{\gamma\gamma}$ measured with the forward detectors using $W_{\gamma\gamma} = \sqrt{s\xi_1\xi_2}$ (left). Distribution of the angle between the leading lepton and E_T^{miss} (right). The effect of the λ^γ anomalous parameter appears at high $\gamma\gamma$ invariant mass (dashed line). The SM background is indicated in dot-dashed line, the DPE background as a shaded area and their combination in full line. The black points show ATLAS pseudo data smeared according to a Poisson distribution.

7.8.6 Discussion - leptonic and semi-leptonic channels

The disadvantage of the full leptonic (e/μ) channel of the boson decays is the small rates since only $\approx 4\%$ of the signal is kept. In the work presented in [1], we performed a quite simple analysis assuming that $\gamma\gamma \to WW$ and DPE$\to WW$ are the only important backgrounds, but keeping also the semileptonic events. More precisely, the events are selected using

- both protons are tagged in the forward detectors in the acceptance $0.0015 < \xi < 0.15$
- at least one electron or muon is detected with $p_T > 30\,\text{GeV}$ and $|\eta| < 2.5$ in the main detector

Both the full-leptonic and semi-leptonic decays are kept which is about 50% of the Ws decays. The obtained 95% c.l. at $30\,\text{fb}^{-1}$, with the form factor (7.22) included in the calculation are

	$\Delta\kappa^\gamma$	λ^γ
95% c.l	[-0.051, 0.043]	[-0.041, 0.034]

The improvement for λ^γ with respect to the analysis with leptonic decays is only modest, since the selection was not optimized for high masses where the signal appears. On the other hand, the larger signal sample when semileptonic decays are included yields a better separation of the signal due to the $\Delta\kappa^\gamma$ anomalous parameter with respect to the SM $\gamma\gamma \to WW$ production and the sensitivity is improved by a factor 4. Again we note, that the sensitivity using standard inelastic events is about the same.

Having more events to analyze, the differential spectra can be used to extract the sensitivities fitting their shapes. This is illustrated in Figure 7.17 (left) where the missing mass distribution of the signal

due to the λ^γ parameter and the SM two-photon and DPE backgrounds are plotted for a substantial integrated luminosity of $\mathscr{L} = 200\,\text{fb}^{-1}$. The signal appears as a deviation at high mass as anticipated. Similarly, the anomalous coupling can also be visible in the lepton p_T distribution or in the distribution of the angle between lepton and the missing transverse energy. The latter is shown in Figure 7.17 (right).

In the preceding sections we have seen that the DPE$\to ll$ and $\gamma\gamma \to ll$ are quite large at small missing masses W or p_T so the requirements mentioned above would have to be tighten to include the dilepton channel in the search.

Another possibility is to register the semi-leptonic decays only. Since the results above are dominated by semi-leptonic decays, we conclude that the sensitivities presented in [1] would not change much if the full-leptonic decays are rejected. However, in this case another type of background arises from the central exclusive production of $q\bar{q}$ pairs which was not considered and which might be important. If one of the quarks radiates a W boson and one of the final state jets is missed, the W+jet+jet final state mimics the semi-leptonic WW decays in two-photon production. This background process is planned to be included in the future releases of FPMC to allow a complete study of the two-photon WW production even in the semi-leptonic decay mode.

7.9 Conclusion

In this chapter, it was first shown how the SM two-photon production $pp \to pWWp$ process with both Ws decaying leptonically could be selected from the diffractive or exclusive background. Using the forward detectors, about 50 events can be observed with $30\,\text{fb}^{-1}$ of collected luminosity corresponding approximately to 3 years of data taking whereas the number of background processes could be kept at a few events level. No multiple interaction background was studied, but the boson invariant mass $2 \times m_W$ threshold could be used to suppress using AFP this background in addition to the time information about the proton arrival time.

The sensitivities to triple and quartic gauge anomalous couplings were studied using the standalone ATLFast simulation. First, we showed that even with a low collected luminosity of $\sim 10\,\text{pb}^{-1}$ which corresponds to few weeks of good data, the sensitivity to anomalous quartic couplings could be improved by a factor of 100 in comparison to the current limits coming from the LEP measurements. Using a high luminosity of $200\,\text{fb}^{-1}$ with the forward detectors to tag the exclusive two-photon events, the knowledge of the quartic couplings can be improved by a factor of 10000.

On the other hand, the improvement of the triple gauge coupling experimental constraints is smaller. In the full-leptonic channel, the $\Delta\kappa^\gamma$ analysis cannot yield than the current limits coming from OPAL; however, it can give better results than those from the Tevatron. On the other hand, the λ^γ parameter can be fully constrained by a factor 2 better with respect to OPAL and by about a factor 5 with respect to the Tevatron.

7.10 Statistical analysis

Before closing this chapter we provide the formulae that were used throughout this chapter to calculate the significances of the signal.

First, we used the P-value to quantify the significance of the new observed signal. Given a number of observed events n_{obs} and μ_b the number of expected background events, the P-value is defined as the

probability α that background would yield the number of observed events n_{obs} or more. Assuming that the background follows a Poisson distribution, such probability α, the significance, is given by

$$\alpha = \sum_{n=n_{obs}}^{\infty} \frac{\mu_b^n}{n!} e^{-\mu_b} \tag{7.37}$$

Using the normalization of the Poisson distribution to 1, the P-value is then given by

$$P-\text{value} = 1 - \sum_{n=0}^{n_{obs}-1} \frac{\mu_b^n}{n!} e^{-\mu_b} \tag{7.38}$$

So the smaller the $P-$value the bigger the confidence that the observed signal does not come from background.

The second formula which was extensively used to calculate the one-sided confidence intervals on the anomalous parameters reads

$$\alpha = e^{-\mu_s} \frac{\sum_{n=0}^{n_{obs}} (\mu_s + \mu_b)^n / n!}{\sum_{n=0}^{n_{obs}} \mu_b^n / n!} \tag{7.39}$$

where μ_s, μ_b are the mean number of expected signal and background events, respectively. Knowing the expected number of background events and setting the confidence level $1 - \alpha$, the upper limits on the number of signal for a given number of events observed in the experiment n_{obs} is obtained solving this formula for μ_s. From which the corresponding limits on anomalous couplings are derived. In our calculation, we set n_{obs} to the mean number of expected background events rounded to the nearest smallest integer.

Bibliography

[1] O. Kepka and C. Royon, Phys. Rev. D **78** (2008) 073005 [arXiv:0808.0322 [hep-ph]].

[2] C. Royon, E. Chapon and O. Kepka, arXiv:0909.5237 [hep-ph].

[3] M. G. Albrow *et al.* [FP420 R&D Collaboration], arXiv:0806.0302 [hep-ex].

[4] J. M. Cornwall, D. N. Levin and G. Tiktopoulos, Phys. Rev. Lett. **30** (1973) 1268 [Erratum-ibid. **31** (1973) 572].

[5] J. M. Cornwall, D. N. Levin and G. Tiktopoulos, Phys. Rev. D **10** (1974) 1145 [Erratum-ibid. D **11** (1975) 972].

[6] A. Denner, S. Dittmaier and R. Schuster, arXiv:hep-ph/9601355.

[7] J. Hořejší, *Introduction to electroweak unification: Standard model from tree unitarity* (World Scientific, Singapore 1994).

[8] V. Khoze and M. Riskin, private communication.

[9] C. Amsler *et al.* [Particle Data Group], Phys. Lett. B **667**, 1 (2008).

[10] T. Pierzchala and K. Piotrzkowski, Nucl. Phys. Proc. Suppl. **179-180** (2008) 257 [arXiv:0807.1121 [hep-ph]].

[11] N. Schul and K. Piotrzkowski, Nucl. Phys. Proc. Suppl. **179-180**, 289 (2008) [arXiv:0806.1097 [hep-ph]].

[12] V. A. Khoze, A. D. Martin and M. G. Ryskin, Eur. Phys. J. C **23** (2002) 311.

[13] M. Boonekamp, V. Juránek, O. Kepka, C. Royon, Forward Physics Monte Carlo, Proceedings of the Workshop of the Implications of HERA for LHC physics; arXiv:0903.3861 [hep-ph]; `http://cern.ch/fpmc`.

[14] ATLFast++ package for ROOT, `http://root.cern.ch/root/Atlfast.html`.

[15] K. Hagiwara, R. D. Peccei, D. Zeppenfeld and K. Hikasa, Nucl. Phys. B **282**, 253 (1987).

[16] V. Khoze, W. J. Stirling, private communication.

[17] G. Belanger and F. Boudjema, Phys. Lett. B **288**, 201 (1992).

[18] G. Abbiendi *et al.* [OPAL Collaboration], Phys. Rev. D **70** (2004) 032005 [arXiv:hep-ex/0402021].

[19] G. Aad *et al.* [The ATLAS Collaboration], arXiv:0901.0512 [hep-ex].

[20] J. Alcaraz *et al.* [LEP Electroweak Working Group], arXiv:hep-ex/0612034.

[21] V. M. Abazov *et al.* [D0 Collaboration], arXiv:hep-ex/0803.0030.

Definition of Rapidity Gaps Using the Calorimeter

8

Diffractive and exclusive events have two features which allow their identification: intact protons leaving the interaction point at small angles, and rapidity gaps in the central detector. The forward detectors to tag the outgoing protons presented in Chapter 6 are in approving phase and certainly will not be present during the start-up period of the LHC. The second method relies on the observation of rapidity gaps in these events which are the mark of the underlying colorless exchange. Such colorless exchanges are present in the heart of diffractive and exclusive events in the form of pomeron/reggeon, photon exchange, or two gluon exchange in a color singlet state (in the leading order QCD) as was discussed in the introductory Chapter 2.

The method of tagging the leading protons can be exploited even at high luminosity running conditions. The overlap events due to high multiple interaction rate contribute as a significant background, but it is possible to suppress part of them with ingenious kinematic constraints between the tagged protons and the detected system in the central detector. The rapidity gaps can be, however, reconstructed only in events without additional overlap events. At the Tevatron, the mean number of multiple interactions per bunch crossing is rather modest (~ 5), there is always some fraction of single interactions that can be selected. On the other hand, since the mean number of overlap events range from 13 to 32 during a nominal physics run at the LHC, the probability to have only a single interaction is negligible. That is why only the data taken after the LHC start-up at low luminosity will be suitable for such analysis since the overlap rate is quite small and an important fraction of interactions will be without overlaps. We have estimated in Chapter 3.1.2 that about $\mathscr{L}$=30 pb^{-1} of such clean events could be in principal collected during the first 10 months of running provided that triggers have a reasonable efficiency.

Since protons are intact in diffractive and exclusive events, there is no proton remnants. In these events, the number of reconstructed tracks in the inner detector and the energy deposition in the forward region of the calorimeter will be small. In this chapter, we investigate the second option. In fact, there is always some energy measured in the calorimeter due to the noise fluctuation of the readout electronics. One has to quantify this noise fluctuation, distinguish it from the physics process, in order to properly define the observation of rapidity gaps.

The layout of this chapter is as follows: first, we present the rapidity gap reconstruction at the generator level obtained with FPMC and set the strategy of the analysis. Then, we briefly discuss the algorithms used to read out the energy in the calorimeter and show the rapidity gap reconstruction using

the standard ATLAS tools dedicated for the end-user analysis. After, finding that the performance of rapidity gap reconstruction using the standard tools is limited, we propose an alternative method and demonstrate its performance on a range of physics processes characterized by rapidity gaps.

8.1 Analysis strategy

In order to understand the rapidity gap reconstruction inside the ATLAS detector in detail, we consider three processes with at least one intact proton in the final state. They are the following:

- Two-photon production of dimuon events (QED) $pp \to p \oplus \mu\mu \oplus p$
- Central exclusive production (CEP) of dijets $pp \to p \oplus X \oplus p$
- Single diffractive production (SD) of dijets $pp \to p \oplus$ pom. remnants $+ X +$ proton remnants

Here the rapidity gaps are denoted by the $\oplus$ symbol and the dijet system is represented by X. The two-photon and central exclusive production are unique exclusive events having large rapidity gaps in backward and forward direction. Single diffractive dijet production is characterized by rapidity gap on either the positive or negative side in the z beam direction. Although both configurations occur with an equal chance, only single diffractive dijets with a gap on the negative side $\eta < 0$ will be shown here, for presentation purposes. As mentioned, these processes are expected to have smaller energy flow in the forward region (from now onwards, by forward we will denote a region of high pseudorapidity in both, positive and negative z direction of the beam) than what is observed in non-diffractive collisions. To show this explicitly, the non-diffractive dijet production will be studied. It has the following signature

- non-diffractive dijets $pp \to$ proton remnants $+ X +$ proton remnants

without any gap present.

Two-photon and single diffractive events were generated with the FPMC generator. The central exclusive dijet production was generated using the ExHuME generator, and non-diffractive signal was obtained with PYTHIA 6 (details on the generators were given in Chapter 4). The ATLAS detector response was obtained with a full simulation of the ATLAS detector inside the simulation package ATHENA, version 14.5.0. The datasets for central exclusive production were produced by the central production group. The used dataset name is

- `mc08.106064.ExhumeGG_Et17.recon.ESD.e386_s495_s520_r696`

The other processes were generated, simulated, and reconstructed privately. The dijet samples were generated with the $p_T^{parton} > 17\,\text{GeV}$ threshold. The exclusive production was obtained with a cut on a maximum allowed momentum fraction loss of the proton $\xi_{max} = 0.1$. In case of SD events, this cut was $\xi_{max} = 0.01$ (with few exceptions which we explicitly mention later). The dimuon threshold in two-photon production was $p_T^{\mu} > 10\,\text{GeV}$ and no upper cut on ξ_{max} was applied.

8.2 Rapidity gaps at generator level

In events with rapidity gaps, the central system is separated from the proton. This can be seen in Figure 8.1 where the energy flow distributions in exclusive, SD dijets and non-diffractive events are shown.

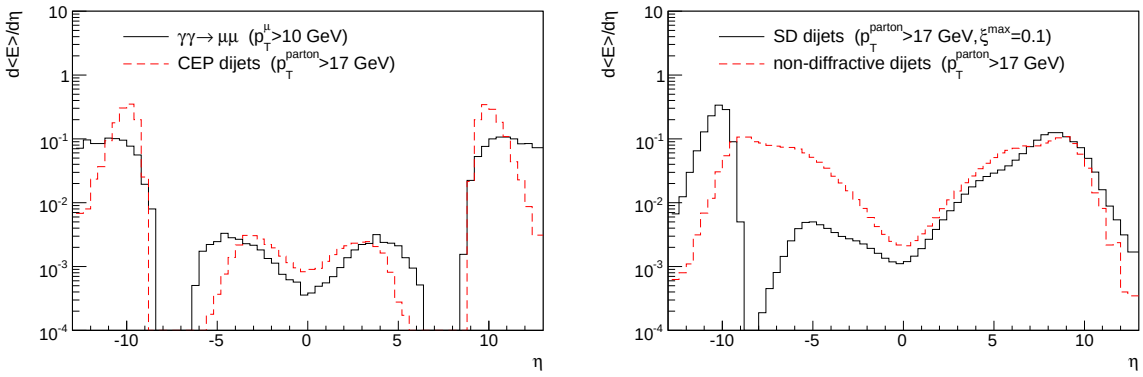

Figure 8.1: Particle level energy flow in two-photon dimuon and CEP dijet events (left), SD dijets and non-diffractive dijets (right). There is a clear rapidity gap between the intact protons and the central system in exclusive and diffractive production. SD events were simulated with a rapidity gap on negative side only.

In the exclusive case, the centrally created system (dimuons or dijets) is located at small rapidities and the outgoing intact protons escape at pseudorapidities $|\eta| \gtrsim 9$. Note that since outgoing protons in the two-photon exchange have typically smaller transverse momenta than those in the CEP production, they are scattered at higher η.

On the contrary, the non-diffractive dijet production in Figure 8.1 (right, dashed) shows no distinct structure in the forward region. The creation of the proton remnants in the collision initiates complicated color interaction mechanism between them which leads to a proliferation of energetic particles in the forward region.

The single diffractive events have the same energy flow on the side where the proton was broken as the non-diffractive dijets. On the negative side, the intact proton is separated by a rapidity gap from the central dijet system. However, the rapidity gap is smaller than in the CEP dijet case due to the presence of pomeron remnants which partially occupy the gap due to pomeron exchange. Note that the average energy deposited within a typical coverage of the ATLAS or CMS calorimeters $|\eta| < 5$ is nonzero, hence only a fraction of all SD/exclusive events can be identified with the central detector because the rapidity gap is often outside the acceptance.

The rapidity gap size varies from event to event. The distribution of the most forward particle η in the SD dijet sample is depicted in Figure 8.2. The diffractive proton peaks on the negative side, whereas the proton remnants span up to high positive pseudorapidities. The most forward particle distribution from the pomeron remnants is depicted by the full curve. It shows that less than half of the SD events have a rapidity gap observable in principal inside the calorimeter. A non-negligible fraction of events have the most forward particle within the calorimeter and the gap could be observed. Looking in the positive direction, the proton remnants always yield very forward particles.

The size of the rapidity gap is approximately related to the momentum fraction loss of the proton ξ as $\Delta\eta \approx -\log(\xi)$. This dependence is illustrated in Figure 8.3 as the distribution of the most forward particles for SD dijets for various allowed maximum $\xi_{max} = 0.1, 0.01, 0.001$. The higher the proton momentum fraction loss, the higher is the boost of the pomeron along z and the smaller the rapidity gaps. Single diffractive dijet events with $\xi \lesssim 0.001$ have practically always a rapidity gap inside the

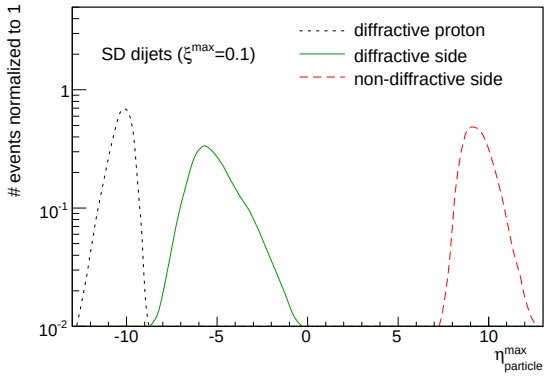

Figure 8.2: Distribuion of the most forward particles on the positive side (red, dashed) and negative side (green, full line) in single diffractive dijets ($p_T^{parton} > 17\,\mathrm{GeV}$). The unaltered proton shown in dotted line are scattered at $\eta \lesssim -10$.

calorimeter. Events with ξ above this value can have a rapidity gap outside the detector acceptance and will be identified as non-diffractive.

The generator cut $p_T^{min} = 17\,\mathrm{GeV}$ was chosen in order to analyze a data set which follows the conditions of the future SD dijet analysis within ATLAS. In early days of the LHC running, only the L1 Trigger selection will be applied and the High Level Triggers (see Section 3.4) will be functioning in the pass-through mode only. One is basically limited by the requirements of the data recording rate to the permanent storage in this case, and the low thresholds of the L1 jet triggers have to be largely prescaled.

It was shown [1] that the SD dijet sample could be selected with the L1_J20 trigger which is very efficient for jets with a transverse momentum above 35 GeV. The effect of the jet threshold on the forward particle pseudorapidity distribution is shown in Figure 8.3 (right). Varying the p_T^{jet} threshold, the profile of the distribution does not change much. This means that selecting events with different jet thresholds (either due to the trigger or in the off-line analysis) reduces the diffractive sample with rapidity gaps only due to the fall of the cross section in a limited range of the p_T threshold. The cross section is not corrected for the soft survival probability factor, which is expected to be 6% for single diffractive events [2].

Let us estimate the number of gap events which could be seen with early data and with the mentioned trigger configuration. Assuming that jets with $p_T^{jet} > 30\,\mathrm{GeV}$ can be identified with 100% efficiency, we obtain an effective cross section $\approx 2 \times 75 \times 0.07 = 9.0\,\mathrm{nb}$ of events with most forward particles $|\eta^{max}| < 4$. i.e. for events with a rapidity gap of at least one unit in pseudorapidity. The factor of 2 comes from the fact that we consider rapidity gaps on both positive and negative sides. It is well known that low p_T triggers are largely prescaled. Let us assume that the L1_J20 prescale is 1000 as shown in Table 3.4. The effective cross section of events with a rapidity gap greater than one is then about 9.0 pb. With about $30\,\mathrm{pb}^{-1}$of early data, about 300 events with gaps could be analyzed. However, let us stress that the L1 prescale mentioned above could be found to be too low in real data. Also, it is important to collect jets with the small p_T^{jet} possible. Any significant increase of the low L1 prescales would probably render the analysis impossible without any additional technique to trigger on the diffractive events at L1.

Having shown the basic properties of the rapidity gap events at the generator level, the observation of this phenomenon with the ATLAS detector follows.

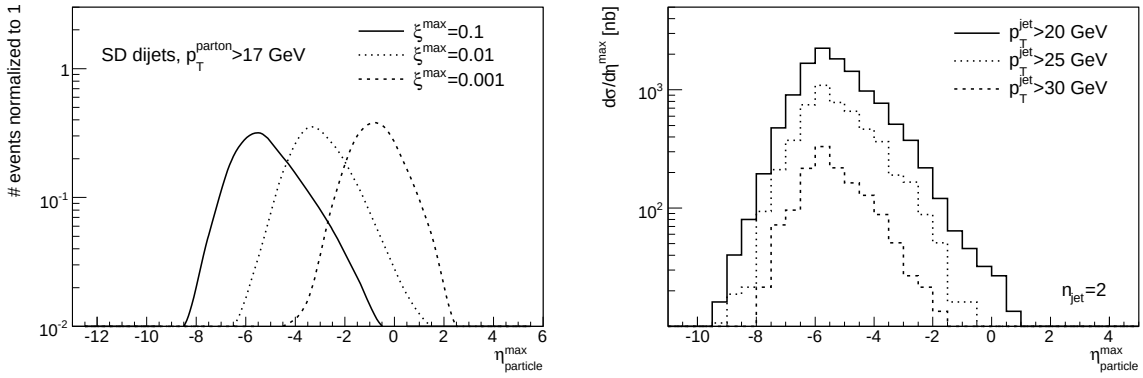

Figure 8.3: Distribution of the most forward particle in single diffractive events on the side with a rapidity gap, shown as a function of the maximum allowed momentum fraction loss of the proton ξ_{max} (left) and as a function of the minimal jet p_T (right). The cross section is not corrected for the soft survival probability which is expected to be 7% and was generated with $\xi_{max} = 0.1$.

8.3 Experimental setup

We have seen that the edge of the rapidity gaps in SD events is usually somewhere between $|\eta| = 5-6$. It is therefore inevitable to use the calorimeter system to define the rapidity gaps because it has the largest acceptance in pseudorapidity, $|\eta| < 4.9$ (the muon system acceptance spans the region $|\eta| < 2.7$ and the inner tracker covers $|\eta| < 2.5$).

A possible better forward coverage of the ATLAS central detector is currently provided by the MBTS trigger, and the two forward systems LUCID detector and ZDC calorimeter (Section 3.2.6, Section 3.3.1, Section 3.3.2). The MBTS coverage is small, spanning only up to $|\eta| < 3.84$. We will see later that the MBTS could be used only in exclusive-like events where the rapidity gaps are considerably larger than in SD events. The application of LUCID and ZDC for triggering is interesting since they could provide an identification of events with small energy flow in the forward region characteristic for diffractive and exclusive events. The L1 jet prescales could be then lowered.

LUCID is designed for relative luminosity measurement, provided by measuring the hit rate over large periods of time. However, the applicability for hard diffraction turned to be small. Due to the reduced detector acceptance in ϕ, there is a significantly large rate of veto counts (a trigger that no energy is present in the detector) even in non-diffractive events with pomeron remnants. The reduction of the L1 rates is therefore quite small in SD events. However, in DPE events or in events with two gaps in general, the veto coincidence in up- and down-stream LUCID stations can slightly improve the tagging on two gap events [1].

The ZDC calorimeter could be used to veto on the number of neutral particles in the collision. Indeed, it was shown that the single photon particle reconstruction is possible with the ZDC. We may expect that in diffractive and exclusive events the number of produced neutral particles is smaller. However, the full simulation is not yet included in the simulation framework (it should be available from the ATHENA release 15).

With these considerations in mind, the hadronic calorimeter is the only detector with a coverage in the forward region. The rapidity gaps will be used in the offline analysis to select the diffractive or

exclusive signal. However, in the later running when HLT triggers will be operating, it would be also possible to include the gap finding tool in the Event Filter trigger.

The ATLAS calorimeter system was described in detail in Section 3.2.2. It is composed of the Electromagnetic Calorimeter which covers the pseudorapidity region $|\eta| < 3.2$ and the Hadronic Calorimeter which reaches up to $|\eta| < 4.9$. For the purpose of the forward physics studies, both detectors can be viewed as one system with a granularity in general equal or better than $\Delta\eta \times \Delta\phi = 0.1 \times 0.1$ for $|\eta| < 3.2$ and $\Delta\eta \times \Delta\phi = 0.2 \times 0.2$ for $3.1 < |\eta| < 4.9$ where there is the Forward Calorimeter (FCAL) only. The FCAL covers the very forward region and plays a major role for most of the diffractive studies.

The smallest independent elements in the calorimeter which are used to read-out deposited energy are calorimeter cells. Their segmentation determines the calorimeter granularity. Since the cells are fundamental for the calorimeter read-out it is worthwhile to review how the cell signal is converted to the measured cell energies.

8.4 Calorimeter energy readout

The analog signal from each cell is sampled and digitized in the front-end electronics boards (FEBs). The digitized signal is then processed by the digital signal processors on the back-end electronics boards. The data are converted to the measured energy using a filtering algorithm minimizing the effect of electronic and pile-up noise. The event reconstruction unpacks the data from the byte stream and stocks them in objects called `LArRawChannel` and `TileRawChannel`. In the latter step the cell energies are corrected to represent the true deposited energy (effects like operation at lower nominal voltage due to local calorimeter defects are taken into account, etc.). Hot cells are identified and removed and the list of calibrated cells is stocked in `CalloCell` objects.

8.4.1 Cells and their noise

The cell-by-cell noise is calculated by the `CaloNoiseTool`. The noise can have two origins: the electronic noise and the pile-up. It varies by orders of magnitude as a function of η and calorimeter layers, see Figure 8.4 (left). At higher luminosities the effect of the pile-up in which the energy from subsequent bunch-crossing or from multiple interactions in one bunch-crossing is superimposed becomes important. The time needed to read out the current of ionized electrons in the sensitive medium (LAr for example) is longer ($\approx$400 ns) than the time between two bunch-crossings (25 ns) . Consequently, the overlay of pulses changes the signal time shape and augment the total cell noise. This effect is especially visible in the forward direction close to the beam axis due to beam remnants, and is shown in Figure 8.4 (right).

In the current state of the readout simulation, the noise characteristics are assumed gaussian for both the electronic and the total noise. This assumption is expected not to be fully valid in reality where non-gaussian tails will appear (due to the bipolar shaping which is performed in FEBs). The exact structure of the noise will be studied using zero-bias events which have no activity in the detector, or using physics runs measuring the negative cell energy distribution which should be subject to the noise fluctuation only. In the following we consider the gaussian electronic noise as calculated by the `CaloNoiseTool` tool.

There are 187616 cells in both electromagnetic and hadronic calorimeters. The resulting random energy fluctuation of a large ensemble of cells due to noise can a have very large impact on the physics

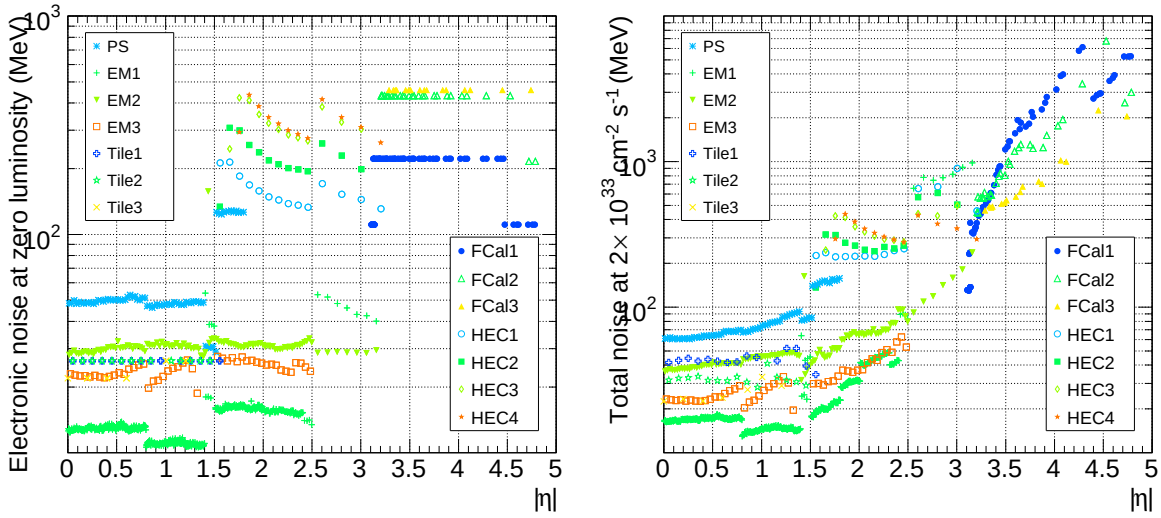

Figure 8.4: Expected RMS of per-cell electronic noise (left) and total noise at medium luminosity (right) for Electromagnetic and Hadronic Calorimeters [4]. The description of the ATLAS calorimeters is in Section 3.2.2. At higher luminosities, more energy is present in the forward region which increases the contribution of pile-ups (energy from previous bunch crossings) in the calorimeter active medium. This contribution is random and adds to the electronic noise.

process to be studied. For example, it can effect the missing energy resolution when the auxiliary noise energy is added. In events with rapidity gaps, the effect of noise is even more apparent because in such events certain regions of the detector should be empty completely. Any noise fluctuation can thus spoil the gap signature. The energy deposition in diffractive events in forward region is small and compatible with noise. It is therefore important to study the definition of "visible energy" due to a physics process and separate it from the noise effects. The noise also depends on instantaneous luminosity and the number of overlap events, so the tuning of such a definition will have to be compared with data.

8.4.2 Signal and noise separation

At first, it is instructive to study the total number of cells in the calorimeter which have signal due to noise. The probability to observe a cell giving the energy E is a random process described by the normal probability density function with a variance σ^{cell}_{noise}. The noise variance changes significantly throughout η. To describe all cells of different noise variance in a compact way, we introduce the significance t as the energy in terms of cell noise standard deviation. As such we are working with energy quantities which are significant in comparison to the typical noise fluctuation and the measure of the significance is the same for electromagnetic or hadronic calorimeters over the whole η range of the detector.

The probability to observe energy t for a given cell is then

$$p(t) = \frac{1}{\sqrt{2\pi}} \mathrm{e}^{\frac{-t^2}{2}} \qquad t \equiv \frac{E}{\sigma^{cell}_{noise}} \tag{8.1}$$

The probability that a cell has an energy above a certain threshold, $|t| > t^{th}$, is given by the integral

$$p(t^{th}) = \sqrt{\frac{2}{\pi}} \int_{t^{th}}^{\infty} \mathrm{e}^{\frac{-t^2}{2}} \mathrm{d}t \tag{8.2}$$

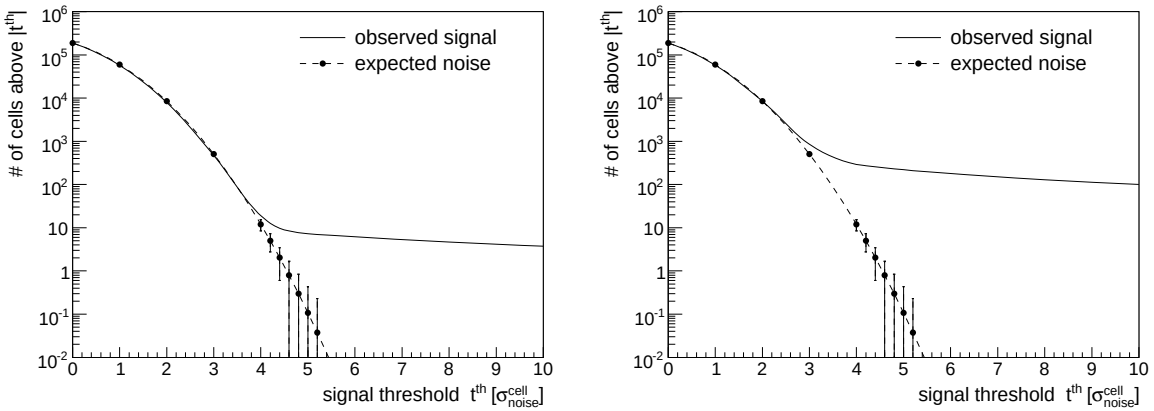

Figure 8.5: Number of cells with energy above threshold $|t| > t^{th}$ for an empty event compared to either two-photon dimuon events (left) or single diffractive dijet events (right).

The motivation for taking the absolute value of t is to cancel large (but rare) positive and negative noise fluctuations. This is useful when energies from a group of cells are added. A positive bias would be introduced if $|t|$ was not considered.

Given a sample of n_{cell}, the probability of observing n cells above the threshold t^{th} follows the Poisson distribution with a mean $\langle n \rangle$ and variance $\sigma^2_{\langle n \rangle} = 1/\langle n \rangle$ given by

$$\langle n \rangle = n_{cell} \times p(t^{th}) \tag{8.3}$$

This dependence is depicted in Figure 8.5 where it is compared to two-photon dimuon events (left) and SD dijets (right). In the case of SD dijets, there is a proliferation of particles coming from jets which deposit some energy in many cells and the signal is visible for a threshold starting at $t^{th} = 3$. On the other hand, in two-photon dimuon events which leave a nearly empty detector, the effect of noise is more pronounced. The typical deposition of a $p_T^{\mu} = 10\,\text{GeV}$ muon in the ATLAS calorimeter is only about 3 GeV (see also Figure 3.7) and about 5 cells in the whole detector are hit by one muon track. A relatively high threshold $t^{th} = 4.5$ has to be used to identify the muon events in the number of cells above a threshold spectrum. These events are suitable to study the definition of the tool to find a gap because it allows to check the reconstruction of small energy deposition inside the calorimeter which is similar to the energy flow on the boundary of the rapidity gap in diffractive events.

8.5 Gap reconstruction using cluster

The end-user analysis is designed to be performed on the Analysis Object Data (AOD) data files which contain a reduced event information. Besides the specialized reconstructed objects like jets, electrons, and photons, the energy deposition inside the calorimeter is available in form of clusters in these files. In this section, we aim to investigate the gap reconstruction capabilities using these objects. First, we quickly review the clustering algorithms and then present the results.

Parameter	EM 633	Had 420
Seed signal definition	E	|E|
t_{seed}	6	4
$t_{neighbor}$	3	2
t_{cell}	3	0

Table 8.1: Parameters used in topological clustering algorithms in ATLAS [4].

8.5.1 Clustering algorithms

Particles traversing calorimeters usually deposit their energy in many cells in both lateral and longitudinal directions. The clustering algorithms are developed to group these cells and sum the deposited energy. They should minimize the effects of the electronic and pile-up noise. There are two types of clustering algorithms: sliding-window and topological clustering [4].

8.5.2 Sliding-window clustering

The sliding-window clustering algorithms are used to build the electromagnetic clusters (using EM calorimeter) which are later used to identify electrons and photons, and combined clusters (using in addition the hadronic calorimeter) for jet and tau reconstruction. The $\eta \times \phi$ space of the chosen calorimeter is divided into $N_\eta \times N_\phi$ grid. The clustering algorithm moves across this grid with a fixed window size. If the transverse tower energy sum inside this window is a local maximum and is above a given threshold, preclusters are formed. The sliding window algorithms are specialized in looking for local peaks in deposited energy and therefore the thresholds are 3 GeV for the electromagnetic clusters and 15 GeV for the hadronic ones. These thresholds are certainly too high for our purposes since hadrons typically deposit an energy of few GeV in diffractive events. The other possibility is to use the topological clusters.

8.5.3 Topological clustering

Topological clustering algorithms are seeded algorithms that cluster cells around the seed cell with energy significantly above the cell noise. They are 3D objects containing a variable number of cells. The algorithm first finds the cells with a significance greater than t_{seed}, which are the cluster seeds. The cells surrounding a seed are added to a cluster if their energy is larger than a low t_{cell} threshold. Should a particular cell be surrounded by two adjacent clusters, the two clusters are merged if the cell significance is greater than $t_{neighbour}$. In the opposite case, the cell is added to the cluster which has a higher total significance (t summed over cells in the cluster). Clusters with negative total energy are not saved.

There are two types of topological clustering algorithms EM “633" and Had “420” whose parameters are summarized in Table 8.1 The “633” algorithm was optimized to reconstruct EM clusters with significantly higher energies whereas “420” was designed to reconstruct low energy clusters without being dominated by noise.

Only the “420" clustering algorithm uses the whole calorimeter coverage which is needed to define the rapidity gaps. Note that in this case, the seed parameter is $t_{seed} = 4$ which will be referred to later.

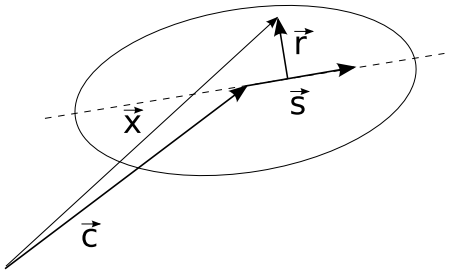

Figure 8.6: Variables used to describe the orientation of the cluster: cluster center $\vec{c}$, shower axis $\vec{s}$, cell position $\vec{x}$, and the distance of a cell from the shower axis $\vec{r}$.

The parameter $t_{cell} = 0$ ensures that the surrounding cells to the protoclusters will be always included in the cluster and thus the tail of the hadronic showers will not be lost. We note, however, that including all surrounding cells in the cluster makes the object more sensitive to the pile-up effects and multiple interactions at high instantaneous luminosities since the outside cluster energies might not be small and have to be understood in data. Besides the position and energy of the clusters, a set of cluster moments are saved in the AOD to allow later identification of the shower type (due to electron, photon, etc.) based on the lateral and longitudinal profiles of the clusters. Since we will use some of the moments to evaluate the size of the rapidity gap, we review how the cluster moments are calculated.

8.5.4 Topological cluster moments

The n-th cluster moment of a variable x is defined as

$$\langle x^n \rangle = \frac{1}{E_{norm}} \times \sum_{\{i|E_i>0\}} E_i x_i^n \tag{8.4}$$

with $E_{norm} = \sum_{\{i|E_i>0\}} E_i$ and i running over all cells with positive energy which were assigned to a cluster. The most basic moments are the mean values of the η and ϕ positions of the cluster. The cluster center is defined as $\vec{c} = (\langle x \rangle, \langle y \rangle, \langle x \rangle)$. The cluster properties are measured with respect to the shower axis $\vec{s}$ which characterizes the direction of the shower development and the shower center $\vec{c}$. The cluster with the meaning of shower axis and the cluster center is illustrated in Figure 8.6 (technically, the shower axis is found as an eigenvector of the energy weighted spacial correlation of the cluster cells with positive energy with respect to the cluster center, more details and complete formulae can be found in [4]). In reality, the shower axis is almost parallel to the cluster center vector $\vec{c}$, because showers typically develop in the particle direction flying from the interaction point.

Once the shower axis $\vec{s}$ and the shower center $\vec{c}$ are defined, the two quantities

$$\begin{aligned} \vec{r}_i &= |(\vec{x}_i - \vec{c}) \times \vec{s}| \\ \lambda_i &= (\vec{x}_i - \vec{c}) \cdot \vec{s} \end{aligned} \tag{8.5}$$

are constructed which characterize the distance of a cell from the shower axis and the distance of a cell from the cluster center along the shower axis. The second moments $\langle r^2 \rangle$ and $\langle \lambda^2 \rangle$ then describe the variance of the energy deposition in the cluster in the transverse and longitudinal directions.

For the rapidity gap analysis it is important to know the size of the cluster in terms of pseudorapidity. Assuming that the shower axis and the cluster center axis coincide, $\vec{c} || \vec{s}$, the radius of a cluster in $\Delta\eta$ and $\Delta\phi$ can be derived by differentiating the pseudorapidity $\eta = \ln(\tan(\theta/2))$ leading to

$$\Delta\phi \backsimeq \Delta\eta \backsimeq \text{atan}\left(\frac{\sqrt{\langle r^2 \rangle}}{c}\right) \times \cosh(\eta). \tag{8.6}$$

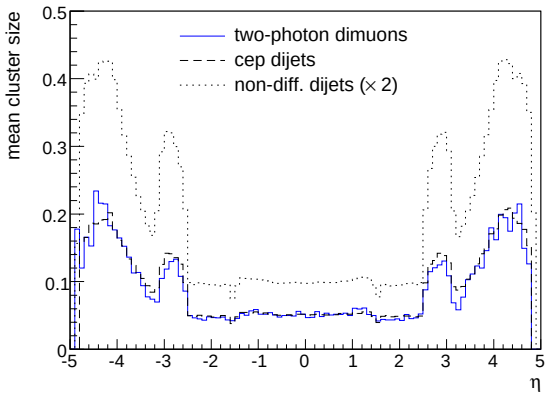

Figure 8.7: Typical cluster size in two-photon dimuon and CEP dijets events. The two distinct processes have very similar cluster sizes. Note that the non-diffractive curve was scaled by a factor of 2, and would otherwise lay on top of the others.

The first equality follows from the fact that the calorimeter has in first approximation the same cell segmentation in η and ϕ.

Let us investigate what is the typical cluster size in two-photon dimuons, CEP dijets, and non-diffractive dijets. We know that the number of cells which were hit in these events greatly differs (only ~ 10 cells are hit in the case of $\mu\mu$ events, whereas this number is of the order of few 1000 when jets are detected, and in non-diffractive events this might be even more). Also, the typical deposited energy is greater in non-diffractive events than in the other processes and the energy spectrum of the clusters is different. On the other hand, the mean cluster size in all these events vary similarly, as shown in Figure 8.7 as a function of η. In the central part of the calorimeter $\Delta\eta < 2.5$ the typical cluster size is low, 0.05 in pseudorapidity units. In the overlap region between EM and LAr Hadronic End-cap $2.5 < \Delta\eta < 3.2$ the cluster can grow over different samplings (see Table 3.2 for a list of calorimeter samplings and their segmentation) and can be as big as 0.15 in η. In the forward region, the FCAL has a fixed segmentation ~ 0.2 which influences the cluster size and the increase in the average cluster size comes simply from the relation between η and the scattering polar angle θ; the shower of a fixed size will have a larger size in η in higher pseudorapidities than in the center of the detector.

We have now gained enough information to define the rapidity gaps using the calorimeter TopoClusters. They are accessed via the `CaloCalTopoCluster` container (ATHENA version 14.5.0).

8.5.5 Rapidity gap definition using TopoClusters

The rapidity gap in the cluster-based analysis is defined as the size of the empty region in pseudorapidity from the detector edge taken to be $\eta = \pm 5$ to the most forward or backward cluster. In addition, the reconstructed mean cluster size $\Delta\eta_{cluster}$ calculated according to formula (8.6) is taken into account, reducing the reconstructed gap slightly. In the forward and backward directions, we thus calculate the rapidity gap in the following way:

- $\Delta\eta_{gap} = 5 - (\eta^{max}_{cluster} + \Delta\eta_{cluster})$

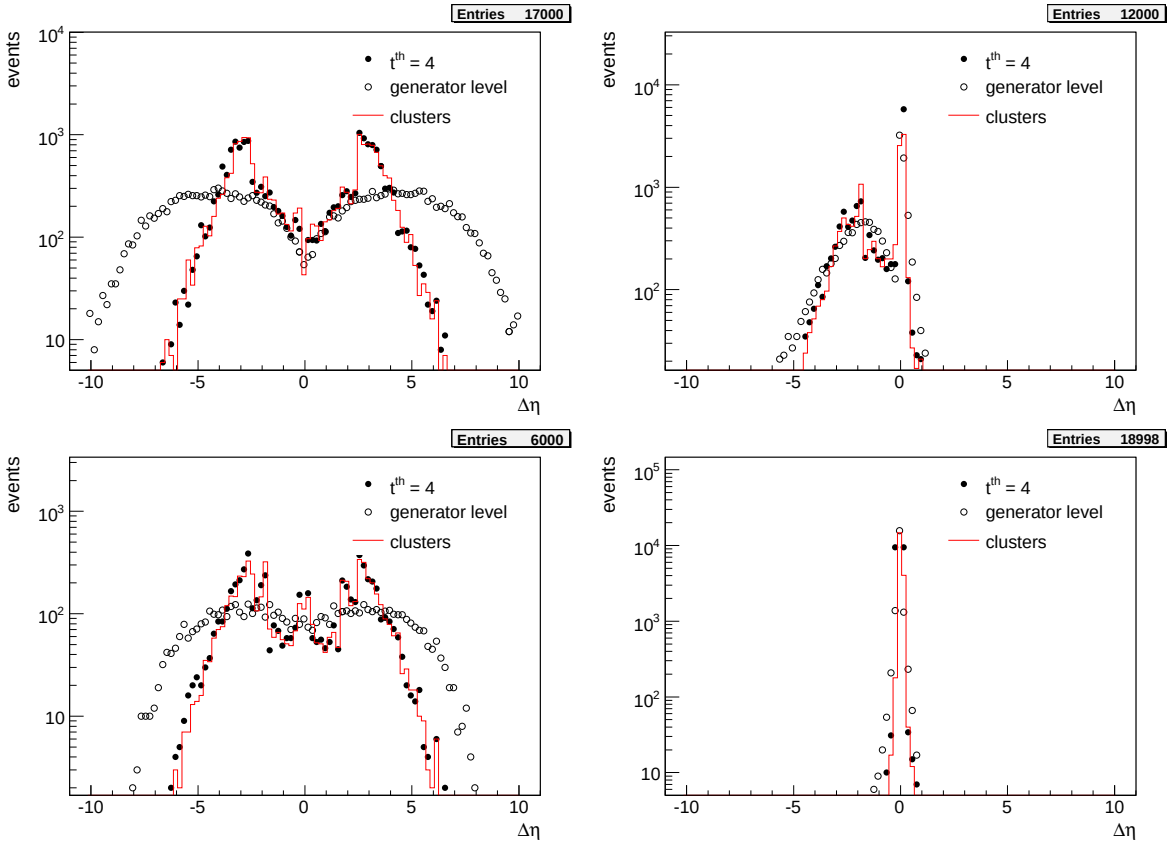

Figure 8.8: The rapidity gap reconstruction using true particles (empty circles) and TopoClusters "420" (full line) for two-photon dimuons (top-left), CEP dijets (bottom-left), SD dijets (top-right), non-diffractive dijets (bottom-right). TopoClusters underestimate large gaps. The reconstruction using the cell-based analysis (see Section 8.6) with $t^{th} = 4$ cell threshold is shown in full circles to illustrate that the cluster seed threshold determines the cluster performance for rapidity gaps. A modification is made in Section 8.6 to improve the gap reconstruction.

- $\Delta\eta_{gap} = -5 - (\eta^{min}_{cluster} - \Delta\eta_{cluster})$

Note that the size of the rapidity gap on the negative side is negative by construction.

In Figure 8.8, the performance of the gap reconstruction using clusters is shown and compared to the true distributions calculated at the particle level where the gap is defined as the distance in pseudorapidity from the edge of the detector to the most forward particle. The event samples are analyzed as they were simulated, i.e. without placing any additional requirement on the number of reconstructed jets/muons nor on their momenta. The gap size reconstruction from clusters is also compared to the cell-based analysis which will be discussed below.

First of all, from the generator level distributions (empty circles) we see that the rapidity gaps can be large in exclusive events. In a small fraction of events, the calorimeter can be found even empty in the case of two-photon dimuons, which corresponds to events with muons outside the detector acceptance (top-left plot for $|\Delta\eta| \sim 10$). In single diffractive events we observe non-zero gaps on the negative side, whereas there are no or very small gaps reconstructed on the positive side of the broken proton. Since the

SD sample was generated with $\xi_{max} = 0.01$, the gap distribution is compatible with the corresponding one for the most forward particle spectrum already shown in Figure 8.3.

In general, the number of rapidity gaps reconstructed using clusters is strongly underestimated for large gaps, greater than $\Delta\eta \geq 5$. This affects the exclusive productions shown on the left. The number of cells which can give noise fluctuations spoiling the gap is larger for large gaps. This indicates that the seed threshold which is used in the clustering algorithm might not be appropriate for exclusive events. However, the cluster performance in single diffractive or non-diffractive events seems to be satisfactory, even though the tendency of underestimating the gap size is still present.

Anticipating the results of the next section, we also compare the cluster-based analysis to the cell-based approach which uses cells above the threshold $t^{th} = 4$ to reconstruct the rapidity gap. Such a reconstruction is depicted by full circles and they lay exactly on top of the cluster-based curve. We can thus conclude that in what concerns the rapidity gap reconstruction resolution, only the "420" cluster seed parameter is important whereas the details of cluster growth and merging/splitting is not.

As previously shown in Figure 8.5, the threshold $t^{th} = 4$ corresponds to the total average number of 12 cells in the calorimeter. Those noise cells spoil the large rapidity gaps. Since the rapidity gap reconstruction is shown as a function of a fixed $\Delta\eta = 0.1$ spacing, the probability to have a noisy cell passing the threshold increases with the calorimeter segmentation in a particular η bin. Looking more closely at Figure 8.8, one sees spikes for $\Delta\eta \sim 3$ and $\Delta\eta \sim 2.5$ which correspond to the regions where the forward calorimeter overlaps respectively with the hadronic end-cap, and the EM end-cap with the hadronic end-cap.

Even though the TopoClusters are built with a rather high seed threshold ($t^{th} = 4$)), the observation of rapidity gaps larger than $\Delta\eta \gtrsim 5$ is very sensitive to the noise. Such large gaps should be observed in exclusive exchanges like two-photon production of leptons or WW, central exclusive production of dijets, but perhaps also in single diffractive production of J/ψ where the created mass is small and we can expect large rapidity gaps. Moreover, the current cluster definition might be sensitive to electronic pile-up in the cluster growing step.

In order to improve the rapidity gap reconstruction, the cell-based analysis of gap reconstruction will be shown in the next section.

8.6 Rapidity gap definition using cells

The cell-based analysis relies on the evaluation of the cell signal with respect to the typical cell noise. The cell noise can either be simulated as mentioned in the previous Section 8.4.1 or directly measured in zero bias events in which the detector is read out for every bunch crossing regardless what happened during the collision. Currently, the cell non-gaussian noise is being studied using cosmic muons. However, they were not introduced into the simulation yet, hence only the simulated noise was used in the following study.

The cell information is only accessible in the Event Summary Data (ESD) files which are not designed for the user analysis, but only for performance studies on limited samples. Hence, even though this analysis was carried out directly on the ESD files, a specific gap finding tool is planned to be included in the ATLAS software dumping its results (which will be quite small in size) to the AOD files. The cells are accessed via the `AllCalo` container.

The rapidity gap reconstruction using cells is done in two steps. First, all cells in the event are

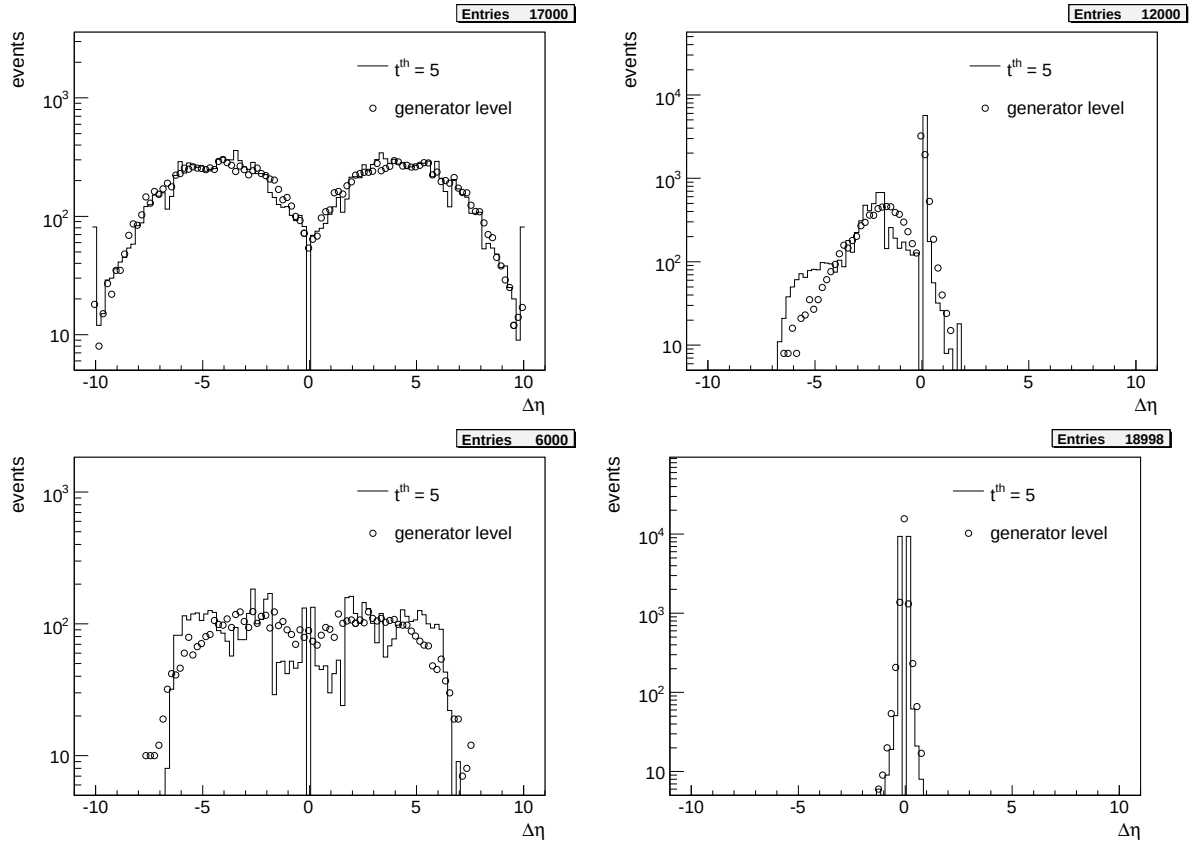

Figure 8.9: Rapidity gap reconstructed with the cell-based method with a threshold $t^{th} = 5$ for two-photon dimuons (top-left), CEP dijets (bottom-left), SD dijets (top-right), non-diffractive dijets (top-bottom).

looped over and only cells with the energy in terms of cell electronic noise above a threshold, $|t| > t^{th}$, are considered. The energy is summed in φ and saved in 100 bins in rapidity for the detector coverage of $-5 < \eta < 5$ creating rings of energy. The threshold on the absolute value of the significance t is applied to cancel possible noise fluctuations.

Secondly, using these bins of visible energy, rapidity gaps are defined as completely empty regions from the detector edge. In the language of the previous sections, the rapidity gap size is defined as

- $\Delta\eta_{gap} = 5 - \eta_{ring}^{max}$
- $\Delta\eta_{gap} = -5 - \eta_{ring}^{min}$

in terms of the most forward/backward ring with non-zero energy η_{ring}^{max} and η_{ring}^{min}, respectively. Note again that the negative size of rapidity gap corresponds to a presence of a gap on the negative side of the detector.

The cell threshold t^{th} serves now as a parameter which can be adjusted to obtain the optimal performance of the gap reconstruction. It should be chosen such that the method could be used in a wider range of processes. We are going to tune it on the already mentioned processes for a gaussian distribu-

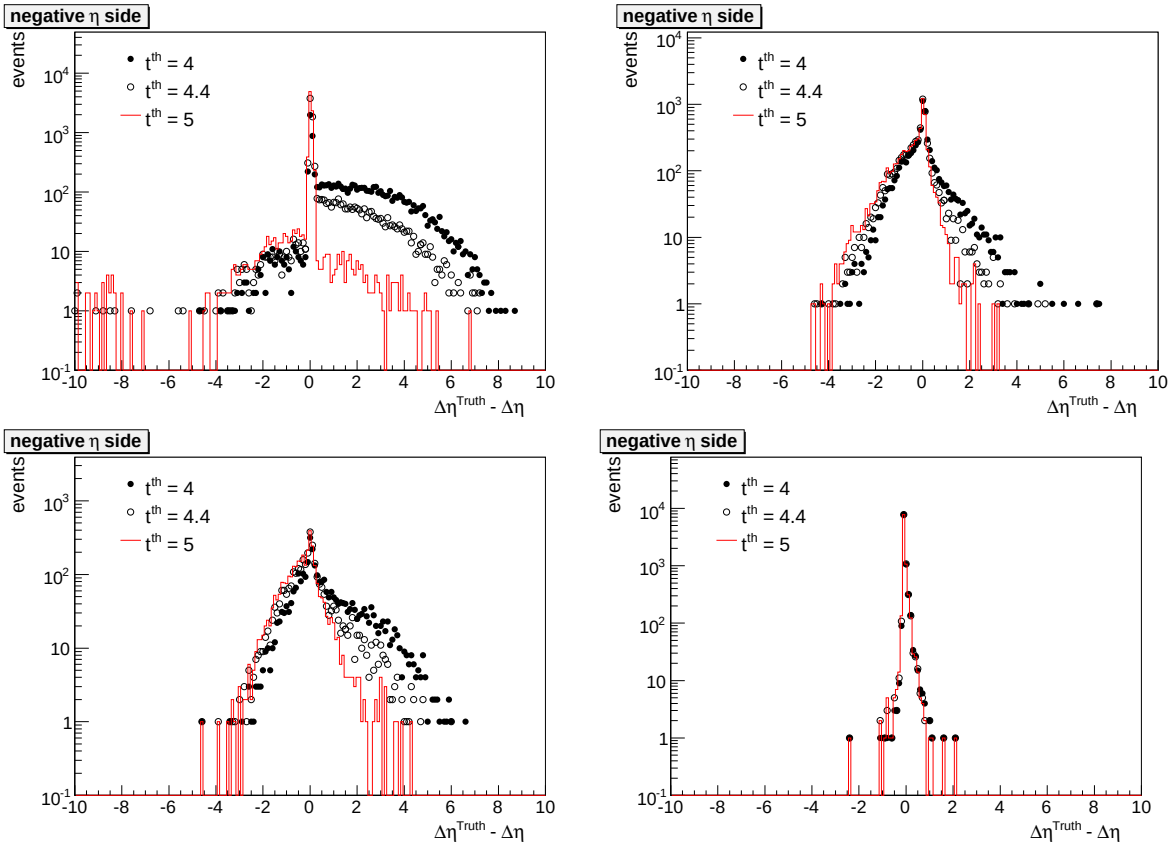

Figure 8.10: Rapidity gap size resolution with cell-based analysis for two-photon dimuons (top-left), CEP dijets (bottom-left), SD dijets (top-right), non-diffractive dijets (top-bottom) shown for various cell thresholds $t^{th} = 4, 4.4, 5$.

tion of the cell noise, but the same will have to be done using data where non-gaussian tails of the noise might play a role.

In Figure 8.9 the reconstruction performance of the cell-based analysis is shown for two-photon dimuons, CEP and SD dijets, and non-diffractive dijets. The cell threshold was set to $t^{th} = 5$ for which the mean number of noise cells in event is small, 0.1 (see Figure 8.5). The rapidity gap distribution is shown in empty circles whereas the results of the cell-based method are shown in full line. The higher threshold leads in general to better performance in the rapidity gap reconstruction.

In Figure 8.10, the rapidity gap size resolution $\Delta\eta_{gap}^{Truth} - \Delta\eta_{gap}$ for three threshold parameters $t^{th} = 4, 4.4, 5$ is shown. For small values of the threshold, the reconstructed gap size is underestimated due to the presence of noise cells. For high values of the threshold, however, a positive bias in the gap reconstruction can be introduced. Increasing the cell threshold generally improves the rapidity gap resolution. The largest improvement is obtained for the two-photon events which have large gaps and the improvement is also important in case of CEP dijets. Although the resolution improvement is smaller for SD dijets, small gaps that were spoiled by noise are correctly reconstructed (top-right). It is important to emphasize that by increasing the cell threshold, we do not get fake gaps from the non-diffractive samples where no rapidity gap should be present. The resolution distribution for non-diffractive events (bottom-right) stays basically the same for all the thresholds.

Threshold t^{th}	two-photon dimuons	CEP dijets	SD dijets	non-diffractive dijets
4.0	1.54±1.76	0.60±1.33	-0.01±0.25	-0.07±0.08
4.4	0.54±1.29	-0.02±1.00	-0.02±0.20	-0.07±0.08
4.8	0.05±0.80	-0.29±0.79	-0.02±0.17	-0.08±0.08
5.0	-0.03±0.77	-0.31±0.75	-0.03±0.17	-0.08±0.08
5.2	-0.07±0.77	-0.37±0.74	-0.03±0.18	-0.08±0.08
5.5	-0.13±0.86	-0.41±0.73	-0.03±0.18	-0.08±0.08
6.0	-0.22±1.09	-0.45±0.73	-0.04±0.18	-0.08±0.08

Table 8.2: Parameters of the gap resolution distributions from Figure 8.10 for various cell thresholds t^{th}.

The mean and variations of the resolution distributions are shown in Table 8.2 for $t^{th} = 4.0 - 6.0$. The optimal value of the threshold parameter for which the variance and mean (bias) of the resolution is the smallest lays between t^{th}=4.8-5.0. In the following, we chose $t^{th} = 5.0$ as the default.

The gap resolution as a function of the rapidity gap size η is shown for $t^{th} = 5$ in Figure 8.11 for the same set of processes. We see that the optimal threshold is such that it interpolates between overestimating small gaps, and underestimating large gaps. This is best visible in the distribution for dimuon events (top-left). Certainly, using the same energy threshold for gaps of different size is the cause of this effect since the probability that large gaps will be spoiled is larger than for the small ones.

An alternative method was therefore developed in which the cell threshold t^{th} varies as a function of the gap size which is to be found. More concretely, the free parameter of the method is a mean number of noise cells $\langle n \rangle$ in a gap (of any size). When looking for a rapidity gap of size $\Delta\eta$ from the side of the detector, the algorithm calculates the number of cells in this $\Delta\eta$ region and evaluates the corresponding cell threshold t^{th}, which would yield the desired $\langle n \rangle$ using (8.3). In this way, large rapidity gaps are reconstructed with a higher threshold and small gaps are reconstructed with a smaller one, depending on the defined $\langle n \rangle$ parameter. Although this method improves the resolution of two-photon dimuons, the improvement in CEP and diffractive dijets is very small. Moreover, the overestimation of gap sizes in these events as already discussed is still present, confirming that this effect is related to small particle energies on the border of the gap in these events. Since this algorithm takes more computing time, because it is necessary to loop over the cell collection many times (for every gap size), the implementation of this algorithm as a general reconstruction tool is not acceptable.

In the case of exclusive and diffractive dijet productions, about the same fraction of events is reconstructed with a larger gap over the whole eta range. This is because some particles from pomeron remnants have small energies which do not pass the cell threshold. It was observed that this effect does not disappear when lowering t^{th}, and hence the energy of these particles must be rather small.

8.7 Final remarks

In this section, we first investigated the rapidity gap reconstruction using calorimeter TopoClusters, the standard ATLAS objects present in AOD files. We found that when these objects are used, the reconstruction of large rapidity gaps ($\Delta\eta > 5$) is not possible because the noise fluctuations always spoil these large gaps. New gap finding tool was then developed with a gap reconstruction based on cell energies

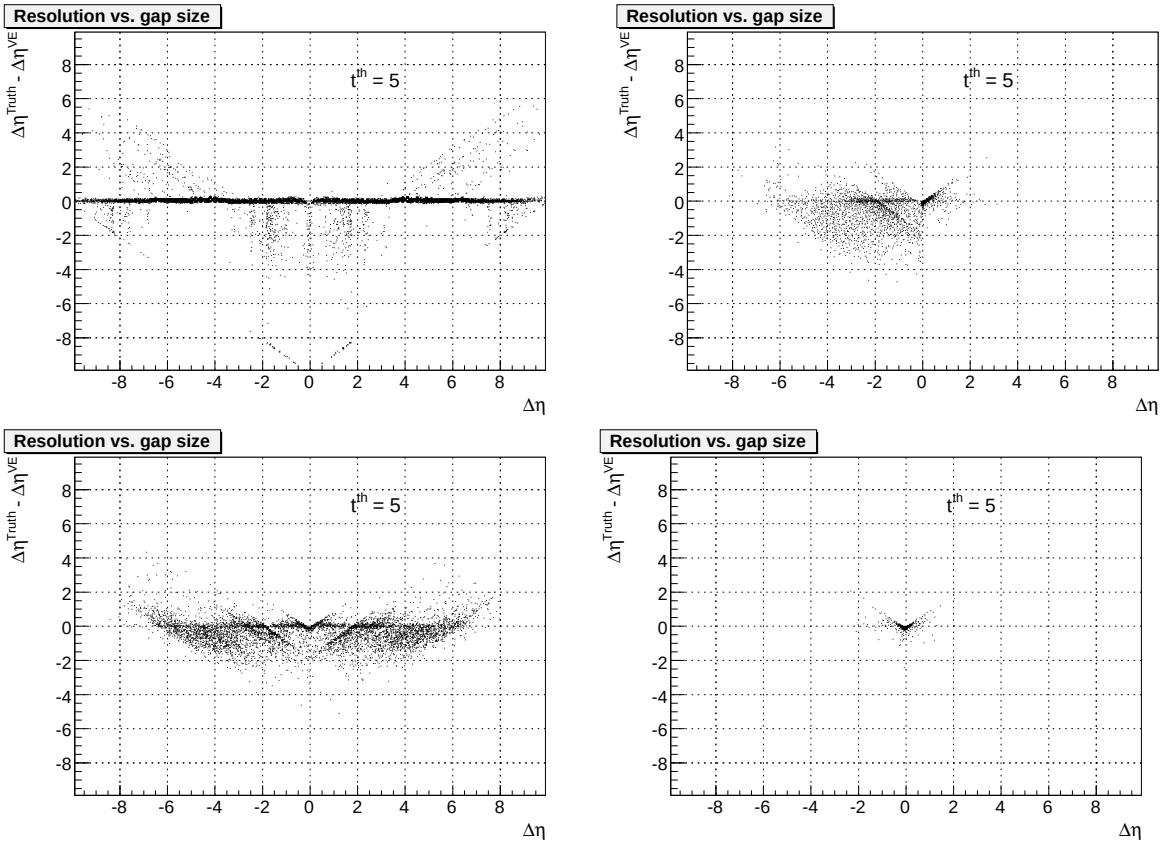

Figure 8.11: The rapidity gap resolution for two-photon dimuons (top-left), CEP dijets (bottom-left), SD dijets (top-right), non-diffractive dijets (top-bottom).

which are sufficiently high in comparison to the cell typical electronic noise σ_{cell}^{noise}. We showed, that large rapidity gaps can be correctly reconstructed if energies higher than 4.8-5σ_{cell}^{noise} are considered. The application of this tool concerns mainly exclusive processes like the two-photon production of dijets, dimuons, WW, or central exclusive production of dijets in which the rapidity gaps are large. The improvement for SD dijets was quite small, but might concern diffractive events with a small produced mass like the SD J/ψ production. The introduction of a higher threshold did not imply the reconstruction of fake rapidity gaps in non-diffractive events which could easily overwhelm the diffractive signal due to large non-diffractive cross sections.

Bibliography

[1] V. Juránek, A. Kupčo, P. Růžička, private communication.

[2] V. A. Khoze, A. D. Martin and M. G. Ryskin, Eur. Phys. J. C **18** (2000) 167 [arXiv:hep-ph/0007359].

[3] Acosta, D *et al.* [CMS Collaboration], CMS physics: Technical design report, CMS-TDR-008-001, p. 197, 2006.

[4] W. Lampl *et al.*, Calorimeter clustering algorithms: Description and performance, ATL-COM-LARG-2008-003, 2008.

[5] `https://twiki.cern.ch/twiki/bin/view/Atlas/ClusterMoments`, Sept. 2009.

Conclusion

9

In this thesis, we have studied the hard diffractive and exclusive processes occurring in hadron-hadron scattering. The most significant characteristics of these processes are an intact proton leaving the interaction point deflected at small angles and an empty or partially empty central detectors.

Much has been learned about these unique diffractive events exhibiting rapidity gaps devoid of particles at the HERA ep collider. Since a hard scale is present in these events (transverse jet momentum for instance) the diffractive proton structure can be defined in terms of partons in the same way as in standard inelastic interactions, where the proton dynamics is governed by perturbative QCD. After presenting the overview of the SM of particle physics, we tried to summarize the main points of hard diffraction in the introductory Chapter 2.

At the Tevatron proton-antiproton accelerator, another special type of events was recorded in which a dijet system was observed and nothing else. The extraction of these rare and strikingly clean events is quite complicated and requires a good understanding of hard diffraction phenomena, the diffractive parton densities, in particular. In Chapter 5, we therefore compared the available inclusive, exclusive and the soft color interaction models to the Tevatron dijet mass fraction measurement. We found that the Ingelman-Schlein factorized model of inclusive diffraction together with the KMR model of exclusive production gives the best description of data.

In the next decade or so, the Large Hadron Collider will be colliding protons at high center-of-mass energies never reached before. The production rates of the central exclusive events in which various final states like dijets, diphotons or the Higgs boson could be produced, will be sufficiently high to investigate these events in detail. The forward physics community has high expectations of the forward physics program at the LHC because for the first time, if the proposed detectors are approved by ATLAS/CMS Collaborations, the central detectors will be equipped by forward detectors tagging the scattered protons on either sides of the main detector. They will allow to measure the tracks of scattered protons produced in hard diffraction or in exclusive events. Such detectors around the ATLAS detector are called Atlas Forward Proton (AFP) detectors. In Chapter 3, we described the main ATLAS detector, whilst in Chapter 6, details on the forward detectors were given and studies of the proton tracking through the beam lattice elements from the ATLAS interaction point to the forward detector stations were presented.

Another unique exclusive process occurring in the collision of high energetic proton beams at the LHC are two-photon exchanges. Protons emit quasi-real photons which interact. As a consequence, the LHC hadron machine will not only be used as a proton machine, but also as the photon-photon collider.

To accommodate as many models as possible concerning forward physics into one simulation framework, several new features were implemented in the Forward Physics Monte Carlo (FPMC) during the three year Ph.D. studies. They are described in Chapter 4. Briefly, the new diffractive parton densities as measured at HERA to enable studies of inclusive diffraction were implemented and used for the search of the exclusive signal at the Tevatron as already mentioned. However, the work focused mainly on the implementation of two-photon exchanges. Having done that, several studies using the two-photon production followed.

The first one to be mentioned is the investigation of the position alignment of the AFP detector located at 220 m downstream and upstream from ATLAS. It was shown that comparing the scattered proton kinematics calculated from the dimuon pairs detected in the central detector to the information obtained from the forward detectors, a detector alignment to 10 μm could be achieved as described in the second part of Chapter 6.

Second, two-photon events can be used to search for new beyond standard model physics. In Chapter 7, the sensitivities to anomalous quartic $WW\gamma\gamma/ZZ\gamma\gamma$ and triple gauge $WW\gamma$ couplings are discussed. Besides the fact that the two-photon production offers a complementary method to the standard inelastic events to determine these couplings, the interesting result is that the sensitivities to anomalous quartic couplings could be carried out already with a limited collected luminosity.

Since the start-up of the LHC machine should take place within two months or so from now, it is quite important to prepare the analyses studying the diffractive and exclusive events because data with small number of multiple interactions per bunch crossing, required for these analysis will be taken in a short time after the start-up. The result of this effort is presented in Chapter 8, where a new tool to identify rapidity gaps in the diffractive and exclusive events using the ATLAS calorimeter is presented.

As the waiting for the data was sometimes frustrating, the author looks forward to the interesting physics which will come out from the ingenious machine and challenging detectors at CERN, Geneva. In the same time he hopes that the work summarized in this manuscript will be helpful to others.